University of New Mexico
UNM Digital Repository

Nuclear Engineering ETDs | Engineering ETDs

7-12-2014

Moment-Based Accelerators for Kinetic Problems with Application to Inertial Confinement Fusion

William Taitano

Follow this and additional works at: https://digitalrepository.unm.edu/ne_etds

Recommended Citation
Taitano, William. "Moment-Based Accelerators for Kinetic Problems with Application to Inertial Confinement Fusion." (2014).
https://digitalrepository.unm.edu/ne_etds/7

This Dissertation is brought to you for free and open access by the Engineering ETDs at UNM Digital Repository. It has been accepted for inclusion in Nuclear Engineering ETDs by an authorized administrator of UNM Digital Repository. For more information, please contact disc@unm.edu.

William T. Taitano

Candidate

Nuclear Engineering

Department

This dissertation is approved, and it is acceptable in quality and form for publication:

Approved by the Dissertation Committee:

Anil K. Prinja , Chairperson

Dana A. Knoll

Cassiano Ricardo Endres De Oliveira

Deborah Sulsky

Moment-Based Accelerators for Kinetic Problems with Application to Inertial Confinement Fusion

by

William Tsubasa-Tsutsui Taitano

B.S., Space Physics, Embry-Riddle Aeronautical University, 2007
M.S., Nuclear Engineering, University of Idaho, 2010

DISSERTATION

Submitted in Partial Fulfillment of the
Requirements for the Degree of

Doctor of Philosophy
Engineering

The University of New Mexico

Albuquerque, New Mexico

May, 2014



©2014, William Tsubasa-Tsutsui Taitano

Dedication

To ICF kinetic plasma physics with charge-separation,

For being so nonlinear, so multi-scale both in time and space, so impossibly difficult, and so completely unreasonable from the get go. She always made me cry. I love but also hate her at the same time. It is such a complicated relationship.

-Will

Biography

William Tsubasa Taitano was born on December 08, 1985 at Seattle, Washington to parents Carlos and Wakaba Taitano, along side older brother, Carlos, and younger brother, Matthew. He spent his childhood growing up in Seattle (USA), Kobe (Japan), and Guam (USA). He attended the C.L. Taitano elementary school, bishop Baumgartner middle school, and the Evangelical Christian Academy high school. During his middle school and high school years, William was heavily devoted to his musical interest, however, decided to shift his focus during his senior year in high school. After graduating from high school in 2003, he attended the Embry-Riddle Aeronautical University (ERAU) with a major in Space Physics and minor in Aerospace Engineering. There, he was exposed for the first time in life, to engineering, science, and math. An influential point in his university life was his exposure to the possibilities of anti-matter and nuclear technology in space exploration through a presentation that was given by Dr. Gerald Jackson from the Hbar Technologies, LLC. The subsequent exposures to plasma physics through Dr. Richard Link and computational fluid dynamics (CFD) through Dr. Shigeo Hayashibara during his junior year solidly rooted his interest in computational plasma physics. During his senior year, his undergraduate thesis of *"Magnetohydrodynamic control of flow through a converging-diverging nozzle"* has caught the attention of Dr. Steve Howe at the Center for Space Nuclear Research (CSNR) at the Idaho National Laboratory (INL).

Upon completing his bachelor's degree at ERAU in December of 2007, he subsequently begun his job at CSNR/INL in May of 2008. The job opportunity allowed him to apply his CFD skills to perform a thermal hydraulic analysis of fission-based space nuclear and terrestrial nuclear systems applications. The job opportunity had also led William to Dr. Dana A. Knoll, who at the time was working at INL (currently at LANL). Dr. Dana A. Knoll brought William deeper into the field of computational plasma physics. During his stay at CSNR, William pursued the master's of science degree in Nuclear Engineering at the local Idaho Falls branch of University of Idaho under the advise of Dr. Dana A. Knoll. William's master's thesis titled *"Development of a Jacobian-Free Newton-Krylov method with kinetic enslavement to implicitly solve Vlasov-Poisson system in plasma physics"* exposed him to the rich field of implicit methods for nonlinear system of equations, which is currently one of his strongest interest in research. Upon completing his master's degree in August of 2010, William moved to the University of New Mexico in January of 2011 to pursue his doctor of philosophy in nuclear engineering under the advise of Dr. Anil K. Prinja and Dr. Dana A. Knoll. He is extremely fortunate to be able to do computational physics, both algorithm development and application, as well as plasma physics. William did not think he would be able to continue pursuing plasma physics after completing his undergraduate degree, and he is greatly in-debt to Dr. Dana A. Knoll for leading him back into the field and providing him with countless opportunities. In May of 2011, William married his long time fianceé, and the love of his life, Mika Tsutsui, Las Vegas (NV not NM) style, and lived happily ever after... or did he?

Acknowledgments

The three years of Ph.D. experience have been, with no doubt, the most demanding period of my life and it would have been impossible to achieve without the support of many people. I believe that every step along the way, even prior to beginning my Ph.D. research, paved my path and helped me be the person who I am today. It is therefore impossible to name everyone who has contributed to my achievement today, both from a psychological and technical point of view. However, I will try to name all whom I can.

From the University of New Mexico (UNM), I would like to first and foremost, thank my advisors Dr. Anil K. Prinja and Dr. Dana A. Knoll (also at LANL), who trained and grew me as both, a researcher and a human being. They have been a constant source of inspiration and enlightenment. Although their intellectual greatness have occasionally played a role in my mild symptoms of depression, the immense amount of material I have learned from them offsets that damage. To put it simply, it is impossible to describe the sense of gratitude I have for them. Especially Dr. Dana A. Knoll who was also my masters thesis advisor. I thank him for putting up with me for all the years and being extremely patient even during my low days of productivity and motivation. I would like to thank all of my other committee members, Dr. Deborah Sulsky and Dr. Cassiano Ricardo Endres De Oliveira for always being supportive and showing interest in my work. I appreciate Dr. Cassiano for agreeing to be in my committee member at such short notice. I thank Dr. Deborah Sulsky for providing me reading materials concerning issues with non-monotonicity of first order upwind discretization for first order operators on a highly skewed nonuniform mesh. Although I was not able to resolve the issue, the reading materials provided me with additional future research ideas. I will like to also especially thank Dr. Norm Roderick, who could not be in my committee member due to University restrictions and guidelines. I thank him for the special topics class he taught me on the subject of radiation-magnetohydrodyanmics (RMHD), which introduced me to various hydrodynamic instabilities, the intricate coupling between plasmas and radiation, and other various inertial confinement fusion (ICF) physics. I will like to thank the University of New Mexico for the use of the official seal on the title page of this dissertation. Also, from the Office of Graduate Studies (OGS), I will like to thank Mr. Douglas Weintraub for being very laid back with my dissertation. It's been a pleasure to interact with him and I will like to thank him for being extremely flexible with my dissertation document and allowing me to express my sense of humor in it.

From the UNM nuclear engineering department, I will like to thank my fellow office mates Mr. Dave Dixon, Mr. Matt Gonzales, and Mr. Nick Myers who have from the earliest days, been supportive of my work and showing interest. The student seminars were especially intellectually stimulating and it was constantly a source for new research ideas. I will also

like to thank Dr. Mike Rising, who has graduated before me and is currently working in the XCP-3 group for sharing his UNM LaTeX template for the proposal documentation. From the chemical engineering department, I will like to thank Mr. Eric Benner and Mr. Mike Fleharty for always being a constant source of interdisciplinary inspiration. The field of *Density Funcitonal Theory* (DFT) has provided me with a new idea of extending the HOLO moment-based acceleration scheme for quantum mechanical system. Finally, I would like to thank all of them for joining me with the occasional lunch beers and conversations. It is difficult to stress how much it helped me to *vent the steam*.

From the Los Alamos National Laboratory (LANL), I will like to thank the *Computational Co-design for Multi-Scale Application to Natural Science* (COCOMANS) for funding my graduate research assistantship (GRA) position at both UNM and LANL. I will like to personally thank both Dr. Anil K. Prinja (UNM) and Dr. Dana A. Knoll from the T-3 group for working around the mind boggling bureaucracy to get me funded full time for my dissertation research. I will like to thank Dr. Luis Chacón from the T-5 group for his insights into asymptotic theory and conservation property preserving discretizations, which has influenced a large portion of my dissertation. His insights into both physics and numerics have always amazed me. I would like to thank Dr. Andrei Simakov from the XCP-6 group for the advice on the interview talk presentation that I had to give for his group on December 17th of 2013 along with other ICF physics discussions. I would also like to thank **Doctor** Jeffrey Willert from the T-3 group for listening to my distress during lunch on a daily basis, especially when my dissertation research was not progressing, but also for the intellectual interaction which always inspired me. I also thank him for introducing me to the Anderson acceleration scheme, and residual monte carlo methods which gave me more ideas for research. I will like to thank **Master** Joshua Payne from the CCS-7 group for his assistance on programming related questions. I will like to thank Dr. Guangye Chen for all of the numerics and physics discussions for the particle-in-cell (PIC) in modeling a collisionless plasmas. I will like to thank Dr. Ryosuke Park and Dr. Christ Newman from the T-3 group for their technical and psychological support throughout my days since Idaho National Laboratory (INL). I will also like to thank them for all the beers and dinners they bought me, and quite frankly, am terrified of all the tabs I have. I will like to thank Dr. Jon Reisner from the XCP-4 group for the discussions on single fluid gas dynamics and physics insights on the subject. Finally, I will like to thank Dr. Erik Vold from the XCP-2 group, who I see in the bus commute to Los Alamos on a fairly frequent basis for always showing interest in my work, but also inviting me to his house for Christmas during the final days of my Ph.D. research and giving me a psychological boost.

From the Embry-Riddle Aeronautical Univerusity (ERAU), I will like to notify my undergraduate advisors and professors, Dr. Phillip Anz-Meador, Dr. Darrel Smith, Dr. Shigeo Hayashibara, and Dr. Richard Link for this achievement. Although I did believe in myself, considering my first semester grades at Embry-Riddle (FYI, it was not good), it is still difficult to believe how far I have come. I will like to thank them for providing me the opportunity to venture into the field of plasma physics, computational physics, and science in general. It has been, and hopefully will continue to be an adventure. From the University of Idaho (UofI), I will like to thank my master's committee members, Dr. Fred Gunnerson

(aka Freddy-G) and Dr. Akira Tokuhiro for their words of encouragements. From the University of Colorado, Boulder, I will like to thank Mr. Chris Leibs from the applied math department for helping me understand Krylov methods better, but also for providing me a LaTeX template for notes and quick write-ups, which has helped a lot. I will also like to thank Dr. Yu Takahashi, who is now working at the Jet Propulsion Laboratory (JPL), but graduated from UC Boulder in Summer of 2013. I will like to thank him for being a source of encouragement and inspiration although we haven't interacted much in the last few years. It was encouraging to see that a person who graduated the same year from the same undergraduate institution finishing his Ph.D. and moving onto a full time professional position at such a prestigious institution. From the University of Wisconsin, Madison, and a long time colleague from the days at Embry-Riddle Aeronautical University, I will like to thank Mr. Adrian Akerson for his words of encouragement. We both had our difficulties with our dissertation projects and it was great to be able to have another person to just relate the experience with. From the EVA airlines I will like to acknowledge Mr. Tatsunori Makidao, who was also my room mate during our days at ERAU. I will like to thank him for sparing his busy time during our first (or second) semester at ERAU, teaching me the basics and some applications of trigonometric identities as well as tricks in easily memorizing them. These tricks helped me pass my calculus II course during my Freshmen year. I still treasure many of these tricks to date. From the Idaho National Laboratory (INL), I will like to thank Dr. Steven Howe at the Center for Space Nuclear Research (CSNR) for hiring me on after completing my undergraduate degree (and saving me from becoming homeless). He provided me the privilege of *getting my foot into the door*. I enjoyed all of the ideas and opportunities he provided. I especially enjoyed the Mars Hopper project, which kept me working late nights (voluntarily). I thank Ms. Kristy Martin, Ms. Delisa Rogers, Dr. Robert O'brien, Mr. Brian Gross, and everyone else who have made my life enjoyable at my first work outside of school. From the Areva Corporation, I will like to thank Dr. Jon Webb, who I also very enjoyed working with on the conceptual and numerical design of a CERMET based nuclear thermal rocket (NTR) during our days at INL. The birthdays were always the best.

From my family, I thank both of my parents, Carlos and Wakaba Taitano, for their love, encouragement, and support throughout the years. I appreciate all the financial sacrifices made for me and regret my lack of performance during my first year in undergraduate. I hope this achievement makes them both proud. I will like to thank my siblings, Carlos and Matthew, for their once started, never give-up spirit, which has always been an encouragement for me. It helps to have siblings who are constantly challenging themselves. I thank them both for listening to my complaints on my constant fatigue, especially during the final years of my Ph.D. research. I will like to thank all of my cousins: Peter, Michael, Matthew, Lourdes Diaz; Naoki and Yumi Nakamura; George, Rita, Jacqueline, Christopher Taitano-Johnson; Kana Taitano; John, Norma, and Daniel Phillips; my aunts and uncles: Jeanine and Alan Diaz; Maki and Hiromi Nakamura; Sean and Evangeline Phillips; Billy and Sachiko Taitano; George and Therese Taitano-Johnson; Ralph Unpingco; and my grandmother and grandfather Virginia and Burt Unpingco; for always keeping me in their prayers, supporting, and encouraging me for my academic pursuit. Also, I would like to thank my grandparents on my mothers side: Kuni and Chikae Nakamura, who did not live to see this day come. Al-

lowing us brothers to stay with them in Japan during our K-12 summer vacation gave us the opportunity to appreciate the Japanese culture and heritage in a much deeper manner than one can otherwise do without living in Japan. I still believe that this childhood experience ultimately led me to meet my wife, who has given me much of the strength to endure this highly demanding Ph.D. experience. Finally, I will like to thank my wife's family, Yoshiaki and Taeko Tsutsui; Tsutomu, Emi, Yuuki, Yui, and Yuuka Nakao; Kazuyuki, Miyoshi, Ayaka, and Suzuna Kanada; for all of their psychological support and words of encouragements for my academic pursuit, and being very understanding of my situation, especially during the final years of my Ph.D.

Finally, I will like to thank my wife, Mika Tsutsui. １０年間、本当に支えてもらってばかりで何一つとして美加のためにしてやれる事が出来なくて本当に申し訳ない。毎日俺より早く起きて、俺より後に寝て、毎日欠かさず弁当を作ってくれて、帰りが遅くても寝ないで、温かい晩ご飯を作って待っててくれて、博士の３年間は得に支えてもらって感謝してもしきれません。美加が俺と結婚するために犠牲にした家族との時間、仕事、友達、その辛さは想像も出来ません。異国の地での新しい言葉の壁、新しい友達、新しい仕事探しなど、何も助けてあげられなく、自分の無力さを痛感したと同時に、力をもらえました。美加はどんな逆境にいても、この三年間、一度も文句を言わず、俺と一緒に居る時はいつも笑顔を絶やさなかったね。美加のこの芯の強さには本当にいつも感心しました。正直、美加のこの内面の強さに励まされたおかげで、博士のゴールラインまでなんとか辿り着けました。研究が全然進まなくて挫折を何度も経験して、その度に美加には慰めてもらっては「もうちょっと！最後までがんばって！」と励ましてもらったね。いつも元気を与えてくれてありがとう。キツくて心が折れそうになった時にいつも持ち上げてくれてありがとう。美加にはいつも与えてもらってばかりで何も返してあげられなくてほんとうにごめん。美加のおかげで俺の人生、本当に満ち足りています、ありがとう。 I know I don't say this enough, but I love you, and appreciate all of the sacrifices you have made for me, and I really can't ask for anything more in my life.

Moment-Based Accelerators for Kinetic Problems with Application to Inertial Confinement Fusion

by

William Tsubasa-Tsutsui Taitano

B.S., Space Physics, Embry-Riddle Aeronautical University, 2007
M.S., Nuclear Engineering, University of Idaho, 2010

Ph.D., Engineering, University of New Mexico, 2014

Abstract

In inertial confinement fusion (ICF), the kinetic ion and charge separation field effects may play a significant role in the difference between the measured neutron yield in experiments and the predicted yield from fluid codes. Two distinct of approaches exists in modeling plasma physics phenomena: fluid and kinetic approaches. While the fluid approach is computationally less expensive, robust closures are difficult to obtain for a wide separation in temperature and density. While the kinetic approach is a closed system, it resolves the full 6D phase space and classic explicit numerical schemes restrict both the spatial and time-step size to a point where the method becomes intractable. Classic implicit system require the storage and inversion of a very large linear system which also becomes intractable. This dissertation will develop a new implicit method based on an emerging moment-based accelerator which allows one to step over stiff kinetic time-scales. The new method converges the solution per time-step stably and efficiently compared to a standard Picard iteration. This new algorithm will be used to investigate mixing in Omega ICF fuel-pusher interface at early time of the implosion process, fully kinetically.

Contents

List of Figures **xix**

List of Tables **xxiv**

List of Algorithms **xxvi**

1 Introduction **1**

2 Inertial Confinement Fusion (ICF) Physics **5**

2.1 Controlled Fusion Reaction and Confinement Schemes 6

2.2 ICF Physics 9

2.3 ICF Neutron Yield Difficiency and Low Fuel Temperature 13

2.4 Recent Studies and Motivation for Kinetic Treatment of Ions 15

2.5 A New Early Mix Mechanism 18

3 Background on Numerical Methods **21**

3.1 Time Integration Schemes 21

3.2 Nonlinear Solvers 23

3.3 Moment-Based Nonlinear Accelerator 28

4 Moment Acceleration of Collisionless Plasma 38

4.1 Introduction 39

4.2 Moment Accelerated Vlasov Ampère 41

4.2.1 Problem Statement 42

4.2.2 Derivation of moment system for Vlasov-Ampère System 43

4.2.3 Motivation for a moment approach 45

4.2.4 Modification of the LO equations: discrete consistency 46

4.2.5 Modification of the LO equations: density-normalized stress-tensor . . 48

4.3 Solver and Discretization 50

4.3.1 Higher Order System: Implicit Charge-Conserving Particle in Cell . . 50

4.3.2 Lower Order System: Staggered Finite Differencing 53

4.4 Algorithm: Nested HOLO Iteration 55

4.5 Benchmark and Test Case Results 57

4.5.1 Single species: Landau damping 58

4.5.2 Single species: Two stream instability 61

4.5.3 Two species: Ion acoustic shockwave 62

4.5.4 Picard Convergence Properties vs. Δt 64

4.6 Importance of Consistency Term and density normalized stress-tensor 65

4.7 Conclusions 69

5 Conservative Discretization for a Collisionless Plasma 70

5.1 Introduction 71

5.2 HOLO Equations for the Vlasov-Ampère System 73

5.2.1 Derivation of the coupled moment/Vlasov-Ampère System 74

5.2.2 Discrete Consistency Terms 76

5.3 Charge, Momentum, and Energy Conserving Discretization 77

5.3.1 Charge-Conserving Discretization 79

5.3.2 Momentum-Conserving Discretization 80

5.3.3 Energy-Conserving Discretization 82

5.3.4 Charge-and-Momentum Conserving Discretization 85

5.3.5 Charge-and-Energy Conserving Discretization 86

5.3.6 Combined Charge, Momentum, and Energy Conserving Discretization 88

5.4 Discretization and Solver: HO and LO System 89

5.4.1 HO System: Fully Implicit Charge, Momentum, and Energy Conserving Preconditioned JFNK Solver 89

5.4.2 LO System: Physics Based Preconditioned JFNK 91

5.4.3 HOLO Accelerator Algorithm with Charge Momentum and Energy Conserving Discretization 93

5.5 Numerical Results 94

5.5.1 Landau Damping 95

5.5.2 Two-Stream Instability 95

5.5.3 Ion Acoustic Shockwave (IASW) Problem 96

5.6 Conclusion 99

6 Moment Acceleration of Collisional Neutral Gas 101

6.1 Introduction 102

6.2 Neutral Gas Dynamics Boltzmann Transport Equation (HO System): BGK Collision Operator 104

6.2.1 Implicit Time Integration and Picard (Source) Iteration (HO System) 105

6.3 Self-Consistent Fluid Moment equations 108

6.4 HOLO Moment Acceleration Algorithm 111

6.4.1 HO Discretization 113

6.4.2 LO Discretization 114

6.4.3 Discrete Consistency Terms 115

6.4.4 HOLO Algorithm 117

6.5 Results 118

6.5.1 Sod shock tube 119

6.5.2 Strong Shock tube with Variable τ 126

6.6 Conclusion 130

7 Moment Acceleration of a Collisional Plasma 132

7.1 Introduction . . . 133

7.2 Governing Equations . . . 134

7.2.1 Vlasov-Fokker-Planck Equation (HO System) . . . 135

7.2.2 Time- and Length-Scales of VFPA . . . 138

7.2.3 Ampère's equation . . . 140

7.2.4 Moment System + Ampère's Equation (LO System) . . . 140

7.3 HOLO Moment Acceleration Algorithm . . . 143

7.3.1 Discrete HO System . . . 144

7.3.2 Discrete LO System . . . 148

7.3.3 HOLO Iteration Algorithm . . . 151

7.4 Numerical Tests . . . 152

7.4.1 Two-Species Thermal Equilibration Problem . . . 153

7.4.2 Two-Species Collisional Ion-Acoustic-Wave Problem . . . 155

7.4.3 Periodic Two-Species Collisional Density Gradient Evolution Problem 158

7.5 Conclusion . . . 161

8 Kinetically Enhanced Mixing of ICF Omega Capsule Pusher into Fuel 165

8.1 Introduction . . . 165

8.2 Setup of Ionization Gradient at Fuel-Pusher Interface . . . 168

8.3 Charge Separation and Double Layer Field . . . 169

8.4 Early Time Double-Layer Assisted Kinetic Enhancement of Pusher Mix into Fuel 173

8.5 Problem Setup 173

8.5.1 Models and Approximations 175

8.5.2 Numerical Initial Conditions 176

8.6 Solver 179

8.6.1 Nonuniform Mesh Generation 179

8.6.2 Adaptive Time Stepping 180

8.6.3 Remapping 182

8.6.4 Hybrid Solver 184

8.6.5 Open Boundary Condition 186

8.6.6 Code Framework and Architecture 187

8.7 Initial Field Structure, Pre-Sheath, and Ion-Acceleration 189

8.8 Sensitivity Study of Early Time Field 192

8.8.1 Sensitivity to Density 193

8.8.2 Sensitivity to Driver Strength 194

8.8.3 Sensitivity to Temperature 195

8.8.4 Sensitivity to Configuration Space Cell Resolution 196

8.8.5 Sensitivity to Initial Gradient Scale-Length 197

8.9 Sustained Kinetic Effects 198

8.10 Carbon Ion mix into Fuel 200

8.11 Conclusion 204

9 Conclusions **205**

9.1 Review of the Algorithm Development 205

9.2 Review of the Interface Physics 208

9.3 Future Work 210

References **212**

Appendices **222**

A Exposure of Stiff Hyperbolic Wave in the VA LO System **223**

B JFNK to Solve for VA LO moment System **225**

C Asymptotic Preserving Time Discretization **228**

D VFPA LO System: Continuity, Momentum, and Ampère's Equation **231**

E Block Preconditioning for VFPA LO System **234**

F Discrete Consistency Terms for VFPA **236**

F.0.1 LO Consistency Terms 237

F.0.2 HO Consistency Terms 240

G Picard Iteration for a 0D1V Fokker-Planck Equation **243**

H Moment Acceleration of a Purely Differential HO System **245**

Curriculum Vitae **252**

List of Figures

2.1 Nuclear binding energy versus atomic mass [26]. 6

2.2 Fusion reaction rate coefficients for the DT, DD, D-He^3, and p-B^{11} reaction [26]. 7

2.3 Illustration of the DT reaction. 8

2.4 A very simple illustration comparing different confinement schemes. 8

2.5 Comparison of Omega (left) and NIF (right) capsule. 10

2.6 Illustration of various sources for energy balance. 12

2.7 Relationship between ignition, hot-spot temperature, and areal density, $\rho_h r_h$ [26]. 13

2.8 Process of ionization gradient setup. 19

2.9 Illustration of the Ion phase-space evolution due to a double-layer field. . . 20

3.1 Comparison of convergence rate between Picard and Newton iteration for the nonlinear diffusion equation. 27

3.2 Scalar flux (left) and convergence rate (right) between the standard source iteration and QDA iteration. 34

3.3 Relative difference between the HO and LO scalar flux, ϕ, without discrete consistency. 35

3.4 Relative difference between the HO and LO scalar flux, ϕ, with discrete consistency. 37

4.1 Decay rate comparison for Landau damping 59

4.2 Time convergence study result. 59

4.3 Electric field energy growth rate for two stream instability. 62

4.4 Number density plot for both electron (left) and ion (center) is shown with the resultant electric field (right) due to the charge separation. 64

4.5 Normalized residual convergence rate of ion and electron momentum equation for the different Δt cases for the first time-step. 65

4.6 Relative difference of $\overline{nu}^{k+1/2}$ upon convergence of the improved IMM method (left) and the standard IMM (right). 66

4.7 Relative total energy of the system as a function of time. 67

4.8 Electric field structure at various times. 67

4.9 Demonstration of exposure of stiff wave physics and consequently, the reduction in nonlinear iteration with density-normalized stress-tensor (DAS) and comparison with non-density-normalized stress-tensor (NDAS). 68

5.1 Decay rate comparison for Landau damping 96

5.2 Electric field energy growth rate for two stream instability. 97

5.3 Conservation properties of the new charge-momentum-and-energy conserving discretization. 99

5.4 Solution for the ion acoustic shockwave. 99

6.1 Comparison of moments with respect to varying τ at $t = 0.065$ 121

6.2 Comparison of solutions to Sod shock tube with different discretization for the Euler limit. 122

6.3 Relative difference of n, nu, and U with tolerance = 10^{-4}, with discrete consistency enforced. 123

6.4 Relative difference of n, nu, and U with tolerance = 10^{-8}, with discrete consistency enforced. 124

6.5 Relative difference of n, nu, and U with tolerance = 10^{-8}, without discrete consistency enforced. 124

6.6 Comparison of Sod shock tube solution with implicit WENO5+ULTRA-SHARP and step differenceing (top) and the relative difference between the analytical solution (bottom). 126

6.7 Comparison of strong shock tube solution with variable τ at $t = 1$. 128

6.8 Comparison of τ and λ_{mfp} for different $\widetilde{\tau}$ for a strong shock tube at $t = 1$. . 129

6.9 K_n throughout the domain at $t = 1$. 129

7.1 Thermalization test result. 154

7.2 Plots of electron (blue) and ion (red) moments and electric field at different times in the right half of the periodic domain (note the solution is anti-symmetric for the left half). 163

7.3 Temperature of electron and ion with (left) and without (right) energy conserving discretization. A significant numerical heating of electrons is observed. 164

7.4 Comparison of charge (left), momentum (middle), and energy (right) conservation property. 164

8.1 Omega plastic ablator capsule filled with equal mixture DT fuel. 168

8.2 Surface blow off and capsule implosion process. 169

8.3 Setup of ionization gradient at the fuel-pusher interface. 169

8.4 Initial charge separation and electric field. 170

8.5 Setup of double layer. Initial setup of ionization gradient (left), evolution of density of electron and ion density (middle), and the structure of charge density ρ, electrostatic potential, ϕ, and the electric field, E (right) [130]. The double layer electric field is the region enclosed by the dashed lines. . . 171

8.6 Illustration of sheath region. 171

8.7 Illustration of pre-sheath region. 172

8.8 Early time double layer mix and later time hydrodynamic shock drag mix. . 174

8.9 Lagrangian time-history (left) and the effective ionization state (right) near the fuel-pusher interface versus time. 175

8.10 Initial condition for the interface problem. 176

8.11 Flow diagram of adaptive time-stepping. 182

8.12 Remapping process. 183

8.13 Illustration of standard inflow B.C. 186

8.14 Illustration of boundary cell 188

8.15 Illustration of the open B.C. 188

8.16 Comparison of MATLAB and C++ work distribution. 189

8.17 Initial charge separation field due to electron streaming. 190

8.18 Later double layer field at carbon ion contact surface. 191

8.19 Pre-sheath zone and ion acceleration to $\geq c^*_{s,carbon}$ (carbon ion sound speed). 193

8.20 Peak field vs. time for various $\widehat{n}$ cases. 194

8.21 Peak field vs. time for various $\widehat{u}_L$ cases. 195

8.22 Peak field vs. time for various $[\widehat{T}_L, \widehat{T}_R]$ cases. 196

8.23 Peak field vs. time for N_x cases. 197

8.24 Peak field vs. time for χ cases. 198

8.25 Knudsen number of carbon ions at later time. 199

8.26 Time history of mix. 201

8.27 Inferred experimental mix from reference [126]. 202

8.28 Kinetic mix depth of carbon ion into fuel at $t \approx 0.6$[ns]. 203

List of Tables

4.1 Algorithm Performance for Landau Damping 60

4.2 Algorithm Performance for two Stream Instability. 62

4.3 Algorithm Performance for ion acoustic shockwave. 64

5.1 Moments and their associated conservation properties. 85

5.2 HOLO solver performance with varying Δt on a collisionless IASW problem. 98

6.1 Performance comparison of moment acceleration scheme versus the standard scheme 120

6.2 Performance comparison of moment acceleration scheme versus the standard scheme for a strong shock problem 128

7.1 Comparison in performance of the new HOLO algorithm and a standard Picard iteration for varying $\Delta\widehat{t}$. 155

7.2 Number of HOLO iterations with varying $\Delta\widehat{t}$ and $\Delta\widehat{x}$ for a collisional IAW problem. 156

7.3 Number of HOLO iteration with varying $\Delta\widehat{t}$ and N for a collisional IAW problem with the heat-flux closed entirely from the HO system. 157

7.4 Number of HOLO iteration with varying $\Delta\widehat{t}$ and $\Delta\widehat{x}$ for a collisional IAW problem with LO system carrying only the continuity, momentum, and Ampère equations. 158

List of Algorithms

1 Picard iteration algorithm for the nonlinear diffusion equation. 25

2 Newton iteration algorithm for the nonlinear diffusion equation. 26

3 Source iteration algorithm for neutron transport. 31

4 QDA source iteration for neutron transport. 33

5 HOLO algorithm for Vlaosv-Ampère system. 56

6 Charge-momentum-and-energy conserving HOLO acceleration. 93

7 Picard (source) iteration for the BGK collision operator. 108

8 Nonlinear implicit moment accelerated iteration for the BGK collision operator. 118

9 HOLO accelerated iteration for the VFPA system. 152

10 Picard iteration algorithm for solving the Fokker-Planck equation. 244

Chapter 1

Introduction

In laser-based inertial confinement fusion (ICF), a capsule containing a mixture of Deuterium and Tritium (DT) fuel is compressed with a high energy laser rapidly to fusion condition. The two approaches to achieving fusion condition are: 1) direct drive [27] and 2) indirect drive [28, 29]. Recently, the National Ignition Facility (NIF) at the Lawrence Livermore National Laboratory (LLNL), which is an indirect drive ICF device, has completed it's National Ignition Campaign (NIC) in which they attempted to achieve fuel ignition. Fuel ignition is classified as the condition in which the fuel self-sustains the fusion reaction without additional external source of energy. However, during NIC, the NIF experiment consistently measured neutron yield that were orders of magnitude lower than what was expected from ignition.

To design the fuel-capsule and predict the conditions during the implosion and blow-off, single-fluid, neutral-radiation, hydrodynamic (SFNRH) codes have been used extensively [7, 8, 9, 10, 11, 12, 13]. According to the simulation, the NIF lasers and the capsule design had the correct configuration and energy to achieve ignition. However, this turned out to be incorrect. For a fluid simulation to be accurate, several assumptions must hold. One of the key assumption is that the collisional mean-free-path (mfp) of the plasma ions and electrons

must be shorter than the gradient scale-length of the system, such as the shock thickness and fuel hot-spot size. However, in ignition relevant conditions, the mfp of the high-energy fuel particle which maximizes the fusion reaction may be comparable to the shock thickness and fuel hot-spot size, invalidating the core assumption of fluid approaches. In conditions in which the mfp is comparable to the shock thickness, studies in [1, 2, 3] have shown that the fluid heat-flux predicted via Braginskii theory [117] was an order of magnitude lower than the true self-consistent heat-flux calculated from a kinetic simulation. Additionally, a neutral fluid calculation assumes an ambipolar field, which assumes no electric-field from charge-separation. In most parts of the geometry, the ambipolar treatment is appropriate. However, for ICF calculations, strong discontinuities may exist in parts of the geometry which gives rise to shockwaves [17]. At the interface of the shock, high-energy electrons are able to stream across the discontinuities. This streaming of electrons and subsequent charge-separation will give rise to a strong electric-field that cannot be explained by ambipolar theory alone [15, 16]. These strong shocks may alter the dynamic evolution of the implosion phase on the ion time-scales. Therefore, for a more accurate prediction of the physics relevant to ICF conditions, a kinetic approach with charge-separation must be carried out.

However, kinetic plasma physics simulation for ICF is not trivial. There exist multiple length- and time-scales due to the mass difference between the ions and electrons. In particular, for investigating the evolution of the fuel (ion) dynamics, one is interested in following the ion time-scales. However, charge-separation gives rise to the stiff electron plasma wave time-scale which may be orders of magnitude faster than the ion time-scales. With explicit time-integration methods [19], the fastest numerical time-scale must be resolved for numerical stability. On the other hand, implicit time-integration methods do not require one to respect the fast time-scales for stability reasons [79]. One is allowed to take a time-step size that resolves the dynamical time-scale of interest. However, for a kinetic plasma physics simulation with charge-separation, the standard Picard iteration (source iteration) [73] will require an intractable amount of iteration to nonlinearly converge the system of equations when the time-step size is chosen to step over the stiff time-scales and in some

cases, the iteration may diverge [119]. Newton's method [73], used in conjunction with a Krylov method [59] and nonlinear elimination [21, 54, 55] can reduce the number of nonlinear iterations required to converge the nonlinear system implicitly. However, for a large time-step size, relative to the stiff physical time-scales, the Jacobian may become large and dense and preconditioning can become a challenge [21].

In this research, we will study the kinetic ion effects on the early time condition of implosion of an Omega ICF fuel capsule while allowing for charge-separation. The study will investigate a new mechanism for pusher mix into the fuel that may reduce the fusion reactivity of the ICF capsule. In order to investigate these effects, traditional numerical approaches will not be sufficient. In this research, we will develop a nonlinear accelerator to the standard Picard iteration to efficiently and stably converge the kinetic plasma physics equations. The new method will rely on an emerging *moment-based* accelerator [50, 51, 53, 41, 42, 43, 44, 75, 118] which will use the lower dimensional, self-consistent set of moment equations of the original kinetic equation to *accelerate* the convergence of the original kinetic plasma physics equations. We will also develop an energy conserving discretization scheme, an important property that is not rigorously preserved in many existing solvers, and will become important for long time-integration problems for ICF simulation.

The remainder of this dissertation is organized as follows. In chapter 2, we provide the background of ICF, and the relevant processes. We describe the current state of ICF capsule ignition, previous works on the numerical modeling of the process, and recent experimental observations that lead to a new pusher mix mechanism that can reduce the fusion reactivity and prevent ignition. In chapter 3, we provide a brief overview of the numerical methods for solving an initial value problem. We also provide an example of moment-based accelerators by using a kinetic neutron transport equation. In chapter 4, we discuss the application of the moment-based accelerator to a collisionless electrostatic plasma, modeled using a particle-in-cell (PIC) method [32]. We use the collisionless model to isolate the ability to implicitly step over the inverse electron plasma frequency, $\omega_{p,e}^{-1}$, while allowing for charge-

separation. It is seen that for a collisionless problem, only the 0^{th} and 1^{st} velocity moments of the underlying kinetic equation are required to step over $\omega_{p,e}^{-1}$. In chapter 5, we develop an Eulerian version of the same method developed in chapter 4, but with the addition of a charge, momentum, and energy conserving discretization. We introduce the concept of discrete nonlinear constraints to develop a general approach to developing a conservative discretization scheme for the Vlasov-Ampère system. In chapter 6, we develop a moment-baesd accelerator for a *collisional* neutral gas kinetics application with a Bhatnagar-Gross-Kropp (BGK) collision operator [72]. The neutral, collisional model will be used to isolate the ability to step over the collisional physics time-scale, τ, where the collision operator is a function of the temperature, T, which is a 2^{nd} velocity moment of the distribution function. We therefore show that unlike the collisionless systems in chapters 4 and 5, the 0^{th}, 1^{st}, and 2^{nd} velocity moments of the kinetic equation will be required to effectively step over τ. In chapter 7, we combine all of the techniques developed in chapters 4, 5, and 6 to develop a moment-based accelerator for a multi-species, electrostatic, collisional plasma. The collision operator is modeled using a reduced Fokker-Planck operator [104, 103]. We show that in order to step over the fast electron time-scales, the electron thermal conduction physics must be exposed in the moment system to achieve algorithmic efficiency. In chapter 8, we use the algorithm developed in chapter 7 to solve a fuel-pusher interface problem (to be discussed in detail). The simulation results from this unique solver capability are used to provide some validation and the next-level physics understanding of the proposed new pusher mix mechanism. Finally, in chapter 9, we provide conclusions of the dissertation. We provide a brief summary of the work done on both algorithms, and fuel-pusher interface physics.

Chapter 2

Inertial Confinement Fusion (ICF) Physics

In this chapter, a brief introduction to controlled nuclear fusion reactions and an overview on relevant physics for the laser based ICF will be given. Then we discuss the lower neutron yield measured in experiments compared to simulations. We discuss the traditional modeling procedures and their limitations in the predictive capability for ICF conditions. Finally, we provide some recent numerical and experimental observations made on an Omega ICF capsule, which leads to a new mechanism that may further extend our understanding of the failed ignition attempt at NIF. This new mechanism cannot be modeled using a traditional hydrodynamic approach and thus requires a kinetic multi-species plasma physics modeling approach which also allows for charge-separation.

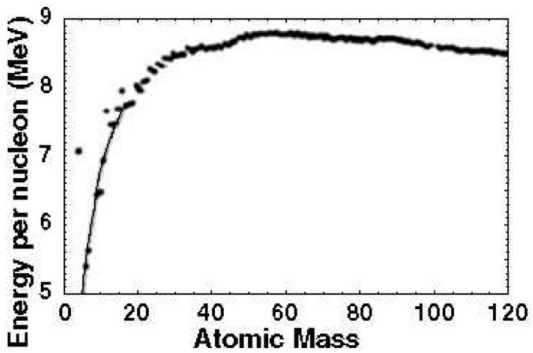


Figure 2.1: Nuclear binding energy versus atomic mass [26].

2.1 Controlled Fusion Reaction and Confinement Schemes

A fusion reaction consists of the fusing of two (or more) light nuclei. The nuclei fuse when they overcome the Coulombic repulsion force and come close enough for their nuclear strong forces to bind them. When the nuclei fuse, the resulting nuclear reaction can either be *exothermic* (net release of energy) or *endothermic* (net absorption of energy). Whether or not the reaction is exothermic or endothermic depends on the masses of the nuclei involved in the fusion reaction. If the difference in the mass, Δm, between the reactant nucleus and the initial nuclei is positive, there is a net release of energy and the reaction is exothermic. If Δm is negative, then a net absorption of energy occurs and the reaction is endothermic. The binding energy is the energy that is required to disassemble the nucleus into individual protons and neutrons. The binding energy is proportional to the mass difference between the individual protons and neutrons and the nucleus. One can investigate the binding energy of the resulting nucleus to determine if the resulting reaction is exothermic or endothermic, refer to Figure 2.1. For energy production, one is interested in an exothermic reaction. In general, lower the nuclei's atomic number, there are fewer charges and the Coulombic repulsion force between the nuclei is lower. For this reason, we consider the following light

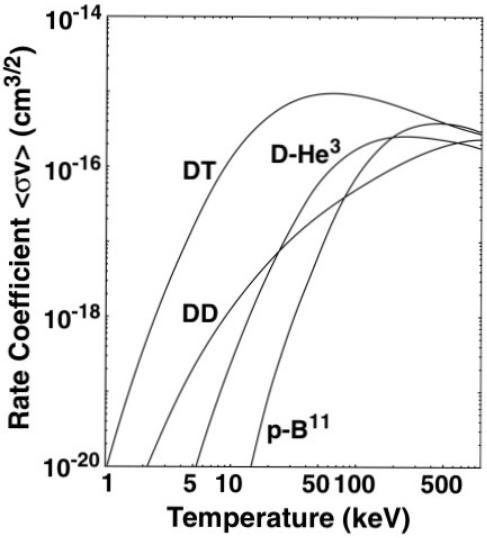


Figure 2.2: Fusion reaction rate coefficients for the DT, DD, D-He^3, and p-B^{11} reaction [26].

nuclei fusion reactions:

$$\mathrm{D} + \mathrm{T} \rightarrow^4 \mathrm{He}\,(3.5\mathrm{MeV}) + n\,(14.1\mathrm{MeV})\,, \tag{2.1}$$

$$\mathrm{D} + \mathrm{D} \rightarrow^3 \mathrm{He}\,(0.82\mathrm{MeV}) + n\,(2.45\mathrm{MeV})\,, \tag{2.2}$$

$$\mathrm{D} + \mathrm{D} \rightarrow \mathrm{T}\,(1.01\mathrm{MeV}) + H\,(3.02\mathrm{MeV})\,, \tag{2.3}$$

$$\mathrm{D} +^3 \mathrm{He} \rightarrow^4 \mathrm{He}\,(3.6\mathrm{MeV}) + H\,(14.7\mathrm{MeV})\,. \tag{2.4}$$

In Figure 2.2, the Maxwellian averaged fusion reaction rate coefficient as a function of temperature is shown for the above reactions. It is readily seen that the fusion reaction rate is maximized for the DT reaction with the lowest temperature. For this reason, in order to demonstrate a controlled, sustained fusion reaction, almost all current experimental fusion devices are focused in using deuterium and tritium as the fuel.

There are three approaches in achieving a controlled, sustained fusion reaction: 1) gravitational confinement, 2) magnetic confinement, and 3) inertial confinement. In a gravitational confinement approach, the Coulombic repulsion force between the nuclei is overcome by the sheer gravitational force and immense pressure at the center of stellar bodies. In a magnetic

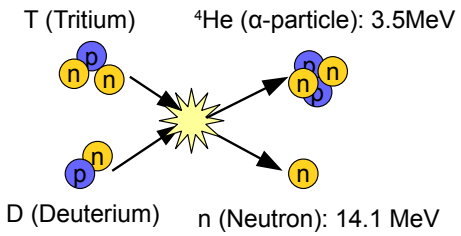


Figure 2.3: Illustration of the DT reaction.

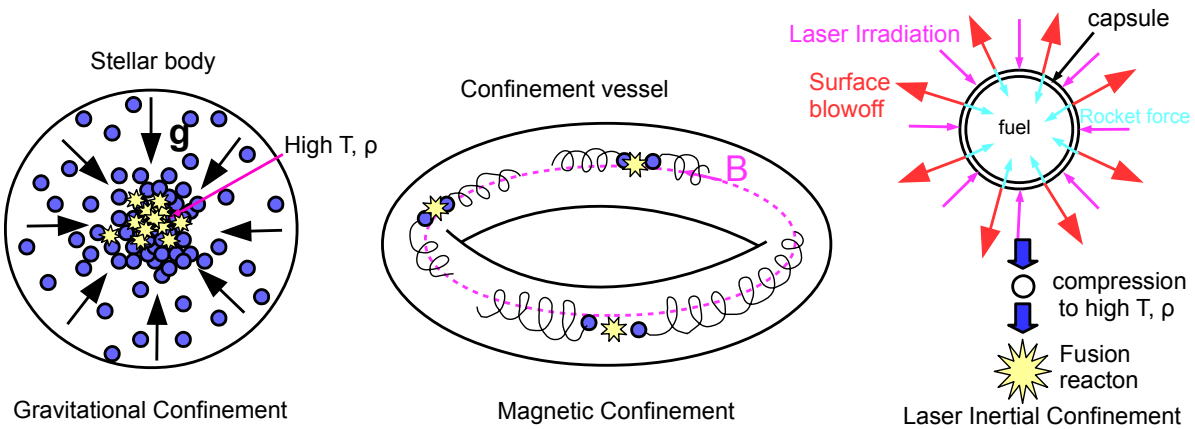


Figure 2.4: A very simple illustration comparing different confinement schemes.

confinement approach, the fuel is ionized in a confinement vessel such as a Tokamak [114] to high temperature via neutral beam injection, Ohmic heating, and other heating mechanisms. The high energy ionized fuel must be prevented from coming in contact with the confinement vessel by using a strong magnetic field until the ions collide and fuse. In a laser-based inertial confinement approach, a powerful laser pulse is used to rapidly compress a capsule filled with DT, to high temperature and density until the DT nuclei fuse, refer to Figure 2.3. The three approaches are illustrated in Figure 2.4. From a practical standpoint, a gravitational confinement approach is not feasible for terrestrial applications. For this reason, great effort has been put into both magnetic and inertial confinement approaches. In this dissertation,

we focus on the physics of a laser-based inertial confinement fusion approach.

2.2 ICF Physics

With the completion of the national ignition facility (NIF), we are ever closer to achieving fusion ignition and *break-even* for the inertial confinement fusion (ICF) concept. The ICF concept is based on rapidly *compressing* the fuel-capsule containing a deuterium-tritium (DT) mixture with a high energy density laser. The capsule is compressed to fusion density and temperature to achieve *ignition* condition [28]. Ignition is classified as a condition in which the fuel is *confined* by the surrounding dense shell and the alpha particles from the fusion reaction of fuel heat and sustain a thermonuclear reaction without any external energy source (such as a laser). A break-even is achieved when the energy from the fusion reaction is equal to that from the energy required by the laser to compress the fuel capsule to ignition condition. In order to implode, compress, and confine the fuel to fusion density and temperature, two broad approaches exist for ICF: 1) direct-drive [27] and 2) indirect-drive [28, 29]. In the direct-drive approach, the laser beams are targeted directly on the capsule to convert the laser energy to compress the fuel. In the indirect-drive approach, a high atomic number material surrounding the fuel capsule will convert the laser energy into X-rays that in turn compress the fuel.

A primary example of an indirect drive facility is NIF (although it may also be used as a direct drive facility [39]) while the Omega is a direct drive facility. The Omega facility has been used as a test bed for the NIF experiments and to validate and calibrate the SFNRH based fluid codes. However, between the two facilities, there are several more important differences beyond the approach in converting the laser energy to compress the fuel capsule. The Omega laser facility has a much lower laser energy of $\mathcal{O}(10$ kJ) while NIF is $\mathcal{O}(1$ MJ), and the Omega capsule is smaller than the ignition scale NIF capsules. Additionally, the *composition* of the capsule is noticeably different. In an Omega capsule, typically the fuel is

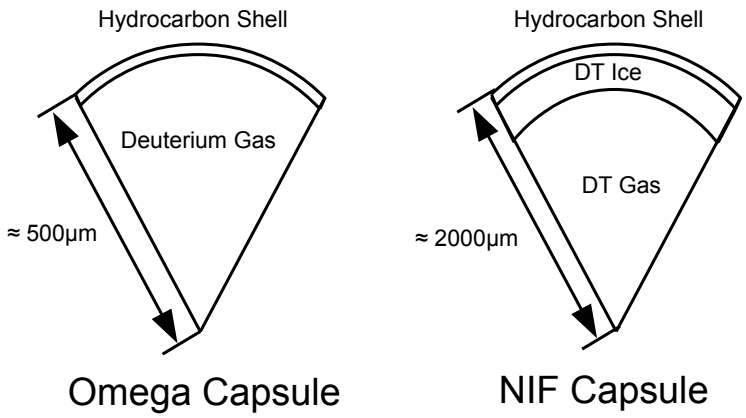


Figure 2.5: Comparison of Omega (left) and NIF (right) capsule.

a deuterium gas surrounded by a hydrocarbon (plastic) or silicon-oxide (glass) shell and is at ambient temperature (however, experiments have also been conducted with deuterium-tritium (DT) gas, ^3He gas, and other gases [122]). On the other hand, NIF targets are generally cryogenic, with a DT gas fuel, surrounded by a DT ice layer, encapsulated by a plastic shell. The comparison of fuel capsule composition for the two facilities is illustrated in Figure 2.5.

In a direct drive facility such as Omega, upon the laser impingement on the capsule surface, a low density coronal plasma forms around the capsule into which the laser energy is absorbed by electrons which couple to the laser frequency. The combination of the laser and the high energy electrons will transfer energy towards the center of the fuel-capsule via radiation waves and heat-flux. The heated shell will ablate outwards and from momentum conservation, produce a rocket like momentum flux inwards to the capsule center, initiating the implosion phase.

During the implosion phase of the fuel-capsule, the laser will drive a shock through the outer shell of the capsule. As this shock propagates into the fuel region and the laser intensity rises, a second *compression* wave is launched inwards, together with the imploding shell, compressing the fuel. The imploding shell will converge until a point where it stops

(stagnation) at which peak density, temperature, and pressure are achieved and most of the kinetic energy is converted into internal energy through *pdV* (compression) work. At this point, the center of the fuel-capsule is at a higher temperature than the outer shell. At this point, the central *hot-spot* is comprised of a low-density, high-temperature fuel, surrounded by a high-density, low-temperature shell. This, cold-dense shell provides the *confinement* of the hot-spot. Upon achieving peak compression, and confinement of the fuel, it is possible to estimate the *burn fraction*, ϕ_{burn}, of the fuel by [26]:

$$\phi_{burn} = \frac{\rho_h r_h}{\rho_h r_h + 6[\mathrm{g/cm^2}]}. \tag{2.5}$$

Here, ρ_h is the density of the fuel hot-spot, r_h is the radius of the fuel hot-spot, and the product, $\rho_h r_h$ is referred to as the *areal density*, which governs the burn fraction of an ICF fuel.

The central hot-spot, or fuel region, will have a lower density than the shell. The compression work from the laser and subsequent shell ablation will make the fuel temperature higher than the shell region. For NIF targets, this temperature is typically in the keV regime. At this temperature, the average fusion reactivity, $\langle \sigma v \rangle$, is maximized for a deuterium-tritium (DT) fuel mixture (Figure 2.2). The DT reaction produces a 3.5MeV alpha particle (^4He) and a 14.1MeV neutron as shown in equation (2.1). During the fusion reaction, the neutrons will escape from the target without much interaction with the fuel or the shell due to the large neutron mean-free-path (mfp) relative to the fuel geometry upon stagnation and ignition conditions ($\lambda_{n_D} \approx \lambda_{n_T} \approx mm \gg r_h \approx \mu m$). The alpha particles on the other hand are expected to be confined in the capsule through collisions with the electrons and fuel ions, depositing energy in the hot-spot. When the rate of fusion reaction in the hot-spot overcomes the rate of energy loss from heat-flux, radiation, and decompression from the outward expanding fuel, the DT reaction is considered self-sustained, and ignition is achieved. As the fusion reaction is sustained and temperature and pressure rise further in the central hot-spot, the shell continues to expand outward. This outward expansion will thus further decompress

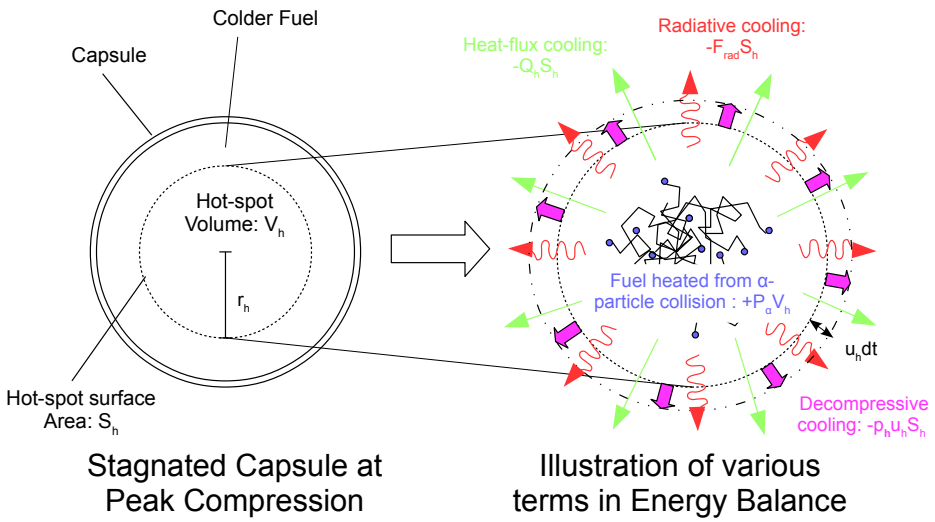


Figure 2.6: Illustration of various sources for energy balance.

and cool the fuel, suppressing the fusion reaction. Assuming a constant fuel density in the hot-spot, the condition to achieve ignition can be estimated from a careful energy balance of the above discussed energy deposition/loss mechanisms using the following equation [26]:

$$\rho_h V_h \frac{d\epsilon_{int,h}}{dt} = P_\alpha V_h - Q_h S_h - F_{rad} S_h - p_h u_h S_h. \tag{2.6}$$

Here, ρ_h is the hot-spot fuel density, V_h is the hot-spot volume, $\epsilon_{int,h}$ is the hot-spot internal energy density, P_α is the volumetric energy deposition rate from the α particle from the DT reaction, Q_h is the thermal conduction heat-flux across the hot-spot surface, S_h is the hot-spot surface area, F_{rad} is the radiative energy flux across the hot-spot surface, p_h is the pressure at the hot-spot surface, and u_h is the outward pointing velocity at the fuel hot-spot surface. Ignition is achieved when the left-hand side (LHS) of equation (2.6) is greater than zero. An illustration of the discussed energy balance is shown in Figure 2.6. The means by which this central hot-spot is created will ultimately determine if ignition can be achieved or not. However, the *areal density*, $\rho_h r_h$, discussed earlier, and the hot-spot temperature can

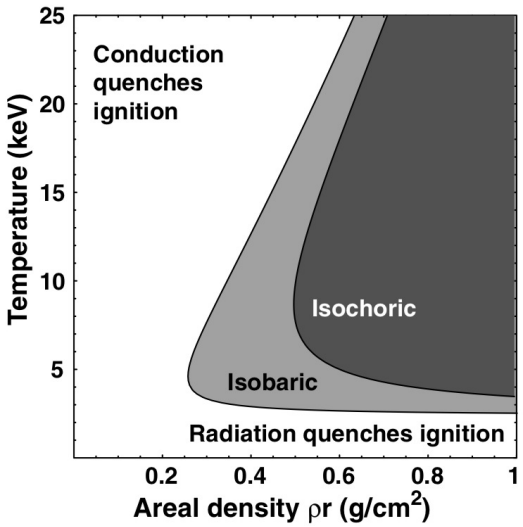


Figure 2.7: Relationship between ignition, hot-spot temperature, and areal density, $\rho_h r_h$ [26].

be used to estimate the parameter regime in which ignition is *possible*. In Figure 2.7, the white zone shows the region of temperature and $\rho_h r_h$ in which ignition cannot be achieved while the grey zones show the regions in which ignition is possible (i.e. $\rho_h V_h \frac{d\epsilon_{int,h}}{dt} > 0$). For a more detailed discussion on the effect of temperature and areal density on the various terms in equation (2.6), we refer the readers to reference [26].

2.3 ICF Neutron Yield Difficiency and Low Fuel Temperature

To date, the majority of numerical studies on ICF has been based on radiation-hydrodynamic (rad-hydro) codes such as DRACO [12], LASNEX [7, 8, 9], and HYDRA [10]. There have been increasing efforts to include magnetohydrodynamic (MHD) and two fluid effects into the model. However, most of the calculations do not consider the plasma physics effects, not to mention, kinetic effects.

The measured neutron yields from the NIF experiment are at least many factors below, and occasionally, an order of magnitude lower then the predicted, expected value for ignition from the rad-hydro codes [31]. This may be attributed to a lower fuel temperature achieved in experiments compared to numerical simulations. There are many mechanisms to reduce the deposition of laser energy into the fuel such as the two plasmon decay instability, stimulated Raman scattering (SRS), and stimulated Brillouin scattering amongst many others [26]. All mechanisms will ultimately reduce the final fuel temperature during the hot-spot formation. We propose two other reasons for the difference in the fuel temperature between the experiment and simulation based on plasma kinetic theory. One of the key reasons for the lower neutron yield may be due to the fact that no kinetic ion effects are taken into account and another is charge-separation being neglected. There are many instances in which the two effects may become important for ICF simulation.

One of the many kinetic effects that can cause a reduction in the fuel temperature is the kinetic enhancement of ion heat-flux and viscous dissipation and the consequent shock broadening [4]. An enhanced ion heat-flux will form an ion pre-heating layer (non-existent in a rad-hydro calculation), which will also *enhance* the electron pre-heating layer thickness via collisional energy transfer between the cold down-stream electrons and the hot ions. This enhanced pre-heat layer thickness may produce anisotropic heating of the fuel, which may result in inaccurate laser timing to generate a sequence of shocks to maximize the hot-spot temperature and pressure.

A strong self-consistent charge-separation field which can exist near shocks at the Debye length-scale may enhance the separation between the ion species. In ICF, the separation between the fuel species will result in reduction in the DT reaction which maximizes fusion reactivity [16], resulting in a degradation of the neutron yield. If the field is strong enough, ions can be significantly accelerated, evolving the distribution function of the ions to a highly non-Maxwellian state. Hydrodynamic codes assume a small perturbation from a Maxwellian distribution. If the collision time-scale is slow compared to the acceleration, this will further

enhance the heat-flux out of the system, causing a reduction in the peak fuel temperature and reducing the fusion reactivity and neutron yield. All of these effects cannot be captured by the single-fluid, neutral-radiation hydrodynamic (SFNRH) assumption typically employed in hydrodynamic codes.

Additionally, in ICF, the mixing of high Z (ion charge state) material into the fuel is a key concern as the rate of thermal Bremsstrahlung radiation loss [114] scales as $\dot{\mathcal{P}} \propto Z^2/T^{1/2}$, where $\dot{\mathcal{P}}$ is the time rate of change of the power-density. If a significant amount of pusher material can mix inside the central hot-spot region due to radiative heat-loss, the fuel cannot achieve the ignition temperature necessary to self-sustain the fusion reaction. Additionally, due to the increase in the bulk heat-capacity resulting from the mixing, the peak fuel temperature that can be achieved becomes lower. The change in the bulk internal energy density can be expressed as $\Delta\epsilon_{int} = \int_{T_0}^{T_f} c_p\,(T)\,dT$. Here, $\Delta\epsilon_{int}$ is the change in the internal energy density, T_0 is the initial temperature, T_f is the final temperature, and $c_p\,(T)$ is the specific heat-capacity at constant pressure as a function of temperature, T. If the pusher can mix into the fuel, an increase in c_p will occur, splitting the contribution of thermal energy into both, the fuel and the pusher. This will ultimately cause a reduction in the peak fuel temperature, which will reduce the fusion reactivity and neutron yield.

2.4 Recent Studies and Motivation for Kinetic Treatment of Ions

A multi ion-species baro- and electro-diffusion effect was recently investigated by reference [14]. Due to the mass and charge-to-mass ratio difference between the fuel species (deuterium and tritium), separation can occur due to the difference in the pressure force and acceleration from the electric field. The study demonstrates through a multi-fluid simulation that when a strong shock propagates through the capsule, a strong separation is observed be-

tween the fuel species upon initial convergence of the capsule. Furthermore, compared to an hydrodynamic simulation with SFNRH assumptions, an overall reduction in the DT reaction was observed with the multi-fluid simulation. In a separate theoretical study in references [24, 25], reduction of the neutron yield due to kinetic effects was investigated. In their study, it is postulated that a reduction in the neutron yield can occur due to a *tail depletion* mechanism in which the ion population in the high energy tail that maximizes the DT reaction can be depleted kinetically. The depletion of the ion population is predicted since high energy fuel ions with long collisional mean-free-path stream out of the fuel hot-spot. In [24] it is concluded that the resulting ion kinetic heat-flux, and thus reduced ion temperature is in the need more of an impact on yield.

A numerical study for an Omega ICF capsule was carried out in reference [120], where a kinetic, multi-ion species simulation with fluid electron and a quasi-neutral field was considered. In the study, the full shock convergence and rebounce phase was studied to investigate the role of baro-diffusion in fuel species separation. The study concludes that during the shock convergence, fuel separation is observed. However, during the shock rebounce phase, the two fuel species mixes and a clear separation was not observed. Furthermore, an increase in the neutron yield as opposed to a decrease was observed. Therefore, the baro-diffusion induced fuel separation cannot explain the neutron deficiency observed between experiments and simulations. Additionally, due to the high energy fuel ions in the hot-spot having long-mean-free path, they were able to *enhance* as oppose to *deplete* the high-energy population near the fuel and pusher interface. Therefore, the tail depletion mechanism cannot answer the neutron deficiency issue either. The same study suggests a more detailed treatment of the fuel-pusher interface at earlier times. If a kinetic enhancement of fuel-pusher mixing can occur, the subsequent Bremsstrahlung and increased bulk heat-capacity effects can cause a reduction in the peak fuel temperature.

In a traditional SFNRH assumption, the mix of pusher into the fuel is modeled through a Rayleigh-Taylor instability (RTI) and Richtmeyer-Meshkov instability (RMI). In both RTI

and RMI, the mixing rate is dependent on the modes of the initial perturbation of surface features. In general, the higher the perturbation mode, the greater the growth rate of the feature, and the deeper the mixing rate is [26]. A recent NIF study in reference [127] estimates that in order to match the neutron yield between the numerical simulations and some experiments, the NIF simulations require a $3 \sim 5\%$ atom fraction mixture of the pusher material into the fuel. In a separate study [121], in order for a simulation to achieve a similar level of impurity mixing through RTI, pusher surface features were required to be significantly larger than what was engineered, and an alternative mechanism to cause mixing is being sought. Furthermore, there has been an experimental demonstration of deep mixing of pusher into the fuel. In an Omega ICF experiment in reference [126], compared to a hydrodynamic simulations based on an SFNRH assumptions, the pusher carbon ions were measured to mix more deeply into the fuel. In the same study, the experimental results yield approximately a $5 \sim 10\%$ atom fraction mix of carbon into the fuel. In a more recent study[128], a titanium dopant was placed at the Omega fuel-pusher interface in order to spectroscopically obtain a time-history of the location of the fuel-pusher interface. The tracking was performed through means of measuring the spectroscopic line emission of titanium. The experiment observed an early time mix of this titanium liner that is not explained by a hydrodynamic mix model. Finally, yet another Omega experiment by reference [123] performed a shot on a carbon-deuterium (CD) capsule filled with a ^3He fuel (as opposed to a CH capsule with DT fuel). Unlike the DT fuel which can support many fusion reactions, the dominant mechanism for fusion reaction for this experiment is the $D +^3 He \rightarrow^4 He + H$ reaction (equation (2.4)). In the experiment, the fusion reaction can only occur as a result of pusher-fuel mix, as the deuterium is only in the pusher. They measured a significantly higher amount of proton yield from the D^3He reaction than is explained through hydrodynamic mix models. Unless the capsule material containing the deuterium mixed deep into the fuel hot-spot, this cannot happen. The suite of recent experimental evidence of non-hydrodynamic mixing points one to an alternative (kinetic) treatment of the early time fuel-pusher mixing.

2.5 A New Early Mix Mechanism

In an Omega ICF experiment described in reference [124] a strong electric field was measured which could not be explained by an ambipolar or quasi-neutral theory. In a study in reference [15], a theoretical analysis was performed to explain the source of this strong field. The study proposed many sources including a shock induced field and an ionization gradient at the fuel-pusher interface. We focus on the ionization gradient source to explain a new pusher mix mechanism. As the initial thermal radiation wave and high energy electron heat-flux ionizes the fuel-pusher interface, a strong gradient in the electron number density will set up due to the difference in the effective ionization state between the fuel and the pusher. As the ionization gradient sets up, electrons will stream across this strong gradient, causing a charge-separation electric field to setup. This electric field will eventually evolve to a structure referred to as a double-layer electric-field [125], which is similar to a sheath field [61], and cannot be described by an ambipolar or quasi-neutral field theory. The process of ionization gradient setup and generation of a subsequent charge-separation field is shown in Figure 2.8. If the field can be sustained long enough, a significant number of pusher ions will be *accelerated* and *mixed* into the fuel, and a drift from a classic Maxwellian distribution can occur, as is illustrated in Figure 2.9. This transport mechanism cannot be modeled through a hydrodynamic assumption and requires a multi-species kinetic description. In this dissertation, we study only the early time multi-species kinetically enhanced mix effect due to the strong double-layer electric field. At the later time, when a hydrodynamic shock propagates in, these pusher-ions which were kinetically mixed can be dragged deep into the fuel hot-spot via Coulomb friction. If the mix is significant enough, the combination of the increase in the bulk heat-capacity and Bremsstrahlung radiation loss can reduce the fuel temperature to suppress the self-sustaining fusion reaction, preventing ignition of the fuel.

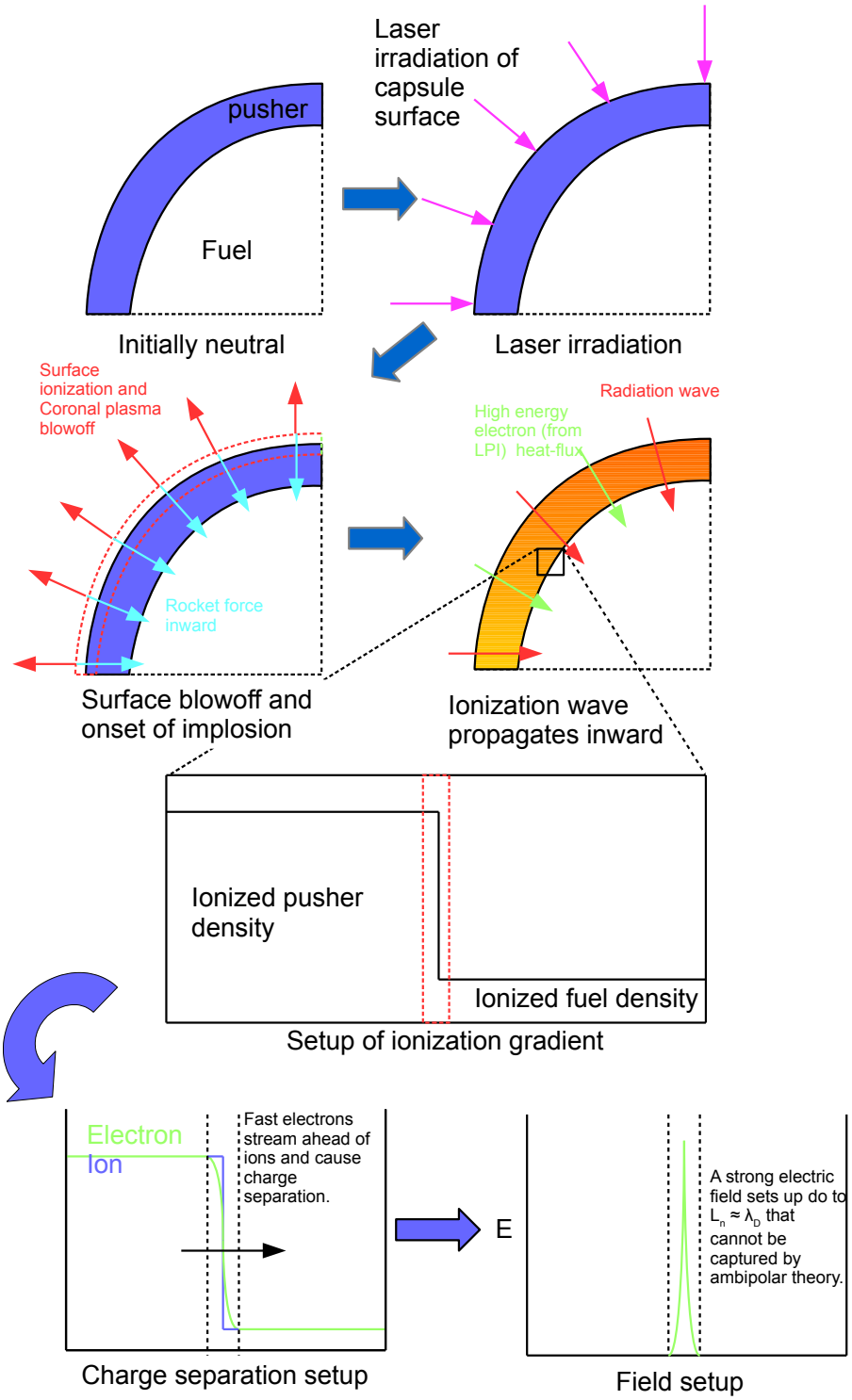


Figure 2.8: Process of ionization gradient setup.

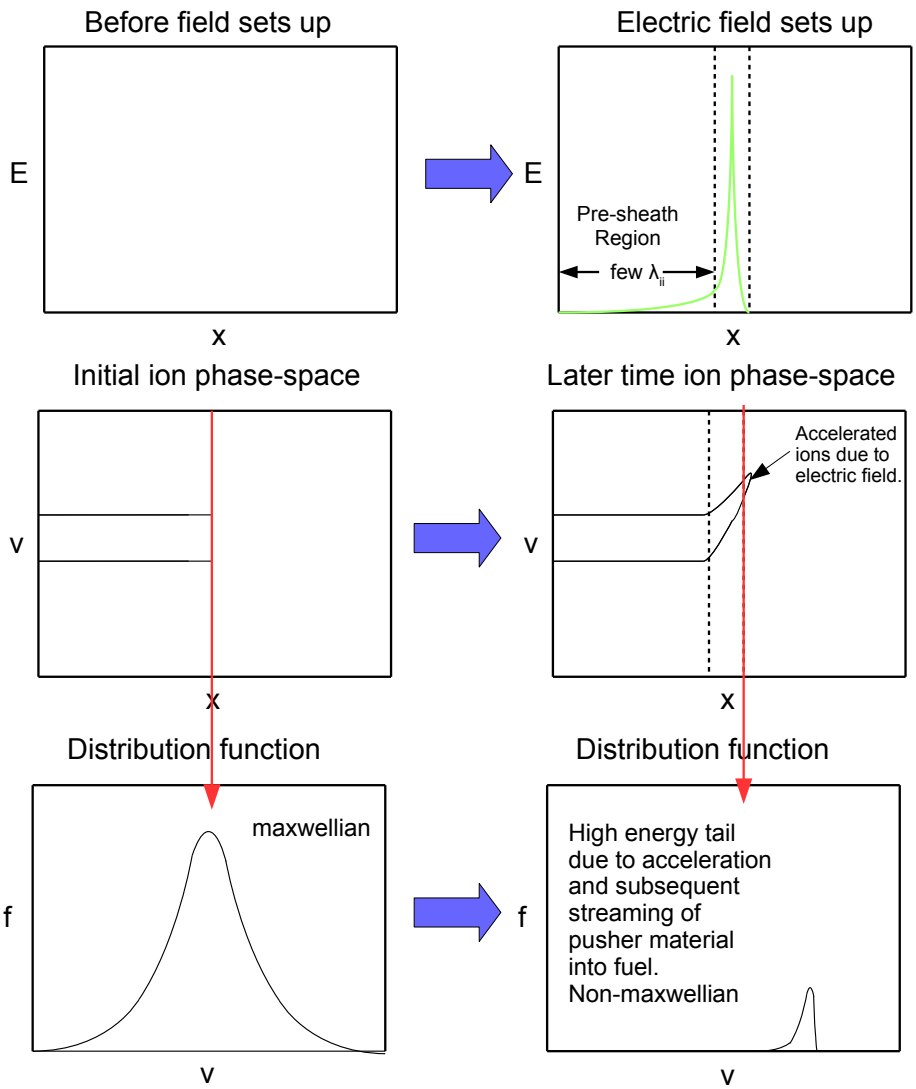


Figure 2.9: Illustration of the Ion phase-space evolution due to a double-layer field.

Chapter 3

Background on Numerical Methods

The necessity for kinetic plasma modeling for ICF simulation has become apparent in the desire to improve the predictive capability on the system time- and space-scales. However, an efficient numerical approach to model many kinetic systems efficiently remains elusive. In this chapter, we provide a brief overview of methods for solving an initial value problem (IVP), and the general types of iterative nonlinear solvers that are available. We discuss each of their limitations in kinetically modeling a long time-scale and system length-scale ICF relevant problem. In order to address the shortcomings of the existing nonlinear solvers for kinetic problems, a *moment-based* convergence acceleration algorithm is developed. We will introduce the concept of a moment-based acceleration method by providing an example through a neutron transport application.

3.1 Time Integration Schemes

In numerical modeling, there are two broad approaches to time integration of a system of equations: 1) explicit, and 2) implicit schemes. Both have their advantages and disadvantages. Explicit schemes require minimal storage, are computationally fast per time-step, and

are simple to implement code-wise. However, classic explicit schemes are limited by the CFL stability condition [19] which for numerical stability purposes, requires the time-step size to become smaller as the mesh size becomes smaller. For illustration purposes, we consider the following one dimensional (1D) linear diffusion equation:

$$\frac{\partial u}{\partial t} - D\frac{\partial^2 u}{\partial x^2} = 0. \tag{3.1}$$

Here, $u = u\,(x, t)$ is the solution variable, x is the position, t is the time, and D is the constant diffusion coefficient. Assuming a uniform grid, a periodic boundary condition, performing a forward Euler discretization in time, and using a second-order central differencing in space, the following discrete equation is obtained:

$$\frac{u_i^{k+1} - u_i^k}{\Delta t} - D\frac{u_{i+1}^k - 2u_i^k + u_{i-1}^k}{\Delta x^2} = 0. \tag{3.2}$$

Here, k is the discrete time index, u_i^{k+1} is the solution for time-step $k+1$ and at cell-index i, Δt is the time-step size, and Δx is the discrete cell size in space. For this discrete system, the CFL stability constraint requires Δt to be,

$$\Delta t \leq \frac{\Delta x^2}{D}. \tag{3.3}$$

Hence the number of required time-step to integrate to t_{max} is, $N_t = \lceil t_{max}/\Delta t \rceil$. It is clear that for an increasingly finer mesh, Δx, the required number of time-step will increase quadratically. Additionally, the CFL stability constraint requires that the time-step size resolves the fastest physical time-scale of the system. In plasma physics for example, this time-scale can be the inverse electron plasma frequency, $\omega_{p,e}^{-1}$ [61]. In plasma physics, phenomena occurring on ion time-scales may be of interest and we wish to take a time-step size that steps over electron time-scales. However, with explicit schemes, the stiff inverse electron plasma frequency must be resolved for stability purposes. One could remove the electron time-scales from the model prior to the numerical solution, but this would preclude

the impact of these time-scales over the entire simulation geometry and the entire simulation time-history and what we are not interested in doing.

The implicit approach on the other hand does not restrict one to respect the CFL stability condition and time-step sizes can be chosen such as to resolve the dynamical time-scale of interest (for accuracy consideration). For illustration purposes, we consider the same linear diffusion equation as in equation (3.1), but with forward Euler time-discretization:

$$\frac{u_i^{k+1} - u_i^k}{\Delta t} - D\frac{u_{i+1}^{k+1} - 2u_i^{k+1} + u_{i-1}^{k+1}}{\Delta x^2} = 0. \tag{3.4}$$

Unlike the explicit scheme, the solution for u_i^{k+1} is not a simple evaluation, but requires an inversion of a linear system which may require large computational storage. Additionally, for implicit solutions to a *nonlinear* systems of equations, a nonlinear iteration is required for convergence. Convergence of nonlinear systems for plasma physics is critical for energy conservation, which affects long term accuracy of the physics solution [54].

3.2 Nonlinear Solvers

We discuss two common approaches for solving a nonlinear system of equations implicitly. The first is the Picard, or Richardson fixed-point iteration scheme, and the second is the Newton iteration scheme [73]. The Picard iteration is usually linearly convergent and requires an evaluation and update to the nonlinear solution based on fixed point map from iteration to iteration [73]. The Newton iteration is generally quadratically convergent and requires an inversion of a *Jacobian matrix* in order to calculate the nonlinear update to the solution from iteration to iteration.

Both methods have their advantages and disadvantages. The advantage to the Picard iterative scheme is that no large massive global inversion of a Jacobian matrix is required to calculate the update to the nonlinear solution. Additionally, the inversion of the nonlinear

system can be naturally blocked for sparse inversion utilizing a very efficient multi-grid preconditioner for parabolic systems [63]. The disadvantage is the rate of convergence and the issue of *stagnation* of the iteration. For a complex multi-physics simulation with multiple time-scale, as in a plasma physics application, when Δt is chosen to step over the fast time-scale physics (electron time-scales), the Picard iteration scheme may be slow to converge, and the convergence may stagnate after a certain number of iterations, or even diverge in certain cases [119]. To illustrate a Picard iteration scheme, we consider the following nonlinear diffusion equation:

$$\frac{\partial u}{\partial t} - \frac{\partial}{\partial x} D\left(u\right) \frac{\partial u}{\partial x} = 0, \tag{3.5}$$

where the nonlinear diffusion coefficient, $D\left(u\right)$, is defined as,

$$D\left(u\right) = u^2. \tag{3.6}$$

By discretizing equation (3.5) using a backward Euler scheme and central differencing scheme the following discrete equation is obtained:

$$\frac{u_i^{k+1,z} - u_i^k}{\Delta t} - \frac{D_{i+1/2}^{k+1,z-1}\left[u_{i+1}^{k+1,z} - u_i^{k+1,z}\right] - D_{i-1/2}^{k+1,z-1}\left[u_i^{k+1,z} - u_{i-1}^{k+1,z}\right]}{\Delta x^2} = 0, \tag{3.7}$$

where the discrete nonlinear diffusion coefficient is defined on cell-face as:

$$D_{i+1/2}^{k+1,z-1} = \left[\left(u_{i+1}^{k+1,z-1}\right)^2 + \left(u_i^{k+1,z-1}\right)^2\right]/2, \tag{3.8}$$

and z is the Picard iteration index. By linearizing the diffusion coefficient, one can invert the linear system for $u_i^{k+1,z}$. The iteration is performed until the L_2 norm of the residual,

$$F_i^z = \frac{u_i^{k+1,z} - u_i^k}{\Delta t} - \frac{D_{i+1/2}^{k+1,z}\left[u_{i+1}^{k+1,z} - u_i^{k+1,z}\right] - D_{i-1/2}^{k+1,z}\left[u_i^{k+1,z} - u_{i-1}^{k+1,z}\right]}{\Delta x^2}, \tag{3.9}$$

decreases below a specified convergence tolerance, *tol*. The Picard iteration algorithm to converge equation (3.9) for a given time-step, k, is summarized in Algorithm 1.

Algorithm 1: Picard iteration algorithm for the nonlinear diffusion equation.

```
Set z = 1;
while Equation (3.9) not converged do
    Compute D^{k+1,z-1} from equation (3.8);
    Solve u_i^{k+1,z} from equation (3.7);
    Check convergence: |F^{k+1,z}|_2 < tol;
    Increment z = z + 1;
end
```

Newton iteration on the other hand is generally quadratically convergent, that is, the nonlinear residual error from iteration to iteration decreases quadratically. Newton iteration also has a robust convergence property unlike Picard iteration, which may stagnate. However, the quadratic convergence property holds strictly when the solution in a particular iteration is within the ball of convergence. Additionally, for a large system of nonlinear equations such as a kinetic system, which requires storage of the full 6D phase space solution, the Jacobian matrix may become unforgivingly large. The Jacobian matrix may also become dense depending on the time-scales associated with the nonlinear system and the Δt size chosen. This dense Jacobian may not have an analytical form. To illustrate a Newton's method, we consider the same nonlinear diffusion equation shown in equation (3.7). The z^{th} Newton iteration is summarized as:

$$\mathbb{J}^{z-1}\delta\vec{u}^{z} = -\vec{F}^{z-1}, \tag{3.10}$$

$$\mathbb{J}^{z-1} = \frac{\partial\vec{F}^{z-1}}{\partial\vec{u}^{z-1}}, \tag{3.11}$$

$$\vec{u}^{k+1,z} = \vec{u}^{k+1,z-1} + \delta\vec{u}^{z}, \tag{3.12}$$

where $\mathbb{J}^{z-1}$ is the Jacobian matrix, $\delta\vec{u}$ is the Newton update vector, and $\vec{F}$ is the residual vector, defined in equation (3.9). Similar to the Picard iteration scheme, the Newton iteration is continued until the L_2 norm of the residual, F, decreases below a specified tolerance, *tol*. The Newton iteration algorithm is summarized in Algorithm 2.

Algorithm 2: Newton iteration algorithm for the nonlinear diffusion equation.

```
Set z = 1;
while Equation (3.9) not converged do
    Compute 𝕁^{z-1} and F^{z-1} from equations (3.11), and (3.8);
    Solve δu^z from equation (3.10);
    Update u⃗^{k+1,z} from equation (3.12);
    Check convergence: |F^{k+1,z}|_2 < tol;
    Increment z = z + 1;
end
```

In Figure 3.1, we compare the convergence rate between the Picard and Newton iteration algorithm applied to the nonlinear diffusion equation. It is clearly seen that Newton's method has a superior convergence property over Picard. For the simple 1D nonlinear diffusion equation, an analytical Jacobian is simple to construct and invert. However, for a more complicated problems, such as in plasma physics, this may not be true. The issue of lack of analytical form for the Jacobian has been resolved via the use of Jacobian-Free Newton-Krylov (JFNK) method [62]. JFNK is a synergistic method between a classic Newton's method and Krylov linear iterative inversion method [59]. The basic concept of JFNK is to approximate the product of the Jacobian-matrix and the Krylov-vector (mat-vec) via finite differencing,

$$\mathbb{J}\vec{v}_k \approx \frac{\vec{F}\left(\vec{u}+\epsilon\vec{v}_k\right)-\vec{F}\left(\vec{u}\right)}{\epsilon}, \tag{3.13}$$

where $\vec{v}_k$ is the Krylov vector, and ϵ is a small perturbation factor for finite differencing. Hence the storage requirement can be significantly reduced. However, even with JFNK,

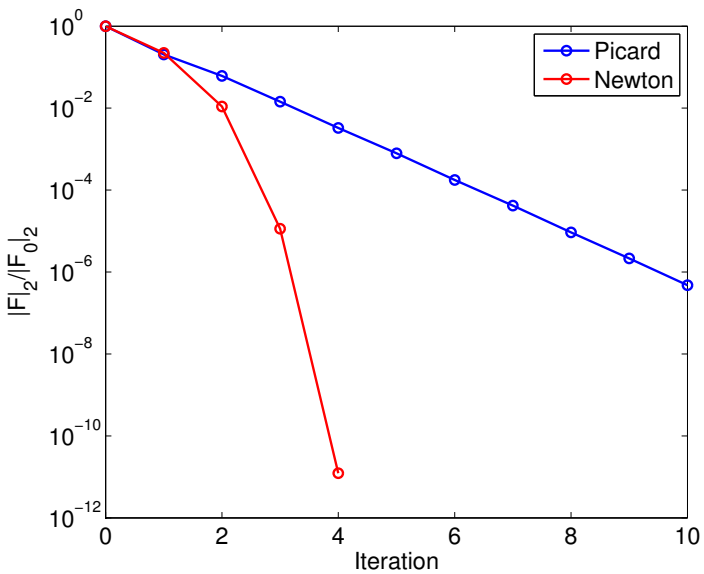


Figure 3.1: Comparison of convergence rate between Picard and Newton iteration for the nonlinear diffusion equation.

for a kinetic system, the storage size may become prohibitively large due to the increased storage of the Krylov vectors from Krylov iteration to iteration. In order to address the issue of kinetic problem storage requirement, a technique of kinetic enslavement has been developed in references [21, 51, 54, 55]. The concept of kinetic enslavement is to enslave the solution to the kinetic system as a function evaluation for another nonlinear equation (that is a function of the kinetic system). This has been demonstrated in references [21] and [54, 55] via a Vlasov-Poisson and Vlasov-Ampère system by enslaving the underlying kinetic Vlasov equation [61] as a function evaluation for the field equation (Poisson equation or Ampère's equation). Similarly, in reference [51], the solution to the linear Boltzmann transport equation was enslaved as a function evaluation for the scalar flux. The methods have seen success in achieving orders of magnitude gain in CPU speed compared to classic explicit schemes and source iteration schemes. However, for the plasma physics application, the issue of a dense Jacobian, and hence the *preconditioning* of a such dense system has become a problem [21] for $\Delta t \gg \omega_{p,e}^{-1}$.

3.3 Moment-Based Nonlinear Accelerator

Recall that a Picard iteration scheme does not require an inversion of a very large global Jacobian matrix, however, is slow to converge when time-step sizes are chosen to significantly step over the fast time-scales. In order to address the short-comings of the classic Picard iteration scheme, moment-based accelerators have been developed by others in various fields [52, 41, 43, 44]. The idea behind the moment-based accelerator is to use the set of self-consistent moment equations in order to accelerate the nonlinear convergence of the original kinetic system using a Picard iteration scheme. The original idea has been around since the early 1960's and has been successfully used in neutron transport applications and plasma physics. However, the original methods encountered issues with discrete inconsistency between the kinetic system and the moment system [51, 44]. For time dependent problems, this discrete inconsistency may result in issues such as inaccuracy in problems with long time integration. A technique of enforcing discrete consistency has been developed [50] and successfully implemented in a collisionless electrostatic plasma physics problem [75] (chapter 4 of this thesis), thermal radiation transport problem [53], and neutron transport problem [50, 51]. In this section, in order to describe the machinery of the moment-based accelerator, a historical overview of the classic quasi-diffusion-acceleration (QDA) scheme will be provided from the neutron transport community along with results.

Consider the following 1D, steady-state, single energy group linear Boltzmann transport equation with a general scattering kernel that obeys the assumption of rotational invariance [78]:

$$\mu \frac{\partial \psi}{\partial x}(x,\mu) + \Sigma_t(x)\,\psi(x,\mu) = \left[\int_{4\pi} \Sigma_s(\mu' \cdot \mu, x)\,\psi(x,\mu')\,d\Omega' + \frac{1}{4\pi} Q(x)\right]. \tag{3.14}$$

Here, $\psi(x,\mu)$, $\mu \in [-1,1]$, x, Σ_t, Σ_s, Ω and Q are the angular flux, direction cosine, position, total collision cross-section, differential scattering cross-section, solid-angle, and an internal isotropic fixed source, respectively. In neutron transport, the differential scattering cross-

section is typically expanded in terms of the Legendre polynomial expansion [78]:

$$\Sigma_s\left(\mu'\cdot\mu\right)=\Sigma_s\left(x\right)\sum_{l=0}^{L}\frac{2l+1}{4\pi}b_l P_l\left(\mu\right)P_l\left(\mu'\right)\ . \tag{3.15}$$

Here, P_l is the l^{th} Legendre polynomial, b_l is the l^{th} Legendre moment of the scattering cross-section, and L is the summation limit. Substituting equation (3.15) into equation (3.14), we obtain:

$$\mu\frac{\partial\psi}{\partial x}\left(x,\mu\right)+\Sigma_t\left(x\right)\psi\left(x,\mu\right)=$$
$$\left[\Sigma_s\left(x\right)\sum_{l=0}^{L}\frac{2l+1}{4\pi}b_l P_l\left(\mu\right)\int_{4\pi}P_l\left(\mu'\right)\psi\left(x,\mu'\right)d\Omega'+\frac{1}{4\pi}Q\left(x\right)\right]\ , \tag{3.16}$$

where for 1D, azimuthal symmetry is implied and therefore the integral $\int_{4\pi}d\Omega'$ becomes,

$$\int_{4\pi}d\Omega'=\int_0^{2\pi}d\widetilde{\phi}'\int_{-1}^{+1}d\mu'=2\pi\int_{-1}^{+1}d\mu,$$

where $\widetilde{\phi}'\in[0,2\pi]$ is the azimuthal angle. We define the l^{th} Legendre moment of the angular flux as:

$$\psi_l\left(x\right)=2\pi\int_{-1}^{+1}P_l\left(\mu'\right)\psi\left(x,\mu'\right)d\mu'. \tag{3.17}$$

Therefore, the transport equation can now be written as:

$$\mu\frac{\partial\psi}{\partial x}\left(x,\mu\right)+\Sigma_t\left(x\right)\psi\left(x,\mu\right)=$$
$$\frac{1}{4\pi}\left[\Sigma_s\left(x\right)\sum_{l=0}^{L}\left(2l+1\right)b_l P_l\left(\mu\right)\psi_l\left(x\right)+Q\left(x\right)\right]\ . \tag{3.18}$$

As seen, the differential scattering cross-section is expanded in terms of the *natural* basis function for the angular flux (Legendre polynomial) which diagonalizes the collision operator

in terms of the corresponding Eigen-values (i.e. ψ_l). Here, ψ_l precisely represents, the coefficients for the angular flux ψ. The angular flux is expanded accordingly:

$$\psi(x,\mu) = \sum_{l=0}^{\infty} \psi_l(x) P_l(\mu). \tag{3.19}$$

Now, we have all the essential tools to be able to explain the moment-based accelerator for the neutron transport application. However, before we do so, a classic numerical approach to the solution of equation (3.18) is discussed. In classic steady-state neutron transport, equation (3.18) is solved through a scattering *source iteration* [78]. For simplicity, assume isotropic scattering where $L = 0$ and $b_0 = 1$. ψ_0 is the 0^{th} Legendre moment of ψ and will be re-represented as ϕ which will be defined as the *scalar flux*. With the isotropic scattering assumption, the transport equation is written as:

$$TE = \mu\frac{\partial\psi}{\partial x} + \Sigma_t\psi - \frac{1}{4\pi}\left(\Sigma_s\phi + Q\right) = 0. \tag{3.20}$$

The source iteration will solve the transport equation for the angular flux, ψ, for the z^{th} source iteration as:

$$\psi^z = \mathcal{L}^{-1}S^{z-1}. \tag{3.21}$$

Here, $\mathcal{L}$ is the *transport operator*:

$$\mathcal{L} = \mu\frac{\partial}{\partial x} + \Sigma_t, \tag{3.22}$$

S^{z-1} is the total source:

$$S^{z-1} = \frac{1}{4\pi}\left(\Sigma_s\phi^{z-1} + Q\right), \tag{3.23}$$

and, ϕ^{z-1} is the lagged scattering source, defined as:

$$\phi^{z-1} = \int_{4\pi}\psi^{z-1}d\vec{\Omega} = 2\pi\int_{-1}^{+1}\psi^{z-1}d\mu.$$

The iteration is continued until a specified convergence tolerance is met. The source iteration procedure is summarized in Algorithm 3,

Algorithm 3: Source iteration algorithm for neutron transport.

```
Initialize z = 0, φ^{z=0};
Initialize S^{z=0}; while not converged do
    Increment, z = z + 1;
    Calculate, ψ^z = L^{-1} S^{z-1} ;
    Calculate, φ^z = 2π ∫_{-1}^{1} ψ^z dμ;
    Check for convergence;
end
```

This lag of scattering physics from iteration to iteration is an example of a Picard iteration scheme. The convergence rate is directly proportional to the cross-section ratio, Σ_s/Σ_t. When $\Sigma_s/\Sigma_t \approx 1$ and $\lambda/L_x \ll 1$, the method is known for slow convergence. Here, λ and L_x are the mean-free-path of a particle in the medium and the system size, respectively. The classic paper by reference [52] is one of the first in the literature which discusses the acceleration of this source iteration (Picard iteration) scheme. The method works by introducing the angular moments of the transport equation. Consider the 0^{th} and 1^{st} angular moments of the transport equation (3.20):

$$2\pi \int_{-1}^{+1} TE d\mu = \frac{\partial J}{\partial x} + (\Sigma_t - \Sigma_s)\,\phi - Q = 0, \tag{3.24}$$

$$2\pi \int_{-1}^{+1} TE\mu d\mu = \frac{\partial \mathcal{E}\phi}{\partial x} + \Sigma_t J = 0. \tag{3.25}$$

Here, J and $\mathcal{E}$ are the current and the Eddington factor, defined as:

$$J = 2\pi \int_{-1}^{+1} \mu\psi d\mu, \tag{3.26}$$

$$\mathcal{E} = \frac{2\pi \int_{-1}^{+1} \mu^2 \psi d\mu}{2\pi \int_{-1}^{+1} \psi d\mu}. \tag{3.27}$$

Therefore, by solving for J in equation (3.25) and substituting into equation (3.24), we obtain:

$$-\frac{\partial}{\partial x}\left[\frac{1}{\Sigma_t}\frac{\partial \mathcal{E}\phi}{\partial x}\right] + \left(\Sigma_t - \Sigma_s\right)\phi - Q = 0. \tag{3.28}$$

In a collision dominated region, $\mathcal{E} = 1/3$ and the classic diffusion equation can be retrieved. Next, a nonlinearly coupled system of a high-order (HO) equation (functions of x, μ) and low-order (LO) equation (functions of only x) are defined as:

HO Equation:

$$\mu\frac{\partial \psi}{\partial \mu} + \Sigma_t\psi - \frac{1}{4\pi}\left(\Sigma_s\phi^{LO} + Q\right) = 0, \tag{3.29}$$

LO Equation:

$$-\frac{\partial}{\partial x}\left[\frac{1}{\Sigma_t}\frac{\partial \mathcal{E}^{HO}\phi^{LO}}{\partial x}\right] + \left(\Sigma_t - \Sigma_s\right)\phi^{LO} - Q = 0, \tag{3.30}$$

where,

$$\mathcal{E}^{HO} = \frac{2\pi\int_{-1}^{+1}\mu^2\psi d\mu}{\phi^{HO}} = \frac{2\pi\int_{-1}^{+1}\mu^2\psi d\mu}{2\pi\int_{-1}^{+1}\psi d\mu}. \tag{3.31}$$

It is worthwhile to note that the two equations are solved exactly when either one is solved. The HO equation is solved exactly when ϕ^{LO} is known while the LO equation is solved exactly when $\mathcal{E}^{HO}$ is known. Here, unlike the diffusion approximation, the closure in $\mathcal{E}^{HO}$ comes directly from the solution to the HO equation for ψ. The new iterative scheme now iterates between the HO transport equation (equation (3.29)) and the LO moment equation (equation (3.30)). The QDA source iteration reads as:

Algorithm 4: QDA source iteration for neutron transport.

Initialize $z = 0$, $\phi^{LO,z=0}$;
Initialize $S^{z=0} = \frac{1}{4\pi}\left(\Sigma_s \phi^{LO,z=0} + Q\right)$;
while *not converged* **do**
    Increment, $z = z + 1$;
    Calculate, $\psi^z = \mathcal{L}^{-1} S^{z-1}$;
    Calculate, $\mathcal{E}^{HO,z} = \frac{2\pi \int_{-1}^{1} \mu^2 \psi^z d\mu}{2\pi \int_{-1}^{1} \mu^2 \psi^z d\mu}$;
    Solve, $-\frac{\partial}{\partial x}\left[\frac{1}{\Sigma_t}\frac{\partial \mathcal{E}^{HO,z}\phi^{LO,z}}{\partial x}\right] + \left(\Sigma_t - \Sigma_s\right)\phi^{LO,z} - Q$, for $\phi^{LO,z}$;
    Calculate, $S^z = \frac{1}{4\pi}\left(\Sigma_s \phi^{LO,z} + Q\right)$;
    Check for convergence;
end

The acceleration in the convergence of the HO transport equation is achieved by isolating and accelerating the convergence of the long wavelength mode to ψ. To be precise, the scalar flux, ϕ is in fact, the 0^{th} Legendre moment of ψ (the longest wavelength mode), hence is the slowest to converge in the classic source iteration. The LO moment equation isolates this long wavelength mode and therefore accelerates the convergence of the overall source iteration. This procedure is analogous to the standard geometric multigrid method [115]. It is similar in the sense that iterative methods such as Jacobi or Gauss-Siedel are slow in converging the long wavelength modes of the solution when working on a fine mesh. In order to accelerate the convergence of the iterative method, the problem is solved on different meshes with varying coarseness. The coarse mesh will allow accelerated convergence of the long wavelength modes that are slow in convergence on a fine mesh. The converged solution on the coarse mesh is then interpolated to a finer mesh to converge the shorter wavelength modes, which are fast in convergence. The procedure is continued until all modes are converged. In the QDA method, essentially, the LO system is the coarse mesh accelerator to the HO system.

In order to demonstrate the performance of QDA over the standard source iteration, a 1D single energy group example is discussed. Consider the following problem parameters:

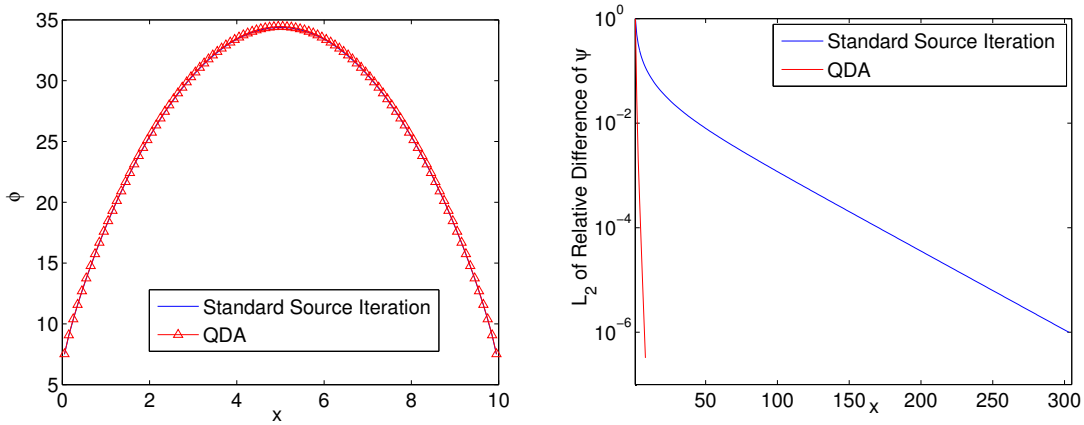


Figure 3.2: Scalar flux (left) and convergence rate (right) between the standard source iteration and QDA iteration.

the mean-free-path of a neutron, $\lambda = 1$, the total cross-section, $\Sigma_t = 1$, the scattering cross-section, $\Sigma_s = 0.99$, the absorption cross-section, $\Sigma_a = 0.01$, the system length, $L_x = 10$, the fixed internal source, $Q = 1$, number of spatial cells, $N_x = 100$, number of discrete quadrature points, $N_\mu = 32$, and the convergence tolerance, tol $= 10^{-6}$. For brevity and illustration purposes only, we simply state that the HO transport equation is solved using a linear discontinuous Galerkin (LDG) discretization [77] in space, x, and a standard Gauss-quadrature [30] set in the angular domain, μ.

The result of the converged scalar flux and the convergence rate plot comparing the standard source iteration and the QDA source iteration is shown in Figure 3.2. As seen, for a system length of many mean-free-paths and scattering dominant problem, the QDA method provides orders of magnitude acceleration over the standard source iteration. However, an important point on the *discrete inconsistency* between the two solution has not been addressed. The LO system and the HO moment system are consistent in the *continuum* however, once discretized, the two systems are not guaranteed to converge to a consistent solution. This is a result of separate truncation error associated with the two systems. In order to enforce discretization consistency between the two system, the concept of consistency term will be

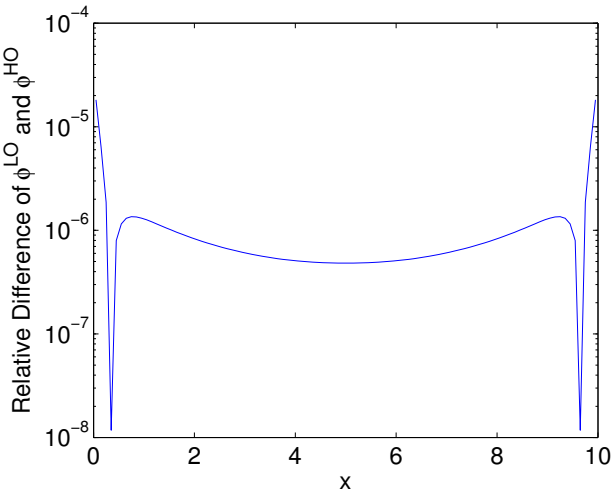


Figure 3.3: Relative difference between the HO and LO scalar flux, ϕ, without discrete consistency.

discussed. To highlight this error in the solution, ϕ^{LO} and $\phi^{HO} = \int_{-1}^{1} \psi d\mu$, are compared for the QDA solution in Figure 3.3. The error, although small, is more than an order of magnitude larger than the convergence tolerance set ($tol = 10^{-6}$). For a steady state neutron transport problem, this difference may be negligible. However, for a time-dependent plasma physics problem, this error may accumulate rapidly, leading to an unphysical evolution of the solution.

The moment equation should only act as a convergence accelerator, without changing the solution to the original discretized HO equation. Therefore, we will add a well defined term to the LO system so as to enslave the LO solution to have identical truncation error as the discrete HO problem. In order to enforce discretization consistency between the two systems, a discrete consistency term will be introduced such that the LO moment equation is modified as follows:

$$\frac{\partial J^{LO}}{\partial x} + (\Sigma_t - \Sigma_s)\,\phi^{LO} = Q, \tag{3.32}$$

$$\frac{\partial \mathcal{E}^{HO}\phi^{LO}}{\partial x} + \Sigma_t J^{LO} = \gamma_J^{HO}\phi^{LO}. \tag{3.33}$$

Solving for J^{LO},

$$J^{LO} = \frac{1}{\Sigma_t}\left[-\frac{\partial \mathcal{E}^{HO}\phi^{LO}}{\partial x} + \gamma_J^{HO}\phi^{LO}\right], \tag{3.34}$$

and substituting into equation (3.32), we obtain:

$$\frac{\partial}{\partial x}\left[\frac{1}{\Sigma_t}\left(-\frac{\partial \mathcal{E}^{HO}\phi^{LO}}{\partial x} + \gamma_J^{HO}\phi^{LO}\right)\right] + \left(\Sigma_t - \Sigma_s\right)\phi^{LO} = Q. \tag{3.35}$$

Here, γ_J^{HO} is what we will refer to as the *discrete consistency term* and is calculated as:

$$\gamma_J^{HO} = \frac{\frac{\partial \mathcal{E}^{HO}\phi^{HO}}{\partial x} + \Sigma_t J^{HO}}{\phi^{HO}}\ . \tag{3.36}$$

The calculation of γ_J is performed such that it is calculated using the *identical* discretization used for the LO system, but with moments from the HO solution,

$$\phi^{HO} = 2\pi\int_{-1}^{1}\psi d\mu, \tag{3.37}$$

$$J^{HO} = 2\pi\int_{-1}^{1}\mu\psi d\mu, \tag{3.38}$$

$$\mathcal{E}^{HO} = \frac{2\pi\int_{-1}^{1}\mu^2\psi d\mu}{2\pi\int_{-1}^{1}\psi d\mu}. \tag{3.39}$$

The result of this process is that we've enslaved the LO truncation error to be identical to the HO error. In order to demonstrate the significance of the consistency term, a relative difference plot between the HO and LO scalar flux is plotted in Figure 3.4. As is clearly

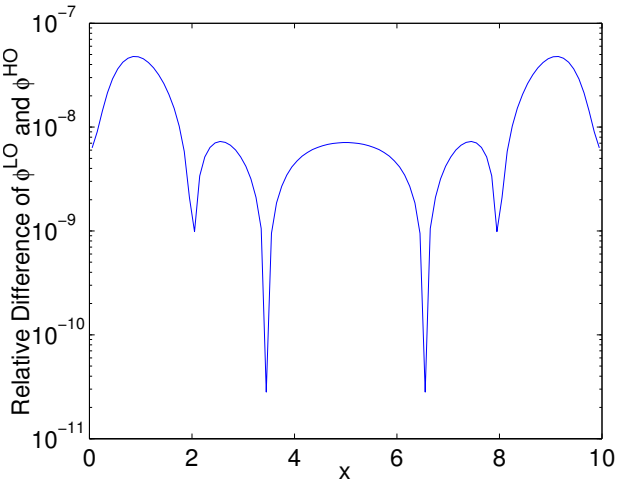


Figure 3.4: Relative difference between the HO and LO scalar flux, ϕ, with discrete consistency.

demonstrated, the difference between the LO and HO scalar flux is significantly reduced, especially near the boundary where the transport effects become important. It is worthwhile to state that γ_J may appear to be a source, but the term is simply used to enforce *discretization error consistency* between the HO and LO system and $\gamma_J \to 0$ as the discrete truncation error,$\Delta \to 0$. For a more detailed discussion of consistency term, the reader is referred to reference [51].

Chapter 4

Moment Acceleration of Collisionless Plasma

The application of the HOLO moment-based acceleration algorithm for a collisionless plasma, modeled with a particle-in-cell (PIC) approach [32] is discussed in this chapter. The purpose of this study is to: 1) develop a method which allows one to efficiently converge the non-linear field-particle system per time-step, and 2) step over the stiff inverse electron plasma frequency, $\omega_{p,e}^{-1}$, without the complication of collisions. The new algorithm is used to solve a *collisionless* electrostatic ion-acoustic shock wave problem, which is a multi-scale problem both in time and space. The problem evolves on the slow ion acoustic time-scale while still supporting a much faster inverse electron plasma frequency time-scale, $\omega_{p,e}^{-1}$. The initial structure of the wave is on the order of the ion acoustic wave length, however, the shock front evolves on the length-scale of a much shorter Debye length, λ_D. Classic explicit algorithms are forced to take time-step size, Δt, that is some fraction of $\omega_{p,e}^{-1}$ but we show that our new algorithm is capable of taking $\Delta t \gg \omega_{p,e}^{-1}$ while still efficiently and accurately being able to solve the nonlinear field-particle system.

4.1 Introduction

The dynamic evolution of coupled electromagnetic fields and a collisionless plasma are described by the Vlasov-Maxwell system. The Maxwell equations evolve the self-consistent fields based on moments of the ion-electron distribution functions (density and current). The plasma distribution function evolution is governed by the Vlasov equation, which is coupled back to the Maxwell system through the electromagnetic forces. In this study, we will focus on a particle in cell (PIC) simulation approach [32] for this coupled system.

Historically, explicit particle in cell (PIC) approaches have been used to model collisionless kinetic plasmas [32]. The method is parallelizable, simple to implement and is, most of all, computationally inexpensive per time step. The method has been successfully implemented on advanced computer architectures, producing an impressive plasma physics simulation capability [48, 49].

However, explicit momentum conserving PIC implementations can encounter numerical instabilities due to the properties of spatial aliasing [32, 47]. The so-called finite-grid stability constraint requires the mesh size to resolve the Debye length everywhere. In addition, with explicit PIC, the usual temporal instabilities arise in cases when the time step size, Δt, does not respect the CFL condition [32]. These stability constraints make the method restrictive when investigating large spatial-scale and long time-scale problems. For finite Δt size, the lack of conservation of energy becomes an important concern in long time integration.

On the other hand, implicit PIC schemes do not suffer from the CFL limitations of the explicit scheme. In addition, finite-grid instabilities can be eliminated [54, 55]. With implicit schemes, time-step size, Δt, may be chosen such that the largest dynamical time-scale of interest may be followed.

Historically, two routes have been considered for implicit PIC. One is the direct implicit method (DIM) [33, 34, 35, 36, 37, 38] and the other is the implicit moment method (IMM)[41,

42, 43, 45]. In the DIM approach, some level of a nonlinear iteration between particles and field is done, to some level of convergence, within a time step. Initial efforts established that the method is capable of stepping over CFL limitations. Due to solver technology limitations, initial DIM efforts relied on semi-implicit linearization within a time step. Without tight nonlinear convergence between the particles and fields, large numerical errors are allowed to develop [40]. Furthermore, for a large particle number and in a multidimensional setting, the nonlinear system size may become prohibitively large, making memory storage intractable for fully implicit iterative schemes. Recent work in [54, 55] has addressed the issue of nonlinear system size through the use of a kinetic enslaved Jacobian-Free Newton-Krylov (JFNK) algorithm. In [54], it has been demonstrated that by nonlinearly converging particles and fields, one can exactly conserve energy, and take time step sizes that are orders of magnitude larger than the CFL condition stably and accurately, with an overall CPU speedup compared to the explicit PIC scheme. The work by [54, 55] may be regarded as a modern, tractable, and accurate route to the DIM approach.

IMM approaches, on the other hand, are based on the formulation of a coupled fluid moment system of the original Vlasov equation and Maxwell's equations. This coupled moment system is solved to evaluate implicitly the new-time fields. The particles are pushed with these fields and this particle solution is used to self-consistently close the moment system at the stress-tensor level. The method has been successful in addressing several challenging plasma physics problems [45]. However, previous IMM approaches face the issue of *discrete truncation error consistency* between the kinetic system and the moment system. Inconsistency between the discrete systems results in energy conservation errors and numerical instability, as we will show. Inconsistent evolution of the moment system and kinetic system within a time-step was acknowledged as problematic and mitigating strategies have been proposed [44]. However, to date, nonlinear convergence between the two systems to a discretely consistent solution has not been demonstrated.

In this study, we put forth a modern approach to IMM which converges particles and

fields, enforces discrete consistency, conserves energy, and is second-order accurate in time. In this work, we will utilize the advanced particle push developed by Chen et al [54]. This is a significant departure from the classic IMM approaches. The adaptive, subcycled, particle push faithfully follows the individual ion and electron orbits. Furthermore, this particle pusher will allow for energy conservation down to the nonlinear convergence tolerance between the kinetic and moment system.

The remainder of this chapter is organized as follows. Section 4.2 introduces the governing set of equations for a one dimensional in space (1D), and one dimensional in velocity space (1V) Vlasov-Ampére system. The derivation of the moment system based on the continuum definition of moments of the velocity distribution function of the kinetic Vlasov equation are presented. Then, the approach to enforce discrete truncation error between the kinetic and moment systems by means of a consistency term, and the formulation of a density normalized stress-tensor are discussed. Section 4.3 briefly discusses the discretization scheme applied to our kinetic and moment system, followed with section 4.4 providing the actual overall algorithm. Section 4.5 provides benchmark and test case results, and discusses performance of the algorithm for the multiscale ion acoustic shockwave problem. Demonstration of the importance of the consistency term and the formulation of the density-normalized stress-tensor are given in section 4.6. Concluding remarks are provided in section 7.5.

4.2 Moment Accelerated Vlasov Ampère

The moment accelerated technique we propose may be regarded as an improvement to the original pioneering work on implicit moment method (IMM) first investigated in [41, 42, 43, 45]. We will extend the IMM concept by 1) enforcing discrete consistency between the moment and kinetic system and 2) efficiently converging the moment and kinetic system within a time step using a density-normalized, stress-tensor to *expose* the stiff hyperbolic waves in the fluid moment system. In order to describe the moment-based accelerator scheme

applied to our kinetic plasma physics problem, the governing set of equations is derived with proper modifications to enforce the *discrete consistency* between the kinetic system and the fluid moment system. A discussion on formulation of a density-normalized stress-tensor is provided to complete the equation set which is discretized and solved numerically in section 4.3.

4.2.1 Problem Statement

For a proof of principle study, following the work of Chen et al. [54], a 1D configuration space and 1D velocity space electro-static two species Vlasov Ampère problem is considered:

$$\frac{\partial f_e}{\partial t} + v\frac{\partial f_e}{\partial x} + \frac{q_e}{m_e}E\frac{\partial f_e}{\partial v} = 0 \,, \tag{4.1}$$

$$\frac{\partial f_i}{\partial t} + v\frac{\partial f_i}{\partial x} + \frac{q_i}{m_i}E\frac{\partial f_i}{\partial v} = 0 \,, \tag{4.2}$$

$$\epsilon_0\frac{\partial E}{\partial t} + \sum_\alpha q_\alpha n u_\alpha - \overline{\left\langle \sum_\alpha q_\alpha n u_\alpha \right\rangle} = 0 \,. \tag{4.3}$$

Equations (4.1), (4.2) and (4.3) are the electron and ion Vlasov equations and the Ampère equation respectively. m_e, m_i, f_e, f_i, v, q_e, q_i, E, ϵ_0, and nu_α are the electron and ion mass, electron and ion distribution function, electron and ion velocity in the x component, electron and ion charge, the x component of electric field, permeability constant of vacuum, and the momentum of species α respectively. The $\overline{\langle \cdot \rangle}$ term denotes a spatially averaged quantity and is included to enforce Galilean invariance [54]. The Vlasov equations are functions of space, velocity, and time. The Ampère equation is solved for the self-consistent electric field, which is a function of space and time.

The coupled set of nonlinear equations is solved fully implicitly. Again, for this study,

a particle-in-cell (PIC) approach will be adopted to solve Vlasov equation. However, the general IMM approach is also applicable when deterministically solving the discrete Vlasov equation.

4.2.2 Derivation of moment system for Vlasov-Ampère System

In this section, we formulate a coupled higher dimensional (independent variables are x, v, and t) kinetic system (HO), and lower dimensional (independent variables are x, and t) moment system of equations (LO) for the Vlasov-Ampère system to accelerate the nonlinear solve for the electric field. The Vlasov equation for species α, (VE_α), is defined according to equations (4.1) and (4.2), as:

$$\text{VE}_\alpha = \frac{\partial f_\alpha}{\partial t} + v\frac{\partial f_\alpha}{\partial x} + \frac{q_\alpha}{m_\alpha}E\frac{\partial f_\alpha}{\partial v} = 0\,. \tag{4.4}$$

We define the w^{th} moment of the velocity distribution function of species α as follows,

$$\mathcal{M}_\alpha^w = \int_{-\infty}^{+\infty} v^w f_\alpha dv = \langle v^w, f_\alpha \rangle_v\,. \tag{4.5}$$

With this definition, the number density, n_α, number density flux, nu_α, and total stress-tensor, S_α which are the 0^{th}, 1^{st} and 2^{nd} moments of the distribution function, respectively, can be written as:

$$\begin{aligned} n_\alpha &= \langle 1, f_\alpha \rangle_v\ , \\ nu_\alpha &= \langle v, f_\alpha \rangle_v\ , \\ S_\alpha &= \left\langle v^2, f_\alpha \right\rangle_v\ . \end{aligned}$$

The governing equations for the fluid moments (the LO problem) are obtained by taking the 0^{th} and 1^{st} moment of the Vlasov equation to find:

$$\langle 1, \mathrm{VE}_\alpha \rangle_v = \frac{\partial n_\alpha}{\partial t} + \frac{\partial}{\partial x} n u_\alpha = 0 \ , \tag{4.6}$$

$$\langle v, \mathrm{VE}_\alpha \rangle_v = \frac{\partial}{\partial t} n u_\alpha + \frac{\partial}{\partial x} S_\alpha - \frac{q_\alpha}{m_\alpha} n_\alpha E = 0 \ . \tag{4.7}$$

Equations (4.6) and (4.7) are the continuity and momentum conservation equations, respectively, for each species. Now consider the coupled HO kinetic system and a LO moment system for an ion-electron system.

HO (Kinetic) System:

$$\frac{\partial f_e}{\partial t} + v \frac{\partial f_e}{\partial x} + \frac{q_e}{m_e} E \frac{\partial f_e}{\partial v} = 0, \tag{4.8}$$

$$\frac{\partial f_i}{\partial t} + v \frac{\partial f_i}{\partial x} + \frac{q_i}{m_i} E \frac{\partial f_i}{\partial v} = 0. \tag{4.9}$$

LO (Moment-Field) System:

$$\frac{\partial n_e}{\partial t}^{LO} + \frac{\partial}{\partial x} n u_e^{LO} = 0, \tag{4.10}$$

$$\frac{\partial}{\partial t} n u_e^{LO} + \frac{\partial}{\partial x} S_e^{HO} - \frac{q_e}{m_e} n_e^{LO} E = 0, \tag{4.11}$$

$$\frac{\partial n_i}{\partial t}^{LO} + \frac{\partial}{\partial x} n u_i^{LO} = 0, \tag{4.12}$$

$$\frac{\partial}{\partial t} n u_i^{LO} + \frac{\partial}{\partial x} S_i^{HO} - \frac{q_i}{m_i} n_i^{LO} E = 0, \tag{4.13}$$

$$\epsilon_0 \frac{\partial E}{\partial t} + \sum_\alpha q_\alpha n u_\alpha^{LO} - \overline{\left\langle \sum_\alpha q_\alpha n u_\alpha^{LO} \right\rangle} = 0. \tag{4.14}$$

The closure required for the LO fluid momentum system is provided via the HO total stress-tensor, S_α^{HO},

$$S_\alpha^{HO} = \left\langle v_\alpha^2, f_\alpha \right\rangle_v \ .$$

The HO system is driven by the electric field, E, computed from the LO system. It is important to point out that, in the continuum, both the HO and LO equations are solved by the ion and electron distribution functions and the electric field. If an exact closure to S_α^{HO} is provided for both species, the correct electric field is retrieved. On the other hand, if the exact electric field is known, the correct f_α can be found. This structure between the HO and LO equations will be utilized to our advantage to formulate an acceleration algorithm for a Picard iteration that iterates between the HO and LO equations. The purpose of the LO system is to accelerate convergence of the kinetic HO system.

4.2.3 Motivation for a moment approach

Chen et al. [54] developed a fully implicit framework to solve the electrostatic Vlasov Ampère system through a kinetically enslaved Jacobian-Free Newton-Krylov method. However, the method requires an implicit particle push for each GMRES iterations within the JFNK iteration for a given time step. As we step over electron time-scales $\left(\Delta t \gg \frac{\Delta x}{v_{th,e}}\right)$, the Jacobian matrix becomes dense via electron plasma propagation through many cells [21]. Without a good preconditioner, the required number of GMRES iteration per Newton iteration becomes large. Development of an effective preconditioner is a currently ongoing active research topic [58].

We propose in this study an alternative implicit method which relies on a simple Picard iteration between the HO kinetic particle system and the LO field-moment system. In this approach, we will require one implicit particle push per Picard iteration between the HO and LO systems within a time step. This work may be regarded as an improvement to

the standard IMM [41, 42, 43]. Specific improvements to the standard IMM approach put forth in this study are 1) effectively addressing the discrete consistency issue between the moment system and the kinetic system, and 2) developing a stable and efficient iteration scheme between the moment and kinetic system through the use of a density-normalized stress-tensor, and 3) exact energy and charge conservation.

4.2.4 Modification of the LO equations: discrete consistency

As discussed in the preceding section, the HO and LO systems are exactly equivalent in the continuum given the exact closure to S_α^{HO} and E. However, an issue arises in the discrete. Upon discretization of the HO and LO system of equations, discretization errors arise in both systems. While we cannot avoid discretization error, we also cannot tolerate the discretization error of the two systems (HO and LO) being *different*. If such a situation occurs, then over many time steps, the two systems will drift apart, leading to inaccuracies, instabilities, and nonlinear divergence of the solver. Traditionally, this numerical divergence between the two systems was partially relaxed by resetting the LO moments to those obtained by the HO solution at the end of each time-step. However, this does still allow for inconsistent solutions between the kinetic and moment system within a time-step, resulting in lack of energy conservation. The charge-conserving particle integrator developed in [54] is designed such that the discrete continuity equation evaluated with n_α^{HO} and nu_α^{HO} is satisfied to round-off. Thus, we focus on enforcing discrete consistency for the 1^{st} moment equation.

In order to address this discretization error mismatch between the two systems, we borrow the concept of a *consistency term* from the neutral particle transport community using moment-based accelerations [50, 51, 53]. Consider the following modified LO moment equations,

$$\frac{\partial n_e}{\partial t}^{LO} + \frac{\partial}{\partial x} n u_e^{LO} = 0 \,, \tag{4.15}$$

$$\frac{\partial}{\partial t} n u_e^{LO} + \frac{\partial}{\partial x} S_e^{HO} - \frac{q_e}{m_e} n_e^{LO} E = \gamma_{nu_e}^{HO} n_e^{LO} \ , \tag{4.16}$$

$$\frac{\partial n_i}{\partial t}^{LO} + \frac{\partial}{\partial x} n u_i^{LO} = 0 \ , \tag{4.17}$$

$$\frac{\partial}{\partial t} n u_i^{LO} + \frac{\partial}{\partial x} S_i^{HO} - \frac{q_i}{m_i} n_i^{LO} E = \gamma_{nu_i}^{HO} n_i^{LO} \ , \tag{4.18}$$

$$\epsilon_0 \frac{\partial E}{\partial t} + \sum_\alpha q_\alpha n u_\alpha^{LO} - \overline{\left\langle \sum_\alpha q_\alpha n u_\alpha^{LO} \right\rangle} = 0 \ . \tag{4.19}$$

The $\gamma_{nu,\alpha}^{HO}$ terms in equations (4.16) and (4.18) are the so-called *consistency* terms and they will be used to force the truncation error of the LO problem to be equivalent to the truncation error of the HO problem. Similar to [50, 51], this goal is achieved by calculating $\gamma_{nu,\alpha}^{HO}$ using the same discretization scheme for the 1^{st} moment equations, but evaluated with HO solution moments,

$$\gamma_{nu,\alpha}^{HO} = \frac{\frac{\partial}{\partial t} n u_\alpha^{HO} + \frac{\partial}{\partial x} S_\alpha^{HO} - \frac{q_\alpha}{m_\alpha} n_\alpha^{HO} E}{n_\alpha^{HO}} \ . \tag{4.20}$$

The HO moment variables are calculated by numerical integration of the HO solution to f_α. In this study, a particle-in-cell (PIC) approach is used and the moments are calculated by summing over particles:

$$\begin{aligned}
n_{\alpha,i}^{HO} &= \langle 1, f_{\alpha,i} \rangle_v \approx \frac{\omega_\alpha}{\Delta x_i} \sum_p^{N_p} \mathcal{S}_p \left(x_i - x_{p,\alpha} \right) \ , \\
n u_{\alpha,i}^{HO} &= \langle v, f_{\alpha,i} \rangle_v \approx \frac{\omega_\alpha}{\Delta x_i} \sum_p^{N_p} v_{p,\alpha} \mathcal{S}_p \left(x_i - x_{p,\alpha} \right) \ , \\
S_{\alpha,i}^{HO} &= \left\langle v^2, f_{\alpha,i} \right\rangle_v \approx \frac{\omega_\alpha}{\Delta x_i} \sum_p^{N_p} v_{p,\alpha}^2 \mathcal{S}_p \left(x_i - x_{p,\alpha} \right) \ .
\end{aligned}$$

Here, N_p is number of particles, $v_{p,\alpha}$ is the velocity of the p'th particle for species α, $x_{p,\alpha}$ is the particle position, x_i is i'th cell node location, Δx_i is the i'th cell size, ω_α is the weight of the species, and $\mathcal{S}$ is the shape (interpolation) function. We will refer the reader to standard text on PIC for details [47] . When γ_α^{HO} is evaluated in this manner, and then used in (4.16) and (4.18), discrete consistency is enforced upon convergence of the HO-LO iteration. Again, we note that the consistency term, $\gamma_{nu_\alpha}^{HO}$, is required only for the 1^{st} moment equation and not in the 0^{th} moment equation. The discrete 0^{th} moment equation conservation is exactly satisfied when we use the charge conserving particle integrator of Chen et al. [54]. Finally, we state here that the choice of the consistency is highly flexible and one may wish to implicitly solve the consistency operator (RHS of equations (4.16) and (4.18)) by normalizing the expression by the HO density or not. In this study, density normalization is performed to be consistent with the original use in the neutron transport application [50].

The consistency term may appear to be a physical *source* term in the conservation equation for the LO system. However, this is not the correct interpretation. Once we discretize our system, we are not solving the original continuum equation, but a numerically *approximate*, discrete form. The consistency term strictly exists only in the *discrete* LO system, and is used to force discretization error of the LO system to be exactly that of the HO system upon nonlinear convergence. The magnitude of the consistency term decreases with Δt and Δx refinement, as was shown in [53].

4.2.5 Modification of the LO equations: density-normalized stress-tensor

We discuss next our use of a density-normalized stress-tensor to enhance the convergence rate of the Picard HO-LO solver. The density normalization of the stress-tensor will produce a LO formulation that will effectively capture stiff-wave phenomena, thus producing an effective

accelerator. Consider the following modified LO system of equations,

$$\frac{\partial n_e}{\partial t}^{LO} + \frac{\partial}{\partial x} n u_e^{LO} = 0 \,, \tag{4.21}$$

$$\frac{\partial}{\partial t} n u_e^{LO} + \frac{\partial}{\partial x} \underline{n_e^{LO} \tilde{S}_e^{HO}} - \frac{q_e}{m_e} n_e^{LO} E = \gamma_{nu_e}^{HO} n_e^{LO} \,, \tag{4.22}$$

$$\frac{\partial n_i}{\partial t}^{LO} + \frac{\partial}{\partial x} n u_i^{LO} = 0 \,, \tag{4.23}$$

$$\frac{\partial}{\partial t} n u_i^{LO} + \frac{\partial}{\partial x} \underline{n_i^{LO} \tilde{S}_i^{HO}} - \frac{q_i}{m_i} n_i^{LO} E = \gamma_{nu_i}^{HO} n_i^{LO} \,, \tag{4.24}$$

$$\epsilon_0 \frac{\partial E}{\partial t} + \sum_\alpha q_\alpha n u_\alpha^{LO} - \overline{\left\langle \sum_\alpha q_\alpha n u_\alpha^{LO} \right\rangle} = 0 \,. \tag{4.25}$$

The modification is in the HO density-normalized stress-tensor, $\tilde{S}_\alpha^{HO}$, and is defined below.

$$\widetilde{S}_{\alpha,i}^{HO} = \frac{\langle v^2, f_{\alpha,i} \rangle_v}{\langle 1, f_{\alpha,i} \rangle_v} \approx \frac{\sum_p^{N_p} v_{p,\alpha}^2 \mathcal{S}_p \left(x_i - x_{p,\alpha} \right)}{\sum_p^{N_p} \mathcal{S}_p \left(x_i - x_{p,\alpha} \right)}.$$

This formulation of the density-normalized stress-tensor exposes the stiff hyperbolic waves in the LO moment system (refer to appendix A). In doing so, we significantly enhance the convergence rate of the HO-LO iteration within a time step when the time step is large compared to the stiff waves.

Again, recall that the issues of discrete consistency and a density-normalized stress-tensor have not been addressed in previous efforts on the implicit moment method (IMM) [41, 42, 43, 44]. Through the consistency term, the kinetic and moment systems can consistently evolve. The density normalization of stress-tensor allows a stable and efficient iteration scheme between the HO kinetic system and the LO moment system. The importance of the consistency term in the solution evolution and energy conservation will be demonstrated.

The importance of working with a density-normalized stress-tensor in the LO system will also be demonstrated.

4.3 Solver and Discretization

With the general methodology of moment-based acceleration for the Vlasov-Ampère problem outlined, we discuss next the technique to solve the equations and the discretization scheme applied to both the HO and LO system of equations.

4.3.1 Higher Order System: Implicit Charge-Conserving Particle in Cell

As mentioned in section 4.2.1, we solve the Vlasov equation via PIC, which requires integrating particle orbits. In this study, a charge-conserving scheme [54] is adopted. Again, this is a significant departure from the particle push used in previous IMM approaches. We will include some discussion in this section on how the charge-conserving particle pushing algorithm works.

The equations of motion for each particle are,

$$\frac{\partial x_p}{\partial t} = v_p \ , \tag{4.26}$$

$$\frac{\partial v_p}{\partial t} = \frac{q_p}{m_p} E_p \left(x_p \right) \ . \tag{4.27}$$

Here, m_p, x_p, v_p, and E_p are the particle mass, position, velocity, and electric field at the particle position. The subscript p denotes individual particle quantities. Since the electric

field lives on the grid, the field is interpolated to the particle via a shape function [32].

Equations (4.26) and (4.27) are discretized using a 2^{nd} order Crank-Nicolson time discretization with adaptive orbit integrator scheme [54],

$$\frac{x_p^{\nu+1} - x_p^{\nu}}{\Delta\tau^{\nu}} = v_p^{\nu+1/2} \ , \tag{4.28}$$

$$\frac{v_p^{\nu+1} - v_p^{\nu}}{\Delta\tau^{\nu}} = \frac{q_p}{m_p} E_p^{k+1/2}\left(x_p^{\nu+1/2}\right) \ . \tag{4.29}$$

Here k and ν superscripts denote the global time index and the particle subcycle time index, and $\Delta\tau^{\nu}$ is the ν^{th} subcycle time step size. The coupled nonlinear ODE system is solved through a Picard iteration. The relation between the global time step and the subcycle time step is,

$$\Delta t = \sum_{\nu=1}^{N_\nu} \Delta\tau_\nu \ .$$

The time centered averaged quantities are,

$$\begin{aligned} x_p^{\nu+1/2} &= \frac{1}{2}\left(x_p^{\nu+1} + x_p^{\nu}\right) \ , \\ v_p^{\nu+1/2} &= \frac{1}{2}\left(v_p^{\nu+1} + v_p^{\nu}\right) \ , \\ E_p^{k+1/2}\left(x_p^{\nu+1/2}\right) &= \frac{1}{2}\left[E_p^{k+1}\left(x_p^{\nu+1/2}\right) + E_p^{k}\left(x_p^{\nu+1/2}\right)\right] \ . \end{aligned}$$

1^{st} order shape functions, $\mathcal{S}_1$, are used to interpolate the electric field and accumulate the number density flux while a 2^{nd} order shape functions, $\mathcal{S}_2$, are used to accumulate the density and stress-tensor.

$$\mathcal{S}_1\left(x - x_p\right) = \left\{ \begin{array}{c} 1 - \frac{|x-x_p|}{\Delta x}, \ \text{ for } |x - x_p| \ \leq \ \Delta x \\ \\ 0, \ \text{ otherwise} \end{array} \right\}$$

$$\mathcal{S}_2\left(x-x_p\right)=\left\{\begin{array}{c} \frac{3}{4}-\left(\frac{|x-x_p|}{\Delta x}\right)^2, \ \text{ for } |x-x_p| \ \leq \ \frac{\Delta x}{2} \\ \\ \frac{1}{2}\left(\frac{3}{2}-\frac{|x-x_p|}{\Delta x}\right)^2, \ \text{ for } \frac{\Delta x}{2} \ \leq \ |x-x_p| \ \leq \ \frac{3\Delta x}{2} \\ \\ 0, \ \text{ otherwise} \end{array}\right\}$$

The field and momentum shape functions must be one order lower than the density shape function to conserve charge, as discussed in detail in [54]. The density and stress-tensor are evaluated at cell centers, while the momentum is evaluated at cell faces,

$$n_i=\frac{1}{\Delta x}\sum_p w_p\mathcal{S}_2\left(x_i-x_p\right) \ , \tag{4.30}$$

$$S_i=\frac{1}{\Delta x}\sum_p v_p^2 w_p\mathcal{S}_2\left(x_i-x_p\right) \ , \tag{4.31}$$

$$nu_{i+1/2}=\frac{1}{\Delta x}\sum_p v_p w_p\mathcal{S}_1\left(x_{i+1/2}-x_p\right) \ . \tag{4.32}$$

Here, w_p is the particle weight, subscripts i and $i+1/2$ are the integer cell node and half integer cell face index. The electric field is interpolated to the particle at a subcycle time step as follows,

$$E_p^{k+1/2}\left(x_p^{\nu+1/2}\right)=\sum_{i=1}^{N_x}E_{i+1/2}^{k+1/2}\mathcal{S}_1\left(x_{i+1/2}-x_p^{\nu+1/2}\right) \ . \tag{4.33}$$

Here, N_x is the total number of cells in the system. In order to enforce energy conservation, an orbit averaged momentum is evaluated at cell faces,

$$\overline{nu}_{i+1/2}^{k+1/2}=\frac{1}{\Delta x\Delta t}\sum_p\sum_{\nu=1}^{N_\nu}w_p v_p^{\nu+1/2}\mathcal{S}_1\left(x_p^{\nu+1/2}-x_{i+1/2}\right)\Delta\tau^\nu \ . \tag{4.34}$$

For a full and complete discussion of the adaptive orbit integrator algorithm, the reader is referred to the original work by Chen et al. [54].

4.3.2 Lower Order System: Staggered Finite Differencing

For spatial discretization of the LO system on a 1D mesh, we employ a staggered finite difference method. Similar to the HO definition of density and number density flux, we wish to solve for densities at cell centers while solving for the number density flux and electric fields at cell faces.

The following equations represent the time and space discretization of the LO system,

$$\frac{n_{\alpha,i}^{LO,k+1} - n_{\alpha,i}^{HO,k}}{\Delta t} + \frac{\overline{nu}_{\alpha,i+1/2}^{LO,k+1/2} - \overline{nu}_{\alpha,i-1/2}^{LO,k+1/2}}{\Delta x} = 0 \ , \tag{4.35}$$

$$\begin{aligned} &\frac{\overline{nu}_{\alpha,i+1/2}^{LO,k+1/2} - nu_{\alpha,i+1/2}^{HO,k}}{\Delta t/2} + \\ &\frac{n_{\alpha,i+1}^{LO,k+1/2}\tilde{S}_{\alpha,i+1}^{HO,k+1/2} - n_{\alpha,i}^{LO,k+1/2}\tilde{S}_{\alpha,i}^{HO,k+1/2}}{\Delta x} \\ -\frac{q_\alpha}{m_\alpha} n_{\alpha,i+1/2}^{LO,k+1/2} E_{i+1/2}^{LO,k+1/2} &- \gamma_{nu_\alpha,i+1/2}^{HO} n_{\alpha,i+1/2}^{LO,k+1} = 0 \ , \end{aligned} \tag{4.36}$$

$$\epsilon_0 \frac{E_{i+1/2}^{LO,k+1} - E_{i+1/2}^{LO,k}}{\Delta t} + \sum_\alpha q_\alpha \overline{nu}_{\alpha,i+1/2}^{LO,k+1/2} - \overline{\left\langle \sum_\alpha q_\alpha \overline{nu}_{\alpha,i+1/2}^{LO,k+1/2} \right\rangle} = 0 \ . \tag{4.37}$$

We have performed a non-standard discretization in time. The discretization may seem like a classic Crank-Nicolson scheme due to the evaluation of the number density at half time $k + 1/2$. However, the momentum equation is solved for the half time momentum for each species in order to satisfy the continuity equation *such that* both $n_{\alpha,i}^{LO,k+1}$ and $\overline{nu}_{\alpha,i}^{LO,k+1/2}$ are consistent with $n_{\alpha,i}^{HO,k+1}$ and $\overline{nu}_{\alpha,i+1/2}^{HO,k+1/2}$. The density and the electric field are time averaged

and space averaged for the momentum equation,

$$n_{\alpha,i}^{LO,k+1/2} = \frac{1}{2}\left(n_{\alpha,i}^{LO,k+1} + n_{\alpha,i}^{LO,k}\right) ,$$

$$n_{\alpha,i+1/2}^{LO,k+1/2} = \frac{1}{2}\left(n_{\alpha,i+1}^{LO,k+1/2} + n_{\alpha,i}^{LO,k+1/2}\right) ,$$

$$E_{i+1/2}^{LO,k+1/2} = \frac{1}{2}\left(E_{i+1/2}^{LO,k+1} + E_{i+1/2}^{LO,k}\right) .$$

The time centered HO density normalized stress-tensor is calculated as,

$$\tilde{S}_{\alpha,i}^{HO,k+1/2} = \frac{S_{\alpha,i}^{HO,k+1} + S_{\alpha,i}^{HO,k}}{n_{\alpha,i}^{HO,k+1} + n_{\alpha,i}^{HO,k}} = \frac{\frac{1}{\Delta x \Delta t}\sum_p w_{\alpha,p}\left[v_{\alpha,p}^{2,k+1}\mathcal{S}_2\left(x_{\alpha,p}^{k+1} - x_i\right) + v_{\alpha,p}^{2,k}\mathcal{S}_2\left(x_{\alpha,p}^{k} - x_i\right)\right]}{n_{\alpha,i}^{HO,k+1} + n_{\alpha,i}^{HO,k}} .$$

The consistency term, $\gamma_{nu_\alpha,i+1/2}^{HO}$, is calculated as follows.

$$\gamma_{nu_\alpha,i+1/2}^{HO} = \left[\frac{\overline{nu}_{\alpha,i+1/2}^{HO,k+1/2} - nu_{\alpha,i+1/2}^{HO,k}}{\Delta t/2} + \frac{n_{\alpha,i+1}^{HO,k+1/2}\tilde{S}_{\alpha,i+1}^{HO,k+1/2} - n_{\alpha,i}^{HO,k+1/2}\tilde{S}_{\alpha,i}^{HO,k+1/2}}{\Delta x} - \frac{q_\alpha}{m_\alpha} n_{\alpha,i+1/2}^{HO,k+1/2} E_{i+1/2}^{LO,k+1/2}\right] / n_{\alpha,i+1/2}^{HO,k+1} \tag{4.38}$$

Due to the presence of the consistency term, which effectively enslaves the LO moment solution to the HO kinetic solution upon nonlinear convergence, the LO moment systems can be discretized in a variety of forms and *solved* in many ways. It is stressed that the *choice* of the LO moment system discretization and solver is not key but the correct calculation of the consistency term is. As a result of the consistency terms, the LO system will be second-order accurate in time, as it is enslaved to the HO system. The implicit solution of the LO system, which is required in every outer HO-LO iteration can be accomplished with either a Picard iteration or a JFNK [62] iteration as options. Both are briefly discussed in appendix B.

4.4 Algorithm: Nested HOLO Iteration

This section will outline the algorithm to solve the the overall HOLO system of equations. The algorithm is, in essence, a nested outer-inner iteration as described below. Inside the outer HOLO Picard iteration, there are required iterations in the nonlinear implicit HO system and the nonlinear implicit LO system. The convergence of both the outer iteration and inner LO system are measured through the residuals of the *moment* equations. Consider the residual of our moment system in terms of both the HO and LO variables in a time semi-discretized form,

$$G_{n_e} = \frac{n_e^{LO,k+1} - n_e^{HO,k}}{\Delta t} + \frac{\partial}{\partial x}\overline{nu}_e^{LO,k+1/2} \,, \tag{4.39}$$

$$G_{nu_e} = \frac{\overline{nu}_e^{LO,k+1/2} - nu_e^{HO,k}}{\Delta t/2} + \frac{\partial}{\partial x} n_e^{LO,k+1/2}\tilde{S}_e^{HO,k+1/2,y} - \frac{q_e}{m_e} n_e^{LO,k+1/2} E^{k+1/2} - \gamma_{nu_e}^{HO,k+1,y} n_e^{LO,k+1} \,, \tag{4.40}$$

$$G_{n_i} = \frac{n_i^{LO,k+1} - n_i^{HO,k}}{\Delta t} + \frac{\partial}{\partial x}\overline{nu}_i^{LO,k+1/2} \,, \tag{4.41}$$

$$G_{nu_i} = \frac{\overline{nu}_i^{LO,k+1/2} - nu_i^{HO,k}}{\Delta t/2} + \frac{\partial}{\partial x} n_i^{LO,k+1/2}\tilde{S}_i^{HO,k+1/2,y} - \frac{q_i}{m_i} n_i^{LO,k+1/2} E^{LO,k+1/2} - \gamma_{nu_i}^{HO,k+1,y} n_i^{LO,k+1} \,, \tag{4.42}$$

$$G_E = \epsilon_0 \frac{\partial E}{\partial t} - \left(\sum_\alpha q_\alpha \overline{nu}_\alpha^{LO,k+1/2} - \overline{\left\langle \sum_\alpha q_\alpha \overline{nu}_\alpha^{LO,k+1/2} \right\rangle} \right) \,, \tag{4.43}$$

$$\mathbf{G} = \begin{Bmatrix} G_{n_e} \\ G_{nu_e} \\ G_{n_i} \\ G_{nu_i} \\ G_E \end{Bmatrix} \,. \tag{4.44}$$

The superscript y in equations (4.40) and (4.42) denotes the outer iteration index. With the expression for residuals given, the HOLO moment-based acceleration algorithm is shown in Algorithm 5 for each time step, k.

Algorithm 5: HOLO algorithm for Vlaosv-Ampère system.

1 Begin outer Picard iteration, $y = 0$;

2 With the initial $\tilde{S}_\alpha^{HO,k}$, $n_\alpha^{LO,k}$, $nu_\alpha^{LO,k}$ and $E^{LO,k}$, calculate the initial outer moment system residual, $||\mathbf{G}||_0^{out}$, from equations (4.39) to (4.43);

3 **while** *HOLO system not converged* **do**

4 Execute inner LO moment system solve, using Picard or JFNK using the known $\tilde{S}^{HO,k+1/2,y}$ and $\gamma^{HO,k+1,y}$, solve for LO quantities: $n_\alpha^{LO,k+1}$, $\overline{nu}_\alpha^{LO,k+1/2}$, E^{k+1} to convergence by solving equations (4.39) to (4.43);

5 Increment outer HOLO index, $y = y + 1$;

6 With new E^{k+1}, execute HO kinetic system solve by solving for particle equations of motion from equations (4.28) and (4.29);

7 Evaluate moment quantities: $n_\alpha^{HO,k+1,y}$, $\overline{nu}_\alpha^{HO,k+1/2,y}$, $\tilde{S}_\alpha^{HO,k+1/2,y}$;

8 Evaluate $\gamma_{nu_\alpha}^{HO,k+1,y}$ from equation (4.38);

9 With new $\left(n_\alpha^{LO,k+1}, \overline{nu}_\alpha^{LO,k+1/2}, E^{k+1}\right)$, and $\tilde{S}_\alpha^{HO,k+1,y}$ and $\gamma_\alpha^{HO,k+1,y}$, calculate new outer residual, $||\mathbf{G}||_y^{out}$, from equations (4.39) to (4.43);

10 Check for outer residual convergence, $||\mathbf{G}||_y^{out} \leq \text{tol}_{out}||\mathbf{G}||_0^{out}$. Here, tol_{out} is some outer convergence tolerance. If converged, $\left(n_\alpha^{k+1}, nu_\alpha^{k+1}\right)^{LO} = \left(n_\alpha^{k+1}, nu_\alpha^{k+1}\right)^{HO}$, move to next time step.

11 **end**

It is stressed that the moment equations are simply used to *accelerate* the convergence of the HO solution (the true kinetic solution) and are not evolved from time step to time step. Hence upon outer nonlinear convergence, the new time LO moments are anchored to the HO solution moments, i.e. $\left(n_\alpha^{k+1}, nu_\alpha^{k+1}\right)^{LO} = \left(n_\alpha^{k+1}, nu_\alpha^{k+1}\right)^{HO}$.

4.5 Benchmark and Test Case Results

This section presents single species benchmark results for classic Landau damping and two stream instability cases with algorithm performance. The primary purpose of the single species case is to demonstrate the accuracy of the advanced IMM method presented in this study by comparing to linear theory. These problems are typically solved very well with explicit methods due to lack of stiffness. In order to demonstrate algorithm performance on a true multiscale problem, an ion acoustic shockwave simulation will be performed. This multiscale problem is exactly the type of problem our implicit moment method is intended for.

For all of our test cases, the particles are initialized based on the following initial condition, unless otherwise specified:

$$f_0\left(x,v,u,T\right)=\frac{n_0}{\sqrt{2\pi T_0/m}}\exp\left[-\frac{m\left(v-u_0\right)^2}{2T_0}\right]\ . \tag{4.45}$$

$$n_0=n_0\left(t=0,x\right)=1+\alpha_n\cos\left(kx\right)$$

Here x, v, n_0, u_0, T_0, α_n, k and m are the position and velocity of particle, initial number density, initial fluid velocity, initial temperature, perturbation amplitude for number density, wave vector of perturbation, and the species mass, respectively. The code is written in MATLAB, with the HO particle solver written in C++ and coupled to MATLAB via built-in MEX functions. The LO solver utilized the MATLAB built-in GMRES solver (for JFNK) and ILU (for semi-implicit Picard iteration and preconditioning). In these benchmark problems, the LO solver cost is negligible ($\approx 1\%$ of total CPU time) and the majority of CPU time is spent on the particle pushing components of the algorithm. The hardware in which calculations were performed is a 2GHz Intel Core i7 with 8 GB RAM 1333MHz DDR3 memory on a serial implementation.

4.5.1 Single species: Landau damping

For the first single species test case, the classic Landau damping problem [60] is chosen. For Landau damping, the rate at which the field energy is converted to the wave energy is found from the linear dispersion relation,

$$1 + \frac{1}{k^2}\left[1 + \frac{\omega}{\sqrt{2}k} Z\left(\frac{\omega}{\sqrt{2}k}\right)\right] = 0 \,. \tag{4.46}$$

Here k, ω, and Z are the wave vector of the perturbation, wave frequency and dispersion function of Fried and Conte, respectively. Solving for ω, a complex solution is obtained in terms of the oscillatory (real) $\tilde{\omega}$ and decaying (imaginary) γ components of the frequency. The problem parameters used for this single species test case are [65], $L_x = 4\pi$, the periodic system length, $N_x = 32$, the number of cells, $t_{max} = 15\tau_e$, the maximum duration of simulation in terms of the electron plasma wave time-scale τ_e, $\Delta t = 0.5\tau_e,\ 1.0\tau_e,\ 2.0\tau_e,\ 4.0\tau_e$, the time step size in terms of τ_e, $N_p = 1250$, the mean number of particles per cell, $k = 2\pi/L_x$, the wave vector of the perturbation, $\text{tol}_{out} = 10^{-6}$ and $\text{tol}_{in} = 10^{-6}$, the outer and inner iteration convergence tolerance, $n_0 = 1.0$, $\alpha_n = 0.01$, $u_0 = 0$, and $T_0 = 1.0$. For these given parameters, γ = -0.155 [65]. The results for the Landau damping case are shown in Fig. 5.1. As seen, good agreement between the numerical simulation and linear theory is achieved for time step sizes which are larger than the electron plasma wave time-scale but that still resolve the damping rate, γ (i.e. $\gamma\Delta t < 1/2$). As expected, for time step sizes larger than the oscillation frequency $\tilde{\omega}$, the solution is unable to capture the oscillation accurately. To demonstrate second-order convergence of the overall method, a simple time convergence study was performed by calculating the L_2 error of the electric field between successive Δt refinements. The L_2 of error in the electric field is defined as,

$$L_2^E = \sqrt{\sum_i^{N_x} \left| E_{i+1/2}^{\Delta t} - E_{i+1/2}^{ref} \right|^2 \Delta x} \,.$$

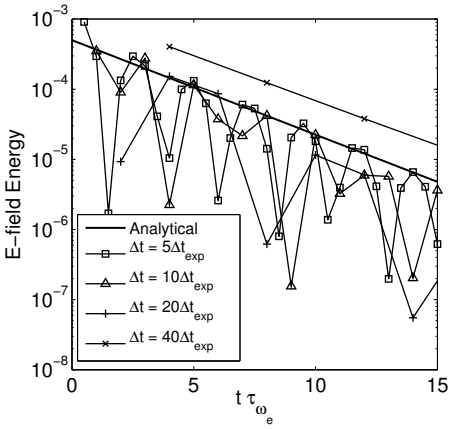


Figure 4.1: Decay rate comparison for Landau damping

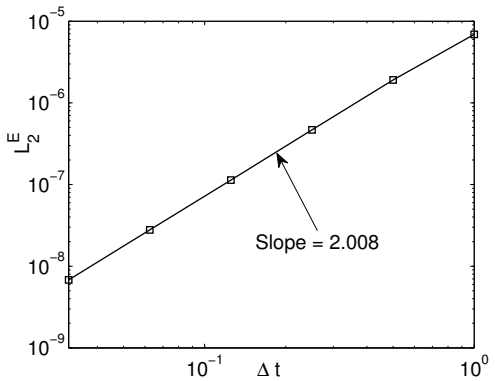


Figure 4.2: Time convergence study result.

Here, i is the cell index, $E_{i+1/2}^{\Delta t}$ is the electric field calculated for a specific Δt at cell face $i+1/2$, $E_{i+1/2}^{ref}$ is the reference electric field value at cell face $i+1/2$. E^{ref} was calculated with a very fine Δt size. Fig. 4.2 shows that the slope of the L_2^E with respect to Δt size is approximately equal to 2 in a log-log plot, demonstrating second-order temporal convergence.

We choose to define the explicit time step size as, $\Delta t_{exp} = 0.1\tau_e$ as is typically used in explicit simulation. The algorithm performance for the test case with various Δt is given in Table 4.1. The first row gives the average number of outer Picard iterations per time

	$\Delta t = 5\Delta t_{exp}$	$\Delta t = 10\Delta t_{exp}$	$\Delta t = 20\Delta t_{exp}$	$\Delta t = 40\Delta t_{exp}$
$\frac{Picard_{outer}}{\Delta t}_{avg}$	4.469	5.063	6	9
$\frac{Newton_{inner}}{Picard_{outer}}_{avg}$	1.532	1.500	1.559	1.596
$\frac{Subcycle}{\Delta t \ particle}_{avg}$	2.695	4.706	8.698	16.817
CPU Time [sec]	98.054	92.762	98.878	141.398

Table 4.1: Algorithm Performance for Landau Damping

step that was required for the outer iteration. As Δt grows, the required number of outer iterations grows as expected from a Picard iteration scheme. The second row provides the average inner Newton iterations per time step to converge the inner LO moment system. The inner LO solve was performed using a JFNK iteration with a semi-implicit preconditioning as discussed in appendix B. The inner Newton iteration count is flat with respect to Δt due to the rapid quadratic convergence property of the method. The third row provides the average number of sub-cycling steps required per particle per global time step. This count grows almost linearly as a function of Δt size. This is also expected since, as Δt grows, the particles are able to traverse *more* cells. The fourth row is the *total* CPU time required to complete the simulation. From simply observing the average outer Picard iteration trend in row 1, the algorithm may seem to scale very well. However it is important to consider the increase in the particle pushing cost. As the Δt size increases, the outer Picard iteration *count* may not be increasing significantly, but the CPU cost *per* outer Picard iteration increases since the particle pushing cost increases. This is clearly shown in the slowdown in the CPU execution time of the simulation. For serial processing, this result may appear discouraging. However we wish to take advantage of the emerging computer architectures in which we may be able to use GPGPU's to push the particles highly efficiently and reduce the communication cost in massively parallel computing [56]. The study in [54] has also shown that even without taking advantage of massively parallel computing architectures, the implicit method with kinetically enslaved JFNK with an energy and charge conserving particle pusher scheme can achieve CPU speedups of over an order of magnitude compared to an explicit scheme for a

two species ion acoustic shockwave simulation where a large separation in time-scale exists.

4.5.2 Single species: Two stream instability

For the second benchmark case, we choose to solve the single species two stream instability problem [61]. The dispersion relation for the two stream instability case is given below.

$$1 - \frac{1}{(\omega + v_b k)^2} - \frac{1}{(\omega - v_b k)^2} = 0 \tag{4.47}$$

Here v_b is the beam velocity and ω is again the wave frequency. The simulation is initialized as follows.

$$f_0(x, v, t = 0) = (1 + \alpha_n \cos kx)\, \delta(v \pm v_b) \tag{4.48}$$

The simulation parameters are $L_x = 1$, $N_x = 32$, $t_{max} = 35\tau_e$, $\Delta t = 0.5\tau_e = 5\Delta t_{exp}$, $1.0\tau_e = 10\Delta t_{exp}$, $2\tau_e = 20\Delta t_{exp}$, $N_p = 1560$, $k = 2\pi/L_x$, $\alpha_n = 0.001$, $v_b = 0.1$, and $\text{tol}_{out} = \text{tol}_{in} = 10^{-6}$. From linear theory, the growth rate, γ, is 0.353. The comparison plot of analytical and numerical solutions for the electric field energy vs. time for various Δt is shown in Fig. 5.2. Again, good agreement between the theory and the numerical solution is observed in the linear growth regime. Similarly to the Landau damping case, algorithm performance is shown for different Δt in Table 4.2. Similar performance trends to the Landau damping case are observed with an increase in the average outer Picard iteration for the given Δt. For $\Delta t = 2.0\tau_e = 20\Delta t_{exp}$, the required outer Picard iteration for the two-stream case is more than double the Landau damping case. This is expected, as the growth rate, γ, is 0.353 and the Δt is stepping over the dynamical growth time-scale.

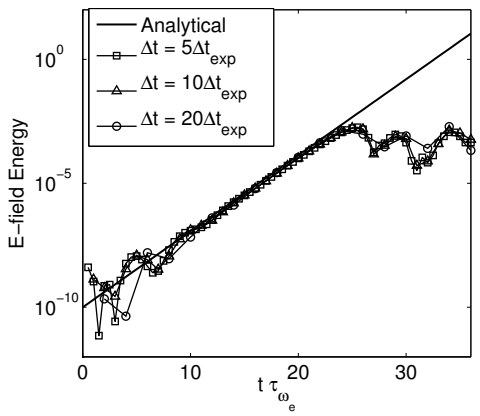


Figure 4.3: Electric field energy growth rate for two stream instability.

	$\Delta t = 5\Delta t_{exp}$	$\Delta t = 10\Delta t_{exp}$	$\Delta t = 20\Delta t_{exp}$
$\frac{Picard_{outer}}{\Delta t}_{avg}$	4.181	5.777	14.722
$\frac{Newton_{inner}}{Picard_{outer}}_{avg}$	1.592	1.657	1.654
$\frac{Subcycle}{\Delta t\ particle}_{avg}$	5.744	10.730	19.065
CPU Time [sec]	90.04	107.55	233.866

Table 4.2: Algorithm Performance for two Stream Instability.

4.5.3 Two species: Ion acoustic shockwave

Next, we consider a two species ion acoustic shockwave (IASW) problem. The evolution of the problem occurs in the ion time-scale while the solution structure is impacted by the electron distribution function. The shock thickness occurs on the Debye length scale, while the acoustic wavelength is much larger. In a classic explicit PIC algorithm, the CFL condition is defined typically as $\Delta t_{exp} = 0.1\tau_e$. For the IASW problem, we adopt this CFL condition.

The problem is initialized as follows.

$$f_{0,\alpha}\left(x, v_i, t = 0\right) = \frac{n_{0,\alpha}}{\sqrt{2\pi T_{0,\alpha}/m_\alpha}} \exp\left[-\frac{m\left(v_\alpha - u_{0,\alpha}\right)^2}{2T_{0,\alpha}}\right]$$

$$n_{0,i} = n_{0,i}\left(x, t = 0\right) = 1 + \alpha_n \sin\left(kx\right)$$

$$n_e = n_e\left(x, t = 0\right) = 1 + \alpha_n \sin\left(kx\right)$$

$$u_i = u_i\left(x, t = 0\right) = \alpha_u \sin\left(kx\right) - v_{shift}$$

$$u_e = u_e\left(x, t = 0\right) = \alpha_u \sin\left(kx\right) - v_{shift}$$

The following problem parameters are used [54], $L_x = 144$, $N_x = 144$, $\Delta x = \lambda_D = L_x/N_x$, $k = 2\pi/L_x$, $m_i = 2000$, $m_e = 1$, $T_e = 1.0$, $T_i = 2 \times 10^{-4}$, $v_{shift} = \frac{\omega_{IAW}}{k} = 2.234 \times 10^{-2}$, $N_p = 5000$, $\alpha_n = 0.4$, $\alpha_u = \alpha_n v_{shift} = 9.36 \times 10^{-3}$, $t_{max} = 3000$, $\tau_e = 1$, $\tau_i = 44.7$, $\Delta t_{exp} = 0.1\tau_e$, $\Delta t = 1\Delta t_{exp},\ 50\Delta t_{exp},\ 100\Delta t_{exp}$, $\text{tol}_{out} = \text{tol}_{in} = 10^{-6}$. Here, λ_D is the Debye length, τ_e and τ_i are the electron and ion inverse plasma frequency, and Δt_{exp} is the explicit CFL time-step size. In order to evolve the problem in the frame of reference of the ion acoustic wave, the distribution is shifted by the ion acoustic wave speed:

$$v_{IAW} = \frac{\omega_{IAW}}{k} = \left[\frac{1}{m_i}\frac{T_e}{1 + k^2\lambda_{De}^2} + \frac{T_i}{m_i}\right]^{1/2}, \tag{4.49}$$

The dynamical time-scale of interest in this problem is the ion plasma time-scale, $\Delta t_{dyn} = \tau_i = 44.7$. Fig. 4.4 shows the number density for ions and electrons as well as the electric field at t_{max} for three time step sizes. The standard ion acoustic shockwave solution can be seen with the formation of the soliton packets near the shock front where particle trapping occurs. The results demonstrate that the implicit scheme with large Δt can accurately predict the evolution of the solution without encountering numerical instabilities. Algorithm performance is given for the IASW case in Table 4.3. For the two species case, particle statistics on subcycling is given for both species and denoted by a subscript e and i. As expected for the $\Delta t = 10\tau_e$ case, the required sub-cycling for electrons is considerably larger than the ions.

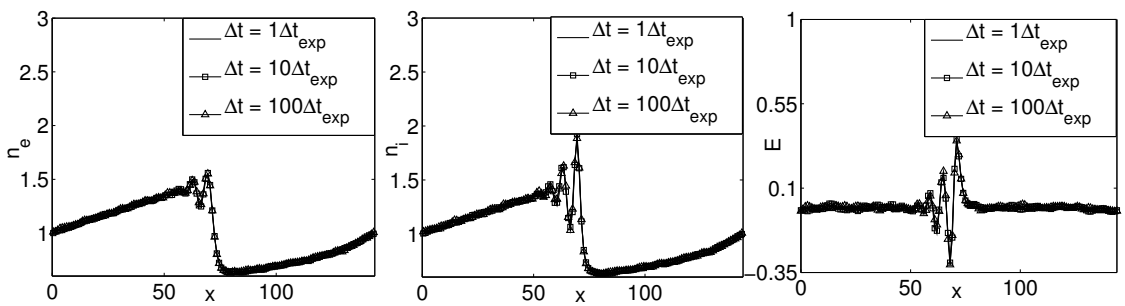


Figure 4.4: Number density plot for both electron (left) and ion (center) is shown with the resultant electric field (right) due to the charge separation.

	$\Delta t = 1\Delta t_{exp}$	$\Delta t = 50\Delta t_{exp}$	$\Delta t = 100\Delta t_{exp}$
$\frac{Picard_{outer}}{\Delta t}_{avg}$	3.63	15.40	18.96
$\frac{Newton_{inner}}{Picard_{outer}}_{avg}$	1.28	1.58	1.60
$\frac{GMRES}{Newton_{inner}}_{avg}$	2.22	4.85	5.59
$\frac{Subcycle}{\Delta t \ particle}_{avg,e}$	1.23	37.16	74.94
$\frac{Subcycle}{\Delta t \ particle}_{avg,i}$	1.00	1.26	2.104
CPU Time [sec]	66597.2	48657.8	62767.3

Table 4.3: Algorithm Performance for ion acoustic shockwave.

4.5.4 Picard Convergence Properties vs. Δt

Convergence of the algorithm is investigated. Normalized residual convergence rate histories for the outer Picard iteration are given in Fig 4.5. For the Vlasov-Ampére system, the convergence rate is controlled by the electron and ion momentum equation due to the coupling through the stress-tensor. Both the electron (4.40) and ion (4.42) momentum conservation equation residuals are included in the computation of residual norm. The Picard iteration is linearly convergent, and the residual convergence exhibits a linear convergence rate as expected. As Δt size grows, the number of Picard iterations for a given convergence tolerance also grows as we step over stiff electron time-scales.

It is worth-while to note that, out of the 300 time steps required for the $\Delta t = 10\tau_e =$

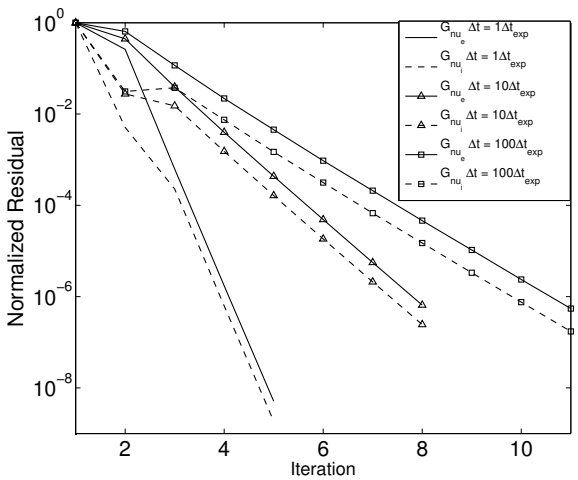


Figure 4.5: Normalized residual convergence rate of ion and electron momentum equation for the different Δt cases for the first time-step.

$100\Delta t_{exp}$ case discussed in section 4.5.3, 9 time steps failed to converge to the specified *outer* convergence tolerance (10^{-6}). Although the residuals did not converge below 10^{-6}, they stagnated below 10^{-5}. A separate simulation with a fixed $\text{tol}_{out} = 10^{-5}$ with $\Delta t = 100\Delta t_{exp}$ was performed and no stagnation occurred. The required average outer Picard iteration for the $\text{tol}_{out} = 10^{-5}$ case was 14.98. Furthermore, visually, the solution structures did not differ compared to the case with fixed $\text{tol}_{out} = 10^{-6}$ with $\Delta t = 100\Delta t_{exp}$. The HOLO iteration was forced to end for a time step after 40 outer iterations were executed.

4.6 Importance of Consistency Term and density normalized stress-tensor

This section demonstrates, using the IASW problem, the importance of the consistency terms for long-term accuracy and to highlight the role of the density-normalized stress-tensor in the algorithmic properties of the scheme. Recall that the standard IMM does not 1) rigorously address discrete consistency (which automatically violates energy conservation), 2) does not

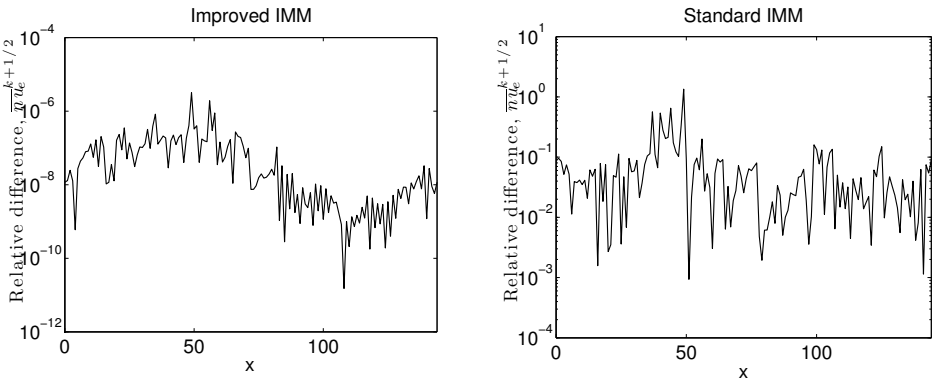


Figure 4.6: Relative difference of $\overline{nu}^{k+1/2}$ upon convergence of the improved IMM method (left) and the standard IMM (right).

iterate between the HO-LO system to converge the particles and fields to a tight nonlinear tolerance.

Consider the IASW case discussed in section 4.5.3 with $\Delta t = 5\Delta t_{exp}$. In Fig. 4.6, the relative difference of the HO and LO $\overline{nu}_e^{k+1/2}$ is shown for the improved IMM (upon nonlinear convergence of the HO-LO system), and the standard IMM (which does not iterate). It is seen that the relative difference between the two systems is within the nonlinear tolerance (10^{-6}) when γ_{nu}^{HO} is used (improved IMM). Without γ_{nu}^{HO} (standard IMM), the difference ranges from 1$\sim$10%. It is clearly demonstrated that without the consistency term, the HO and LO moments can converge to inconsistent values.

Now, we consider the energy conservation property between the improved and standard IMM. To highlight the improvements, the improved IMM simulation will use a Δt size of $100\Delta t_{exp}$ while the standard IMM will use a Δt size of $5\Delta t_{exp}$. Fig. 4.7 shows the relative total energy error with respect to time between the improved and standard IMM while Fig. 4.8 shows the resulting electric field at various times in the simulation. As can be seen, the energy is not conserved within the nonlinear convergence tolerance set in the study ($\text{tol}_{out} = \text{tol}_{in} = 10^{-6}$) when the consistency term, γ_{nu}^{HO}, is *not* used. This is expected as the electric field is evaluated based on $\overline{nu}^{LO,k+1/2}$, and, with $\overline{nu}^{LO,k+1/2} \neq \overline{nu}^{HO,k+1/2}$, i.e., the field is

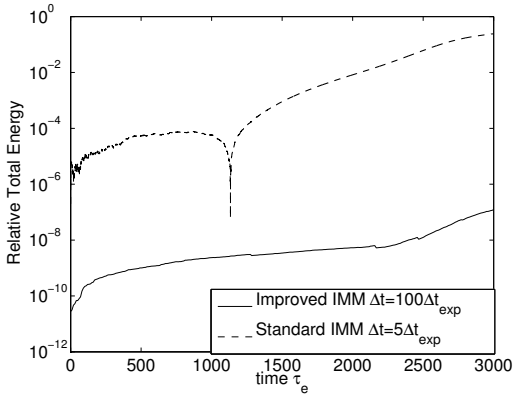


Figure 4.7: Relative total energy of the system as a function of time.

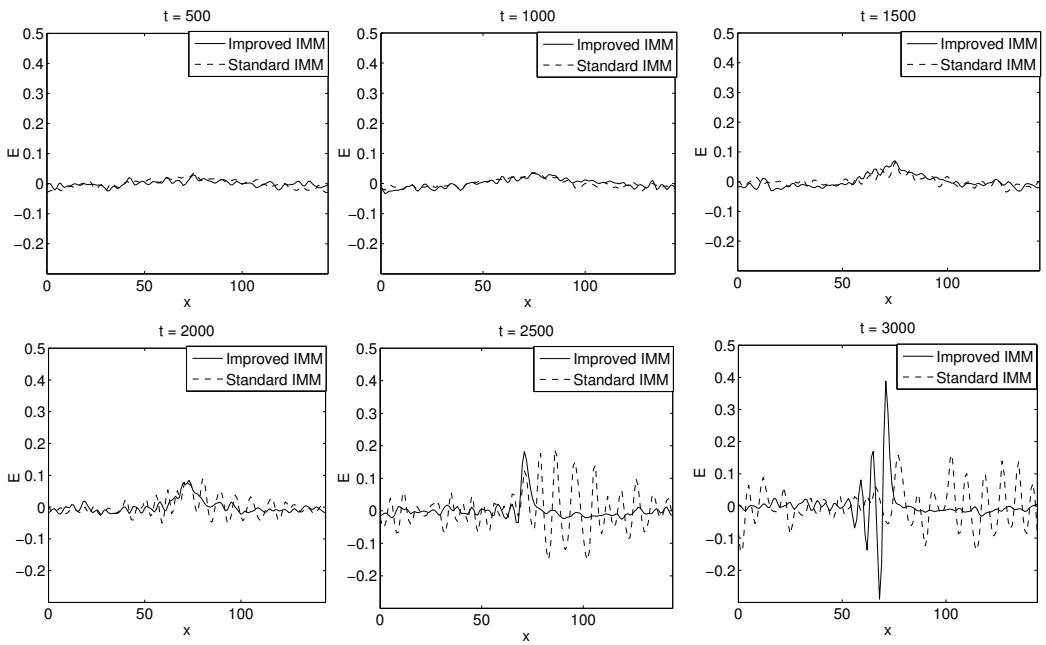


Figure 4.8: Electric field structure at various times.

not determined self-consistently with the solution to the HO kinetic system. Also seen is that the IMM without the consistency term and iteration can represent a relatively accurate evolution of the field for some intermediate time. However, as we evolve the problem further, the solution becomes non-physical. Although no iteration is required in the standard IMM

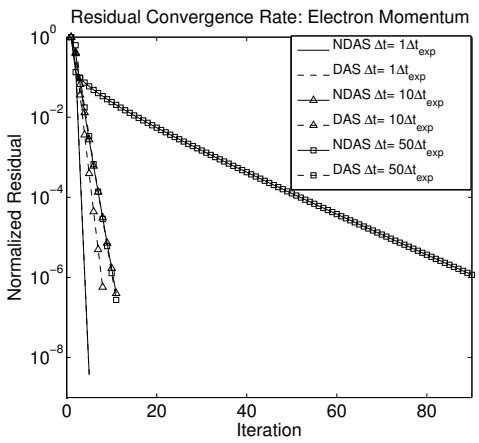


Figure 4.9: Demonstration of exposure of stiff wave physics and consequently, the reduction in nonlinear iteration with density-normalized stress-tensor (DAS) and comparison with non-density-normalized stress-tensor (NDAS).

and thus a faster execution per time-step is achievable, the solution for certain long time integration problems such as the IASW case is not dependable.

To illustrate the algorithmic impact of density-normalized stress-tensor, the normalized residual convergence rate for the electron momentum equation is compared for the IASW case with and without the density-normalized stress-tensor with various Δt within a single time step. As discussed in section 4.2.4 (and in Appendix A), the density normalization of stress-tensor effectively *exposes* the stiff hyperbolic isothermal wave, thus accelerating convergence of the overall method. Accordingly, we expect fewer nonlinear iterations for the HO-LO solver when using density-normalized stress-tensor than with the standard stress-tensor closure. Refer to Fig. 4.9. As can be seen, the required number of outer iterations is reduced by nearly an order of magnitude for $\Delta t = 5\tau_e = 50\Delta t_{exp}$ when using the density-normalized stress-tensor.

4.7 Conclusions

In this chapter, we have demonstrated the feasibility of a fully implicit, nonlinear kinetic simulation capability based on a HOLO coupled formulation. The following key features for the HOLO moment based accelerator were demonstrated in this chapter:

- Nonlinear convergence of the HO kinetic system and the LO moment system to discretely consistent solutions through the use of consistency term, γ_{nu}^{HO}.
- Effectiveness of a density normalized stress-tensor in accelerating the nonlinear convergence of the coupled HOLO system by exposing the stiff hyperbolic wave in the LO system.
- Exact energy conservation of the scheme based on *implicit* second order Crank-Nicolson time discretization between the HO kinetic particle system and the LO field-moment system.

These are clear improvements on the original IMM approach. Using the charge and energy conserving particle push developed by Chen et al. [54] has been key. We have also borrowed the idea of a consistency term and density normalization of the second moment of distribution function (stress-tensor) from the neutron transport community [50, 51, 52] in order to enforce energy conservation and acceleration of the original IMM approach. Through the consistency term, γ_{nu}^{HO}, consistent HOLO solutions were achieved upon nonlinear convergence of the two systems, allowing exact energy conservation. Through the density-normalization of the stress-tensor, stiff hyperbolic waves are exposed and addressed in the LO moment system, significantly improving the nonlinear convergence of the HOLO approach versus the original IMM. In the next chapter, we extend the HOLO algorithm developed for the PIC approach to an Eulerian, grid based Vlasov-Ampère system. We will also develop a novel charge, momentum, and energy conserving nonlinear discretization as well. These properties will be critical for long-time integration of an ICF problem.

Chapter 5

Conservative Discretization for a Collisionless Plasma

In this chapter, we extend the work developed in the previous chapter to an Eulerian grid-based system where the Vlasov equation is solved on a stationary 1D1V grid instead of being represented by particles. We also develop a simultaneous charge, momentum, and energy conserving discretization for the coupled Vlasov-Ampère system. The new conservative discretization scheme is based on a set of additional *discrete* nonlinear constraints which enforces the conservation properties in the discrete system. Since the new conservative discretization is nonlinear, a nonlinear iteration is required to preserve the conservation properties. We show that the nonlinearity in the discretization is automatically dealt with through the HOLO iteration. We test the new algorithm to simulate a similar ion-acoustic shock-wave problem which was investigated in the previous chapter, and present both the algorithmic performance and the discrete conservation properties of the new solver.

5.1 Introduction

The dynamic evolution of coupled electromagnetic fields and collisionless plasmas is described by the Vlasov-Maxwell system. The Maxwell equations evolve the self-consistent fields based on moments of the ion-electron distribution functions (charge and current densities). The plasma distribution function evolution is governed by the Vlasov equation, which is coupled back to the Maxwell system through electromagnetic fields. In this study, we will focus on a deterministic solution approach for this nonlinearly coupled system.

Historically, explicit and operator-split-based methods have been used to model collisionless kinetic plasmas [84, 85, 86, 87, 88]. The explicit method is massively parallelizable, simple to implement and is computationally inexpensive per time step. However, the method is hampered by the well-known CFL stability limit for a given cell size of the problem. For a multi length-scale and time-scale problem, this limitation makes the explicit method inefficient. On the other hand, operator-split-based semi-implicit methods are not limited by the CFL limitations and allow larger time-steps [87, 86]. However, for long time-scale integrations, low-order splitting errors can accumulate and become significant. Additionally, operator-split-based methods lack discrete conservation properties such as momentum and energy and can accumulate large conservation errors for long time integrations.

In contrast, a fully implicit, unsplit approach for the Vlasov-Ampère/Poisson system aims to converge the nonlinear residual to a tight tolerance within a time-step. By converging the nonlinear system to a tight tolerance, much larger time-steps can be used without accumulating large errors from time-step to time-step. In this study, we put forth a modern, fully implicit method which accelerates the convergence of the nonlinearly coupled Vlasov-Ampère system. The algorithm is based on a new, discretely consistent implicit moment method (IMM) [75] for the Eulerian approach. The new IMM scheme is based on a high-order (HO) low-order (LO) nonlinear convergence acceleration method which has seen success in neutron transport [51], thermal radiation transport [53], neutral gas kinetics [118], and

collisionless plasma physics (using a PIC approach [75]). In the proposed algorithm, a LO moment-field system is used to accelerate the convergence of the HO Vlasov-Ampère system. The LO system provides the HO system with the accelerated evaluation of the electric field for the Vlasov operator. In turn, the HO system provides the LO system with the closure at the total stress tensor level.

Sophisticated approaches in both implicit and explicit schemes have been developed to enforce exact conservation properties. In the context of particle-in-cell (PIC) approaches, a fully implicit algorithm for the Vlasov-Ampère system has been demonstrated to conserve charge and energy exactly in the discrete [54]. A recent study [89] proposes an implicit energy conserving discretization for an Eulerian-based Vlasov-Ampère system. Additionally, a novel *explicit* method has been developed which conserves both momentum and energy in the limit of $\Delta t \to 0$ using a variational formulation of the Vlasov-Ampère system and a truncated Fourier basis [133], making the method closely resembling a spectral scheme. However, to our knowledge, a scheme for the Vlasov-Ampère system which conserves charge, momentum, and energy for finite Δt does not exist. In this study, we develop a novel nonlinear discretization scheme which will achieve a simultaneous conservation of charge, momentum, and energy by enforcing two additional set of discrete nonlinear constraints.

The remainder of the chapter is organized as follows. Section 2 introduces the governing set of equations for a one spatial dimension and one velocity space dimension (1D1V) Vlasov-Ampère system. The derivation of the moment system is presented and a general flavor of the HOLO algorithm is provided. In section 3, we discuss the charge, momentum, and energy conserving discretization of the coupled Vlasov-Ampère system. We prove discrete charge, momentum, and energy conservation theorems, and introduce the required set of discrete nonlinear constraints. We also provide the HOLO moment-based algorithm to fully implicitly solve the coupled Vlasov-Ampère system.Section 4 discusses the discretization method used for both the HO kinetic and LO moment-field systems in both time and space. Finally, in section 5, we demonstrate the discrete conservation properties and the performance of the

HOLO moment-based acceleration algorithm via numerical experiment. Concluding remarks are provided in section 6.

5.2 HOLO Equations for the Vlasov-Ampère System

The moment acceleration technique we propose in this study is a direct extension of the method developed for the particle-in-cell (PIC) approach in reference [75]. The method is based on a coupled, higher dimensional (HO) kinetic system and lower dimensional (LO) moment-field system. The solution of the LO system takes the HO stress tensor to solve for the implicit electric field based on the moment equations. The HO system employs the new electric field from the LO system and returns the self-consistent stress-tensor closure to the LO system.

For a proof of principle study, a 1D configuration space and 1D velocity space (1D1V), electrostatic, two-species Vlasov-Ampère formulation is considered:

$$\frac{\partial f_e}{\partial t} + v\frac{\partial f_e}{\partial x} + \frac{q_e}{m_e}E\frac{\partial f_e}{\partial v} = 0, \tag{5.1}$$

$$\frac{\partial f_i}{\partial t} + v\frac{\partial f_i}{\partial x} + \frac{q_i}{m_i}E\frac{\partial f_i}{\partial v} = 0, \tag{5.2}$$

$$\epsilon_0\frac{\partial E}{\partial t} + \sum_{\alpha}^{N_s} q_\alpha n u_\alpha = 0. \tag{5.3}$$

Equations (5.1), (5.2), and (5.3) are the electron and ion Vlasov equations and the Ampère's equation, respectively. In these equations, m_e, m_i, f_e, f_i, v, q_e, q_i, E, ϵ_0, and nu_α are the electron and ion mass, electron and ion distribution function, electron and ion velocity, electron and ion charge, the electric field, permittivity constant of vacuum, and the number

density flux of species α, respectively. The Vlasov equation is a function of position, velocity, and time. The Ampère's equation is solved for the self-consistent electric field, which is a function of space and time. The coupled set of nonlinear equations are solved fully implicitly. Again for this study, a deterministic, Eulerian approach will be adopted to discretize the Vlasov equation.

5.2.1 Derivation of the coupled moment/Vlasov-Ampère System

In this section, we formulate the HO Vlasov equation, and the LO moment-field equations which are used to accelerate the nonlinear convergence of the Vlasov-Ampére system. The Vlasov equation for species α, (VE_α), is defined according to equations (5.1) and (5.2) as:

$$\text{VE}_\alpha = \frac{\partial f_\alpha}{\partial t} + v\frac{\partial f_\alpha}{\partial x} + \frac{q_\alpha}{m_\alpha}E\frac{\partial f_\alpha}{\partial v} = 0. \tag{5.4}$$

We define the l^{th} moment of the velocity distribution function of species α as follows,

$$\mathcal{M}_\alpha^l = \int_{-\infty}^{+\infty} v^l f_\alpha dv = \left\langle v^l, f_\alpha \right\rangle_v. \tag{5.5}$$

With this definition, the number density, n_α, number density flux, nu_α, and total stress-tensor, S_α are the 0^{th}, 1^{st}, and 2^{nd} moments of the distribution function, respectively, and can be written as:

$$n_\alpha = \left\langle 1, f_\alpha \right\rangle_v, \tag{5.6}$$

$$nu_\alpha = \left\langle v, f_\alpha \right\rangle_v, \tag{5.7}$$

$$S_\alpha = \left\langle v^2, f_\alpha \right\rangle_v. \tag{5.8}$$

The governing equations for the fluid moments (LO problem) are obtained by taking the 0^{th}, and 1^{st} moment of the Vlasov equation to find:

$$\langle 1, \mathrm{VE} \rangle_v = \frac{\partial n_\alpha}{\partial t} + \frac{\partial}{\partial x} n u_\alpha = 0, \tag{5.9}$$

$$\langle v, \mathrm{VE} \rangle_v = \frac{\partial}{\partial t} n u_\alpha + \frac{\partial}{\partial x} S_\alpha - \frac{q_\alpha}{m_\alpha} n_\alpha E = 0. \tag{5.10}$$

Equations (5.9) and (5.10) are the continuity and momentum conservation equations, respectively, for each species. We consider the coupled HO kinetic system and a LO moment-field system for an ion-electron system:

HO (Kinetic) System:

$$\frac{\partial f_e}{\partial t} + v \frac{\partial f_e}{\partial x} + \frac{q_e}{m_e} E \frac{\partial f_e}{\partial v} = 0, \tag{5.11}$$

$$\frac{\partial f_i}{\partial t} + v \frac{\partial f_i}{\partial x} + \frac{q_i}{m_i} E \frac{\partial f_i}{\partial v} = 0, \tag{5.12}$$

LO (Moment-Field) System:

$$\frac{\partial {n_e}^{LO}}{\partial t} + \frac{\partial}{\partial x} n u_e^{LO} = 0, \tag{5.13}$$

$$\frac{\partial}{\partial t} n u_e^{LO} + \frac{\partial}{\partial x} n_e^{LO} \widetilde{S}_e^{HO} - \frac{q_e}{m_e} n_e^{LO} E = \gamma_{n u_e}^{HO}, \tag{5.14}$$

$$\frac{\partial {n_i}^{LO}}{\partial t} + \frac{\partial}{\partial x} n u_i^{LO} = 0, \tag{5.15}$$

$$\frac{\partial}{\partial t} n u_i^{LO} + \frac{\partial}{\partial x} n_i^{LO} \widetilde{S}_i^{HO} - \frac{q_i}{m_i} n_i^{LO} E = \gamma_{nu_i}^{HO}, \tag{5.16}$$

$$\epsilon_0 \frac{\partial E}{\partial t} + \sum_{\alpha}^{N_s} q_\alpha n u_\alpha^{LO} = 0. \tag{5.17}$$

The closure required for the LO fluid moment system is provided by the HO density-normalized total stress-tensor $\widetilde{S}_\alpha^{HO}$,

$$\widetilde{S}_\alpha^{HO} = \frac{\langle v^2, f_\alpha \rangle_v}{\langle 1, f_\alpha \rangle_v}, \tag{5.18}$$

and the *discrete consistency term*, γ_α^{HO} [75]. The purpose of the density normalization is to expose the stiff isothermal wave in the LO system [75]. In doing so, we enhance the convergence rate of the HO-LO iteration within a time step when the time step is large compared to the stiff acoustic time-scales. We introduce the discrete consistency terms and their purpose in the next section.

5.2.2 Discrete Consistency Terms

As discussed in the preceding section, the HO and LO systems are exactly equivalent in the continuum when the exact closures for S_α^{HO} and E are employed. However, an issue arises in the discrete. Upon discretization of the HO and LO system of equations, discretization errors arise in both systems. While we cannot avoid *discretization error*, we also cannot tolerate the discretization error of the two systems (HO and LO) being different. If such situation arises, then, over many time steps, the two systems will drift apart, leading to inaccurate solution and solver breakdown. The purpose of $\gamma_{nu_\alpha}^{HO}$ is to enslave the discretization error of the LO system to the discretization error of the HO system [75]. The continuum expression for $\gamma_{nu_\alpha}^{HO}$ is given as,

$$\gamma_{nu_\alpha}^{HO} = \frac{\partial}{\partial t} n u_\alpha^{HO} + \frac{\partial}{\partial x} n_\alpha^{HO} \widetilde{S}_\alpha^{HO} - \frac{q_\alpha}{m_\alpha} n_\alpha^{HO} E \tag{5.19}$$

The HO moment variables are calculated by numerical integration of the HO solution to f_α. In this study, the moments are calculated as:

$$n_\alpha^{HO} = \langle 1, f_\alpha \rangle_v \approx \sum_j^{N_v} \Delta v_{\alpha_j} f_{\alpha_j}, \tag{5.20}$$

$$nu_\alpha^{HO} = \langle v, f_\alpha \rangle_v \approx \sum_j^{N_v} \Delta v_{\alpha_j} v_{\alpha_j} f_{\alpha_j}, \tag{5.21}$$

$$\widetilde{S}_\alpha^{HO} = \frac{\langle v^2, f_\alpha \rangle_v}{\langle 1, f_\alpha \rangle_v} \approx \frac{\sum_j^{N_v} \Delta v_{\alpha_j} v_{\alpha_j}^2 f_{\alpha_j}}{\sum_j^{N_v} \Delta v_{\alpha_j} f_{\alpha_j}}. \tag{5.22}$$

Here, j is the discrete velocity space grid point, Δv_{α_j} is the j^{th} discrete velocity space size for species α, N_v is the number of velocity space cell, v_{α_j} is the j^{th} discrete velocity space location, and f_{α_j} is the distribution function at the j^{th} discrete velocity space grid point. When $\gamma_{nu_\alpha}^{HO}$ is evaluated in this manner, and then used in (5.14) and (5.16), discrete consistency is enforced upon convergence of the HO-LO iteration. We only require the consistency term, $\gamma_{nu_\alpha}^{HO}$ in the 1^{st} moment equation and not in the 0^{th} moment equation. This is so because we choose a conservative, finite-volume discretization of the Vlasov equation in this study, which will trivially enforce the discrete 0^{th} moment equation.

5.3 Charge, Momentum, and Energy Conserving Discretization

We first consider a charge-and-momentum conserving scheme, and then a charge-and-energy conserving scheme. These will be nonlinearly combined later to produce a charge, momentum, and energy conserving scheme. In what follows, we consider a periodic system in

physical space. We begin by fully discretizing the Vlasov-Ampère system on a staggered mesh,

$$\mathrm{VE}_{\alpha_{i,j}}^{k+1} = \frac{f_{\alpha_{i,j}}^{k+1} - f_{\alpha_{i,j}}^{k}}{\Delta t} + v_{\alpha_j} \frac{\widehat{f}_{\alpha_{i+1/2,j}}^{k+1/2} - \widehat{f}_{\alpha_{i-1/2,j}}^{k+1/s}}{\Delta x_i} + \frac{q_\alpha}{m_\alpha} E_i^{k+1/2} \frac{\widetilde{f}_{\alpha_{i,j+1/2}}^{k+1/2} - \widetilde{f}_{\alpha_{i,j-1/2}}^{k+1/2}}{\Delta v_{\alpha_j}} = 0, \tag{5.23}$$

$$\epsilon_0 \frac{E_{i+1/2}^{k+1} - E_{i+1/2}^{k}}{\Delta t} + \sum_{\alpha}^{N_s} q_\alpha n u_{\alpha_{i+1/2}}^{k+1/2} = 0, \tag{5.24}$$

where we have used a Crank-Nicolson discretization in time and a finite-volume discretization in space and velocity. Here i is the spatial cell index, j is the velocity space cell index, k is the time index, Δt is the time-step-size, Δx_i is the cell size of the i^{th} spatial cell, Δv_{α_j} is the velocity space cell size of the j^{th} velocity space cell for the α species, $E_{i+1/2}^{k+1}$ is the cell-face electric field, $E_i^{k+1/2}$ is the time-centered cell-center electric field,

$$E_i^{k+1/2} = \frac{E_{i+1/2}^{k+1/2} + E_{i-1/2}^{k+1/2}}{2} = \frac{\left(E_{i+1/2}^{k+1} + E_{i+1/2}^{k}\right) + \left(E_{i-1/2}^{k+1} + E_{i-1/2}^{k}\right)}{4}, \tag{5.25}$$

$\widehat{f}_{\alpha_{i+1/2,j}}^{k+1/2}$ is the time-centered cell-face configuration space numerical flux for species α,

$$\widehat{f}_{\alpha_{i+1/2,j}}^{k+1/2} = \frac{1}{2}\left(\widehat{f}_{\alpha_{i+1/2,j}}^{k+1} + \widehat{f}_{\alpha_{i+1/2,j}}^{k}\right), \tag{5.26}$$

and $\widetilde{f}_{\alpha_{i,j+1/2}}^{k+1/2}$ is the time-centered cell-face velocity space numerical flux for species α,

$$\widetilde{f}_{\alpha_{i,j+1/2}}^{k+1/2} = \frac{1}{2}\left(\widetilde{f}_{\alpha_{i,j+1/2}}^{k+1} + \widetilde{f}_{\alpha_{i,j+1/2}}^{k}\right). \tag{5.27}$$

At this point, we do not wish to specify the definition of $nu_{\alpha_{i+1/2}}^{k+1/2}$ in terms of $f_{\alpha_{i,j}}^{k+1}$ yet.

5.3.1 Charge-Conserving Discretization

Discrete charge conservation is enforced by satisfying the discrete equivalence between the Poisson's equation,

$$\epsilon_0 \frac{E^{k+1}_{i+1/2} - E^{k+1}_{i-1/2}}{\Delta x_i} - \sum_{\alpha}^{N_s} q_\alpha n^{k+1}_{\alpha_i} = 0, \tag{5.28}$$

and Ampère's equation,

$$\epsilon_0 \frac{E^{k+1}_{i+1/2} - E^{k}_{i+1/2}}{\Delta t} + \sum_{\alpha}^{N_s} q_\alpha n u^{k+1/2}_{\alpha_{i+1/2}} = 0. \tag{5.29}$$

The conditions for discrete equivalence can be found by discretely differentiating equation (5.28) in time,

$$\epsilon_0 \frac{\left(E^{k+1}_{i+1/2} - E^{k}_{i+1/2}\right) - \left(E^{k+1}_{i-1/2} - E^{k}_{i-1/2}\right)}{\Delta t \Delta x_i} - \sum_{\alpha}^{N_s} q_\alpha \frac{n^{k+1}_{\alpha_i} - n^{k}_{\alpha_i}}{\Delta t} = 0, \tag{5.30}$$

discretely differentiating equation (5.29) in space,

$$\epsilon_0 \frac{\left(E^{k+1}_{i+1/2} - E^{k}_{i+1/2}\right) - \left(E^{k+1}_{i-1/2} - E^{k}_{i-1/2}\right)}{\Delta x_i \Delta t} + \sum_{\alpha}^{N_s} q_\alpha \frac{n u^{k+1/2}_{\alpha_{i+1/2}} - n u^{k+1/2}_{\alpha_{i-1/2}}}{\Delta x_i} = 0, \tag{5.31}$$

and using the discrete 0^{th} moment of the Vlasov equation,

$$\sum_{j}^{N_v} \Delta v_j \left\{ \frac{f^{k+1}_{\alpha_{i,j}} - f^{k}_{\alpha_{i,j}}}{\Delta t} + v_{\alpha_j} \frac{\widehat{f}^{k+1/2}_{\alpha_{i+1/2,j}} - \widehat{f}^{k+1/2}_{\alpha_{i-1/2,j}}}{\Delta x_i} + \frac{q_\alpha}{m_\alpha} E^{k+1/2}_i \frac{\widetilde{f}^{k+1/2}_{\alpha_{i,j+1/2}} - \widetilde{f}^{k+1/2}_{\alpha_{i,j-1/2}}}{\Delta v_{\alpha_j}} \right\} =$$

$$\frac{n^{k+1}_{\alpha_i} - n^{k}_{\alpha_i}}{\Delta t} + \frac{n u^{k+1/2}_{\alpha_{i+1/2}} - n u^{k+1/2}_{\alpha_{i-1/2}}}{\Delta x_i} = 0 \tag{5.32}$$

From equations (5.30), (5.31), and (5.32), we see that discrete equivalence between the Poisson's equation and Ampère's equation (and thus charge conservation) is enforced by the

following definitions for the number density,

$$n_{\alpha_i}^{k+1} = \sum_{j}^{N_v} \Delta v_{\alpha_j} f_{\alpha_{i,j}}^{k+1}, \tag{5.33}$$

and number density flux,

$$nu_{\alpha_{i+1/2}}^{k+1/2} = \sum_{j}^{N_v} \Delta v_{\alpha_j} v_{\alpha_j} \widehat{f}_{\alpha_{i+1/2,j}}^{k+1/2}. \tag{5.34}$$

5.3.2 Momentum-Conserving Discretization

Discrete momentum conservation is enforced by satisfying the discrete momentum balance of all species. In the discrete, the total momentum is defined by the sum of the species momentum,

$$TM^{k+1} = \sum_{\alpha}^{N_s} m_\alpha \sum_{i}^{N} \Delta x_i n u_{\alpha_i}^{k+1}, \tag{5.35}$$

where $nu_{\alpha_i}^{k+1}$ is the cell centered number density flux, defined as,

$$nu_{\alpha_i}^{k+1} = \sum_{j}^{N_v} \Delta v_{\alpha_j} v_{\alpha_j} f_{\alpha_{i,j}}^{k+1}. \tag{5.36}$$

The discrete momentum conservation is enforced when:

$$TM^{k+1} - TM^{k} = \sum_{\alpha}^{N_s} m_\alpha \sum_{i}^{N} \Delta x_i \left(nu_{\alpha_i}^{k+1} - nu_{\alpha_i}^{k} \right) = 0. \tag{5.37}$$

Substituting equation (5.36) into (5.37) and using equation (5.23), we obtain,

$$TM^{k+1} - TM^{k} = \sum_{\alpha}^{N_s} m_\alpha \sum_{i=1}^{N} \Delta x_i \sum_{j}^{N_v} \Delta v_{\alpha_j} v_{\alpha_j} \left(f_{\alpha_{i,j}}^{k+1} - f_{\alpha_{i,j}}^{k} \right) =$$

$$-\Delta t \sum_{\alpha}^{N_s} m_\alpha \sum_{i=1}^{N} \Delta x_i \sum_{j}^{N_v} \Delta v_{\alpha_j} v_{\alpha_j} \left(\underbrace{v_{\alpha_j} \frac{\widehat{f}_{\alpha_{i+1/2,j}}^{k+1/2} - \widehat{f}_{\alpha_{i-1/2,j}}^{k+1/2}}{\Delta x_i}}_{\text{ⓐ}} + \frac{q_\alpha}{m_\alpha} E_i^{k+1/2} \frac{\widetilde{f}_{\alpha_{i,j+1/2}}^{k+1/2} - \widetilde{f}_{\alpha_{i,j-1/2}}^{k+1/2}}{\Delta v_{\alpha_j}} \right) \quad (5.38)$$

With periodic boundary conditions, term ⓐ vanishes exactly when summed over all configuration space cells. The expression in equation (5.38) simplifies to,

$$TM^{k+1} - TM^{k} = -\Delta t \sum_{\alpha}^{N_s} \sum_{i=1}^{N} \Delta x_i \sum_{j}^{N_v} v_{\alpha_j} q_\alpha E_i^{k+1/2} \left(\widetilde{f}_{\alpha_{i,j+1/2}}^{k+1/2} - \widetilde{f}_{\alpha_{i,j-1/2}}^{k+1/2} \right). \quad (5.39)$$

Now, telescoping the velocity domain sum and using the identity,

$$v_{\alpha_j} - v_{\alpha_{j+1}} = -\Delta v_{\alpha_{j+1/2}}, \quad (5.40)$$

we obtain,

$$TM^{k+1} - TM^{k} = \Delta t \sum_{\alpha}^{N_s} q_\alpha \sum_{i=1}^{N} \Delta x_i E_i^{k+1/2} n_{\alpha_i}^{k+1/2}, \quad (5.41)$$

where we have defined the density at time level $k+1/2$, $n_{\alpha_i}^{k+1/2}$, in equation (5.41) as:

$$n_{\alpha_i}^{k+1/2} = \sum_{j}^{N_v} \Delta v_{\alpha_{j+1/2}} \widetilde{f}_{\alpha_{i,j+1/2}}^{k+1/2}. \quad (5.42)$$

Now, we use the discrete Gauss' law (Poisson's equation), at time level $k+1/2$:

$$\epsilon_0 \frac{E_{i+1/2}^{k+1/2} - E_{i-1/2}^{k+1/2}}{\Delta x_i} = \sum_{\alpha}^{N_s} q_\alpha n_{\alpha_i}^{k+1/2}, \quad (5.43)$$

and substitute into equation (5.41), to find:

$$TM^{k+1} - TM^k = -\Delta t \epsilon_0 \sum_{\alpha}^{N_s} \sum_{i=1}^{N} E_i^{k+1/2} \left(E_{i+1/2}^{k+1/2} - E_{i-1/2}^{k+1/2} \right), \tag{5.44}$$

which, with equation (5.25) and for a periodic system, finally gives:

$$TM^{k+1} - TM^k = \Delta t \frac{\epsilon_0}{2} \sum_{i=1}^{N} \left[\left(E_{i+1/2}^{k+1/2} \right)^2 - \left(E_{i-1/2}^{k+1/2} \right)^2 \right] = 0. \tag{5.45}$$

The critical assumption in the analysis is equation (5.43).

5.3.3 Energy-Conserving Discretization

The total energy is defined by the sum of the kinetic energy and field energy. We begin by multiplying equation (5.23) by m_α, Δt, and take the second velocity moment to obtain:

$$\Delta t m_\alpha \sum_{i}^{N} \Delta x_i \sum_{j}^{N_v} \Delta v_{\alpha_j} \frac{v_{\alpha_j}^2}{2} \times$$

$$\left\{ \frac{f_{\alpha_{i,j}}^{k+1} - f_{\alpha_{i,j}}^{k}}{\Delta t} + \underbrace{v_{\alpha_j} \frac{\widehat{f}_{\alpha_{i+1/2,j}}^{k+1/2} - \widehat{f}_{\alpha_{i-1/2,j}}^{k+1/2}}{\Delta x_i}}_{\text{ⓐ}} + \frac{q_\alpha}{m_\alpha} E_i^{k+1/2} \frac{\widetilde{f}_{\alpha_{i,j+1/2}}^{k+1/2} - \widetilde{f}_{\alpha_{i,j-1/2}}^{k+1/2}}{\Delta v_{\alpha_j}} \right\} =$$

$$\sum_{i}^{N} \Delta x_i \left\{ m_\alpha \left(U_{\alpha_i}^{k+1} - U_{\alpha_i}^{k} \right) - \Delta t q_\alpha n u_{\alpha_i}^{k+1/2} E_i^{k+1/2} \right\} = 0, \tag{5.46}$$

where, ⓐ vanishes due to periodic boundary conditions. Here, $U_{\alpha_i}^{k+1}$ is the total energy density of species α at cell i,

$$U_{\alpha_i}^{k+1} = \sum_{j}^{N_v} \Delta v_{\alpha_j} \frac{v_{\alpha_j}^2}{2} f_{\alpha_{i,j}}^{k+1}, \tag{5.47}$$

and $nu_{\alpha_i}^{k+1/2}$ is the number density flux at cell centers, defined as,

$$nu_{\alpha_i}^{k+1/2} = -\sum_{j}^{N_v} \cancel{\Delta v_{\alpha_j}} \frac{v_{\alpha_j}^2}{2} \frac{\widetilde{f}_{\alpha_{i,j+1/2}}^{k+1/2} - \widetilde{f}_{\alpha_{i,j-1/2}}^{k+1/2}}{\cancel{\Delta v_{\alpha_j}}}. \tag{5.48}$$

Telescoping the sum and using the following identities,

$$v_{\alpha_j}^2 - v_{\alpha_{j+1}}^2 = \left(v_{\alpha_j} - v_{\alpha_{j+1}}\right)\left(v_{\alpha_j} + v_{\alpha_{j+1}}\right), \tag{5.49}$$

$$v_{\alpha_j} - v_{\alpha_{j+1}} = -\Delta v_{j+1/2}, \tag{5.50}$$

we obtain:

$$nu_{\alpha_i}^{k+1/2} = \sum_{j}^{N_v} \Delta v_{\alpha_{j+1/2}} v_{\alpha_{j+1/2}} \widetilde{f}_{\alpha_{i,j+1/2}}^{k+1/2}. \tag{5.51}$$

We sum equation (5.46) over all species,

$$\sum_{\alpha}^{N_s} \sum_{i}^{N} \Delta x_i \left\{ m_\alpha \left(U_{\alpha_i}^{k+1} - U_\alpha^k\right) - \Delta t q_\alpha n u_{\alpha_i}^{k+1/2} E_i^{k+1/2} \right\} = 0, \tag{5.52}$$

which we rearrange to obtain:

$$\sum_{\alpha}^{N_s} \sum_{i}^{N} \Delta x_i m_\alpha \left(U_{\alpha_i}^{k+1} - U_{\alpha_i}^k\right) = \sum_{\alpha}^{N_s} \sum_{i}^{N} \Delta x_i \Delta t q_\alpha n u_{\alpha_i}^{k+1/2} E_i^{k+1/2}. \tag{5.53}$$

Since the field is defined on cell faces, we expand $E_i^{k+1/2}$ in terms of cell-face quantities to obtain:

$$\sum_{\alpha}^{N_s} \sum_{i}^{N} \Delta x_i m_\alpha \left(U_{\alpha_i}^{k+1} - U_{\alpha_i}^k\right) = \sum_{\alpha}^{N_s} \sum_{i}^{N} \Delta x_i \Delta t q_\alpha n u_{\alpha_i}^{k+1/2} \frac{E_{i+1/2}^{k+1/2} + E_{i-1/2}^{k+1/2}}{2}. \tag{5.54}$$

Now, we telescope the sum on the RHS to obtain:

$$\sum_{\alpha}^{N_s}\sum_{i}^{N}\Delta x_i m_\alpha\left(U_{\alpha_i}^{k+1}-U_{\alpha_i}^{k}\right)=-\sum_{\alpha}^{N_s}\sum_{i}^{N}\Delta x_{i+1/2}\Delta t q_\alpha n u_{\alpha_{i+1/2}}^{k+1/2}E_{i+1/2}^{k+1/2}. \tag{5.55}$$

Here, we used the following definition:

$$\Delta x_{i+1/2} n u_{\alpha_{i+1/2}}^{k+1/2}=\frac{\Delta x_i n u_{\alpha_i}^{k+1/2}+\Delta x_{i+1} n u_{\alpha_{i+1}}^{k+1/2}}{2}, \tag{5.56}$$

where $\Delta x_{i+1/2}=x_{i+1}-x_i$. Finally, using equation (5.29) and solving for $\Delta t\sum_{\alpha}^{N_s} q_\alpha n u_{\alpha_{i+1/2}}^{k+1/2}$,

$$\Delta t\sum_{\alpha}^{N_s} q_\alpha n u_{\alpha_{i+1/2}}^{k+1/2}=-\epsilon_0\left(E_{i+1/2}^{k+1}-E_{i+1/2}^{k}\right), \tag{5.57}$$

and substituting into equation (5.55), we can show with a few additional algebraic manipulations that,

$$\sum_{\alpha}^{N_s}\sum_{i}^{N}\Delta x_i m_\alpha\left(U_{\alpha_i}^{k+1}-U_{\alpha_i}^{k}\right)=-\frac{\epsilon_0}{2}\sum_{i}^{N}\Delta x_{i+1/2}\left[\left(E_{i+1/2}^{k+1}\right)^2-\left(E_{i+1/2}^{k}\right)^2\right]. \tag{5.58}$$

This is a statement of discrete *total* energy conservation between the plasma species and field. From here on, we define the total energy as:

$$TE^{k+1}=\sum_{\alpha}^{N_s}\sum_{i}^{N}\Delta x_i m_\alpha U_{\alpha_i}^{k+1}+\frac{\epsilon_0}{2}\sum_{i}^{N}\Delta x_{i+1/2}\left(E_{i+1/2}^{k+1}\right)^2. \tag{5.59}$$

The analysis shows that for energy conservation, the number density flux, $n u_{\alpha_{i+1/2}}^{k+1/2}$, must be defined as:

$$n u_{\alpha_{i+1/2}}^{k+1/2}=\frac{\Delta x_i n u_{\alpha_i}^{k+1/2}+\Delta x_{i+1} n u_{\alpha_{i+1}}^{k+1/2}}{2\Delta x_{i+1/2}}, \tag{5.60}$$

with:

$$n u_{\alpha_i}^{k+1/2}=\sum^{N_v}\Delta v_{j+1/2} v_{j+1/2}\widetilde{f}_{\alpha_{i,j+1/2}}^{k+1/2}. \tag{5.61}$$

	Charge Conservation	Momentum Conservation	Energy Conservation
$n_{\alpha_i}^{k+1/2} = \sum_j^{N_v} \Delta v_{\alpha_j} f_{\alpha_{i,j}}^{k+1/2}$	Yes	No	N/A
$n_{\alpha_i}^{k+1/2} = \sum_j^{N_v} \Delta v_{\alpha_{j+1/2}} \widetilde{f}_{\alpha_{i,j+1/2}}^{k+1/2}$	No	Yes	N/A
$nu_{\alpha_{i+1/2}}^{k+1/2} = \sum_j^{N_v} \Delta v_{\alpha_j} v_{\alpha_j} \widehat{f}_{\alpha_{i+1/2,j}}^{k+1/2}$	Yes	Yes	No
$nu_{\alpha_{i,j}}^{k+1/2} = \sum_j^{N_v} \Delta v_{\alpha_{j+1/2}} v_{\alpha_{j+1/2}} \widetilde{f}_{\alpha_{i,j+1/2}}^{k+1/2}$	No	No	Yes

Table 5.1: Moments and their associated conservation properties.

5.3.4 Charge-and-Momentum Conserving Discretization

We organize the definition of moments and their associated conservation properties in Table 5.1. From the previous analysis, the definitions of $n_{\alpha_i}^{k+1/2}$ required for charge conservation and momentum conservation are not guaranteed to be consistent. Thus, in general, one will not achieve simultaneous conservation of charge and momentum. To enforce conservation we introduce an additional nonlinear constraint to deal with the inconsistency between the definition of charge conserving number density and the momentum conserving number density. First, we present the modification of the Vlasov equation which will enforce both charge and momentum conservation:

$$\frac{f_{\alpha_{i,j}}^{k+1} - f_{\alpha_{i,j}}^{k}}{\Delta t} + v_{\alpha_j} \frac{\widehat{f}_{\alpha_{i+1/2,j}}^{k+1/2} - \widehat{f}_{\alpha_{i-1/2,j}}^{k+1/2}}{\Delta x_i} + \frac{q_\alpha}{m_\alpha} E_i^{k+1/2} \left(\frac{\widetilde{f}_{\alpha_{i,j+1/2}}^{k+1/2} - \widetilde{f}_{\alpha_{i,j-1/2}}^{k+1/2}}{\Delta v_{\alpha_j}} + \underbrace{\phi_{\alpha_i}^{k+1} \frac{\widetilde{f}_{\alpha_{i,j+1/2}}^{k+1,*} - \widetilde{f}_{\alpha_{i,j-1/2}}^{k+1,*}}{\Delta v_{\alpha_j}}}_{\text{ⓐ}} \right) = 0. \tag{5.62}$$

Here, term ⓐ is a truncation error term which enforces that the momentum-conserving number density be equal to the charge-conserving number density. In this term, the coefficient $\phi_{\alpha_i}^{k+1}$ will enforce the nonlinear constraint, and $\widetilde{f}_{\alpha_{i,j+1/2}}^{k+1,*}$ is the numerical flux at the cell face. The * simply denotes that the choice of numerical flux estimation can be different from the physical acceleration operator. In order to determine the expression for $\phi_{\alpha_i}^{k+1}$, we introduce

the following nonlinear constraint,

$$\underbrace{\widetilde{n}_{\alpha_i}^{k+1/2} + \Phi_{0,\alpha_i}^{k+1}}_{\text{momentum conserving density}} = \underbrace{n_{\alpha_i}^{k+1/2}}_{\text{charge conserving density}}, \tag{5.63}$$

where,

$$n_{\alpha_i}^{k+1/2} = \frac{\sum_j^{N_v} \Delta v_j \left(f_{\alpha_{i,j}}^{k+1} + f_{\alpha_{i,j}}^{k} \right)}{2}, \tag{5.64}$$

$$\widetilde{n}_{\alpha_i}^{k+1/2} = \sum_j^{N_v} \Delta v_{j+1/2} \widetilde{f}_{\alpha_{i,j+1/2}}^{k+1/2}, \tag{5.65}$$

and

$$\Phi_{0,\alpha_i}^{k+1} = \phi_{\alpha_i}^{k+1} \sum_j^{N_v} \Delta v_{j+1/2} \widetilde{f}_{\alpha_{i,j+1/2}}^{k+1,*}. \tag{5.66}$$

From equations (5.64), (5.65), and (5.66), we can solve for $\phi_{\alpha_i}^{k+1}$ as,

$$\phi_{\alpha_i}^{k+1} = \frac{n_{\alpha_i}^{k+1/2} - \widetilde{n}_{\alpha_i}^{k+1/2}}{\sum_j^{N_v} \Delta v_{j+1/2} \widetilde{f}_{\alpha_{i,j+1/2}}^{k+1,*}}. \tag{5.67}$$

Hence the discretization is inherently nonlinear, and requires an iterative scheme to converge the system. However, this is not a disadvantage in our algorithm, as the nonlinearity in the discretization can be absorbed in the HOLO iteration.

5.3.5 Charge-and-Energy Conserving Discretization

From the previous analysis, the discrete definitions of $nu_{\alpha_{i+1/2}}^{k+1/2}$ required for charge and energy conservation are inconsistent. As before, we introduce an additional nonlinear constraint

to deal with this discrete inconsistency. First, we present the modification of the Vlasov equation which will enforce both charge and energy conservation,

$$\frac{f^{k+1}_{\alpha_{i,j}} - f^{k}_{\alpha_{i,j}}}{\Delta t} + v_{\alpha_j}\frac{\widehat{f}^{k+1/2}_{\alpha_{i+1/2,j}} - \widehat{f}^{k+1/2}_{\alpha_{i-1/2,j}}}{\Delta x_i} + \underbrace{\left|v_{\alpha_j}\right|\frac{\xi^{k+1}_{\alpha_{i+1/2}}\widehat{f}^{k+1,*}_{\alpha_{i+1/2,j}} - \xi^{k+1}_{\alpha_{i-1/2}}\widehat{f}^{k+1,*}_{\alpha_{i-1/2,j}}}{\Delta x_i}}_{\text{ⓐ}} + \frac{q_\alpha}{m_\alpha}E^{k+1/2}_i\frac{\widetilde{f}^{k+1/2}_{\alpha_{i,j+1/2}} - \widetilde{f}^{k+1/2}_{\alpha_{i,j-1/2}}}{\Delta v_{\alpha_j}} = 0. \tag{5.68}$$

Here, ⓐ is a truncation error term that enforces the charge-conserving flux be equal to the energy conserving flux, $\xi^{k+1}_{\alpha_{i+1/2}}$ will enforce the nonlinear constraint, and $\widehat{f}^{k+1,*}_{\alpha_{i+1/2,j}}$ is the numerical flux at the cell face. As before, the * denotes that the choice of numerical flux estimation can be different from the physical streaming operator. In order to determine the expression for $\xi^{k+1}_{\alpha_{i+1/2}}$, we introduce the following nonlinear constraint,

$$\underbrace{\widehat{nu}^{k+1/2}_{\alpha_{i+1/2}} + \Xi^{k+1}_{\alpha_{i+1/2}}}_{\text{charge conserving flux}} = \underbrace{\widetilde{nu}^{k+1/2}_{\alpha_{i+1/2}}}_{\text{energy conserving flux}}, \tag{5.69}$$

where,

$$\widehat{nu}^{k+1/2}_{\alpha_{i+1/2}} = \sum_{j=1}^{N_v}\Delta v_{\alpha_j}\widehat{f}^{k+1/2}_{\alpha_{i+1/2,j}}, \tag{5.70}$$

$$\widetilde{nu}^{k+1/2}_{\alpha_{i+1/2}} = \frac{\sum_j^{N_v}\Delta v_{\alpha_{j+1/2}}v_{\alpha_{j+1/2}}\left(\Delta x_i\widetilde{f}^{k+1/2}_{\alpha_{i,j+1/2}} + \Delta x_{i+1}\widetilde{f}^{k+1/2}_{\alpha_{i+1,j+1/2}}\right)}{2\Delta x_{i+1/2}}, \tag{5.71}$$

and

$$\Xi^{k+1}_{\alpha_{i+1/2}} = \xi^{k+1}_{\alpha_{i+1/2}}\sum_{j}^{N_v}\Delta v_{\alpha_j}\left|v_{\alpha_j}\right|\widehat{f}^{k+1,*}_{\alpha_{i+1/2,j}}. \tag{5.72}$$

From equations (5.70), (5.71), and (5.72), we can solve for $\xi^{k+1}_{\alpha_{i+1/2}}$,

$$\xi^{k+1}_{\alpha_{i+1/2}} = \frac{\widetilde{nu}^{k+1/2}_{\alpha_{i+1/2}} - \widehat{nu}^{k+1/2}_{\alpha_{i+1/2}}}{\sum_j^{N_v} \Delta v_{\alpha_j} \left|v_{\alpha_j}\right| \widehat{f}^{k+1,*}_{\alpha_{i+1/2,j}}}. \tag{5.73}$$

Similar to $\phi^{k+1}_{\alpha_i}$, $\xi^{k+1}_{\alpha_{i+1/2}}$ is inherently nonlinear, and requires an iterative scheme to converge the system, which we absorb in the HOLO iteration.

5.3.6 Combined Charge, Momentum, and Energy Conserving Discretization

By extending the nonlinear enslavement concept introduced earlier we are able to enforce discrete charge, momentum, and energy conservation simultaneously. As before, the modified discrete Vlasov equation reads:

$$\frac{f^{k+1}_{\alpha_{i,j}} - f^{k}_{\alpha_{i,j}}}{\Delta t} + v_{\alpha_j} \frac{\widehat{f}^{k+1/2}_{\alpha_{i+1/2,j}} - \widehat{f}^{k+1}_{\alpha_{i-1/2j}}}{\Delta x_i} + \left|v_{\alpha_j}\right| \frac{\xi^{k+1}_{\alpha_{i+1/2}} \widehat{f}^{k+1,*}_{\alpha_{i+1/2,j}} - \xi^{k+1}_{\alpha_{i-1/2,j}} \widehat{f}^{k+1,*}_{\alpha_{i-1/2,j}}}{\Delta x_i} + \frac{q_\alpha}{m_\alpha} E^{k+1/2}_i \left(\frac{\widetilde{f}^{k+1/2}_{\alpha_{i,j+1/2}} - \widetilde{f}^{k+1/2}_{\alpha_{i,j-1/2}}}{\Delta v_{\alpha_j}} + \phi^{k+1}_{\alpha_i} \frac{\widetilde{f}^{k+1,*}_{\alpha_{i,j+1/2}} - \widetilde{f}^{k+1,*}_{\alpha_{i,j-1/2}}}{\Delta v_{\alpha_j}} \right) = 0. \tag{5.74}$$

The combined charge, momentum, and energy conservation requires a modification to the nonlinear constraints discussed in sections 5.3.4 and 5.3.5. The energy conserving flux is now defined as,

$$nu^{k+1/2}_{EC,\alpha_{i+1/2}} = \frac{1}{2\Delta x_{i+1/2}} \sum_j^{N_v} \Delta v_{\alpha_{j+1/2}} v_{\alpha_{j+1/2}} \left[\Delta x_i \left(\widetilde{f}^{k+1/2}_{\alpha_{i,j+1/2}} + \phi^{k+1}_{\alpha_i} \widetilde{f}^{k+1,*}_{\alpha_{i,j+1/2}} \right) + \Delta x_{i+1} \left(\widetilde{f}^{k+1/2}_{\alpha_{i+1,j+1/2}} + \phi^{k+1}_{\alpha_{i+1}} \widetilde{f}^{k+1,*}_{\alpha_{i,j+1/2}} \right) \right], \tag{5.75}$$

with the charge conserving flux unchanged,

$$nu_{CC,\alpha_{i+1/2}}^{k+1/2} = \widehat{nu}_{\alpha_{i+1/2}}^{k+1/2} + \Xi_{\alpha_{i+1/2}}^{k+1} = \sum_{j}^{N_v} \Delta v_{\alpha_j} v_{\alpha_j} \widehat{f}_{\alpha_{i+1/2,j}}^{k+1/2} + \xi_{\alpha_{i+1/2}}^{k+1} \sum_{j}^{N_v} \Delta v_{\alpha_j} \left| v_{\alpha_j} \right| \widehat{f}_{\alpha_{i+1/2,j}}^{k+1,*}. \tag{5.76}$$

Simultaneous conservation of charge, momentum, and energy requires,

$$nu_{CC,\alpha_{i+1/2}}^{k+1/2} = nu_{EC,\alpha_{i+1/2}}^{k+1/2}, \tag{5.77}$$

which gives the following relation for $\xi_{\alpha_{i+1/2}}^{k+1}$,

$$\xi_{\alpha_{i+1/2}}^{k+1} = \frac{nu_{EC,\alpha_{i+1/2}}^{k+1/2} - \widehat{nu}_{\alpha_{i+1/2}}^{k+1/2}}{\sum_{j}^{N_v} \Delta v_{\alpha_j} \left| v_{\alpha_j} \right| \widehat{f}_{\alpha_{i+1/2,j}}^{k+1,*}}. \tag{5.78}$$

Again, the nonlinearity in both $\xi_{\alpha_{i+1/2}}^{k+1}$ and $\phi_{\alpha_{i+1/2}}^{k+1}$ will be absorbed in the HOLO iteration.

5.4 Discretization and Solver: HO and LO System

We discuss the discretization and solution strategy for the coupled HOLO system. In this study, both the HO and LO system are solved fully implicitly using a Jacobian-Free Newton-Krylov (JFNK) method [62].

5.4.1 HO System: Fully Implicit Charge, Momentum, and Energy Conserving Preconditioned JFNK Solver

The HO system is discretized with finite volumes on a collocated mesh, using a Crank-Nicolson time-discretization. The time, space, and velocity discretized, conservative Vlasov

equation for species α reads:

$$\mathbb{R}_{ve,\alpha_{i,j}} = \frac{f^{k+1,z}_{\alpha_{i,j}} - f^{k}_{\alpha_{i,j}}}{\Delta t} + v_{\alpha_j}\frac{\widehat{f}^{k+1/2,z}_{\alpha_{i+1/2,j}} - \widehat{f}^{k+1/2,z}_{\alpha_{i-1/2,j}}}{\Delta x_i} + \left|v_{\alpha_j}\right|\frac{\xi^{k+1,z-1}_{\alpha_{i+1/2}}\widehat{f}^{k+1,*,z}_{\alpha_{i+1/2,j}} - \xi^{k+1,z-1}_{\alpha_{i-1/2}}\widehat{f}^{k+1,*,z}_{\alpha_{i-1/2,j}}}{\Delta x_i} + \frac{q_\alpha}{m_\alpha}E^{k+1/2,z}_i\left\{\frac{\widetilde{f}^{k+1/2,z}_{\alpha_{i,j+1/2}} - \widetilde{f}^{k+1/2,z}_{\alpha_{i,j-1/2}}}{\Delta v_{\alpha_j}} + \phi^{k+1,z-1}_{\alpha_i}\frac{\widetilde{f}^{k+1,*,z}_{\alpha_{i,j+1/2}} - \widetilde{f}^{k+1,*,z}_{\alpha_{i,j-1/2}}}{\Delta v_{\alpha_j}}\right\} = 0. \tag{5.79}$$

Here,

$$\phi^{k+1,z}_{\alpha_i} = \frac{n^{HO,k+1/2,z}_{\alpha_i} - \widetilde{n}^{HO,k+1/2,z}_{\alpha_i}}{\sum_{j=1}^{N_v}\Delta v_{j+1/2}\widetilde{f}^{k+1,*,z}_{\alpha_{i,j+1/2}}}, \tag{5.80}$$

and

$$\xi^{k+1,z}_{\alpha_{i+1/2}} = \frac{nu^{HO,k+1/2,z}_{EC,\alpha_{i+1/2}} - \widehat{nu}^{HO,k+1/2,z}_{\alpha_{i+1/2}}}{\sum_{j=1}^{N_v}\Delta v_{\alpha_j}\left|v_{\alpha_j}\right|\widehat{f}^{k+1,*,z}_{\alpha_{i+1/2,j}}}, \tag{5.81}$$

$$\widehat{nu}^{HO,k+1/2,z}_{\alpha_{i+1/2}} = \sum_{j}^{N_v}\Delta v_{\alpha_j}v_{\alpha_j}\widehat{f}^{k+1/2}_{\alpha_{i+1/2,j}}, \tag{5.82}$$

where the HO energy conserving flux is given by:

$$nu^{HO,k+1/2,z}_{EC,\alpha_{i+1/2}} = \frac{1}{2\Delta x_{i+1/2}}\sum_{j=1}^{N_v}\Delta v_{\alpha_{j+1/2}}v_{\alpha_{j+1/2}}\left[\Delta x_i\left(\widetilde{f}^{k+1/2,z}_{\alpha_{i,j+1/2}} + \phi^{k+1,z-1}_{\alpha_i}\widetilde{f}^{k+1,*,z-1}_{\alpha_{i,j+1/2}}\right) + \Delta x_{i+1}\left(\widetilde{f}^{k+1/2,z}_{\alpha_{i+1,j+1/2}} + \phi^{k+1,z-1}_{\alpha_{i+1}}\widetilde{f}^{k+1,*,z-1}_{\alpha_{i,j+1/2}}\right)\right], \tag{5.83}$$

the HO charge conserving density is,

$$n^{HO,k+1/2,z}_{\alpha_i} = \sum_{j=1}^{N_v}\Delta v_{\alpha_j}f^{k+1/2}_{\alpha_{i,j}}, \tag{5.84}$$

and the HO momentum conserving density is,

$$\widetilde{n}_{\alpha_i}^{HO,k+1/2,z} = \sum_{j=1}^{N_v} \Delta v_{\alpha_{j+1/2}} \widetilde{f}_{\alpha_{i,j+1/2}}^{k+1/2,z}. \tag{5.85}$$

Here, the additional superscript z denotes the HOLO iteration index. Note that the evaluation of $\xi_{\alpha_{i+1/2}}^{k+1}$ and $\phi_{\alpha_{i+1/2}}^{k+1}$ is lagged to the previous HOLO iteration. For this study, the Vlasov equation for *each species* are solved for $\mathbb{R}_{ve}$ using JFNK with an ILU preconditioning with a relative convergence tolerance of 10^{-4} and an absolute convergence tolerance of 10^{-6}. We use a QUICK discretization [90] for $\widehat{f}_{\alpha_{i+1/2,j}}^{k+1/2}$, an upwind discretization for $\widehat{f}_{\alpha_{i+1/2,j}}^{k+1,*}$, and central differencing for $\widetilde{f}_{\alpha_{i,j+1/2}}^{k+1/2}$ and $\widetilde{f}_{\alpha_{i,j+1/2}}^{k+1,*}$.

5.4.2 LO System: Physics Based Preconditioned JFNK

The LO system is discretized using staggered finite differences and a Crank-Nicolson time-discretization. The time and space discrete implicit LO system reads:

$$\mathbb{R}_{n_{\alpha_i}} = \frac{n_{\alpha_i}^{LO,k+1,z} - n_{\alpha_i}^{k}}{\Delta t} + \frac{nu_{EC,\alpha_{i+1/2}}^{LO,k+1/2,z} - nu_{EC,\alpha_{i-1/2}}^{LO,k+1/2,z}}{\Delta x_i} = 0, \tag{5.86}$$

$$\begin{aligned}\mathbb{R}_{nu_{\alpha_{i+1/2}}} = \frac{nu_{EC,\alpha_{i+1/2}}^{LO,k+1,z} - nu_{EC,\alpha_{i+1/2}}^{LO,k}}{\Delta t} + \\ \frac{n_{\alpha_{i+1}}^{LO,k+1/2,z}\widetilde{S}_{\alpha_{i+1}}^{HO,k+1/2,z} - n_{\alpha_i}^{LO,k+1/2,z}\widetilde{S}_{\alpha_i}^{HO,k+1/2,z}}{\Delta x_{i+1/2}} - \\ \frac{q_\alpha}{m_\alpha} n_{\alpha_{i+1/2}}^{LO,k+1/2,z} E_{i+1/2}^{k+1/2,z} - \gamma_{nu_{\alpha_{i+1/2}}}^{HO,k+1,z} = 0,\end{aligned} \tag{5.87}$$

$$\mathbb{R}_{E_{i+1/2}} = \epsilon_0 \frac{E_{i+1/2}^{k+1} - E_{i+1/2}^{k}}{\Delta t} + \sum_\alpha q_\alpha nu_{EC,\alpha_{i+1/2}}^{LO,k+1,z} = 0. \tag{5.88}$$

Here, the density normalized total stress-tensor, $\widetilde{S}^{HO,k+1/2,z}$, is computed from the HO solution,

$$\widetilde{S}^{HO,k+1/2,z}_{\alpha_i} = \frac{\sum_{j=1}^{N_v} \Delta v_{\alpha_j} v_{\alpha_j}^2 f^{k+1/2,z}_{\alpha_{i,j}}}{\sum_{j=1}^{N_v} \Delta v_{\alpha_j} f^{k+1/2,z}_{\alpha_{i,j}}}, \tag{5.89}$$

and the discrete consistency term, $\gamma^{HO,k+1,z}_{nu_{\alpha_{i+1/2}}}$, is computed as:

$$\begin{aligned} T\gamma^{HO,k+1,z}_{nu_{\alpha_{i+1/2}}} = \frac{nu^{HO,k+1,z}_{EC,\alpha_{i+1/2}} - nu^{HO,k}_{EC,\alpha_{i+1/2}}}{\Delta t} + \\ \frac{n^{HO,k+1/2,z}_{\alpha_{i+1}} \widetilde{S}^{HO,k+1/2,z}_{\alpha_{i+1}} - n^{HO,k+1/2,z}_{\alpha_i} \widetilde{S}^{HO,k+1/2,z}_{\alpha_i}}{\Delta x_{i+1/2}} - \frac{q_\alpha}{m_\alpha} n^{HO,k+1/2,z}_{\alpha_{i+1/2}} E^{k+1/2,z}_{i+1/2}, \end{aligned} \tag{5.90}$$

where $n^{LO/HO,k+1/2,z}_{\alpha_{i+1/2}}$ is computed by interpolating $n^{LO/HO,k+1/2,z}_{\alpha_i}$ from cell centers to the cell-face. Unlike the HO system, the LO system is fully nonlinear and is solved using a physics-based-preconditioned JFNK for the complete residual vector,

$$\vec{\mathbb{R}} = \begin{Bmatrix} \mathbb{R}_{n_e} \\ \mathbb{R}_{nu_e} \\ \mathbb{R}_{n_i} \\ \mathbb{R}_{nu_i} \\ \mathbb{R}_E \end{Bmatrix}. \tag{5.91}$$

For details on the preconditioner, we refer the reader to [75, 93]. For the Newton iteration, we use a relative convergence tolerance of 10^{-6} and an absolute tolerance of 10^{-7}.

5.4.3 HOLO Accelerator Algorithm with Charge Momentum and Energy Conserving Discretization

To check the convergence of the Picard HOLO iteration, we measure the L_2-norm of the relative difference between the moments of the HO and LO solution,

$$\text{reldiff}^z_{\mathcal{M}} = \left| \frac{\mathcal{M}^{HO,z} - \mathcal{M}^{LO,z}}{\mathcal{M}^{HO,z}} \right|_2, \tag{5.92}$$

where $\mathcal{M}$ is the specific moment of choice (i.e. n or nu). We have chosen a convergence tolerance of 10^{-6} in this study.

We outline the algorithm for the fully implicit, charge, momentum, and energy conserving, moment accelerated Vlasov-Ampere solver in Algorithm 6.

Algorithm 6: Charge-momentum-and-energy conserving HOLO acceleration.

Set $z = 0$;
while *HOLO system not converged* **do**
  Increment, $z = z + 1$;
  Solve the LO system for $\left(n_\alpha^{LO,k+1,z}, nu_{EC,\alpha}^{LO,k+1,z}, E^{k+1,z}\right)$ from equations (5.86) to (5.88);
  Solve the HO system for $f_\alpha^{k+1,z}$ from equation (5.79) using the new $E^{k+1,z}$;
  Update, $\left(n, nu_{EC}, \widetilde{S}\right)_\alpha^{HO,k+1,z}$ from equations (5.83), (5.84), and (5.89);
  Update, $\gamma_\alpha^{HO,k+1,z}$ from equation (5.90);
  Update, $\xi_\alpha^{k+1,z}$, and $\phi_\alpha^{k+1,z}$ from equations (5.81) and (5.80) ;
  Check convergence via equation (5.92);
end

It is stressed here that the charge, momentum, and energy conserving discretization of the Vlasov equation and the HOLO iteration are two completely independent concepts. Thus, the HOLO algorithm is *not needed* to enforce conservation. The advantage of coupling the

conservative discretization of the Vlasov equation with the HOLO acceleration algorithm is that the nonlinearity in the discretization can be absorbed into the HOLO iteration and can be dealt with efficiently.

5.5 Numerical Results

We present the algorithmic and accuracy performance results of the new HOLO solver with the proposed conservative discretization for the Vlasov-Ampere system. We choose the following test problems: 1) an electron Landau damping, 2) electron two-stream instability, and 3) an ion acoustic shockwave problem [92]. The purpose of these numerical tests is 1) to verify the correctness of the implementation, 2) to demonstrate the algorithmic ability to step over stiff time-scales and 3) to demonstrate the advertised conservation properties of the scheme in a periodic system.

For all of our test cases, unless otherwise specified, the distribution function is initialized according to the following initial condition:

$$f_0\left(x,v,u,T\right) = \frac{n_0}{\sqrt{2\pi T_0/m}}\exp\left[-\frac{m\left(v-u_0\right)^2}{2T_0}\right], \tag{5.93}$$

$$n_0 = n_0\left(t=0,x\right) = 1+\alpha_n\cos\left(kx\right).$$

Here x, v, n_0, u_0, T_0, α_n, k, and m are the position and velocity, initial number density, initial fluid velocity, initial temperature, perturbation amplitude for number density, wave vector of perturbation, and the species mass, respectively.

5.5.1 Landau Damping

For the first test case, the classic single-species electron Landau damping problem is chosen. The rate at which the field energy is converted to the wave energy is found from the linear dispersion relation,

$$1 + \frac{1}{k^2}\left[1 + \frac{\omega}{\sqrt{2}k} Z\left(\frac{\omega}{\sqrt{2}k}\right)\right] = 0\ . \tag{5.94}$$

Here k, ω, and Z are the wave vector of perturbation, wave frequency and dispersion function of Fried and Conte, respectively. Solving for ω, a complex solution is obtained in terms of the oscillatory (imaginary) $\tilde{\omega}$ and decaying (real) γ components of the frequency. The problem parameters used for this single species test case are [65]: the periodic system length, $L_x = 4\pi$, the number of configuration cells, $N = 32$, the maximum duration of simulation in terms of the electron plasma wave time-scale, $t_{max} = 50\omega_{p,e}^{-1}$, the time-step size, $\Delta t = 0.1\omega_{p,e}^{-1}$, the number of velocity space cells, $N_v = 512$, the wave vector of perturbation, $k = 2\pi/L_x$, the average density $n_0 = 1.0$, perturbation in density, $\alpha_n = 0.01$, $u_0 = 0$, and temperature, $T_0 = 1.0$. For these given parameters, the growth rate is γ = -0.155 [65]. The simulation result for the Landau damping case is shown in Figure 5.1. As seen, good agreement between the numerical simulation and linear theory is achieved.

5.5.2 Two-Stream Instability

For the second benchmark case, we simulate the single-species two-stream instability [61]. The dispersion relation for the two-stream instability is:

$$1 - \frac{1}{(\omega + v_b k)^2} - \frac{1}{(\omega - v_b k)^2} = 0 \tag{5.95}$$

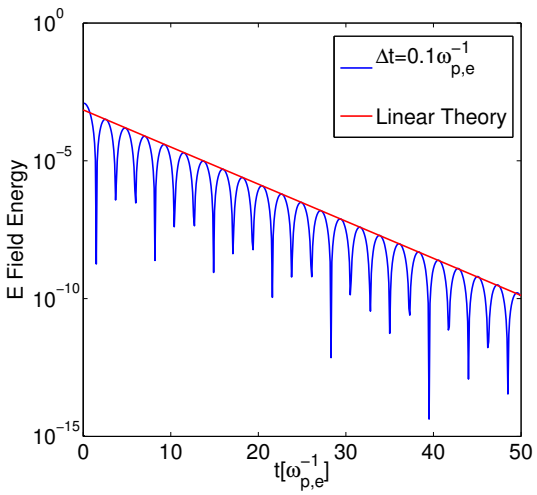


Figure 5.1: Decay rate comparison for Landau damping

Here v_b is the beam velocity and ω is again the wave frequency. The simulation is initialized as follows:

$$f_0\left(x, v, t=0\right) = \left(1 + \alpha_n \cos kx\right) \delta\left(v \pm v_b\right) \tag{5.96}$$

The simulation parameters are $L_x = 1$, $N = 32$, $t_{max} = 35\omega_{p,e}^{-1}$, $\Delta t = 0.25\omega_{p,e}^{-1}$, $0.5\omega_{p,e}^{-1}$, $1.0\omega_{p,e}^{-1}$, $2\omega_{p,e}^{-1}$, $N_v = 512$, $k = 2\pi/L_x$, $\alpha_n = 0.001$, and $v_b = 0.1$. From linear theory, the growth rate, γ, is 0.353. The comparison plot of linear theory and numerical solutions for the electric field energy vs. time for various Δt is shown in Figure. 5.2. Again, good agreement between the linear theory and the numerical solution is observed in the linear growth regime.

5.5.3 Ion Acoustic Shockwave (IASW) Problem

For the IASW problem [92], the parameters are the electron mass, $m_e = 1/1836$, ion mass of $m_{ion} = 1$, Debye length, $\lambda_D = 1/36$, system length, $L_x = 144\lambda_D$, number of configuration space cells, $N = 144$, velocity space domain, $v_{\alpha_{min}} = -10v_{\alpha_{th}}$, $v_{\alpha_{max}} = 10v_{\alpha_{th}}$, number of velocity space cells, $N_v = 400$, inverse ion plasma frequency, $\omega_{p,ion}^{-1} = 1/36$, inverse electron

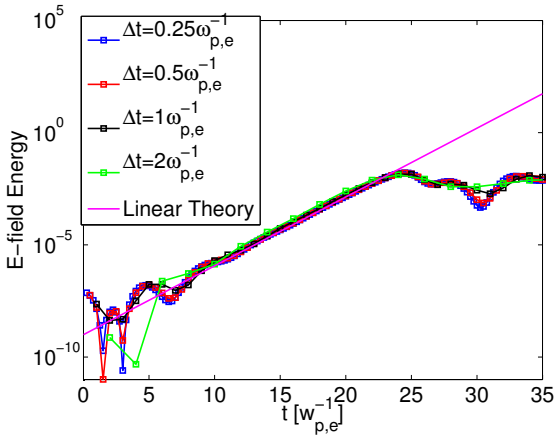


Figure 5.2: Electric field energy growth rate for two stream instability.

plasma frequency, $\omega_{p,e}^{-1} = \omega_{p,ion}^{-1}/\sqrt{1836} = 6.48 \times 10^{-4}$, and simulation duration, $t_{max} = 5000 w_{p,e}^{-1}$. For the initial condition, we use a sinusoidal perturbation in the ion density [92],

$$n_{0,ion} = 1 + 0.2\sin kx,$$

electron density,

$$n_{0,e} = 1 + 0.2(1 - k^2\lambda_D^2)\sin kx$$

and bulk fluid velocity, u, for both species of the form:

$$u_0 = -1 + 0.2\sin kx, \tag{5.97}$$

with isothermal distributions with $T_{0,e} = 1$ and $T_{0,ion} = 0.05$. Here, $k = 2\pi/L_x$ is the wave vector of perturbation.

To demonstrate the algorithmic performance of the solver, we ran the test case for time-step sizes of $\Delta t = 1\omega_{p_e}^{-1}$, $10\omega_{p_e}^{-1}$, and $100\omega_{p_e}^{-1}$. In Table 5.2, we show the implicit time-step-size, relative to the explicit CFL constraint,

$$\Delta t_{exp} = \frac{\Delta x}{v_{e,max}}, \tag{5.98}$$

$\Delta t/\omega_{p_e}^{-1}$	1	10	100
$\Delta t/\Delta t_{exp}$	1.407×10^1	1.407×10^2	1.407×10^3
HOLO Iter_{avg}	3.2	8.2	10.4

Table 5.2: HOLO solver performance with varying Δt on a collisionless IASW problem.

and the average number of HOLO iterations for convergence over the entire simulation. We see that for the IASW problem, the number of HOLO iterations is kept bounded for Δt large relative to the explicit time-step size.

We demonstrate next the advertised conservation properties of the scheme. For the field equation, we use the Ampère's equation. For charge conservation, it is critical that the discrete equivalence with the Poisson's equation be satisfied. For this reason, to measure charge conservation, we compute the L_2-norm of the discrete Gauss-law from time-step to time-step,

$$|GL|_2 = \left| \lambda_D^2 \left(\frac{E_{i+1/2}^{k+1} - E_{i-1/2}^{k+1}}{\Delta x_i} - \frac{E_{i+1/2}^{k} - E_{i-1/2}^{k}}{\Delta x_i} \right) - \sum_{\alpha} q_\alpha \left(n_{\alpha_i}^{k+1} - n_{\alpha_i}^{k} \right) \right|_2 . \tag{5.99}$$

For momentum and energy conservation, we show the relative difference of total energy and momentum with respect to the initial condition (denoted by the superscript 0):

$$\text{reldiff}_{TE}^k = \left| \frac{TE^0 - TE^k}{TE^0} \right|, \tag{5.100}$$

$$\text{reldiff}_{TM}^k = \left| \frac{TM^0 - TM^k}{TM^0} \right|, \tag{5.101}$$

The conservation properties of the solver over the entire duration of the simulation for different time-step sizes are shown in Figure 5.3. We see that all quantities are conserved at or below the convergence tolerance of the HOLO iteration, $\text{tol} = 10^{-6}$. To establish accuracy, we compare the electron and ion density, and electric field structure obtained for the different cases in Figure 5.4. As can be seen, we are able to obtain a solution using $\Delta t = 10\omega_{p,e}^{-1}$, and $100\omega_{p,e}^{-1}$ with similar level of accuracy as the $\Delta t = 1\omega_{p,e}^{-1}$ case, but much more efficiently.

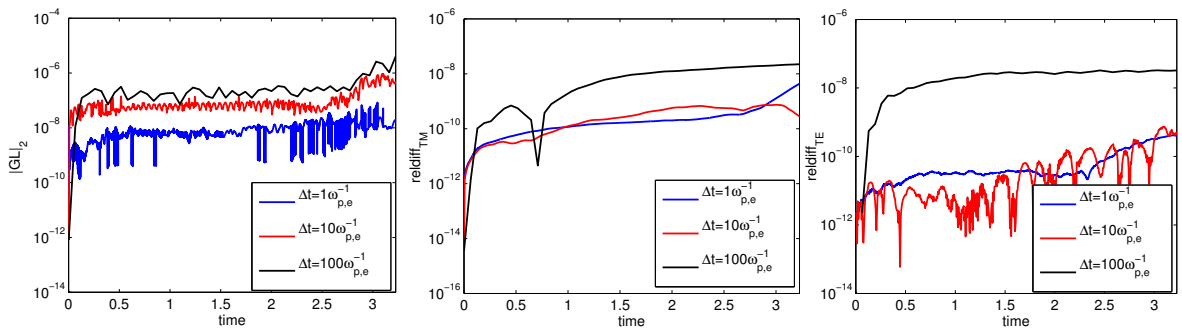


Figure 5.3: Conservation properties of the new charge-momentum-and-energy conserving discretization.

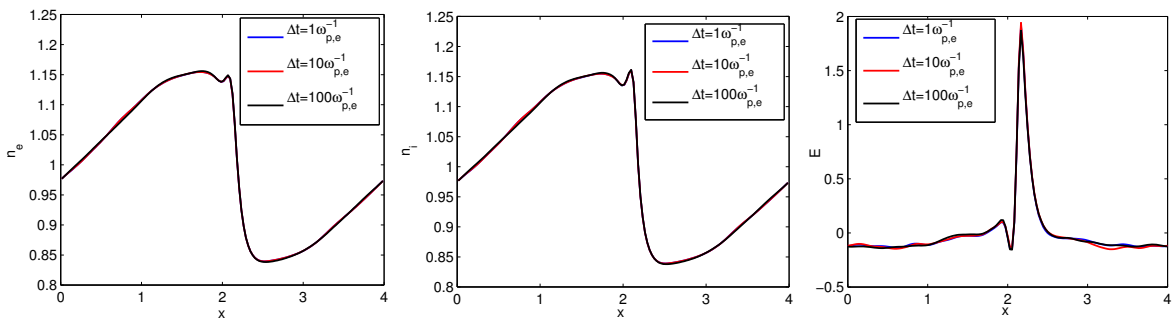


Figure 5.4: Solution for the ion acoustic shockwave.

5.6 Conclusion

In this chapter, we have 1) developed a charge, momentum, and energy conserving Vlasov-Ampère discretization, and 2) extended the HOLO moment-based acceleration algorithm for the Eulerian approach to solve the Vlasov-Ampère system. In order to achieve the conservation properties, a novel nonlinear enslavement scheme was introduced to enslave the momentum conserving density to the charge conserving density, and the charge conserving flux to the energy conserving flux. These enslavements were enforced by introducing two *discrete* nonlinear constraints, which resulted in a nonlinear discretization. However, the nonlinearity in the discretization was dealt with efficiently by the HOLO iteration. The algorithm has been tested on a Landau damping, two-stream instability, and an ion acoustic

shockwave (IASW) problem. The IASW problem demonstrated that we can stably take a time-step-size, Δt, significantly larger than the inverse electron plasma frequency, $\omega_{p,e}^{-1}$, while evolving the solution accurately, with strong conservation properties of charge, momentum, and energy.

Chapter 6

Moment Acceleration of Collisional Neutral Gas

In this chapter, we extend the HOLO moment-based acceleration algorithm to a *collisional neutral gas* Boltzmann transport equation. The purpose of this study is to develop a method which allows one to take time-step sizes, Δt, that are much larger than the collisional relaxation time-scale, τ, while still allowing for an efficient convergence of the nonlinear system. The new HOLO moment-based acceleration algorithm is used to solve a *neutral* and *collisional* strong shock tube problem with a wide variation in τ. When a wide variation in τ exists, naturally, a *transition region* will arise. A transition region is a region where both, a strongly and weakly collisional region can coexist near each other. Solvers that can efficiently handle a transition region are of great interest for ICF problems since these regions are ubiquitous in ICF, and a Picard iteration can be slow to converge the system of nonlinear equations when the time-step size is chosen to step over the fastest collisional time-scale of the system, τ_{min}. We show that the new algorithm is capable of choosing a $\Delta t \gg \tau_{min}$ and can follow the acoustic wave CFL of the problem (dynamical time-scale of the system for propagating shocks).

6.1 Introduction

There exist two broad approaches to following the dynamic evolution of a system such as neutron transport, plasma physics, and neutral gas dynamics: 1) a kinetic approach and 2) a moment approach. The kinetic approach requires one to solve the six dimensional integro-differential Boltzmann transport equation while the moment approach requires one to solve a set of reduced dimensionality (three dimensional) partial differential equations obtained from the original transport equation by moment integration. The kinetic approach encapsulates time-scales of all the phase-space physics as well as the wave physics. The computational effort and memory requirements are very large, but a first-principles phase-space evolution of the system can be studied. On the other hand, the moment approach requires less computer memory compared to the kinetic approach. The stiff phase-space physics time-scales are integrated out of the system, and one can follow the collective "hydrodynamical" time-scales, which are typically much slower than the kinetic time-scales. However, with the moment equations, one must address the issue of the need for closures for higher-order moments. In the moment approach, analytical closures are limited to some small perturbation of the kinetic solution near an equilibrium [74], and/or empirical correlations. In problems where regimes with both a non-equilibrium and equilibrium physics co-exist, it is difficult to formulate a robust closure which is valid for all regimes of interest. Therefore, the need for an efficient kinetic approach becomes evident for high fidelity modeling when non-equilibrium solution exists in phase-space.

Currently, there are two main approaches to solve for the kinetic equation: 1) a direct simulation monte-carlo (DSMC) approach [66] and 2) a deterministic approach of solving the Botzmann equation on a velocity space grid. For the deterministic approach, significant efforts have been invested in developing explicit [84, 68], semi-implicit [69, 70] and asymptotic-preserving schemes [71, **?**]. In this study, we propose an efficient, accelerated *fully* implicit nonlinear iteration scheme for solving the Boltzmann transport equation for the deterministic approach. We achieve the acceleration by solving a discretely-consistent

low-order (LO) moment equation system together with the high-order (HO) kinetic equation. The method originates in the neutron transport community, in which a moment equation was used in order to accelerate the convergence of the scattering source in the linear Boltzmann transport equation [52]. The original method however, did not address the issue of *discrete consistency* between the HO and LO system. In order to achieve nonlinear robustness, our *discrete* LO problem must provide identical solutions to the moments of the *discrete* HO problem. Efforts reported in references [50, 51], have advanced the method by adding a *discrete consistency term* in the LO moment system that enslaved the discrete truncation error of the LO moment equations to that of the discrete moments of the HO kinetic equation. This ensured that the LO equation preserved the moments of the HO equation upon nonlinear convergence. In this study, we extend the original concept of moment acceleration in combination with the concept of discrete consistency in order to develop a powerful new accelerator algorithm for the Boltzmann transport equation with Bhatnagar-Gross-Krook (BGK) collision operator [72].

The remainder of the chapter is organized as follows. Section 6.2 discusses the neutral gas dynamics Boltzmann transport equation with the BGK collision operator and a standard Picard (source) iteration approach. In section 6.3, we derive the self-consistent set of moment equations, which describe the evolution of the macroscopic fluid moment quantities. In section 6.4, we describe the new HOLO algorithm, the concept of discrete consistency, and the discretization schemes used in this study. Section 6.5 demonstrates the performance of the algorithm compared to the standard Picard iteration approach. Finally, we conclude in section 7.5.

6.2 Neutral Gas Dynamics Boltzmann Transport Equation (HO System): BGK Collision Operator

The underlying kinetic equation that we wish to solve is the time dependent neutral gas dynamics Boltzmann transport equation,

$$\frac{\partial f}{\partial t}\left(\vec{r},\vec{v},t\right)+\vec{v}\cdot\nabla f\left(\vec{r},\vec{v},t\right)=\left(\frac{\partial f}{\partial t}\right)_{c}. \tag{6.1}$$

Here, f is the distribution function of particles in the gas, which is a function of the configuration space, $\vec{r}$, the particle velocity, $\vec{v}$, and time, t. The two terms on the left-hand-side (LHS) represent the local time rate of change of f and streaming of the particles, respectively. The right-hand-side (RHS) term is the collision operator. In this study, a simple BGK collision operator [72] is used,

$$\left(\frac{\partial f}{\partial t}\right)_{c}=\frac{1}{\tau\left(\vec{r},t\right)}\left[f_{M}\left(\vec{r},\vec{v},t\right)-f\left(\vec{r},\vec{v},t\right)\right]. \tag{6.2}$$

Here, τ is the collision time scale,

$$\tau=\frac{\widetilde{\tau}}{n\sqrt{T}}, \tag{6.3}$$

with $\widetilde{\tau}$ the scaling constant for the collision operator in a dimensionless setting. f_M is a local Maxwellian distribution,

$$f_{M}\left(\vec{r},\vec{v},t\right)=\frac{n}{\left(2\pi T/m\right)^{d/2}}\exp\left\{-\frac{m}{2T}\sum_{\alpha}\left(v_{\alpha}-u_{\alpha}\right)^{2}\right\}, \tag{6.4}$$

with d the translational degrees of freedom of the gas molecule, and α the index for the direction of the particle ($\alpha = x$, y, or z). The Maxwellian distribution is a function of the local number density, n, the average fluid velocity, $\vec{u}$, and the temperature, T, which are velocity moments of the distribution function, defined as,

$$n=n\left(\vec{r},t\right)=\left\langle 1,f\right\rangle_{\vec{v}}, \tag{6.5}$$

$$\vec{u} = \vec{u}\left(\vec{r}, t\right) = \frac{\langle \vec{v}, f \rangle_{\vec{v}}}{n}, \tag{6.6}$$

$$T = T\left(\vec{r}, t\right) = \frac{1}{d} m \frac{\left\langle \left|\vec{w}\right|^2, f \right\rangle_{\vec{v}}}{n}. \tag{6.7}$$

Here, m is the mass of the particle, $\vec{w}$ is the particular velocity,

$$\vec{w} = \vec{v} - \vec{u}\,, \tag{6.8}$$

and $\langle (\cdot), f \rangle_{\vec{v}}$ is a shorthand notation for the velocity moment, i.e.,

$$\langle (\cdot), f \rangle_{\vec{v}} = \int\int\int (\cdot) f dv_x dv_y dv_z. \tag{6.9}$$

The BGK collision operator will effectively relax the distribution to a Maxwellian in a few collision times, τ. In this study, we consider the one dimensional in configuration-space and one dimensional in velocity-space (1D1V) model of equation (6.1):

$$BBGK = \frac{\partial f}{\partial t}\left(x, v, t\right) + v \frac{\partial f}{\partial x}\left(x, v, t\right) - \frac{1}{\tau}\left[f_M\left(x, v, t\right) - f\left(x, v, t\right)\right] = 0. \tag{6.10}$$

6.2.1 Implicit Time Integration and Picard (Source) Iteration (HO System)

An implicit time integration scheme is not limited by the stability constraints associated with an explicit time integration scheme. Instead, an arbitrary Δt can be chosen to resolve the dynamical time-scale of interest in the system. Consider a first-order backward-Euler time-differencing scheme with a standard finite-volume treatment for the space differencing,

$$\frac{f_{i,j}^{k+1} - f_{i,j}^{k}}{\Delta t} + v_j \frac{\widehat{f}_{i+1/2,j}^{k+1} - \widehat{f}_{i-1/2,j}^{k+1}}{\Delta x} = \frac{1}{\tau_i^{k+1}}\left[f_{M,i,j}^{k+1} - f_{i,j}^{k+1}\right]. \tag{6.11}$$

Here, the indices i, j, and k are the configuration-space cell index, the velocity-space cell index, and the time index, respectively. The hat denotes numerical flux estimation at cell faces. As seen, the streaming operator and the collision operators are evaluated with the solution at the new time step, $k+1$. The discrete Maxwellian is computed with the moments of the distribution function,

$$f_{M,i,j}^{k+1} = \frac{n_i^{k+1}}{\sqrt{2\pi T_i^{k+1}/m}} \exp\left[-\frac{m}{2T_i^{k+1}}\left(v_j - u_i^{k+1}\right)^2\right], \tag{6.12}$$

where,

$$n_i^{k+1} = \sum_j \Delta v f_{i,j}^{k+1}, \tag{6.13}$$

$$u_i^{k+1} = \frac{\sum_j \Delta v v_j f_{i,j}^{k+1}}{n_i^{k+1}}, \tag{6.14}$$

and,

$$T_i^{k+1} = m\frac{\sum_j \Delta v \left(v_j - u_i^{k+1}\right)^2 f_{i,j}^{k+1}}{n_i^{k+1}}. \tag{6.15}$$

Here, Δv is the discrete velocity cell size and v_j is the j^{th} discrete velocity cell center value. The collision time-scale is also defined in terms of the moment quantities as:

$$\tau_i^{k+1} = \frac{\widetilde{\tau}}{n_i^{k+1}\sqrt{T_i^{k+1}}}. \tag{6.16}$$

As can be seen in equations (6.11) to (6.16), all the solution variables are evaluated at time step, $k+1$, leading to a system of nonlinearly coupled equations. The nonlinearity is introduced by the collision operator through the evaluation of moments for the Maxwellian and collision time-scale, which are nonlinear integral functions of f. To solve this equation

implicitly, a nonlinear iterative scheme such as Picard iteration or Newton's method [73] must be employed. The standard approach is a Picard (source) iteration scheme, which reads:

$$\frac{f_{i,j}^{k+1,z} - f_{i,j}^{k}}{\Delta t} + v_j \frac{\widehat{f}_{i+1/2,j}^{k+1,z} - \widehat{f}_{i-1/2,j}^{k+1,z}}{\Delta x} = \frac{1}{\tau_i^{k+1,z-1}} \left[f_{M,i,j}^{k+1,z-1} - f_{i,j}^{k+1,z} \right]. \tag{6.17}$$

Here, z is the Picard iteration index, and the evaluation of the Maxwellian distribution function and collision time-scale is lagged from iteration to iteration. This yields a linear system of equations which can be efficiently solved using a transport sweep algorithm [78]. For convergence, the L_2-norm of the relative difference in the self-consistent moments from iteration to iteration is used,

$$\text{rel-diff}_{\mathcal{M}}^{k+1} = \left| \frac{\mathcal{M}^{k+1,z} - \mathcal{M}^{k+1,z-1}}{\mathcal{M}^{k+1,z}} \right|_2. \tag{6.18}$$

Here, $\mathcal{M}$ is the moment of choice, $\mathcal{M} = (n, nu, U)$, where the number density, n, the number density flux, nu, and the total energy density, U, are defined as the 0^{th}, 1^{st}, and 2^{nd} velocity moments of the distribution function, respectively:

$$n = \langle 1, f \rangle_v ,$$

$$nu = \langle v, f \rangle_v ,$$

$$U = \left\langle \frac{v^2}{2}, f \right\rangle_v .$$

The Picard iteration algorithm per time step reads as follows:

Algorithm 7: Picard (source) iteration for the BGK collision operator.

Set $z = 0$;
Calculate initial $f_{M,i,j}^{k+1,z=0}$ and $\tau^{k+1,z=0}$ with known n_i^k, u_i^k, and T_i^k;
while *not converged* **do**
    Increment $z = z + 1$;
    Solve for $f_{i,j}^{k+1,z}$ from equation (6.17) with known $f_{M,i,j}^{k+1,z-1}$ and $\tau_i^{k+1,z-1}$;
    Calculate $n_i^{k+1,z}$, $u_i^{k+1,z}$, and $T_i^{k+1,z}$ using equations (6.13), (6.14), and (6.15) from $f_{i,j}^{k+1,z}$;
    Compute $f_{M,i,j}^{k+1,z}$ and $\tau_i^{k+1,z}$ using equation (6.12) and (6.16) from $n_i^{k+1,z}$, $u_i^{k+1,z}$, and $T_i^{k+1,z}$;
    Check convergence using equation (6.18);
end

The Picard iteration scheme is simple and has a well understood linear convergence rate [73]. However, when $\Delta t \gg \tau$, the method requires many iterations, becoming inefficient. The moment-based HOLO acceleration method proposed here is intended to *accelerate* the convergence rate of the Picard iteration method.

6.3 Self-Consistent Fluid Moment equations

To derive the self-consistent fluid moment equations, we take the 1, v^1, and $\frac{v^2}{2}$ moments of the 1D1V Botlzmann transport equation in equation (6.10) [74]. The 1, v, and $v^2/2$ moments are said to be collisional invariants of the system (i.e. moments of the collision operator are zero):

$$\left\langle 1, \frac{f_M - f}{\tau} \right\rangle_v = 0, \tag{6.19}$$

$$\left\langle v, \frac{f_M - f}{\tau} \right\rangle_v = 0, \tag{6.20}$$

$$\left\langle \frac{v^2}{2}, \frac{f_M - f}{\tau} \right\rangle_v = 0. \tag{6.21}$$

The 0^{th}, 1^{st}, and 2^{nd} velocity moments of the Boltzmann transport equation are:

$$\left\langle v^0, BBGK \right\rangle_v = \frac{\partial n}{\partial t} + \frac{\partial}{\partial x} nu = 0, \tag{6.22}$$

$$\left\langle v^1, BBGK \right\rangle_v = \frac{\partial}{\partial t} nu + \frac{\partial}{\partial x} S_2 = 0, \tag{6.23}$$

$$\left\langle \frac{v^2}{2}, BBGK \right\rangle_v = \frac{\partial}{\partial t} U + \frac{\partial}{\partial x} S_3 = 0. \tag{6.24}$$

Equations (6.22), (6.23), and (6.24) are the continuity, momentum, and energy equation, respectively. We define the number density, n, the number density flux, nu, the total energy density, U, the total stress tensor, S_2, and the total energy flux, S_3, in terms of the distribution function,

$$n = n\left(x,t\right) = \left\langle 1, f \right\rangle_v, \tag{6.25}$$

$$nu = nu\left(x,t\right) = \left\langle v, f \right\rangle_v, \tag{6.26}$$

$$U = U\left(x,t\right) = \left\langle \frac{v^2}{2}, f \right\rangle_v, \tag{6.27}$$

$$S_2 = S_2\left(x,t\right) = \left\langle v^2, f \right\rangle_v, \tag{6.28}$$

$$S_3 = S_3(x,t) = \left\langle \frac{v^3}{2}, f \right\rangle_v . \tag{6.29}$$

We can expand S_2 and S_3 as [74]:

$$S_2 = nu^2 + P, \tag{6.30}$$

and

$$S_3 = u(U+P) + Q. \tag{6.31}$$

Here, P is the scalar isotropic pressure, defined as,

$$P = \frac{nT}{m} = 2\left(U - \frac{1}{2}nu^2\right), \tag{6.32}$$

with T the temperature,

$$T = \frac{2m\left(U - \frac{1}{2}nu^2\right)}{n}, \tag{6.33}$$

and Q is the heat-flux,

$$Q = \frac{1}{2}\left\langle (v-u)^3, f \right\rangle_v . \tag{6.34}$$

By substituting the expansion for S_2 and S_3 into the momentum and energy equations, we derive the familiar moment equations,

$$\frac{\partial n}{\partial t} + \frac{\partial}{\partial x}nu = 0, \tag{6.35}$$

$$\frac{\partial}{\partial t}nu + \frac{\partial}{\partial x}\left[nu^2 + P\right] = 0, \tag{6.36}$$

$$\frac{\partial}{\partial t}U + \frac{\partial}{\partial x}\left[u\left(U+P\right)+Q\right] = 0. \tag{6.37}$$

Note that, according to kinetic theory [74], the shear viscous stress tensor evaluates to zero for the 1V case. Closure is needed for the heat-flux, Q. In standard gas dynamics, this term is closed with a Fourier model for heat conduction, $q = -\kappa\frac{\partial T}{\partial x}$, and one is required to provide a functional form for κ. We will not do that here. Rather, we will *close* this heat-flux using the most recent iteration level of the distribution function. It is worthwhile to remind the reader that, unlike the original Boltzmann transport equation, the moment equations do not explicitly carry the collisional time-scale. Instead, the natural time-scales for the moment equations are 1) the acoustic time-scale, 2) the advection time-scale, and 3) the heat-flux propagation time-scale.

6.4 HOLO Moment Acceleration Algorithm

A unique relationship exists between the Boltzmann transport equation and the self consistent moment equations. Given the correct moments, n, u, and T, to evaluate the Maxwellian, one can evaluate the correct distribution function, f, in time from equation (6.10). Similarly, with the correct closure for the heat-flux, Q, the moment equations will provide the correct moments to evaluate the collision operator. This unique relationship between the kinetic and fluid-moment system will be used to our advantage to develop an acceleration algorithm to the standard Picard (source) iteration scheme discussed in section 6.2.1. The iterative scheme will rely on the lower dimensional (LO) moment equations, defined on a reduced dimensionality space, (x,t), to accelerate the convergence of the higher dimensional (HO) transport equation defined on the phase-space, (x,v,t).

We begin by formulating a nonlinearly coupled system of HO kinetic and LO fluid-moment equations:

$$\frac{\partial f}{\partial t} + v\frac{\partial f}{\partial x} = \frac{1}{\tau^{LO}}\left[f_M^{LO} - f\right], \tag{6.38}$$

$$\frac{\partial n}{\partial t}^{LO} + \frac{\partial}{\partial x} nu^{LO} = \frac{\partial \gamma_n^{HO}}{\partial x} + \mathcal{I}_n^{HO}, \tag{6.39}$$

$$\frac{\partial}{\partial t} nu_x^{LO} + \frac{\partial}{\partial x}\left[\left(nu^{LO}\right)^2/n^{LO} + P^{LO}\right] = \frac{\partial \gamma_{nu}^{HO}}{\partial x} + \mathcal{I}_{nu}^{HO}, \tag{6.40}$$

$$\frac{\partial}{\partial t} U^{LO} + \frac{\partial}{\partial x}\left[u^{LO}\left(U^{LO} + P^{LO}\right) + Q^{HO}\right] = \frac{\partial \gamma_U^{HO}}{\partial x} + \mathcal{I}_U^{HO}. \tag{6.41}$$

The two systems are coupled through the LO Maxwellian distribution function, f_M^{LO}, in the HO equation and the HO heat-flux, Q^{HO}, and consistency terms, γ_n^{HO}, γ_{nu}^{HO}, γ_U^{HO}, $\mathcal{I}_n^{HO}$, $\mathcal{I}_{nu}^{HO}$, and $\mathcal{I}_U^{HO}$ in the LO system. f_M^{LO} and τ^{LO} are evaluated using the LO variables only:

$$f_M^{LO} = \frac{n^{LO}}{\sqrt{2\pi T^{LO}/m}} \exp\left[-\frac{m}{2T^{LO}}\left(v - u^{LO}\right)^2\right], \tag{6.42}$$

$$\tau^{LO} = \frac{\widetilde{\tau}}{n^{LO}\sqrt{T^{LO}}}, \tag{6.43}$$

where u^{LO} and T^{LO} can be calculated in terms of the moments, n^{LO}, nu^{LO}, and U^{LO},

$$u^{LO} = \frac{nu^{LO}}{n^{LO}}, \tag{6.44}$$

$$T^{LO} = 2m\frac{U^{LO} - \frac{1}{2}(nu^{LO})^2/n^{LO}}{n^{LO}}. \tag{6.45}$$

The HO heat-flux, Q^{HO}, is evaluated from the HO solution as,

$$Q^{HO} = \left\langle \frac{\left(v - u^{HO}\right)^3}{2}, f \right\rangle_v . \tag{6.46}$$

The consistency terms, γ_n^{HO}, γ_{nu}^{HO}, γ_U^{HO}, $\mathcal{I}_n^{HO}$, $\mathcal{I}_{nu}^{HO}$, and $\mathcal{I}_U^{HO}$ are required to enslave the truncation error of the LO system to the HO system as in the neutron transport, thermal radiation transport, and the collisionless plasma physics applications [50, 51, 53, 75]. These terms vanish in the continuum, but remain finite in the discrete. The details of how to compute γ_n^{HO}, γ_{nu}^{HO}, γ_U^{HO}, $\mathcal{I}_n^{HO}$, $\mathcal{I}_{nu}^{HO}$, and $\mathcal{I}_U^{HO}$ will be discussed shortly.

6.4.1 HO Discretization

The HO system in discrete form is,

$$\frac{f_{i,j}^{k+1,z} - f_{i,j}^{k,z}}{\Delta t} + \frac{1}{2}\left[v_j \frac{\widehat{f}_{i+1/2,j}^{k+1,z} - \widehat{f}_{i-1/2,j}^{k+1,z}}{\Delta x} + v_j \frac{\widehat{f}_{i+1/2,j}^{k} - \widehat{f}_{i-1/2,j}^{k}}{\Delta x} \right] - \left[\theta_i^{HO,k} \frac{f_{M,i,j}^{LO,k+1,z-1} - f_{i,j}^{k+1,z}}{\tau_i^{LO,k+1,z-1}} + \left(1 - \theta_i^{HO,k}\right) \frac{f_{M,i,j}^{HO,k} - f_{i,j}^{k}}{\tau_i^{HO,k}} \right] = 0. \tag{6.47}$$

The superscript index, z, represents the HOLO iteration index. The discretization is based on a finite volume formulation where the hat represents numerical flux at cell faces. The equation is linearized for a given evaluation by lagging $f_{M,i,j}^{LO,k+1,z-1}$ and $\tau_i^{LO,k+1,z-1}$. The equation can be solved for $f_{i,j}^{k+1,z}$ at this point by inverting the linear system. The streaming operator is treated with Crank-Nicholson differencing while the collision operator is treated with an asymptotic preserving θ-scheme discretization, which is discussed in Appendix A.

6.4.2 LO Discretization

We use a finite-volume discretization in space and Crank-Nicholson in time for the LO system as well. The LO system in discrete form is,

$$\frac{n_i^{LO,k+1,z} - n_i^{HO,k}}{\Delta t} + \frac{1}{2}\left[\frac{\widehat{nu}_{i+1/2}^{LO,k+1,z} - \widehat{nu}_{i-1/2}^{LO,k+1,z}}{\Delta x} + \frac{\widehat{S}_{1_{i+1/2}}^{HO,k} - \widehat{S}_{1_{i-1/2}}^{HO,k}}{\Delta x}\right] = \frac{\widehat{\gamma}_{n_{i+1/2}}^{HO,z} - \widehat{\gamma}_{n_{i-1/2}}^{HO,z}}{\Delta x} + \mathcal{I}_{n_i}^{HO,z}, \tag{6.48}$$

$$\frac{nu_i^{LO,k+1,z} - nu_i^{HO,k}}{\Delta t} + \frac{1}{2}\left[\frac{\left(\widehat{nu}^2/\widehat{n} + \widehat{P}\right)_{i+1/2}^{LO,k+1,z} - \left(\widehat{nu}^2/\widehat{n} + \widehat{P}\right)_{i-1/2}^{LO,k+1,z}}{\Delta x} + \frac{\widehat{S}_{2_{i+1/2}}^{HO,k} - \widehat{S}_{2_{i-1/2}}^{HO,k}}{\Delta x}\right] = \frac{\widehat{\gamma}_{nu_{i+1/2}}^{HO,z} - \widehat{\gamma}_{nu_{i-1/2}}^{HO,z}}{\Delta x} + \mathcal{I}_{nu_i}^{HO,z}. \tag{6.49}$$

$$\frac{U_i^{LO,k+1,z} - U_i^{HO,k}}{\Delta t} + \frac{1}{2}\left[\frac{\widehat{u}_{i+1/2}^{LO,k+1,z}\left(\widehat{U} + \widehat{P}\right)_{i+1/2}^{LO,k+1,z} - \widehat{u}_{i-1/2}^{LO,k+1,z}\left(\widehat{U} + \widehat{P}\right)_{i-1/2}^{LO,k+1,z}}{\Delta x} + \frac{\widehat{S}_{3_{i+1/2}}^{HO,k} - \widehat{S}_{3_{i-1/2}}^{HO,k}}{\Delta x}\right] + \frac{\widehat{Q}_{i+1/2}^{HO,k+1,z} - \widehat{Q}_{i-1/2}^{HO,k+1,z}}{\Delta x} = \frac{\widehat{\gamma}_{U_{i+1/2}}^{HO,z} - \widehat{\gamma}_{U_{i-1/2}}^{HO,z}}{\Delta x} + \mathcal{I}_{U_i}^{HO,z} \tag{6.50}$$

Here, $\widehat{S}_{1,2,3}^{HO,k}$ are the discrete moments of the numerical flux of the streaming operator at the old time-step,

$$\widehat{S}_{1_{i+1/2}}^{HO,k} = \sum_{j=1}^{N_v} \Delta v \widehat{f}_{i+1/2,j}^{k}, \tag{6.51}$$

$$\widehat{S}^{HO,k}_{2_{i+1/2}} = \sum_{j=1}^{N_v} \Delta v v_j \widehat{f}^{k}_{i+1/2,j}, \tag{6.52}$$

$$\widehat{S}^{HO,k}_{3_{i+1/2}} = \frac{1}{2} \sum_{j=1}^{N_v} \Delta v v_j^2 \widehat{f}^{k}_{i+1/2,j}, \tag{6.53}$$

and $\widehat{Q}^{HO,k+1}_{i+1/2}$ is the heat-flux, interpolated at cell faces:

$$\widehat{Q}^{HO,k+1}_{i+1/2} = \frac{Q^{HO,k+1}_{i+1} + Q^{HO,k+1}_{i}}{2}, \tag{6.54}$$

$$Q^{HO,k+1}_{i} = \frac{1}{2} \sum_{j=1}^{N_v} \Delta v \left(v_j - u^{HO,k+1}_{i} \right)^3 f^{k+1}_{i,j}. \tag{6.55}$$

Here, N_v is the number of velocity space cells. We use HO quantities for the old time terms since the LO system is only an accelerator to the solution of f^{k+1}. Thus the LO solution does not evolve over time-steps. A similar procedure can be seen in the HOLO algorithm applied to collisionless plasma physics [75]. Unlike the HO system, the LO system is nonlinear, and is solved using a Jacobian-Free Newton-Krylov (JFNK) method [62] for the conserved quantities, $(n, nu, U)^{LO,k+1}$. The cost of the LO solver is typically negligible as compared to the cost of the HO system solver.

6.4.3 Discrete Consistency Terms

As previously mentioned, we introduce discrete consistency terms, γ^{HO}_n, γ^{HO}_{nu}, γ^{HO}_U, $\mathcal{I}^{HO}_n$, $\mathcal{I}^{HO}_{nu}$, and $\mathcal{I}^{HO}_U$ in the LO system in order to enslave the truncation error of the LO system to the HO system. In the application of gas dynamics with the BGK operator, the computation of the consistency terms differ from other applications [51, 53, 75] to some degree. For this reason, we explicitly define the expression for γ^{HO}_n, γ^{HO}_{nu}, γ^{HO}_U, $\mathcal{I}^{HO}_n$, $\mathcal{I}^{HO}_{nu}$, and $\mathcal{I}^{HO}_U$. The γ

consistency terms are needed to enslave the interpolation error for the LO numerical flux at the cell face to the *discrete* moments of the HO numerical flux. The γ consistency terms are calculated as follows:

$$\gamma^{HO,z}_{n,i+1/2} = -\sum_j \Delta v v_j \widehat{f}^{k+1,z}_{i+1/2,j} + \widehat{nu}^{HO,k+1,z}_{i+1/2}, \tag{6.56}$$

$$\gamma^{HO,z}_{nu,i+1/2} = -\sum_j \Delta v v_j^2 \widehat{f}^{k+1,z}_{i+1/2,j} + \left[\widehat{nu}^2/\widehat{n} + \widehat{P}\right]^{HO,k+1,z}_{i+1/2}, \tag{6.57}$$

$$\gamma^{HO,z}_{U,i+1/2} = -\sum_j \Delta v \frac{v_j^3}{2} \widehat{f}^{k+1,z}_{i+1/2} + \left[\widehat{u}\left(\widehat{U} + \widehat{P}\right) + \widehat{Q}\right]^{HO,k+1,z}_{i+1/2,j}. \tag{6.58}$$

Here, the HO quantities with a hat are evaluated using the same exact discretization as the LO quantities. For clarity, if one utilizes a standard central differencing operator for estimating the numerical flux for $\widehat{nu}^{LO,k+1,z}_{i+1/2}$ using uniform cells,

$$\widehat{nu}^{LO,k+1,z}_{i+1/2} = \frac{1}{2}\left(nu^{LO,k+1,z}_{i+1} + nu^{LO,k+1,z}_{i}\right), \tag{6.59}$$

then $\gamma^{HO,z}_{n,i+1/2}$ will be calculated accordingly,

$$\gamma^{HO,z}_{n,i+1/2} = -\sum_j \Delta v v_j \widehat{f}^{k+1,z}_{i+1/2,j} + \frac{1}{2}\left(nu^{HO,k+1,z}_{i+1} + nu^{HO,k+1,z}_{i}\right), \tag{6.60}$$

and similarly for γ^{HO}_{nu} and γ^{HO}_{U}.

In the *discrete*, moments of the collision operator are not invariants and do not evaluate to zero. In order for the *discrete* LO moment equations to enforce the collision operator invariance in equations (6.19) to (6.21), the $\mathcal{I}$ consistency terms are needed. The $\mathcal{I}$ consistency terms are calculated as:

$$\mathcal{I}^{HO,z}_{n_i} = \frac{\theta^{HO,k}_i}{\tau^{HO,k+1,z}_i}\sum_j \Delta v \left(f^{HO,k+1,z}_{M,i,j} - f^{k+1,z}_{i,j}\right) + \frac{1-\theta^{HO,k}_i}{\tau^{HO,k}_i}\sum_j \Delta v \left(f^{HO,k}_{M,i,j} - f^{k}_{i,j}\right) \tag{6.61}$$

$$\mathcal{I}_{nu_i}^{HO,z} = \frac{\theta_i^{HO,k}}{\tau_i^{HO,k+1,z}} \sum_j \Delta v v_j \left(f_{M,i,j}^{HO,k+1,z} - f_{i,j}^{k+1,z} \right) + \frac{1-\theta_i^{HO,k}}{\tau_i^{HO,k}} \sum_j \Delta v v_j \left(f_{M,i,j}^{HO,k} - f_{i,j}^{k} \right) \quad (6.62)$$

$$\mathcal{I}_{U,i}^{HO,z} = \frac{\theta_i^{HO,k}}{\tau_i^{HO,k+1,z}} \sum_j \Delta v \frac{v_j^2}{2} \left(f_{M,i,j}^{HO,k+1,z} - f_{i,j}^{k+1,z} \right) + \frac{1-\theta_i^{HO,k}}{\tau_i^{HO,k}} \sum_j \Delta v \frac{v_j^2}{2} \left(f_{M,i,j}^{HO,k} - f_{i,j}^{k} \right) \quad (6.63)$$

Therefore, in the discrete, the collision operator acts as a finite (but discrete) source to the LO system. As before, $\mathcal{I}_i^{HO} \to 0$ as $\Delta v \to 0$ and $|v_{min,max}| \to \infty$.

6.4.4 HOLO Algorithm

To measure the convergence between the HO and LO systems, we use the L_2-norm of the relative difference between the HO and LO moments,

$$\text{rel-diff}_{\mathcal{M}}^{k+1,HOLO} = \left| \frac{\mathcal{M}^{HO,k+1} - \mathcal{M}^{LO,k+1}}{\mathcal{M}^{HO,k+1}} \right|_2 . \quad (6.64)$$

Alternatively, we could have chosen the L_2-norm of the residual of the HO system as the criterion for convergence. However, we keep equation (6.64) for consistency with the convergence criterion of the Picard (source) iteration approach (section 2).

For each time step, the modified implicit *nonlinearly* accelerated iteration scheme proceeds as follows:

Algorithm 8: Nonlinear implicit moment accelerated iteration for the BGK collision operator.

Set $z = 0$;
while *HOLO system not converged* **do**
  Solve LO system for $(n, nu, U)^{LO,k+1,z}$ from equations (6.48), (6.49), and (6.50), using $Q^{HO,k+1}$ defined from the HO solution ;
  Compute $(u, T)^{LO,k+1}$ from $(n, nu, U)^{LO,k+1,z}$ from equations (6.44) and (6.45);
  Compute $f_M^{LO,k+1,z}$ and τ^{LO} from equation (6.42) and (6.43);
  Increment $z = z + 1$;
  Solve HO system for $f^{k+1,z}$ from equation (6.47) using $f_M^{LO,k+1}$ and $\tau^{LO,k+1}$ defined by the LO solution;
  Compute $Q^{HO,k+1}$ from equation (6.46);
  Compute $\gamma^{HO,z}$ and $\mathcal{I}^{HO,z}$ from equations (6.56) to (6.63) ;
  Check convergence between HO and LO system via equation (6.64);
end

The difference with respect to the standard Picard (source) iteration scheme is in the additional steps of solving the moment equations, evaluating the HO heat-flux, and computing the consistency terms. Again, recall that the LO system is only used to accelerate the HO system. It is key to note that upon convergence, we have obtained the solution to the HO problem (equation (6.47)). However, we have obtained this solution to the HO system in a much more efficient manner (i.e., for fewer transport sweeps).

6.5 Results

We discuss the performance of the new HOLO algorithm applied to 1) a Sod shock tube problem [76] and 2) a strong shock problem with widely varying collision time-scale.

6.5.1 Sod shock tube

In this section, we will compare the performance of the accelerated algorithm with the standard Picard (source) iteration algorithm for a well known Sod shock tube problem for different values of the collision time-scale, τ. We test the algorithm for a constant τ everywhere in the domain. Consider the following initial condition for the Sod shock tube,

- $n_L = 1.0$, $n_R = 0.125$,
- $T_L = 1.0$, $T_R = 0.8$,
- $u_L = 0.0$, $u_R = 0.0$,

where the subscripts L and R denote the values of the flow variable immediately to the left and right of the diaphragm. The kinetic initial condition is assumed to be a Maxwellian, based on the moment values to the left and right side of the diaphragm,

$$f_0 = f\left(x, v, t = 0\right) = \frac{n_0}{\sqrt{2\pi T_0/m}} \exp\left[-\frac{m}{2T_0}\left(v - u_0\right)^2\right].$$

We have tested the algorithm for a gas molecule of mass $m = 1$, a system domain of $L \in [0, 1]$, a spatial grid count of $N = 500$, a velocity space domain of $v \in [-10v_{th_L}, 10v_{th_L}]$, a velocity space grid count of $N_v = 200$, and a simulation time of $t \in [0, 0.065]$. Here, v_{th_L} is the initial thermal velocity of the gas on the LHS of the diaphragm and is defined as,

$$v_{th_L} = \sqrt{\frac{2T_L}{m}}.$$

Standard Transport Discretization

We have used a linear discontinuous Galerkin discretization (LDG)[77] for the streaming operator in equation (6.47) for this test case. A discussion on the extension of the moment

$\Delta t/\tau$	10^{-2}	10^{-1}	10^{0}	10^{1}	10^{2}	10^{3}	10^{4}	10^{5}
Iteration$_{acc}$	4	6	8	9	9	9	9	9
Iteration$_{standard}$	5	13	68	461	2853	>10000	>10000	>10000

Table 6.1: Performance comparison of moment acceleration scheme versus the standard scheme

acceleration algorithm in the context of discontinuous finite elements has not been provided. In short, the LO system will be comprised of the continuity, momentum, and energy equations for the 0^{th} and 1^{st} basis coefficients, in which we use to accelerate the HO BBGK equation.

We first present the convergence acceleration profile of the solver, compared to the standard Picard solver. A convergence tolerance for each time-step was set to 10^{-6} for both the HOLO algorithm and Picard solver using equations (6.64) and (6.18), respectively.

Eight cases of the Sod shock tube were run with a fixed time-step size, $\Delta t = 5 \times 10^{-4}$, and varying collision time-scale, τ, of 5×10^{-2}, 5×10^{-3}, 5×10^{-4}, 5×10^{-5}, 5×10^{-6}, 5×10^{-7}, 5×10^{-8}, 5×10^{-9}. The motives to consider these eight cases are two fold: 1) to demonstrate the performance of the standard linearized Picard iteration scheme as a function of $\frac{\Delta t}{\tau}$ and how it compares to the moment accelerated scheme, and 2) to demonstrate how the moment accelerated scheme can be used to follow the acoustic wave CFL time-scale rather than the collision time-scale.

The performance of the algorithm is shown in Table 6.1 for the eight cases. The first and second row presents the number of transport sweeps required for the moment acceleration algorithm and the standard algorithm, respectively. For a small $\frac{\Delta t}{\tau}$, the collision time scale is resolved and the performance between the two methods is not drastically different. However, as the ratio $\frac{\Delta t}{\tau}$ increases, the standard scheme requires more iterations in order to converge the BBGK equation. The acceleration scheme also shows a similar trend. However, the increase in the iteration is much slower and plateaus. For the $\Delta t/\tau = 10^2$ case, the moment acceleration algorithm shows a reduction in the number of transport sweeps of more than

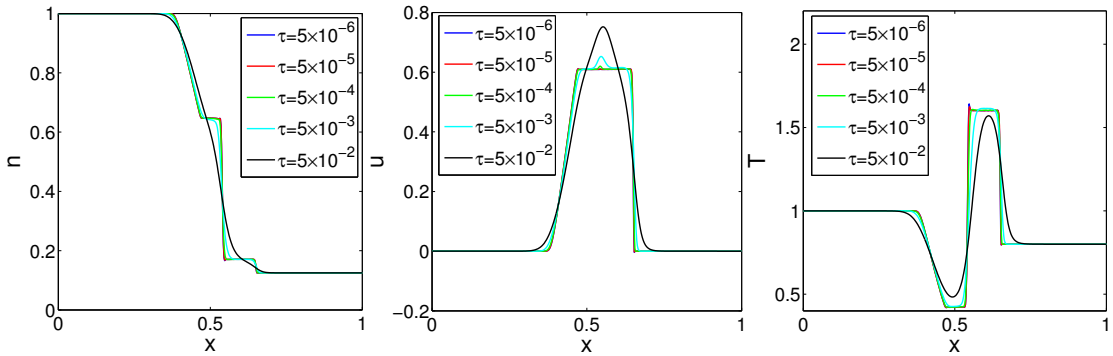


Figure 6.1: Comparison of moments with respect to varying τ at $t = 0.065$

two orders of magnitude.

In order to highlight the time-scale that the moment acceleration scheme allows one to follow, we compare the Δt size with respect to the acoustic wave CFL for the $\tau = 5 \times 10^{-6}$ case. The maximum speed of sound during the entire duration of the simulation was approximately, $c = 2.3$. The acoustic wave CFL is defined as:

$$\Delta t_{A-CFL} = \frac{\Delta x}{c}, \tag{6.65}$$

With a uniform mesh of $\Delta x = 2 \times 10^{-3}$, this equates to a $\Delta t_{A-CFL} = 8.7 \times 10^{-4}$. Thus the implicit time-step size is $\Delta t = 0.3 \Delta t_{A-CFL}$. If one used a standard Picard iteration, one would choose to run at $\Delta t = \tau = 5 \times 10^{-6} = 2.8 \times 10^{-3} \Delta t_{A-CFL}$ for computational efficiency reasons, as can be seen in Table 6.1. This is almost two orders of magnitude smaller than the time-step size that we have used.

Plots of n, u, and T for the $\tau = 5 \times 10^{-2}$, 5×10^{-3}, 5×10^{-4}, 5×10^{-5}, and 5×10^{-6} cases at $t = 0.065$ are shown in Figure 6.1. As τ decreases, the distribution function relaxes to a local Maxwellian more rapidly. In this case, transport effects are minimized and the physical dissipation from the heat-flux, Q, is reduced. The decrease in the dissipation physically makes the system approach the Euler equations. Without any form of additional numerical dissipation via artificial viscosity [79, 83] or flux limiting [77], numerical oscillations can

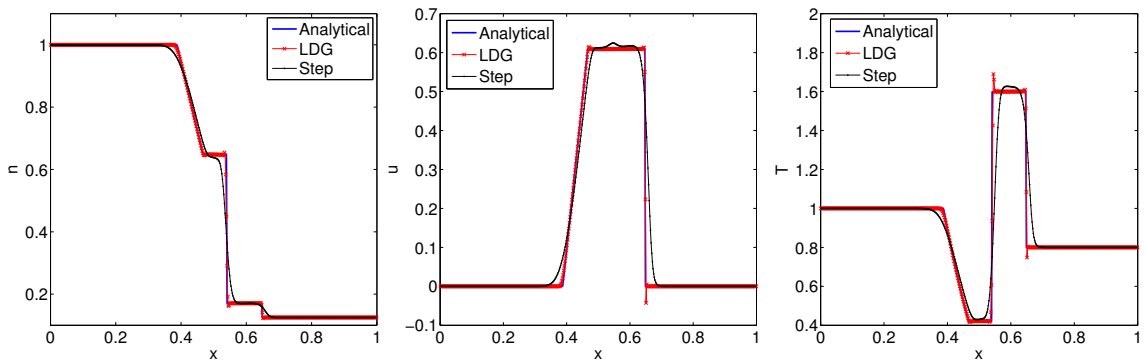


Figure 6.2: Comparison of solutions to Sod shock tube with different discretization for the Euler limit.

occur near the shock front as can be seen clearly for the $\tau < 10^{-4}$ cases. One can dissipate these oscillatory modes by using a first-order discretization such as step differencing [82] of the streaming operator in the HO system. Here, we remind the reader that the algorithm converges to the HO solution, and therefore, the source of the oscillatory modes is not the discretization of the advection terms in the LO system, but rather due to the discretization of the streaming operator in the HO system.

We compare the solution to the Sod shock tube problem using an LDG discretization and step differencing against an analytical Riemann solver solution [80]. For a $\tau = 5 \times 10^{-6}$, the mean-free-path, λ_{mfp}, which is defined as:

$$\lambda_{mfp} = \tau \sqrt{\frac{T}{m}}, \tag{6.66}$$

is approximately 5×10^{-6}. For a $\Delta x = L/N = 2 \times 10^{-3} \gg \lambda_{mfp}$, the solution to the BBGK equation is well approximated by the Euler limit, and the Riemann solver can be used as an analytical benchmark. Refer to Figure 6.2. As seen in Figure 6.2, the step differencing method does not show oscillatory structures near the shock front. However, the discretization is overly dissipative and becomes an accuracy concern. The oscillatory structures are not a major concern for the Sod shock tube, where the discontinuity is not strong. Eventually,

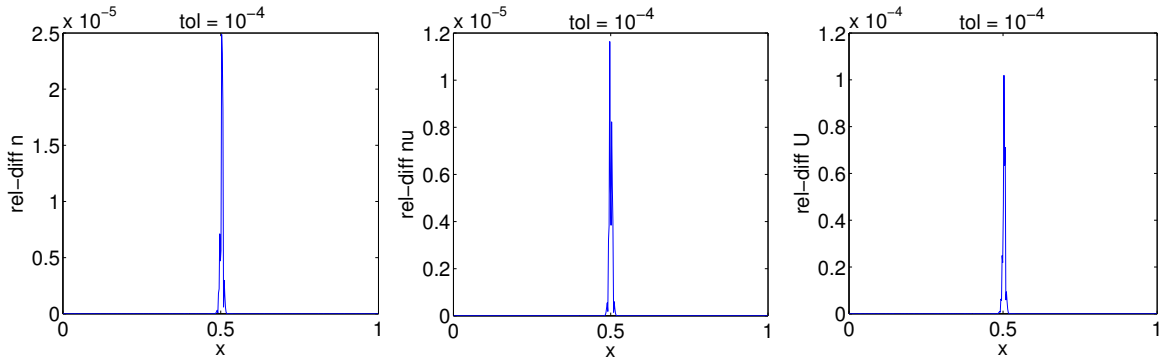


Figure 6.3: Relative difference of n, nu, and U with tolerance $= 10^{-4}$, with discrete consistency enforced.

as one integrates the problem long enough in time, both finite numerical dissipation and physical dissipation will damp out these oscillations. However, for strong shocks expected in transitioning flows where the discontinuity is much stronger, the solution near the oscillatory structure may become negative. In particular, negative density and temperature is a concern as the Maxwellian distribution requires positivity in these quantities for the operator to remain physical.

We have shown the acceleration performance of the solver, relative to the standard iterative scheme. In order to call the solver a true accelerator, however, the solution obtained must be exactly equivalent to the non-accelerated solver. We show that the solution obtained through the accelerator is indeed exactly equivalent down to the nonlinear convergence tolerance set per time-step. In Figure 6.3 and 6.4, we show the relative difference of the moment quantities, n, nu, and U, between the HOLO algorithm and the standard Picard iteration,

$$\text{rel-diff}_{\mathcal{M}}^{SI-HOLO} = \left| \frac{\mathcal{M}^{SI} - \mathcal{M}^{HOLO}}{\mathcal{M}^{SI}} \right|, \tag{6.67}$$

with and without the discrete consistency terms. We choose a time-step-size $\Delta t = 10^{-4}$ and $\tau = 10^{-4}$ with convergence tolerances of tol $= 10^{-4}$ and 10^{-8}. We show the differences in the solution after ten time-steps for their tolerances. As we expect, with the discrete consistency terms the differences between the two solutions are comparable and proportional

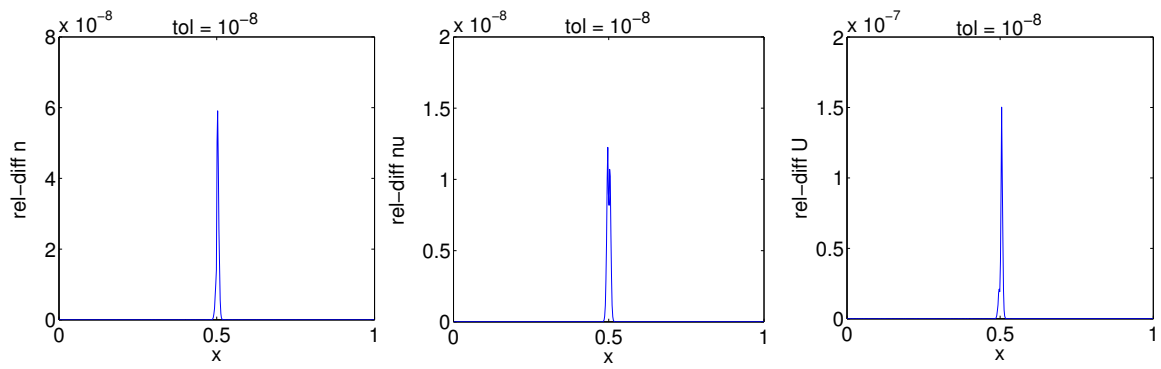


Figure 6.4: Relative difference of n, nu, and U with tolerance = 10^{-8}, with discrete consistency enforced.

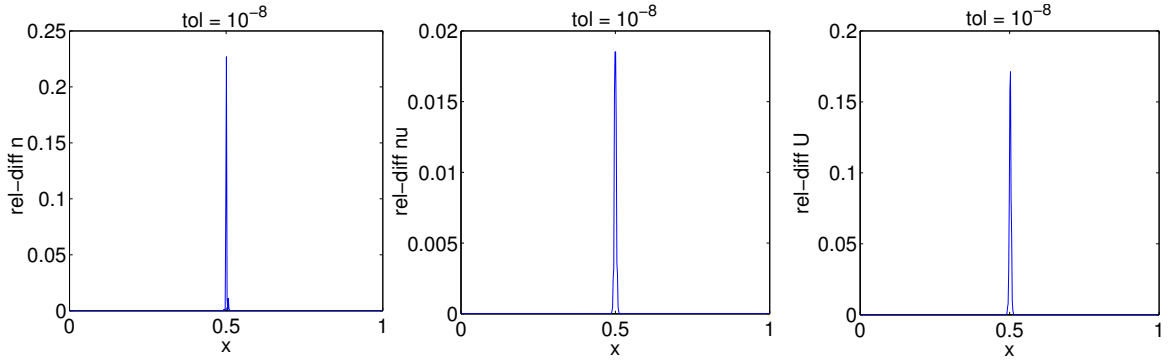


Figure 6.5: Relative difference of n, nu, and U with tolerance = 10^{-8}, without discrete consistency enforced.

to the convergence tolerance of the HOLO solver. However, if we do not enforce consistency, the HO and LO moments do not converge irrespective of the convergence tolerance (Figure 6.5). Note that without discrete consistency, the HOLO convergence criterion in equation (6.64) cannot be used and instead we used the Picard convergence criterion,

$$\text{rel-diff}_{\mathcal{M}} = \left| \frac{\mathcal{M}^{HO,k+1,z} - \mathcal{M}^{HO,k+1,z-1}}{\mathcal{M}^{HO,k+1,z}} \right|_2 . \tag{6.68}$$

High-Order Monotone Transport Discretization

In order to address the issue of lack of positivity in the solution, a nonlinear high resolution discretization with flux-limiting has been implemented for the streaming operator in the HO problem. We have used a WENO5 scheme [81] with an ULTRA-SHARP flux limiter [91]. Since the discretization is now nonlinear, we cannot use a standard transport sweep to invert the BBGK operator. To invert the new nonlinear system, we utilize a preconditioned JFNK solver for the HO system. We formulate a nonlinear residual,

$$\mathcal{R} = f_{i,j}^{k+1} - f_{i,j}^{k} + \Delta t v_j \frac{\widehat{f}_{i+1/2,j}^{k+1/2} - \widehat{f}_{i-1/2,j}^{k+1/2}}{\Delta x} - \Delta t \left\{ \theta_i^{HO,k} \frac{f_{M_{i,j}}^{LO,k+1} - f_{i,j}^{k+1}}{\tau_i^{LO,k+1}} + \left(1 - \theta_i^{HO,k}\right) \frac{f_{M_{i,j}}^{HO,k} - f_{i,j}^{k}}{\tau_i^{HO,k}} \right\} = 0, \tag{6.69}$$

for the distribution function, $f_{i,j}^{k+1}$. Note that the WENO5 scheme by itself is not positivity preserving and an extra flux-limiter is necessary for a very strong shock. For preconditioning, a step-differenced transport sweep was used,

$$\mathcal{P} = 1 + \Delta t v \frac{\partial}{\partial x} + \theta^{HO,k} \frac{\Delta t}{\tau^{LO,k+1}}. \tag{6.70}$$

We test the combined algorithm of moment acceleration and implicit WENO5+ULTRA-SHARP HO solver on the Sod shock tube problem, and demonstrate the better positivity and monotonicity preserving nature of the overall algorithm. Recall that LDG without implicit WENO5+ULTRA-SHARP encountered oscillatory structures near the shock front, and we used a first-order discretization in order to damp these structures. However, a first-order discretization is overly dissipative for shock problems. In Figure 6.6, we compare the solution to the Sod shock tube problem obtained by the WENO5+ULTRA-SHARP and a step differencing scheme. As we expect, with the use of a high resolution discretization with a limiter the spurious modes are damped and a sharper shock front is preserved.

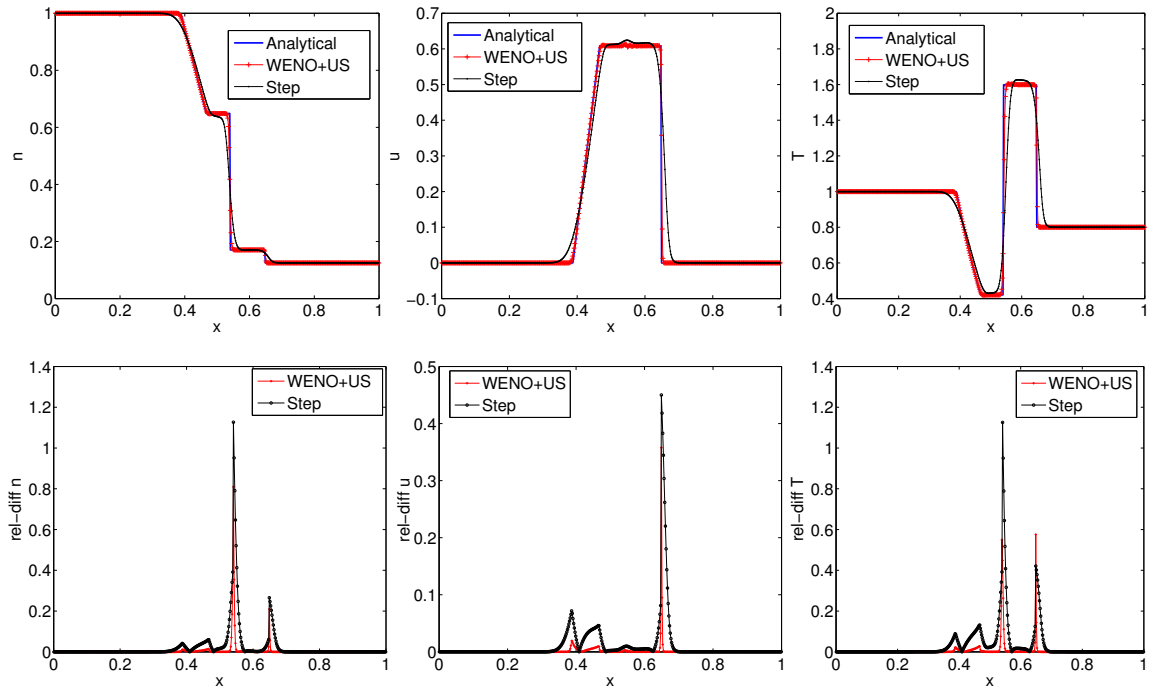


Figure 6.6: Comparison of Sod shock tube solution with implicit WENO5+ULTRA-SHARP and step differenceing (top) and the relative difference between the analytical solution (bottom).

6.5.2 Strong Shock tube with Variable τ

Finally, we perform a simulation for a strong shock tube problem with a solution-dependent collision time-scale. For the strong shock problem, we use the WENO5+ULTRA-SHARP discretization for the streaming operator in the HO system. The high-resolution, positivity-preserving discretization is critical for the strong shock problem as the gradient is much stronger than the Sod problem.

In this example, we show the true multi-scale nature of the BBGK equation for problems with a transition layer and a realistically varying collision time-scale, where a wide separation in Knudsen number [74] exists throughout the domain. The Knudsen number is the ratio between the mean-free-path of particles and the gradient scale-length of the evolving solution.

In this study, we define the Knudsen number as,

$$K_n = \frac{\lambda_{mfp}}{L_T}, \tag{6.71}$$

where,

$$L_T = \left|\left|\left(\frac{1}{T}\frac{\partial T}{\partial x}\right)^{-1}\right|\right|. \tag{6.72}$$

For a variable collision time-scale, we have a varying mean-free-path throughout the domain. For a strong shock, the difference in mean-free-path across the domain may be orders of magnitude. This allows for a large separation in length-scales within the shock layer. For the Navier-Stokes solvers to give an accurate solution, the mean-free-path, λ_{mfp}, must be much smaller than the gradient scale-length, L_T. If λ_{mfp} is larger than L_T, long mean-free-path effects will be introduced, which cannot be captured accurately with the analytical closures used for the Navier-Stokes model. From an algorithmic point of view, the standard iteration scheme for the HO solver will incur many HO evaluations when $\Delta t/\tau_{min} \gg 1$, with τ_{min} the smallest τ in the shock layer. This is exactly the regime where our new algorithm will produce an accurate solution, efficiently.

For the strong shock problem, the system domain length of $L = [0, 9]$ is chosen with a simulation time of $t = [0, 1]$. The following initial conditions are used,

- $n_L = 1.0$, $n_R = 10^{-3}$,
- $P_L = 0.1$, $P_R = 10^{-6}$,
- $u_L = 0$, $u_R = 0$.

A configuration space cell count of $N = 500$, with a velocity domain of $v_{max} = 10v_{th,L}$ and $v_{min} = -10v_{th,L}$, and a velocity space cell count of $N_v = 2000$ is used. We test the shock

$\Delta t/\tau$	5×10^0	1.25×10^1	5×10^1	5×10^2
Iteration_{acc}	4	4	4	10
$\text{Iteration}_{standard}$	51	108	402	>1000

Table 6.2: Performance comparison of moment acceleration scheme versus the standard scheme for a strong shock problem

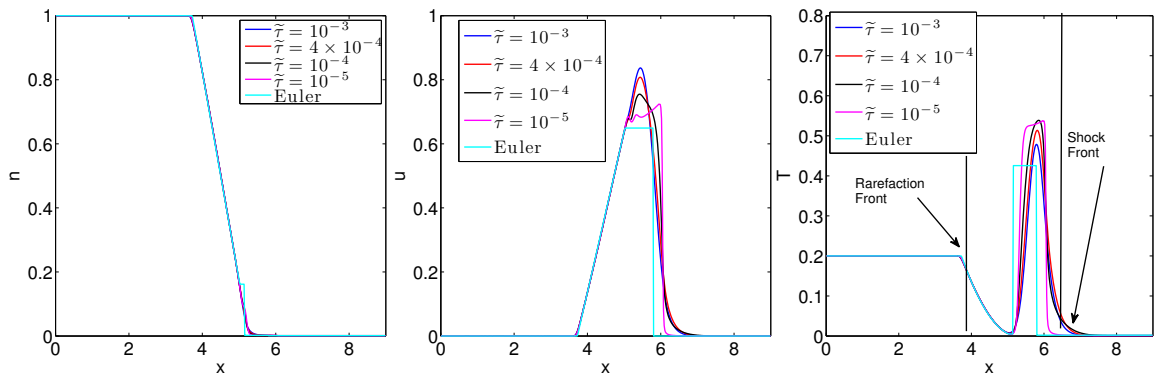


Figure 6.7: Comparison of strong shock tube solution with variable τ at $t = 1$.

tube problem with τ defined by equation (6.3), and $\widetilde{\tau} = 10^{-3}$, 10^{-4}, 4×10^{-4}, and 10^{-5}. In Table 6.2, the performance of the HOLO moment acceleration scheme and the standard Picard (source) iteration is compared. As can be seen, the moment acceleration method requires significantly fewer evaluations of the HO system. Next, we compare the solution structure between the different $\widetilde{\tau}$ at $t = 1$. Refer to Figure 6.7. As can be seen, we encounter high density and (relatively) high temperature near the region of contact discontinuity at the rarefaction front. There, the solution structure does not differ significantly for the different collisional regimes. On the other hand, near the contact discontinuity on the shock front, the gas is rarefied and the temperature is low. Therefore, τ is large, leading to a long λ_{mfp}, which accounts for the dissipated physical structure. We show in Figure 6.8 the τ and λ_{mfp} in log-scale for the 4 cases. For all cases, with a variable τ, we see a separation of about four orders of magnitude in τ and three orders of magnitude in λ_{mfp}. For this set of simulations, the standard iterative solver will struggle for $10^{-5} \leq \widetilde{\tau} \leq 10^{-4}$, for which $\tau \ll \Delta t$. The solution to the Euler equations will break down for $\widetilde{\tau} \geq 10^{-4}$ since the cell size

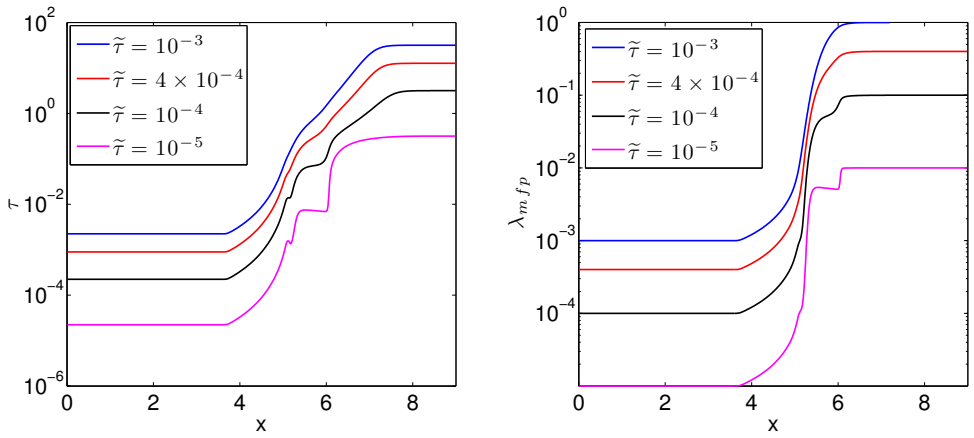


Figure 6.8: Comparison of τ and λ_{mfp} for different $\widetilde{\tau}$ for a strong shock tube at $t = 1$.

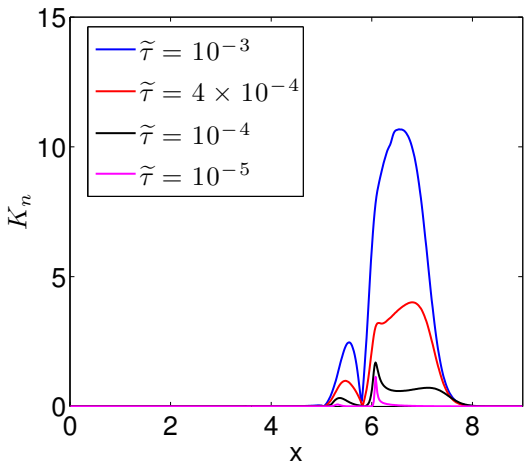


Figure 6.9: K_n throughout the domain at $t = 1$.

($\Delta x = 0.018$) is beginning to resolve λ_{mfp} on the shock front and the Euler/Navier-Stokes solvers cannot capture the correct dissipative effects at these length-scales. This can also be seen by investigating the local K_n throughout the domain in Figure 6.9. As can be seen, even for $\widetilde{\tau} = 10^{-5}$, $K_n \approx \mathcal{O}(1)$ near the shock front. For the hydrodynamic models to be accurate, $K_n \ll 1$. Here, we emphasize that the difference in the solution obtained by the HOLO method and the Euler equation should not be interpreted as a failure in the HOLO method. The dissipative structure in the solution obtained by the HOLO method is due

to kinetic (long mean-free-path) effects which the Euler equations cannot capture. For this reason, for a strong shock, the Euler and Navier-Stokes limit may not be the correct physical model to use and a kinetic solver is required. The new HOLO moment acceleration algorithm is specifically designed for these transition flow regimes.

6.6 Conclusion

In this study, we have developed a moment-based accelerator for a neutral gas dynamics Boltzmann transport equation with a BGK collision operator. The method developed here is an extension of the original work developed for neutron transport applications to the neutral gas dynamics application. We have shown that the standard Picard (source) iteration scheme becomes impractical as $\frac{\Delta t}{\tau} \gg 1$. We have also shown that, for the same $\frac{\Delta t}{\tau}$, the moment acceleration scheme can provide orders of magnitude speed up over the standard scheme.

This study has shown the proof of principle of the moment-based acceleration applied to kinetic gas kinetics problem with both constant and spatially varying collision time-scales. The problems that are of particular interest are situations where a transition region exists with highly collisional and rarified regions. Such configurations cannot be modeled using a standard fluid approach, as the validity of the closure becomes an issue near the transition region. Algorithmically, the standard Picard iteration approach for the HO equation is ineffective due to slow convergence associated with the method when $\Delta t/\tau \gg 1$, as demonstrated. The method we have developed in this study allows one to obtain a converged kinetic solution per time-step with a much more reasonable computational effort compared to the standard approaches. More importantly, the *accelerator* we have developed does not make any further approximations to the kinetic model past the numerical discretization, and upon nonlinear convergence, it is equivalent to the solution obtained by the standard Picard iteration scheme.

In this study, we have investigated a shock tube problem, where the dynamical time-scale

is the acoustic-wave CFL. For a non-shock problem, the dynamical time-scale may be longer, e.g., diffusion time-scales, or other slower processes. Such situations may require larger time steps for efficiency. However, to exploit these regimes a more sophisticated preconditioner will be needed for the LO system. This will be the subject of future work.

Chapter 7

Moment Acceleration of a Collisional Plasma

In this chapter, we develop a charge and energy conserving HOLO moment-based acceleration algorithm for the multi-species, electrostatic, collisional plasma, modeled by a Vlasov-Fokker-Planck-Ampère system. We develop the new algorithm by combining the previously developed techniques of: 1) accelerating the convergence of the collisionless electrostatic Vlasov-Ampère system (chapter 4), 2) enforcing discrete conservation properties via nonlinear discretization for the Vlasov-Ampère system (chapter 5), and 3) accelerating the convergence of the collisional neutral gas kinetics problem (chapter 6). The new algorithm will allow one to step over not only the inverse electron plasma frequency, $\omega_{p,e}^{-1}$, but also the electron-electron collision time-scale, τ_{ee}. We apply the newly developed algorithm to three problems: 1) a 0D1V two-species thermalization problem, 2) a 1D1V collisional ion acoustic wave problem, and 3) a 1D1V strong density gradient problem. The three problems will be used to demonstrate that the algorithm can be used to step over the stiff electron time-scales while still preserving strong conservation properties in charge, and energy.

7.1 Introduction

The dynamic evolution of coupled electromagnetic fields and collisional plasmas is described by the Vlasov-Fokker-Planck-Maxwell system. The Maxwell equations evolve electromagnetic fields based on moments of the ion-electron distribution functions (charge and current densities). The evolution of the distribution function for each species is governed by the Vlasov-Fokker-Planck (VFP) equation, which is coupled to the Maxwell system through electromagnetic forces. In this study, we will focus on an Eulerian approach which the VFP partial-differential equation is solved on a grid.

In the past, the Fokker-Planck equation has been used to model collisional dense plasmas for inertial-confinement-fusion conditions (ICF) [95, 96, 97, 98, 99, 100, 101]. In our work, we are motivated to consider implicit methods with strong conservation properties. A pioneering implicit study was carried out in reference [106], where a fully implicit total mass and energy conserving discretization of the Fokker-Planck operator in one velocity dimension (1V) was developed. In references [107, 108], a 1D2V, fully implicit, mass and energy conserving solver was developed for the bounce averaged Fokker-Planck equation. A fully implicit, one dimension in space and one dimension in velocity space (1D1V), reduced Vlasov-Fokker-Planck-Quasi-Neutral-Field solver was developed in reference [110]. In the study by reference [110], the collision operator was modeled using a reduced Fokker-Planck operator [103, 104] while solving for the field using a quasi-neutral field approximation. However, the method lacked discrete charge and energy conservation properties. Later, a fully implicit Vlasov-Maxwell solver was developed in [112], where the electrons were treated kinetically using a Cartesian tensor expansion [113] and ions were modeled as a cold fluid. For a more thorough recent review of numerical modeling of the Vlasov-Fokker-Planck system, the reader is referred to reference [102].

None of the above studies address the critical charge and energy conservation properties for a fully kinetic electron and ion description, with an electric field driven by self-consistent

charge separation. In a companion paper to this study [94], a moment-based convergence acceleration method was developed for an electrostatic 1D1V Vlasov-Ampère system. In references [94, 75], a coupled system of low-order (LO) moment-field equations was used to accelerate the convergence of the high-order (HO) kinetic equations. The HO system provided the LO system with a self-consistent closure at the stress-tensor level, while the LO system returned to the HO system the electric field, E. The method allowed one to step over the stiff inverse electron plasma frequency time-scale while efficiently converging the nonlinearly coupled HO and LO system. In this study, we extend the moment-based convergence acceleration method in chapter 5 to a coupled, electrostatic, 1D1V, reduced Vlasov-Fokker-Planck-Ampère (VFPA) system. In this study, the VFP equation will be referred to as the HO system and the moment-Ampère system will be referred to as the LO system. In the VFPA application, the HO system will provide the LO system with a self-consistent closure at the heat-flux level, while the LO system provides to the HO system with the collision frequency, collisional velocity space diffusion coefficient, the drag coefficients (both for the reduced Fokker-Planck operator), and the electric field. The method allows one to step over the inverse electron plasma frequency, and electron collision time-scales.

The remainder of the chapter is organized as follows. In section 2, the coupled set of HO Vlasov-Fokker-Planck equation and the LO moment-Ampère system is presented. Relevant time and length-scales associated with the coupled set of equations are discussed. In section 3, the discrete HOLO moment acceleration algorithm is discussed. In section 4, we present a series of numerical tests to quantify the performance of the new HOLO algorithm for the VFPA system, and we conclude in section 5.

7.2 Governing Equations

We consider a 1D1V treatment of phase-space with a reduced Fokker-Planck collision operator. In this section, the governing set of equations for the coupled Vlasov-Fokker-Planck-

Ampère system and the set of self-consistent fluid moment equations of the Vlasov-Fokker-Planck equation are defined.

7.2.1 Vlasov-Fokker-Planck Equation (HO System)

The Vlasov-Boltzmann equation for species α is:

$$\frac{\partial f_\alpha}{\partial t} + \vec{v} \cdot \nabla f_\alpha + \frac{q_\alpha}{m_\alpha}\left(\vec{E} + \vec{v} \times \vec{B}\right) \cdot \nabla_v f_\alpha - \left(\frac{\partial f_\alpha}{\partial t}\right)_c = 0. \tag{7.1}$$

Here, $f_\alpha = f_\alpha(\vec{r}, \vec{v}, t)$ is the distribution function of the plasma species α and is a function of space, $\vec{r}$, velocity, $\vec{v}$, and time, t; q_α and m_α are the charge and mass of species α; $\vec{E} = \vec{E}(\vec{r}, t)$ is the electric field, $\vec{B} = \vec{B}(\vec{r}, t)$ is the magnetic field, and $\left(\frac{\partial f_\alpha}{\partial t}\right)_c$ is the generalized Boltzmann collision integral. We focus on a multi-species, 1D1V, electrostatic system with the collision integral approximated by a reduced Fokker-Planck operator [103, 104, 110]. The Vlasov equation for species α is given as:

$$\frac{\partial f_\alpha}{\partial t} + v\frac{\partial f_\alpha}{\partial x} + \frac{q_\alpha}{m_\alpha}E\frac{\partial f_\alpha}{\partial v} = 0, \tag{7.2}$$

and the reduced Fokker-Planck operator as:

$$\left(\frac{\partial f_\alpha}{\partial t}\right)_c = \sum_\beta^{N_s} \nu_{\alpha\beta}\left\{D_{\alpha\beta}\frac{\partial^2 f_\alpha}{\partial v^2} + \frac{\partial}{\partial v}\left[(v - u_\beta) f_\alpha\right]\right\}. \tag{7.3}$$

Together, they define the Vlasov-Fokker-Planck equation:

$$VFP_\alpha = \frac{\partial f_\alpha}{\partial t} + v\frac{\partial f_\alpha}{\partial x} + \frac{q_\alpha}{m_\alpha}E\frac{\partial f_\alpha}{\partial v} - \sum_\beta^{N_s} \nu_{\alpha\beta}\left\{D_{\alpha\beta}\frac{\partial^2 f_\alpha}{\partial v^2} + \frac{\partial}{\partial v}\left[(v - u_\beta) f_\alpha\right]\right\} = 0. \tag{7.4}$$

Here, N_s is the total number of species in the system, $\nu_{\alpha\beta} = \nu_{\alpha\beta}(x, t)$ is the collision frequency for species α with species β, $D_{\alpha\beta} = D_{\alpha\beta}(x, t)$ is the collisional velocity space diffusion

coefficient of species α with species β, and u_β is the bulk fluid velocity of species β. The VFP equation governs the phase-space evolution of the different plasma species in the presence of an electric field.

The reduced Fokker-Planck operator [103, 104] features several key properties: 1) the equilibrium solution is a Maxwellian, 2) the velocity space diffusion and drag effect in the velocity space is captured, and 3) the operator conserves mass, momentum, and energy. The primary limitation of the reduced Fokker-Planck collision operator is the unphysically fast relaxation of energetic particles in a collisional time-scale, $\nu_{\alpha\beta}^{-1}$. This is to be contrasted with the true Fokker-Planck operator in terms of the Rosenbluth potentials [116], which relaxes the distribution function based on the relative velocities of the particles.

The collisional velocity space diffusion coefficient, $D_{\alpha\beta}$, for like-species interaction ($\beta = \alpha$) is defined as,

$$D_{\alpha\alpha} = \frac{T_\alpha}{m_\alpha}, \tag{7.5}$$

where T_α is the temperature of species α. For light-to-heavy species interactions (i.e. $m_\alpha \ll m_\beta$), the collisional velocity space diffusion coefficient is defined as,

$$D_{\alpha\beta}|_{m_\alpha \ll m_\beta} = \frac{T_\alpha}{m_\alpha} + \epsilon_{\alpha\beta}, \tag{7.6}$$

where $\epsilon_{\alpha\beta}$ is a term that analytically ensures energy conservation for a multi-species reduced Fokker-Planck operator and reads as [111]:

$$\epsilon_{\alpha\beta} = \frac{(T_\beta - T_\alpha)}{m_\beta} + (u_\alpha - u_\beta)\,. \tag{7.7}$$

For heavy-to-light species interaction (i.e. $m_\alpha \gg m_\beta$), the collisional velocity space diffusion coefficient is defined as,

$$D_{\alpha\beta}|_{m_\alpha \gg m_\beta} = \frac{T_\beta}{m_\alpha}. \tag{7.8}$$

The electron-electron collision frequency, ν_{ee}, is [114],

$$\nu_{ee} = 9.174 \times 10^{-17} \frac{n_e \ln\Lambda_{ee}}{T_e^{3/2}} \ [\text{sec}^{-1}], \tag{7.9}$$

with, T in keV, and n in particles per cubic meter (m^{-3}). Here, $\ln\Lambda_{ee}$ is the Coulomb logarithm for electron-electron interactions, set to 10 in this study. The like-ion species collision frequency, ν_{ii}, [114] is,

$$\nu_{ii} = 1.515 \times 10^{-18} \frac{n_i Z_i^4 \ln\Lambda_{ii}}{(m_i/m_p)^{1/2} T_i^{3/2}} [\text{sec}^{-1}]. \tag{7.10}$$

Here, m_p is the proton mass, Z_i is the ion charge state, and $\ln\Lambda_{ii}$ is the Coulomb logarithm for the like-ion species collisions also set to 10 in this study. In order for the interspecies thermal equilibration time-scale to scale as the ratio of mass, and to enforce energy and momentum conservation, we adopt the following expressions for the interspecies collision frequencies,

$$\nu_{\alpha\beta} = \frac{m_\beta}{m_\alpha} \nu_{\beta\beta}, \text{ for } m_\alpha > m_\beta, \tag{7.11}$$

and

$$\nu_{\beta\alpha} = \frac{m_\alpha n_\alpha}{m_\beta n_\beta} \nu_{\alpha\beta}, \text{ for } m_\alpha > m_\beta. \tag{7.12}$$

The number density, n_α, bulk fluid velocity, u_α, and temperature, T_α, are defined in terms of the distribution function, f_α, as,

$$n_\alpha = \langle 1, f_\alpha \rangle_v \,, \tag{7.13}$$

$$u_\alpha = \frac{\langle v, f_\alpha \rangle_v}{\langle 1, f_\alpha \rangle_v}, \tag{7.14}$$

$$T_\alpha = m_\alpha \frac{\left\langle (v-u_\alpha)^2, f_\alpha \right\rangle_v}{\langle 1, f_\alpha \rangle_v}. \tag{7.15}$$

Here, $\langle (\,\cdot\,), f_\alpha \rangle_v$ is a shorthand notation for the inner product between $(\,\cdot\,)$ and f_α,

$$\langle (\,\cdot\,), f_\alpha \rangle_v = \int_{-\infty}^{+\infty} (\,\cdot\,)\, f_\alpha dv. \tag{7.16}$$

7.2.2 Time- and Length-Scales of VFPA

The coupled VFPA system supports a wide range of time-scales. These time-scales include the inverse electron plasma frequency, $\omega_{p,e}^{-1} = \sqrt{m_e \epsilon_0 / n_e q_e^2}$, like-species collision time-scale, $\tau_{\alpha\alpha} = \nu_{\alpha\alpha}^{-1}$, interspecies collision time-scale, $\tau_{\alpha\beta} = \nu_{\alpha\beta}^{-1}$, and slower dynamical time-scales. The time-scale disparity can span many orders of magnitude. For example, if we consider the implosion dynamics of an inertial confinement fusion (ICF) capsule for Omega-facility-relevant conditions [102], the longest time-scale is the capsule stagnation and peak compression, which is of order 10^{-9}[sec]. For the compressed core, the inverse electron plasma frequency is of order 10^{-18}[sec]. From the shortest time-scale of $\omega_{p_e}^{-1}$ to the longest physical time-scale of capsule achieving peak compression, more than nine orders of magnitude separation in *physical* time-scales exists.

Consider a typical numerical time-step constraint given by the electron streaming CFL,

$$\Delta t_{CFL,e,s} = \frac{\min |\Delta x|}{\max |v_e|}, \tag{7.17}$$

where $\min|\Delta x|$ is the minimum spatial cell size, and $\max|v_e|$ is the maximum discrete electron velocity used in the simulation. For a given temperature, in order to be able to compute an accurate heat-flux, one typically defines the velocity phase-space domain of the electron as $10 v_{th,e}$, where,

$$v_{th,e} = \sqrt{\frac{2T_e}{m_e}}, \tag{7.18}$$

$v_{th,e}$ is the thermal velocity, which for electrons of $T_e = 10$[keV], is of order 10^7[m/sec]. Therefore, $\max|v_e| = 10v_{th,e} = 10^8$[m/sec]. For $\min|\Delta x|$, if one is considering charge separation, the gradient length-scale of the solution in some part of the domain should approach λ_D. In these situations, $\min|\Delta x| \leq \lambda_D$. For $T_e = 10$[keV], and $\omega_{p,e}^{-1} \approx 10^{-18}$[sec], $\lambda_D \approx 10^{-11}$[m], and $\Delta t_{CFL,e,s} \approx 10^{-19}$[sec]. Thus, the numerical time-scale separation is approximately ten orders of magnitude. This makes the numerical modeling of multi time-scale VFPA system highly challenging, and drives our motivation for implicit methods.

The coupled VFPA system also supports a wide range of length-scales. These length-scales include the Debye length,

$$\lambda_D = \sqrt{\frac{\epsilon_0 T_e}{n_e q_e^2}}, \tag{7.19}$$

the collisional mean-free path between like-species, $\lambda_{\alpha\alpha}$,

$$\lambda_{\alpha\alpha} = v_{th_\alpha}\tau_{\alpha\alpha}, \tag{7.20}$$

and unlike species, $\lambda_{\alpha\beta}$,

$$\lambda_{\alpha\beta} = v_{th_\alpha}\tau_{\alpha\beta}, \tag{7.21}$$

the gradient length-scale of the solution, $L_{\mathcal{M}}$,

$$L_M = \left(\frac{\partial M}{\partial x}\frac{1}{M}\right)^{-1}, \tag{7.22}$$

and the system length-scale, L_x. Here, M is a moment of choice to compute the gradient length-scale (n, T, etc). In the example above, the system length-scale is the Omega capsule radius which is of order 10^{-4}[m]. If one considers the same conditions discussed for the compressed core ($T_e \approx 10$[keV]), $\min|\Delta x| \approx \lambda_D = 10^{-11}$[m], we have a separation in length scales of seven orders of magnitude, which makes the time integration of VFPA system a challenge as well.

7.2.3 Ampère's equation

The electrostatic Ampère's equation reads:

$$\epsilon_0 \frac{\partial E}{\partial t} + \sum_{\alpha}^{N_s} q_\alpha n u_\alpha = 0. \tag{7.23}$$

Here, ϵ_0 is the permittivity of free space and nu_α is the number density flux of species α,

$$nu_\alpha = \langle v, f_\alpha \rangle_v . \tag{7.24}$$

One common simplification is to neglect electron inertia and use an ambipolar approximation for the field [5]. However, this precludes charge separation effects. In this study, we use the Ampère's equation to evolve the electric field in time to dynamically capture charge-separation fields. Equations (7.4) and (7.23) together define the Vlasov-Fokker-Planck-Ampère (VFPA) system. The system evolves the species distribution function and the field self-consistently in phase-space and time.

7.2.4 Moment System + Ampère's Equation (LO System)

In contrast to the higher-order (HO) VFP equation in equation (7.4), the self-consistent set of lower-order (LO) fluid moment equations describe the reduced dimensionality evolution of plasma through moments. Similarly to other studies [75, 51, 53, 118], we use the moments of the VFP equation as an algorithmic accelerator, akin in spirit to a coarse-grid acceleration in a multigrid method [115].

The moment equations are derived by taking the velocity-space moments of the VFP equation. The l^{th} moment of the VFP equation for species α is defined as,

$$\mathcal{M}_\alpha^l = C_l \left\langle v^l, \mathrm{VFP}_\alpha \right\rangle_v . \tag{7.25}$$

Here, C_l is the coefficient for the l^{th} moment. The standard continuity, momentum, and energy equations can be derived by taking the 0^{th}, 1^{st}, and 2^{nd} velocity moments of the VFP equation. The 0^{th} moment yields the continuity equation,

$$\langle 1, \mathrm{VFP}_\alpha \rangle_v = \frac{\partial n_\alpha}{\partial t} + \frac{\partial}{\partial x} n u_\alpha = 0, \tag{7.26}$$

the 1^{st} moment yields the momentum equation,

$$\langle v, \mathrm{VFP}_\alpha \rangle_v = \frac{\partial n u_\alpha}{\partial t} + \frac{\partial}{\partial x}\left[n u_\alpha^2 + P_\alpha\right] - \frac{q_\alpha}{m_\alpha} n_\alpha E + \sum_{\beta \neq \alpha}^{N_s} \nu_{\alpha\beta} n_\alpha \left(u_\alpha - u_\beta\right) = 0, \tag{7.27}$$

and the 2^{nd} moment yields the energy equation,

$$\frac{1}{2}\left\langle v^2, \mathrm{VFP}_\alpha \right\rangle_v = \frac{\partial U_\alpha}{\partial t} + \frac{\partial}{\partial x}\left[u_\alpha \left(U_\alpha + P_\alpha\right) + Q_\alpha\right] - \frac{q_\alpha}{m_\alpha} n u_\alpha E - \sum_{\beta \neq \alpha}^{N_s} \nu_{\alpha\beta} \left\{D_{\alpha\beta} n_\alpha - \left[S_{2,\alpha} - n u_\alpha u_\beta\right]\right\} = 0. \tag{7.28}$$

Here, P_α is the scalar pressure,

$$P_\alpha = \left\langle \left(v - u_\alpha\right)^2, f_\alpha \right\rangle_v = \frac{n_\alpha T_\alpha}{m_\alpha} = 2\left[U_\alpha - 0.5\left(n u_\alpha\right)^2 / n_\alpha\right], \tag{7.29}$$

Q_α is the heat-flux,

$$Q_\alpha = \frac{1}{2}\left\langle \left(v - u_\alpha\right)^3, f_\alpha \right\rangle_v, \tag{7.30}$$

U_α is the total energy density

$$U_\alpha = \frac{1}{2}\left\langle v^2, f_\alpha \right\rangle_v, \tag{7.31}$$

and $S_{2,\alpha}$ is the total stress tensor,

$$S_{2,\alpha} = \left\langle v^2, f_\alpha \right\rangle_v = \frac{n_\alpha T_\alpha}{m_\alpha} + \left(n u_\alpha\right)^2 / n_\alpha. \tag{7.32}$$

We retain the 2^{nd} moment equation for the temperature, T_α, to provide closure for $S_{2,\alpha}$. This is not the case for the moment-based acceleration algorithm for a collisionless plasma discussed in references [75] and [94]. We note that for a 1V problem, the viscous stress evaluates to zero and only the scalar pressure survives [74].

In the lower-order (LO) moment equation system, kinetic (phase-space) time-scales are removed and low-frequency dynamics are exposed in a reduced dimensionality system. Hydrodynamic length-scales and thermal equilibration time-scales become the natural scales. If one still allows for finite charge separation effects, the inverse plasma frequency time scale, $\omega_{p,e}^{-1}$, and Debye length, λ_D, are also supported. The moment system allows one to follow the coarse-grained evolution of the HO model in a reduced dimensionality setting of space, x, and time, t. However, an appropriate closure for the higher-order moment quantity, Q_α, is necessary. For sufficiently collisional plasmas where the gradient length-scale, L_n is much longer compared to the collisional mean-free-path, λ_{mfp}, a Braginskii closure is appropriate [117]. However, for an intermediate regime where the mean-free-path of the particles is comparable to the gradient length-scales of the solution structure, the Braginskii closure breaks down and one must solve the VFP equation to compute an accurate evolution of the solution.

The VFP equations and the fluid moment equations have the same solution as long as the correct heat-flux, Q_α, is supplied (i.e. if the true definition of Q_α is used). We exploit this hierarchical relationship between the VFP equation and the fluid moment equations to develop a nonlinear accelerator for the VFPA system. The coarse-grained LO system, which lives in the reduced dimensionality space, will be used to accelerate the convergence of the fine-grained (resolving velocity space) HO system within a time-step.

7.3 HOLO Moment Acceleration Algorithm

As discussed in section 7.2, the VFPA system supports disparate time-scales, both numerical and physical. In traditional explicit integration schemes, the time-step size, Δt, is limited by the CFL stability condition. For semi-implicit methods [86, 87], CFL conditions are relaxed and a larger Δt can be chosen. However, if the solution is not iterated nonlinearly, large errors may accumulate from time-step to time-step. If one wishes to iterate the Vlasov-Ampère system using a standard Picard iteration, it can be demonstrated (and will be shown in this study) that for the iteration to converge, the time-step size must resolve the inverse plasma frequency, $\omega_{p,e}^{-1}$ [119]. If the gradient scale-length of the solution is not resolving the Debye length, λ_D, and the dynamical time-scale of the problem is longer than $\omega_{p,e}^{-1}$, then $\omega_{p,e}^{-1}$ becomes the stiff time-scale.

In [75], a HOLO algorithm has been developed to step over $\omega_{p,e}^{-1}$ for a collisionless plasma physics particle-in-cell (PIC) method. The HO (kinetic) system provided the stress tensor to the LO (moment+Ampère) system. In return, the LO system returned the implicit new time evaluation of the field, E. In the current study, we consider a *collisional* plasma, which, in addition, supports the fast electron collision time-scale, τ_{ee}, the ion-ion collision time-scale, τ_{ii}, and the ion-electron thermal relaxation time-scale, τ_{ie}. In order to step over both $\omega_{p,e}^{-1}$ and τ_{ee}, we develop a moment-based accelerator for the VFPA system. In the collisional context, the HO system provides the LO system with the heat-flux, Q_α. In turn, the LO system provides to the HO system the field, E, the collisional velocity space diffusion coefficient, $D_{\alpha\beta}$, the collision frequency, $\nu_{\alpha\beta}$, and the fluid velocity, u_α. In this section, we discuss the discrete treatment of the HO and LO system (in time and space), and at the end of the section we provide the HOLO iteration algorithm.

7.3.1 Discrete HO System

The HO system is discretized using a Crank-Nicholson scheme, and a charge, momentum, and energy conserving [94] finite volume discretization for both configuration and velocity spaces,

$$\frac{f^{k+1,z}_{\alpha_{i,j}} - f^{k}_{\alpha_{i,j}}}{\Delta t} + \underbrace{v_{\alpha_j}\frac{\widehat{f}^{k+1/2,z}_{\alpha_{i+1/2,j}} - \widehat{f}^{k+1/2,z}_{\alpha_{i-1/2,j}}}{\Delta x_i}}_{\text{ⓐ}} + \underbrace{\left|v_{\alpha_j}\right|\frac{\xi^{k+1,z-1}_{\alpha_{i+1/2,j}}\widehat{f}^{k+1,*,z}_{\alpha_{i+1/2,j}} - \xi^{k+1,z-1}_{\alpha_{i-1/2,j}}\widehat{f}^{k+1,*,z}_{\alpha_{i-1/2,j}}}{\Delta x_i}}_{\text{ⓑ}} +$$

$$\frac{q_\alpha}{m_\alpha}E^{k+1/2,z}_i\left\{\underbrace{\frac{\widetilde{f}^{k+1/2,z}_{\alpha_{i,j+1/2}} - \widetilde{f}^{k+1/2,z}_{\alpha_{i,j-1/2}}}{\Delta v_{\alpha_j}}}_{\text{ⓒ}} + \underbrace{\phi^{k+1,z-1}_{\alpha_i}\frac{\widetilde{f}^{k+1,*,z}_{\alpha_{i,j+1/2}} - \widetilde{f}^{k+1,*,z}_{\alpha_{i,j-1/2}}}{\Delta v_{\alpha_j}}}_{\text{ⓓ}}\right\} -$$

$$\sum_{\beta}^{N_s}\left\{\nu^{LO}_{\alpha\beta_i}\left[\underbrace{D^{LO}_{\alpha\beta_i}\frac{\partial_v f_\alpha|_{i,j+1/2} - \partial_v f_\alpha|_{i,j-1/2}}{\Delta v_{\alpha_j}}}_{\text{ⓔ}} + \underbrace{\frac{\widetilde{w}^{LO}_{\alpha\beta_{i,j+1/2}}\widetilde{f}_{\alpha_{i,j+1/2}} - \widetilde{w}^{LO}_{\alpha\beta_{i,j-1/2}}\widetilde{f}_{\alpha_{i,j-1/2}}}{\Delta v_{\alpha_j}}}_{\text{ⓕ}}\right]\right\}^{k+1/2,z} = 0. \tag{7.33}$$

Here, ⓐ is the streaming operator, ⓒ is the acceleration operator, terms ⓑ and ⓓ are truncation error operator which enforces charge, momentum, and energy conservation between the Vlasov operator and the Ampère's equation (chapter 5), $\widehat{f}$ denotes the numerical flux at the configuration space cell face, $\widetilde{f}$ denotes the numerical flux at the velocity space cell face, $*$ indicates that the evaluation of the numerical flux can be different from the physical streaming and acceleration operator, the superscript k denotes the time-index, $k+1/2$ denotes time-centering,

$$f^{k+1/2} = \frac{f^{k+1} + f^{k}}{2}, \tag{7.34}$$

i is the configuration space cell index, j is the velocity space cell index, z is the HOLO iteration index, the LO superscripts denote that the evaluation comes from the solution to

the LO system, $\widetilde{w}_{\alpha\beta}^{LO}$ is the LO numerical interpolation of the thermally fluctuating random velocity between species α and β,

$$w_{\alpha\beta_{i,j}}^{LO} = v_{\alpha_j} - u_{\beta_i}^{LO}, \tag{7.35}$$

$\nu_{\alpha\beta}^{LO}$ is the LO evaluation of the collision frequency, and $D_{\alpha\beta}^{LO}$ is the LO evaluation of the diffusion coefficient. From this point on, we define the HO number density as,

$$n_{\alpha_i}^{HO,k+1} = \sum_{j=1}^{N_v} \Delta v_{\alpha_j} f_{\alpha_{i,j}}^{k+1}, \tag{7.36}$$

the HO **cell-centered** number density flux as,

$$nu_{\alpha_i}^{HO,k+1} = \sum_{j=1}^{N_v} \Delta v_{\alpha_j} v_{\alpha_j} f_{\alpha_{i,j}}^{k+1}, \tag{7.37}$$

the HO **cell-face** number density flux as,

$$nu_{\alpha_{i+1/2}}^{HO,k+1} = \frac{1}{2\Delta x_{i+1/2}} \sum_{j=1}^{N_v} \Delta v_{\alpha_{j+1/2}} v_{\alpha_{j+1/2}}$$
$$\left[\Delta x_i \left(\widetilde{f}_{\alpha_{i,j+1/2}}^{k+1} + \phi_{\alpha_i}^{k+1} \widetilde{f}_{\alpha_{i,j+1/2}}^{k+1,*}\right) + \Delta x_{i+1} \left(\widetilde{f}_{\alpha_{i+1,j+1/2}}^{k+1} + \phi_{\alpha_{i+1}}^{k+1} \widetilde{f}_{\alpha_{i,j+1/2}}^{k+1,*}\right)\right], \tag{7.38}$$

the **cell-centered** fluid velocity as,

$$u_{\alpha_i}^{HO,k+1} = \frac{nu_{\alpha_i}^{HO,k+1}}{n_{\alpha_i}^{HO,k+1}}, \tag{7.39}$$

the HO total energy density as,

$$U_{\alpha_i}^{HO,k+1} = \frac{1}{2} \sum_{j=1}^{N_v} \Delta v_{\alpha_j} v_{\alpha_j}^2 f_{\alpha_{i,j}}^{k+1}, \tag{7.40}$$

and the HO temperature as

$$T_{\alpha_i}^{HO,k+1} = 2m_\alpha \frac{U_{\alpha_i}^{HO,k+1} - 0.5 \left(nu_{\alpha_i}^{HO,k+1}\right)^2 / n_{\alpha_i}^{HO,k+1}}{n_{\alpha_i}^{HO,k+1}}. \tag{7.41}$$

We employ a QUICK discretization [90] with an ULTRA-SHARP limiter [91] for ⓐ, an upwind discretization for ⓑ, a central differencing for ⓒ and ⓓ, a second order central differencing for ⓔ, and a Chang-Cooper discretization for ⓕ [105] (which enforces positivity, and the correct asymptotic limit of the collision operator). The HO system is solved using an ILU preconditioned Jacobian-Free Newton-Krylov (JFNK) method [62]. Note that, in the fully implicit Newton-Krylov based VFP solver developed by [110], the nonlinearity in the collisional velocity space diffusion coefficient, $D_{\alpha\beta}$, fluid velocity u_β, and collision frequency, $\nu_{\alpha\beta}$, were handled in the Newton system with an ILU preconditioning. In our approach, these nonlinear coefficients are provided from the LO system, and JFNK is used to only handle the nonlinearity in the *discretization* of the streaming operator, which uses the ULTRA-SHARP limiter.

Energy Conserving Discretization of Reduced Fokker-Planck Operator

Discrete energy conservation is critical for accurate long-time integration. The lack of energy conservation typically manifests itself as numerical heating, which allows the solution to drift nonphysically. An energy conserving discretization for the reduced Fokker-Planck operator is discussed in this section. Consider a 0D1V reduced Fokker-Planck operator with N_s species,

$$\frac{\partial f_\alpha}{\partial t} = \sum_{\beta=1}^{N_s} \nu_{\alpha\beta} \left\{ D_{\alpha\beta} \frac{\partial^2 f_\alpha}{\partial v^2} + \frac{\partial}{\partial v} \left[w_{\alpha\beta} f_\alpha \right] \right\}. \tag{7.42}$$

Consider a backward-Euler temporal scheme and a finite-volume method in velocity space:

$$\frac{f_{\alpha_j}^{k+1} - f_{\alpha_j}^{k}}{\Delta t} = \sum_{\beta=1}^{N_s} \nu_{\alpha\beta}^{k+1} \left\{ D_{\alpha\beta}^{k+1} \frac{\partial_v \widetilde{f}_{\alpha_{j+1/2}}^{k+1} - \partial_v \widetilde{f}_{\alpha_{j-1/2}}^{k+1}}{\Delta v_{\alpha_j}} + \frac{\widetilde{w}_{\alpha\beta_{j+1/2}}^{k+1} \widetilde{f}_{\alpha_{j+1/2}}^{k+1} - \widetilde{w}_{\alpha\beta_{j-1/2}}^{k+1} \widetilde{f}_{\alpha_{j-1/2}}^{k+1}}{\Delta v_{\alpha_j}} \right\} \tag{7.43}$$

Here, k is the time index, j is the velocity space cell index, Δv_{α_j} is the j^{th} discrete velocity space cell size, and the tilde indicates a numerical flux evaluation at the velocity space cell face. At this point, we do not wish to explicitly define the numerical flux, $\widetilde{f}_{\alpha_{j+1/2}}^{k+1}$. First, recall

that for our reduced Fokker-Planck collision operator, 1) we only consider binary collision between species and 2) considers an analytical energy conservation parameter, $\epsilon_{\alpha\beta}$, which appears only in the light-to-heavy species collision, i.e., the full diffusion coefficient is,

$$D_{\alpha\beta}^{k+1}\big|_{m_\alpha \ll m_\beta} = D_{\alpha\alpha}^{k+1} + \epsilon_{\alpha\beta}^{k+1} = \frac{T_\alpha^{k+1}}{m_\alpha} + \epsilon_{\alpha\beta}^{k+1}, \tag{7.44}$$

$$\epsilon_{\alpha\beta}^{k+1} = \frac{T_\beta^{k+1} - T_\alpha^{k+1}}{m_\beta} + (u_\alpha - u_\beta)^2 . \tag{7.45}$$

We see that by multiplying equation (7.44) by m_α, we obtain,

$$m_\alpha \, D_{\alpha\beta}^{k+1}\big|_{m_\alpha \ll m_\beta} = T_\alpha^{k+1} + \frac{m_\alpha}{m_\beta}\left(T_\beta^{k+1} - T_\alpha^{k+1}\right) + m_\alpha \left(u_\alpha - u_\beta\right)^2 . \tag{7.46}$$

Recognizing that $m_\alpha/m_\beta \ll 1$, for electron-ion-coupling, $\epsilon_{\alpha\beta}$ is minuscule. We exploit the freedom to define $\epsilon_{\alpha\beta}$ to discretely enforce energy conservation of inter-species collisions. Thus in the semi-discrete, for energy conservation between species α and β, we must satisfy for time-step k:

$$\begin{aligned} m_\alpha \nu_{\alpha\alpha}^{k+1} \left\langle \frac{v^2}{2}, \left[D_{\alpha\alpha}^{k+1}\partial_{vv} + \partial_v w_{\alpha\alpha}^{k+1}\right] f_\alpha^{k+1} \right\rangle_v + m_\alpha \nu_{\alpha\beta}^{k+1} \left\langle \frac{v^2}{2}, \left[\left(D_{\alpha\alpha}^{k+1} + \epsilon_{\alpha\beta}^{k+1}\right)\partial_{vv} + \partial_v w_{\alpha\beta}^{k+1}\right] f_\alpha^{k+1} \right\rangle_v = \\ m_\beta \nu_{\beta\beta}^{k+1} \left\langle \frac{v^2}{2}, \left[D_{\beta\beta}\partial_{vv} + \partial_v w_{\beta\beta}^{k+1}\right] f_\beta^{k+1} \right\rangle_v + m_\beta \nu_{\beta\alpha}^{k+1} \left\langle \frac{v^2}{2}, \left[D_{\beta\alpha}^{k+1}\partial_{vv} + \partial_v w_{\beta\alpha}^{k+1}\right] f_\beta^{k+1} \right\rangle_v \end{aligned} \tag{7.47}$$

This allows one to solve for $\epsilon_{\alpha\beta}^{k+1}$ as:

$$\begin{aligned} \epsilon_{\alpha\beta}^{k+1} = -\Bigg\{ m_\alpha \nu_{\alpha\alpha}^{k+1} \left\langle \frac{v^2}{2}, \left[D_{\alpha\alpha}^{k+1}\partial_{vv} + \partial_v w_{\alpha\alpha}^{k+1}\right] f_\alpha^{k+1} \right\rangle_v + m_\alpha \nu_{\alpha\beta}^{k+1} \left\langle \frac{v^2}{2}, \left[D_{\alpha\alpha}^{k+1}\partial_{vv} + \partial_v w_{\alpha\beta}^{k+1}\right] f_\alpha^{k+1} \right\rangle_v + \\ m_\beta \nu_{\beta\beta}^{k+1} \left\langle \frac{v^2}{2}, \left[D_{\beta\beta}\partial_{vv} + \partial_v w_{\beta\beta}^{k+1}\right] f_\beta^{k+1} \right\rangle_v + m_\beta \nu_{\beta\alpha}^{k+1} \left\langle \frac{v^2}{2}, \left[D_{\beta\alpha}^{k+1}\partial_{vv} + \partial_v w_{\beta\alpha}^{k+1}\right] f_\beta^{k+1} \right\rangle_v \Bigg\} / \\ m_\alpha \nu_{\alpha\beta}^{k+1} \left\langle \frac{v^2}{2}, \partial_{vv} f_\alpha^{k+1} \right\rangle_v \end{aligned} \tag{7.48}$$

Thus, for *discrete* energy conservation, $\epsilon_{\alpha\beta}^{k+1}$ is defined discretely as,

$$\epsilon_{\alpha\beta}^{*,k+1} = -\Bigg\{ m_\alpha \nu_{\alpha\alpha}^{k+1} \sum_j^{N_v} \Delta v_{\alpha_j} \frac{v_{\alpha_j}^2}{2} \left[D_{\alpha\alpha}^{k+1} \frac{\partial_v \widetilde{f}_{\alpha_{j+1/2}}^{k+1} - \partial_v \widetilde{f}_{\alpha_{j-1/2}}^{k+1}}{\Delta v_{\alpha_j}} + \frac{\widetilde{w}_{\alpha\alpha_{j+1/2}}^{k+1} \widetilde{f}_{\alpha_{j+1/2}}^{k+1} - \widetilde{w}_{\alpha\alpha_{j-1/2}}^{k+1} \widetilde{f}_{\alpha_{j-1/2}}^{k+1}}{\Delta v_{\alpha_j}} \right] +$$
$$m_\alpha \nu_{\alpha\beta}^{k+1} \sum_j^{N_v} \Delta v_{\alpha_j} \frac{v_{\alpha_j}^2}{2} \left[D_{\alpha\alpha}^{k+1} \frac{\partial_v \widetilde{f}_{\alpha_{j+1/2}}^{k+1} - \partial_v \widetilde{f}_{\alpha_{j-1/2}}^{k+1}}{\Delta v_{\alpha_j}} + \frac{\widetilde{w}_{\alpha\beta_{j+1/2}}^{k+1} \widetilde{f}_{\alpha_{j+1/2}}^{k+1} - \widetilde{w}_{\alpha\beta_{j-1/2}}^{k+1} \widetilde{f}_{\alpha_{j-1/2}}^{k+1}}{\Delta v_{\alpha_j}} \right] +$$
$$m_\beta \nu_{\beta\beta}^{k+1} \sum_j^{N_v} \Delta v_{\beta_j} \frac{v_{\beta_j}^2}{2} \left[D_{\beta\beta}^{k+1} \frac{\partial_v \widetilde{f}_{\beta_{j+1/2}}^{k+1} - \partial_v \widetilde{f}_{\beta_{j-1/2}}^{k+1}}{\Delta v_{\beta_j}} + \frac{\widetilde{w}_{\beta\beta_{j+1/2}}^{k+1} \widetilde{f}_{\beta_{j+1/2}}^{k+1} - \widetilde{w}_{\beta\beta_{j-1/2}}^{k+1} \widetilde{f}_{\beta_{j-1/2}}^{k+1}}{\Delta v_{\beta_j}} \right] +$$
$$m_\beta \nu_{\beta\alpha}^{k+1} \sum_j^{N_v} \Delta v_{\beta_j} \frac{v_{\beta_j}^2}{2} \left[D_{\beta\alpha}^{k+1} \frac{\partial_v \widetilde{f}_{\beta_{j+1/2}}^{k+1} - \partial_v \widetilde{f}_{\beta_{j-1/2}}^{k+1}}{\Delta v_{\beta_j}} + \frac{\widetilde{w}_{\beta\alpha_{j+1/2}}^{k+1} \widetilde{f}_{\beta_{j+1/2}}^{k+1} - \widetilde{w}_{\beta\alpha_{j-1/2}}^{k+1} \widetilde{f}_{\beta_{j-1/2}}^{k+1}}{\Delta v_{\beta_j}} \right] \Bigg\} /$$
$$\left\{ m_\alpha \nu_{\alpha\beta}^{k+1} \sum_j^{N_v} \Delta v_{\alpha_j} \frac{v_{\alpha_j}^2}{2} \frac{\partial_v \widetilde{f}_{\alpha_{j+1/2}}^{k+1} - \partial_v \widetilde{f}_{\alpha_{j-1/2}}^{k+1}}{\Delta v_{\alpha_j}} \right\} \quad (7.49)$$

with the light-to-heavy species diffusion coefficient redefined as:

$$D_{\alpha\beta}^{k+1}\big|_{m_\alpha \ll m_\beta} = D_{\alpha\alpha}^{k+1} + \epsilon_{\alpha\beta}^{*,k+1}. \quad (7.50)$$

7.3.2 Discrete LO System

The LO system is comprised of the fluid moment system and Ampère's equation. It is space and time-discretized using a Crank-Nicholson time discretization and a staggered finite differencing in space. The discrete LO system reads:

$$\frac{n_{\alpha_i}^{LO,k+1,z} - n_{\alpha_i}^{HO,k}}{\Delta t} + \frac{n u_{\alpha_{i+1/2}}^{LO,k+1/2,z} - n u_{\alpha_{i-1/2}}^{LO,k+1/2,z}}{\Delta x_i} = 0, \quad (7.51)$$

$$\frac{nu_{\alpha_{i+1/2}}^{LO,k+1,z} - nu_{\alpha_{i+1/2}}^{HO,k}}{\Delta t} + \frac{[nu^2/n + P]_{\alpha_{i+1}}^{LO,k+1/2,z} - [nu^2/n + P]_{\alpha_i}^{LO,k+1/2,z}}{\Delta x_{i+1/2}} -$$
$$\frac{q_\alpha}{m_\alpha} n_{\alpha_{i+1/2}}^{LO,k+1/2,z} E_{i+1/2}^{k+1/2,z} + \sum_{\beta\neq\alpha}^{N_s} \left\{\nu_{\alpha\beta}^{LO} n_\alpha^{LO} \left(u_\alpha^{LO} - u_\beta^{LO}\right)\right\}_{i+1/2}^{k+1/2,z} - \gamma_{nu_{\alpha_{i+1/2}}}^{HO,k+1,z} = 0, \tag{7.52}$$

$$\frac{U_{\alpha_i}^{LO,k+1,z} - U_{\alpha_i}^{HO,k+1}}{\Delta t} + \frac{\left[\widehat{u}\left(\widehat{U} + \widehat{P}\right)\right]_{\alpha_{i+1/2}}^{LO,k+1/2,z} - \left[\widehat{u}\left(\widehat{U} + \widehat{P}\right)\right]_{\alpha_{i-1/2}}^{LO,k+1/2,z}}{\Delta x_i} -$$
$$\frac{\widehat{Q}_{\alpha_{i+1/2}}^{HO,k+1/2,z} - \widehat{Q}_{\alpha_{i-1/2}}^{HO,k+1/2,z}}{\Delta x_i} + \frac{\widehat{\gamma}_{U_{\alpha,i+1/2}}^{HO,k+1/2,z} - \widehat{\gamma}_{U_{\alpha_{i-1/2}}}^{HO,k+1/2,z}}{\Delta x_i} -$$
$$\frac{q_\alpha}{m_\alpha} nu_{\alpha_i}^{LO,k+1/2,z} E_i^{k+1/2,z} - \sum_{\beta\neq\alpha}^{N_s} \left\{\nu_{\alpha\beta}\left[D_{\alpha\beta} n_\alpha - (S_{2,\alpha} - nu_\alpha u_\beta)\right]\right\}_i^{LO,k+1/2,z} + \eta_{\alpha_i}^{HO,k+1/2,z} = 0, \tag{7.53}$$

$$\epsilon_0 \frac{E_{i+1/2}^{k+1,z} - E_{i+1/2}^{k}}{\Delta t} + \sum_{\alpha}^{N_s} q_\alpha nu_{\alpha_{i+1/2}}^{LO,k+1/2,z} = 0. \tag{7.54}$$

Here, $\gamma_{nu_{\alpha_{i+1/2}}}^{HO,k+1}$ is the discrete consistency term for the momentum equation, $\gamma_{U_{\alpha_{i+1/2}}}^{HO,k+1/2}$ and $\eta_{U_{\alpha_i}}^{HO,k+1/2}$ are the discrete consistency terms for the energy equation, and the hat denotes a numerical flux. All LO numerical flux evaluations are performed using central differences. The subscript $i \pm 1/2$ in n_α, U_α, $D_{\alpha\beta}$, $\nu_{\alpha\beta}$, and κ_α denotes interpolation to a cell face,

$$\mathcal{F}_{C,i+1/2} = \frac{x_{i+1/2} - x_i}{x_{i+1} - x_i}\mathcal{F}_{C,i} + \frac{x_{i+1} - x_{i+1/2}}{x_{i+1} - x_i}\mathcal{F}_{C,i+1}, \tag{7.55}$$

with $\mathcal{F}_C$ a cell-centered quantities. Similarly, the subscript i in cell face quantities nu_α and E denotes interpolation to the cell center,

$$\mathcal{F}_{F,i} = \frac{\mathcal{F}_{F,i+1/2} + \mathcal{F}_{F,i-1/2}}{2}. \tag{7.56}$$

Recall that the LO system is only used to accelerate the convergence of the HO system and the LO system is not evolved in time. For this reason, in the moment equations, all old

time terms are evaluated using the HO quantities as in [75]. In this study, the LO system is solved using a block-preconditioned JFNK solver (Appendix E).

Closure for Heat-Flux

The general ion heat-flux closure in the LO system, $\widehat{Q}^{HO}_{\alpha_{i+1/2}}$, is evaluated for the ions using its definition,

$$\widehat{Q}^{HO}_{\alpha_{i+1/2}} = \frac{x_{i+1/2} - x_i}{x_{i+1} - x_i} Q^{HO}_{\alpha_i} + \frac{x_{i+1} - x_{i+1/2}}{x_{i+1} - x_i} Q^{HO}_{\alpha_{i+1}}, \tag{7.57}$$

$$Q^{HO}_{\alpha_i} = \frac{1}{2} \sum_{j=1}^{N_v} \Delta v_{\alpha_j} \left(v_{\alpha_j} - u^{HO}_{\alpha_i} \right)^3 f_{\alpha_{i,j}}. \tag{7.58}$$

However, for electrons a Braginskii closure is used,

$$\widehat{Q}^{HO}_{\alpha_{i+1/2}} = \widehat{Q}^{LO}_{\alpha_{i+1/2}} = \widehat{Q}^{LO}_{brag,\alpha,i+1/2} = -\frac{\kappa^{LO}_{\alpha_{i+1/2}}}{m_\alpha} \frac{T^{LO}_{\alpha_{i+1}} - T^{LO}_{\alpha_i}}{\Delta x_{i+1/2}}, \tag{7.59}$$

where $\kappa^{LO}_{\alpha_{i+1/2}}$ is the cell face interpolated Braginskii thermal conductivity,

$$\kappa^{LO}_{\alpha_i} = 3.2 \frac{n^{LO}_{\alpha_i} T^{LO}_{\alpha_i} \nu^{-1}_{\alpha\alpha_i}}{m_\alpha}. \tag{7.60}$$

The reasons to consider separate treatment for electrons is because electron thermal conduction evolves in the stiff time-scale, τ_{ee}, and must be exposed in the LO system using the LO variables in order to produce an efficient solver when stepping over τ_{ee}. As we will show, this is a key point to achieve optimal HOLO iteration performance when using $\Delta t > \tau_{ee}$. Although the electron heat-flux is closed in terms of the Braginskii closure, we stress here that the HOLO converged solution will remain faithful to the HO system. This is achieved

through the discrete consistency terms, $\gamma_{U_\alpha}^{HO}$ and $\eta_{U_\alpha}^{HO}$, which are discussed in detail in Appendix F. Thus in the electron 2^{nd} moment equation, a combination of Q_{brag}, γ_U, and η_U are used to represent the true kinetic heat flux closure.

The purpose of the discrete consistency terms for the ion energy equation is similar to the collisionless plasma physics application [75], where they only enforce the discrete truncation error between the HO and LO system. However, for the electrons, the discrete consistency terms have the additional role of picking up the *missing physics* in the Braginskii closure (kinetic effects) as proposed in the nonlinear diffusion acceleration (NDA) method for neutron transport application [51]. In NDA, the LO current is approximated through the Fick's law, and the $\widehat{D}$ consistency term picks up both the truncation error and the physics.

7.3.3 HOLO Iteration Algorithm

To measure the convergence of the coupled VFPA system, we measure the maximum L_2-norm of the relative difference in the moments of the HO and LO system within an iteration,

$$\max \left| L^z_{2,M_\alpha} \right| \text{ for } \alpha \in [1, N_s] \text{ and } M = (n, nu, U)\,. \tag{7.61}$$

with

$$L^z_{2,M_\alpha} = \left| \frac{M_\alpha^{HO,z} - M_\alpha^{LO,z}}{M_\alpha^{HO,z}} \right|_2 . \tag{7.62}$$

Here, M_α is the moment of choice for species α. A convergence tolerance of tol$= 10^{-6}$ is used in this study. The algorithm for the HOLO acceleration method is presented in Algorithm 9.

Algorithm 9: HOLO accelerated iteration for the VFPA system.

Set $z = 0$;
Set all consistency terms, $\left(\gamma^{HO,z=0}, \eta^{HO,z=0}\right)$, to zero;
while *HO-LO system not converged* **do**
    Solve LO system for $(n, nu, U)^{LO,k+1,z}$ and $E^{k+1,z}$ from equations (7.51) to (7.53) ;
    Compute $D_{\alpha\beta}^{LO,k+1,z}$, $\nu_{\alpha\beta}^{LO,k+1,z}$, $w_{\alpha\beta}^{LO,k+1,z}$;
    Solve HO system for $f_{\alpha}^{k+1,z}$ from equation (7.33);
    Increment $z = z + 1$;
    Compute consistency terms, $\left(\gamma^{HO,z}, \eta^{HO,z}\right)$ from equations (F.9), (F.13), (F.1), (F.4), (F.5), (F.8);
    Check convergence between HO and LO system from equation (7.62);
end

7.4 Numerical Tests

We demonstrate the performance of the new charge and energy conserving VFPA HOLO solver on three model problems: 1) a homogeneous 0D1V thermal equilibration test between electrons and a single ion species, 2) a two-species collisional ion-acoustic-wave problem, 3) a periodic collisional density gradient evolution problem. The purpose of the simulations is to demonstrate the algorithmic performance of the new HOLO algorithm for the VFPA system, the importance of the discrete energy conservation when sharp gradient structures exist, and the capability of the methodology applied to a multi-length and time-scale problem.

For all the model problems, we normalize the quantities using the following reference values: $n^* = 10^{28}[\mathrm{m}^{-3}]$, $T^* = 0.1[\mathrm{keV}]$, $m_p^* = 1.67 \times 10^{-27}[\mathrm{kg}]$, and $q_p^* = 1.602 \times 10^{-19}[\mathrm{C}]$. Based on these reference values, we choose the reference time-scale to be the ion-ion collision time-scale, $\tau_{ii}^* = 2.09 \times 10^{-13}[\mathrm{sec}]$, the reference velocity, $u_i^* = \sqrt{T^*/m_p^*} = 9.79 \times 10^4[\mathrm{m/sec}]$, the reference length-scale to be the ion mean-free-path, $\lambda_{ii}^* = u_i^* \tau_{ii}^* = 2.04 \times 10^{-8}[\mathrm{m}]$, a

reference electric field, $E^* = m_p^* \lambda_{ii}^* / q_p^* \tau_{ii}^{*,2} = 4.89 \times 10^9$[V/m], and a reference distribution function, $f^* = n^* / \sqrt{2\pi T^*/m^*} = 4.07 \times 10^{14}$[sec/m^4]. For these reference values, the Debye length is $\lambda_D^* = 7.43 \times 10^{-10}$[m], the inverse plasma frequency is $\omega_{p,e}^{-1,*} = 1.77 \times 10^{-16}$[sec], and the electron collision time-scale is $\tau_{ee}^* = 3.45 \times 10^{-15}$[sec]. The following quantities are normalized to the reference values, accordingly,

$$\widehat{n} = \frac{n}{n^*}, \qquad \widehat{v} = \tfrac{v}{u_i^*}, \qquad \widehat{T} = \frac{T}{T_i^*},$$
$$\widehat{t} = \frac{t}{\tau_{ii}^*}, \qquad \widehat{x} = \tfrac{x}{\lambda_{ii}^*}, \qquad \widehat{q} = \frac{q}{q_p^*},$$
$$\widehat{m} = \frac{m}{m^*}, \qquad \widehat{E} = \tfrac{E}{E^*}, \qquad \widehat{L}_x = \frac{L_x}{\lambda_{ii}^*},$$
$$\widehat{f} = \frac{f}{f^*}, \quad \widehat{w}_{p,e}^{*,-1} = \tfrac{\omega_{p,e}^{*,-1}}{\tau_{ii}^*} = 8.49 \times 10^{-4}, \quad \widehat{\tau}_{ee}^* = \frac{\tau_{ee}^*}{\tau_{ii}^*} = 0.0165,$$
$$\widehat{\lambda}_D^* = \frac{\lambda_D^*}{\lambda_{ii}^*} = 0.036.$$

7.4.1 Two-Species Thermal Equilibration Problem

We begin to test the proposed algorithm with a 0D1V two-species thermal equilibration problem. We consider an electron and proton plasma. We show that the new algorithm allows one to use a time-step size, $\Delta\widehat{t}$, that is much larger than the electron-electron collision time-scale, $\widehat{\tau}_{ee}$, and follow accurately, the electron-ion thermalization time-scale, τ_{ie}. We show that the new algorithm allows one to nonlinearly converge the coupled Fokker-Planck equation with electrons and protons efficiently compared to a standard Picard iteration scheme (discussed in Appendix G). We initialize the problem with an electron temperature $\widehat{T}_e = 1.1$ and a proton ion temperature $\widehat{T}_i = 0.9$. For this test problem, we assume a constant collision time-scale of $\widehat{\tau}_{ee} = \widehat{\nu}_{ee}^{-1} = 1/60.5 = 0.0165$, $\widehat{\tau}_{ii} = \widehat{\nu}_{ii}^{-1} = 1$, and a thermal relaxation time-scale of, $\widehat{\tau}_{ie} = \widehat{\nu}_{ie}^{-1} = 1836/60.5 = 30.29$. We numerically solve the 0D1V reduced

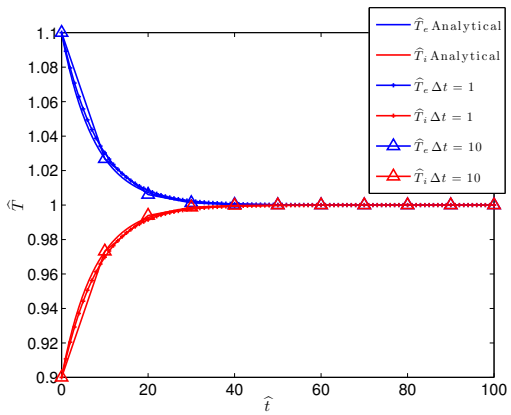


Figure 7.1: Thermalization test result.

Fokker-Planck problem,

$$\frac{\partial f_\alpha}{\partial t} = \sum_{\beta \neq \alpha}^{N_s} \left\{ D_{\alpha\beta} \frac{\partial^2 f_\alpha}{\partial v^2} + \frac{\partial}{\partial v} \left[(v - u_\beta) f_\alpha \right] \right\}, \tag{7.63}$$

and compute the temperature,

$$T_\alpha = m_\alpha \frac{\left\langle (v - u_\alpha)^2, f_\alpha \right\rangle_v}{\langle 1, f_\alpha \rangle_v}, \tag{7.64}$$

and compare against the solution obtained by analytically solving the coupled temperature moment equations,

$$\frac{\partial T_e}{\partial t} = 2\nu_{ie} \left(T_i - T_e \right), \tag{7.65}$$

$$\frac{\partial T_i}{\partial t} = 2\nu_{ie} \left(T_e - T_i \right). \tag{7.66}$$

We choose a time-step size $\Delta\widehat{t} = 1\widehat{\tau}_{ii} = 60.5\widehat{\tau}_{ee}$ and $10\widehat{\tau}_{ii} = 605\widehat{\tau}_{ee}$; refer to Figure 7.1. As can be seen, good agreement is obtained between the numerical solution and the analytical solution. Moreover, the solution converges to the correct asymptotic of $\widehat{T}\left(\widehat{t} = \infty\right) = 1$ for $\Delta\widehat{t} \gg \widehat{\tau}_{ee}$.

	$\Delta\widehat{t} = 1\widehat{\tau}_{ee}$	$\Delta\widehat{t} = 10\widehat{\tau}_{ee}$	$\Delta\widehat{t} = 100\widehat{\tau}_{ee}$
Iteration_{HOLO}	1	1	4
$\text{Iteration}_{Standard}$	12	94	865

Table 7.1: Comparison in performance of the new HOLO algorithm and a standard Picard iteration for varying $\Delta\widehat{t}$.

We demonstrate the solver performance of the new HOLO algorithm and compare it against the standard Picard iteration scheme, which is briefly discussed in Appendix G. For the standard Picard iteration scheme, we do not have a HO and LO temperature, T_α. Therefore, for convergence, we measure the L_2-norm of the relative difference in T_α from iteration to iteration,

$$\text{reldiff}_T = \left| \frac{T_\alpha^z - T_\alpha^{z-1}}{T_\alpha^z} \right|_2 . \tag{7.67}$$

In Table 7.1, we compare the performance of the new HOLO algorithm and a standard Picard iteration applied to the two-species thermal equilibration problem for time-step sizes of $\Delta\widehat{t} = 1\widehat{\tau}_{ee}$, $10\widehat{\tau}_{ee}$, and $100\widehat{\tau}_{ee}$. As can be seen, the performance of the new HOLO algorithm is one to several orders-of-magnitude superior to the standard Picard iteration for all regimes of $\Delta\widehat{t}$. We note that the cost of the LO solver relative to the HO solver is negligible as the unknown for the LO system is much less than the HO system.

7.4.2 Two-Species Collisional Ion-Acoustic-Wave Problem

We test the new algorithm on a 1D1V, two-species collisional ion-acoustic-wave (IAW) problem. The purpose of this problem is to demonstrate the algorithmic performance as a function of $\Delta\widehat{t}$ and demonstrate that we can step over both the inverse electron plasma frequency and the electron collision time-scales. We choose a variable collision frequency according to equations (7.9), (7.10), (7.11), and (7.12). We consider electron and proton with a mass of $\widehat{m}_e = 1/1836$ and $\widehat{m}_i = 1$, respectively, and an initial temperature of $\widehat{T}_{e,0} = \widehat{T}_{i,0} = 1$. The

$\Delta\widehat{t}$	$N = 50$	$N = 100$	$N = 200$
$0.1\widehat{\tau}^*_{ee}$	3	2	2
$1\widehat{\tau}^*_{ee}$	6	5	5
$10\widehat{\tau}^*_{ee}$	10	9	7
$50\widehat{\tau}^*_{ee}$	17	12	12

Table 7.2: Number of HOLO iterations with varying $\Delta\widehat{t}$ and $\Delta\widehat{x}$ for a collisional IAW problem.

problem is initialized using a sinusoidal perturbation in the density and fluid velocity,

$$\widehat{n}_{\alpha,0}\left(\widehat{x},\widehat{t}=0\right) = 1 + 0.2\sin k_x\widehat{x}, \tag{7.68}$$

$$\widehat{u}_{\alpha,0}\left(\widehat{x},\widehat{t}=0\right) = -1 + 0.2\sin k_x\widehat{x}, \tag{7.69}$$

where $k_x = 2\pi/\widehat{L}_x$ is the wave vector of the perturbation, and $\widehat{L}_x = 200$ is the system length and the spatial boundaries are periodic. In the study, we consider several spatial grid resolutions, $N = 50$, 100, and 200, a maximum velocity domain for each species of, $\widehat{v}_{min_\alpha} = -10\widehat{v}_{th,\alpha_0}$ and $\widehat{v}_{max_\alpha} = 10\widehat{v}_{th,\alpha_0}$, with:

$$\widehat{v}_{th,\alpha_0} = \sqrt{\frac{2\widehat{T}_{\alpha,0}}{\widehat{m}_\alpha}}, \tag{7.70}$$

and a total number of velocity space cells of $N_v = 200$. The initial distribution function is assumed to be a Maxwellian,

$$\widehat{f}_\alpha\left(\widehat{x},\widehat{v},\widehat{t}=0\right) = \frac{\widehat{n}_{\alpha,0}}{\sqrt{2\pi\widehat{T}_{\alpha,0}/\widehat{m}_\alpha}}\exp\left[-\frac{\widehat{m}_\alpha\left(\widehat{v}-\widehat{u}_{\alpha,0}\right)^2}{2\widehat{T}_{\alpha,0}}\right]. \tag{7.71}$$

We compare the number of HOLO iterations required for the solver for different $\Delta\widehat{t}$ in Table 7.2. We observe that the increase in the number of HOLO iterations is kept controlled for larger $\Delta\widehat{t}$.

$\Delta\widehat{t}$	$N = 50$	$N = 100$	$N = 200$
$0.1\widehat{\tau}^*_{ee}$	4	3	2
$1\widehat{\tau}^*_{ee}$	6	5	5
$10\widehat{\tau}^*_{ee}$	diverged	diverged	diverged
$50\widehat{\tau}^*_{ee}$	diverged	diverged	diverged

Table 7.3: Number of HOLO iteration with varying $\Delta\widehat{t}$ and N for a collisional IAW problem with the heat-flux closed entirely from the HO system.

In section 7.3.2, we mentioned that the electron heat-flux is evaluated using a Braginskii closure for the purpose of acceleration of the HOLO algorithm and we have mentioned that this was key for algorithmic efficiency. In Table 7.3, we show the performance of the algorithm with the electron heat-flux being evaluated by (7.59). Note that in this case, the electron heat-flux can not be exposed in terms of LO variables. We clearly see the degradation in the solver when the heat-flux is not evaluated using the electron Braginskii closure.The degradation indicates that convergence is very sensitive to the third moment of the distribution function, which is in fact a significant source of numerical stiffness. By introducing the Braginskii heat-flux, which is asymptotically the correct collisional limit, we address the underlying stiffness and thus mitigate the sensitivity of the HOLO iteration.

Finally, we compare the solver against another variation of the LO system. The last variation of the LO system comprises only the continuity, momentum, and Ampère's equations (refer to Appendix D). Therefore, all terms in the LO and HO system where T^{LO}_α appears are evaluated with T^{HO}_α. In references [75, 94], the application of the HOLO algorithm was for a *collisionless* plasma. In collisionless plasmas, one is interested in stepping over the inverse electron plasma frequency. From a dispersion analysis of the two-fluid equation [75], the continuity and momentum equations are sufficient to expose this time-scale in the LO system. In Table 7.4, the performance of the HOLO algorithm with the LO system comprising only the continuity, momentum, and Ampère's equations is shown. As expected, we see that as $\Delta\widehat{t} \gg \widehat{\tau}^*_{ee}$, the number of HOLO iteration grows and eventually stagnates for a large enough $\Delta\widehat{t}$. We emphasize that the three flavors of the LO system **do not** change the HO

$\Delta\widehat{t}$	$N_x = 50$	$N_x = 100$	$N_x = 200$
$0.1\widehat{\tau}^*_{ee}$	4	4	4
$1\widehat{\tau}^*_{ee}$	19	19	19
$10\widehat{\tau}^*_{ee}$	168	167	167
$50\widehat{\tau}^*_{ee}$	stagnated	stagnated	stagnated

Table 7.4: Number of HOLO iteration with varying $\Delta\widehat{t}$ and $\Delta\widehat{x}$ for a collisional IAW problem with LO system carrying only the continuity, momentum, and Ampère equations.

solution to the VFPA system. The LO system is only a convergence accelerator.

7.4.3 Periodic Two-Species Collisional Density Gradient Evolution Problem

Finally, we test the VFPA HOLO algorithm on a periodic two-species, collisional density gradient evolution problem. The purpose of this problem is to demonstrate the importance of energy conservation. When a strong gradient exists in the number density, significant discrete energy conservation errors can occur between the distribution function and the fields. Through the collision operator, this manifests itself as numerical heating via thermalization. For this test, the species parameters are, $\widehat{m}_e = 1/1836$, $\widehat{m}_i = 1$, $\widehat{T}_{0,e} = \widehat{T}_{0,i} = 1$, and $\widehat{u}_0 = 0$. The domain size is $\widehat{L}_x = 100$, the number of cells in space is $N = 2500$, the velocity domain is $\widehat{v}_{min_\alpha} = -10\widehat{v}_{th,\alpha,0}$, $\widehat{v}_{max_\alpha} = +10\widehat{v}_{th,\alpha,0}$, and the number of velocity space cells is $N_v = 200$. The initial density profile is given by the following piecewise hyperbolic tangent function,

$$\widehat{n}(\widehat{x}) = \left\{ \begin{array}{cc} \text{if } x \geq 0 \text{ and } x \leq 0.5L_x & a_n tanh\left[\chi\left(\widehat{x} - \widehat{L}_x/4\right)\right] + b_n \\ \text{else} & c_n tanh\left[\chi\left(\widehat{x} - 3\widehat{L}_x/4\right)\right] + d_n, \end{array} \right\}, \tag{7.72}$$

$$a_n = \frac{\widehat{n}_L + \widehat{n}_R}{2} - \widehat{n}_R, \tag{7.73}$$

$$b_n = \frac{\widehat{n}_L + \widehat{n}_R}{2}, \tag{7.74}$$

$$c_n = \frac{\widehat{n}_R + \widehat{n}_L}{2} - \widehat{n}_L, \tag{7.75}$$

$$d_n = \frac{\widehat{n}_R + \widehat{n}_L}{2}. \tag{7.76}$$

Here, $\chi = 10$ is the hyperbolic tangent smoothing factor, $\widehat{n}_L = 1$, and $\widehat{n}_R = 0.1$. The problem is simulated up to $\widehat{t} \approx 515\widehat{\tau}^*_{ee} = 8.49$. Additionally, we use a non-uniform mesh in x. The non-uniform mesh is intended to resolve the initial high frequency structures near the sharp gradient. The following mapping function is used for the cell face locations,

$$x_{i+1/2} = L_x \left\{ \xi_{i+1/2} + \frac{\gamma_{\Delta x}}{4\pi} \left[\sin\left(4\pi\xi_{i+1/2}\right) \right] \right\}, \tag{7.77}$$

while the cell center locations are defined as geometrical center,

$$x_i = \frac{x_{i+1/2} - x_{i-1/2}}{2}. \tag{7.78}$$

Here, $0 \leq \xi \leq 1$ is the logical coordinate variable and $\gamma_{\Delta x}$ is the mapping factor. For this study, we used $\gamma_{\Delta x} = 0.4$, which yields a compression ratio of $\Delta x_{min}/\Delta x_{max} = 0.429$.

The problem features a wide range of dynamical time-scales based on the point in time of the simulation. Due to the initial sharp gradient structure, many *physical* high frequency modes are excited. Later in time, these modes damp out due to collisions, and the dynamical time-scale gradually approaches the collisional relaxation time-scale. For both accuracy and

performance of the nonlinear solver, we gradually ramp the time-step size as,

$$\Delta\widehat{t}^{k} = \left\{ \begin{array}{cc} \text{if } k = 0, & 5.15 \times 10^{-4}\widehat{\tau}^{*}_{ee} \\ \text{else if } \Delta\widehat{t}^{k-1} < 5.15 \times 10^{-2}\widehat{\tau}^{*}_{ee}, & 1.05\Delta\widehat{t}^{k-1} \\ \text{else if } \widehat{t}^{k} < 25.75\widehat{\tau}^{*}_{ee}, & 5.15 \times 10^{-2}\widehat{\tau}^{*}_{ee} \\ \text{else if } \widehat{t}^{k} \geq 25.75\widehat{\tau}^{*}_{ee} \text{ and } \Delta\widehat{t}^{k-1} < 5.15 \times 10^{-1}\widehat{\tau}^{*}_{ee} & 1.05\Delta\widehat{t}^{k-1} \\ \text{else if } \widehat{t}^{k} < 103\widehat{\tau}^{*}_{ee} & 5.15 \times 10^{-1}\widehat{\tau}^{*}_{ee} \\ \text{else if } \widehat{t}^{k} \geq 103\widehat{\tau}^{*}_{ee} \text{ and } \Delta\widehat{t}^{k-1} < 5.15\widehat{\tau}^{*}_{ee}, & 1.05\Delta\widehat{t}^{k-1} \\ \text{else}, & 5.15\widehat{\tau}^{*}_{ee} \end{array} \right\}.$$

The problem assumes charge neutrality everywhere initially. Immediately as the simulation begins, mobile electrons will stream across the strong density gradient, forming a charge separation region on order λ_D. An electric field immediately sets up in order to cancel the charge separation, decelerating the electrons and accelerating the ions in the dense region. The streaming of electrons across the density gradient will effectively convert the electron thermal energy into field energy. The field energy is then converted to ion kinetic energy via acceleration. In Figure 7.2, we show that these processes are indeed observed. At early time, electrons stream across the density gradient, increasing the effective temperature on the rarefied side and decreasing it on the dense side. However, due to fast electron thermal conduction, this structure dissipates and the electron thermal energy is converted to field energy, leading to electron cooling. At $\widehat{t} \approx 5.15\widetilde{\tau}^{*}_{ee}$, significant ion acceleration has taken place. At the same $\widehat{t}$, a spectrum of wave modes are excited due to possible beam instabilities as can be seen in the $\widehat{u}$ plot. We see in the rarefied side that the frequency of the modes are lower and the amplitudes are higher. This may be due to lower collision frequency in the less dense side, allowing for the waves to survive longer. It is precisely the presence of these high frequency modes that makes the problem highly nonlinear and dynamic. For this reason, it was necessary to use a dynamic time-stepping approach. We see that for long enough times, most of the oscillatory structures eventually damp out.

In Figure 7.3, we compare the ion and electron temperature obtained using the new charge-and-energy conserving scheme and a charge only conserving scheme [94] at $\widehat{t} = 5.15\widehat{\tau}_{ee}^{*}$. From the initial condition, the field is zero everywhere initially. Physically, we expect to observe the electron temperature to decrease early on, due to the conversion of electron thermal energy to field energy. However, without discrete energy conservation, we observe the inverse effect due to numerical heating. In Figure 7.4, we show the comparison of the degree of conservation of charge, momentum, and energy as a function of time. As can be seen, a clear difference in the total energy conservation is seen between the charge only conserving scheme and the charge-and-energy-conserving scheme.

7.5 Conclusion

In this chapter, we have extended the HOLO moment-based acceleration algorithm presented in chapter 5 to the multi-species Vlasov-Fokker-Planck-Ampére system. We have developed a charge and energy conserving discretization for the reduced Fokker-Planck operator.The energy conserving discretization for the reduced Fokker-Planck operator was developed by numerically redefining the $\epsilon_{\alpha\beta}$ term which ensures exact energy conservation. The combined discretization simultaneously achieves discrete charge and energy conservation.

In order to ensure exact conservation properties, to achieve algorithmic acceleration, and to be able to step over the electron-electron collision time-scales, it has been necessary to 1) add the energy equation in the LO system, 2) implicitly expose the electron thermal conduction physics in the LO system, and 3) introduce consistency terms in the HO system (Appendix C). A comparison study has been performed between a LO system with and without the energy equation. We observe that in order to efficiently converge the HOLO iteration when $\Delta t \gg \tau_{ee}$, it is necessary to include the energy equation in the LO system. Additionally, approximating the electron heat-flux through a Braginskii closure to expose the electron conduction physics was critical for the effectiveness of the algorithm.

We have demonstrated the importance of discrete energy conservation with a density gradient problem in periodic domain. Without it, significant numerical heating was observed when a strong gradient in the density was present, leading to unphysical results. Future work will focus in extending the algorithm to a more realistic form of the Fokker-Planck operator [116], possibly in multi-velocity-space dimensions, and in spherical coordinates.

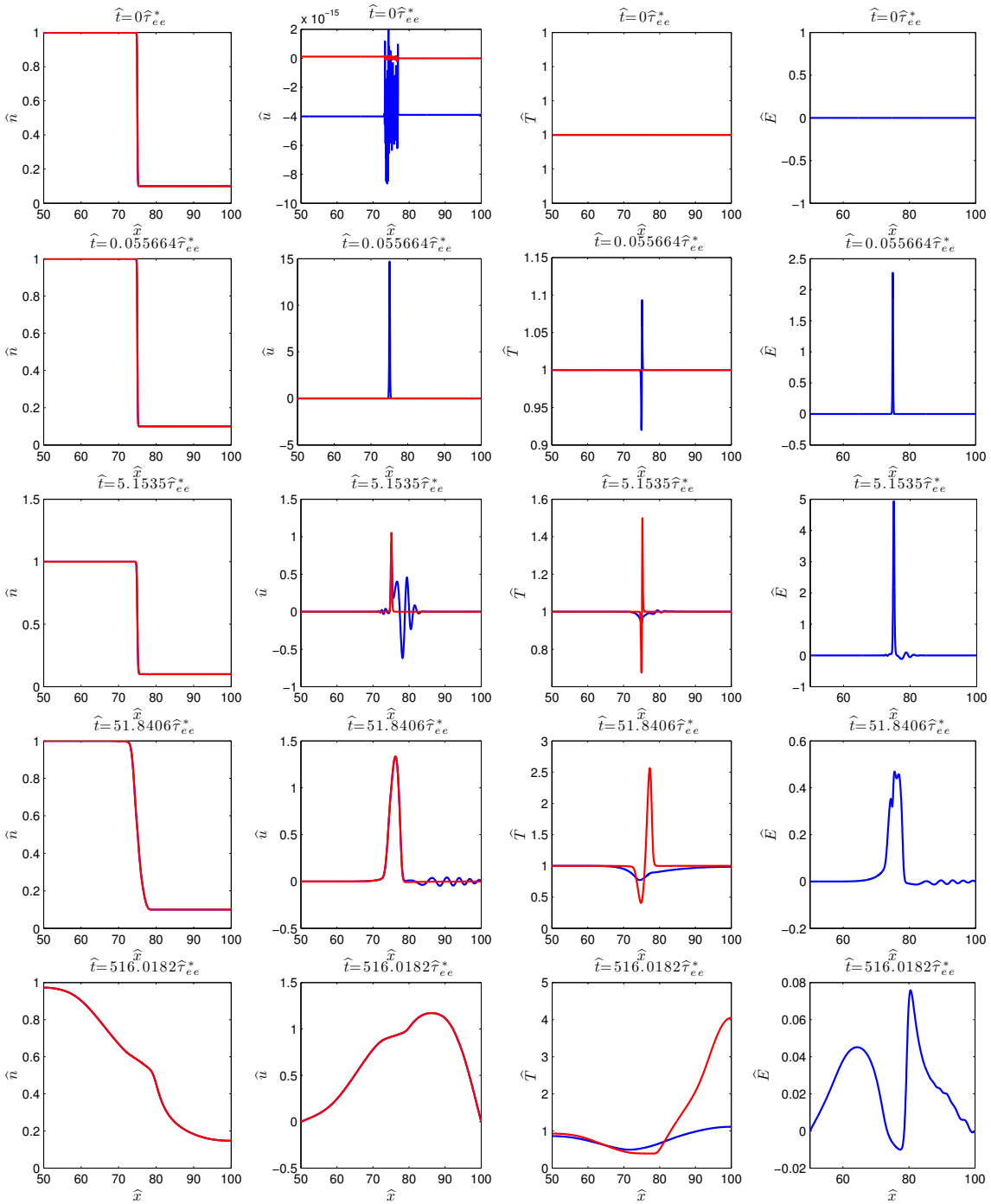


Figure 7.2: Plots of electron (blue) and ion (red) moments and electric field at different times in the right half of the periodic domain (note the solution is anti-symmetric for the left half).

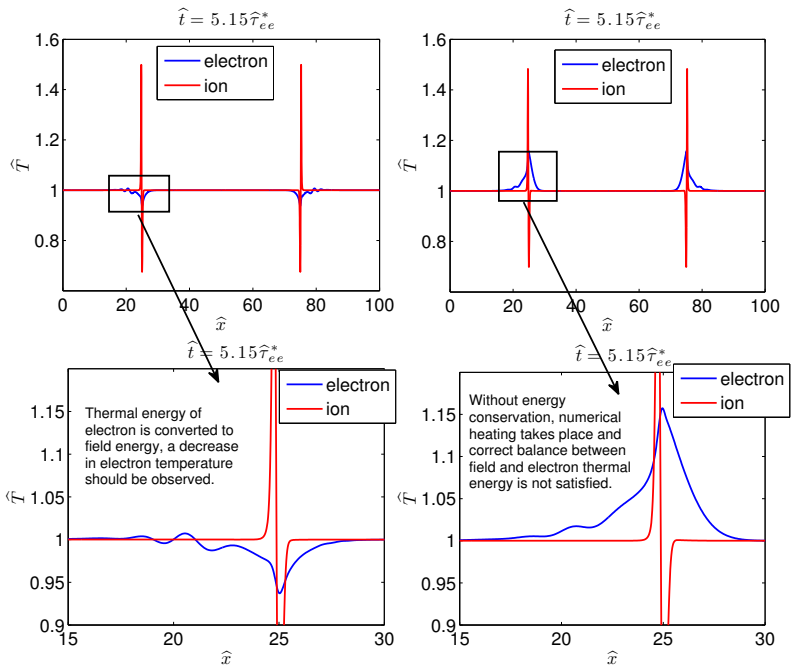


Figure 7.3: Temperature of electron and ion with (left) and without (right) energy conserving discretization. A significant numerical heating of electrons is observed.

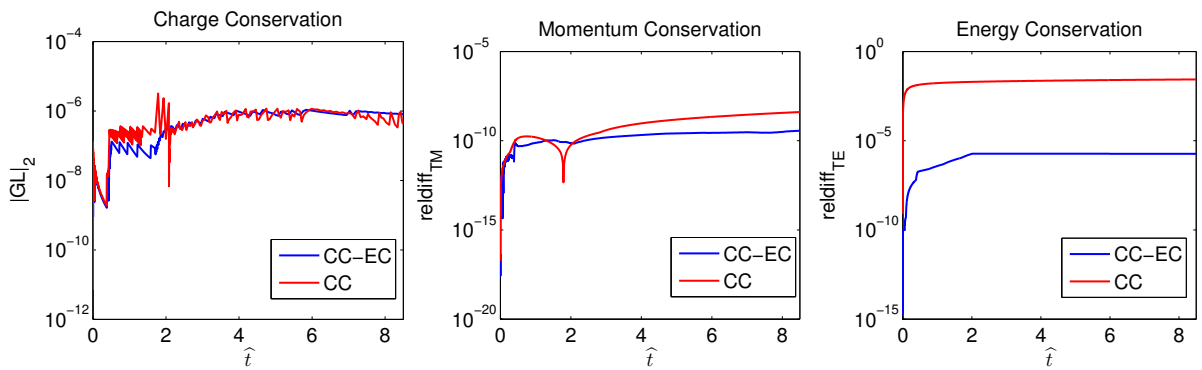


Figure 7.4: Comparison of charge (left), momentum (middle), and energy (right) conservation property.

Chapter 8

Kinetically Enhanced Mixing of ICF Omega Capsule Pusher into Fuel

In this chapter, we use the newly developed fully implicit moment-based acceleration algorithm to simulate an ICF problem. The problem we will study is the early time, kinetically enhanced mixing of pusher ions into the fuel due to a double layer electric field that sets up at the fuel-pusher interface. We describe the process of ionization gradient setup, the evolution of the double-layer electric field, and its impact on pusher ion acceleration and mixing into the fuel for an Omega ICF capsule. We provide numerical results on the sensitivity of the electric field as a function of initial conditions for very early times. We also present a long time integration of the problem to quantify the fractional mix of pusher into the fuel, and compare against theoretical predictions and experimental measurements.

8.1 Introduction

The National Ignition Campaign (NIC) at the National Ignition Facility (NIF) was intended to achieve ignition of the inertial confinement fusion (ICF) capsule. However, NIF has not

achieved ignition to date. The experiments at NIF consistently measure a lower neutron yield compared to hydrodynamic codes used to design the fuel capsule. There are many mechanisms that can cause a deficiency in neutron yields, that are not included in the standard analysis. We specifically mention three: 1) fuel species separation due to shock induced electric field and barodiffusion [16], and the subsequent reduction of DT fusion reaction, 2) tail depletion of long mean-free-path (mfp) high energy fuel ions escaping out of the hot-spot [25], reducing the fusion reaction, and 3) mixing of high Z ablator pusher material into the fuel and causing an increase in bulk heat-capacity as well as Bremsstrahlung radiative cooling of fuel.

Hydrodynamic codes based on single-fluid, neutral-radiation, hydrodynamic (SFNRH) assumptions do not allow for fuel species separation which is inherently a multi-species effect, and a tail depletion mechanism which is a kinetic phenomenon. Additionally, for hydrodynamic codes based on an SFNRH assumption, the primary mechanism for pusher mixing into the fuel is via Rayleigh-Taylor instability (RTI) and Richtmyer-Meshkov instability (RMI) [26]. However, a recent suite of Omega ICF experiments measured a large amount of pusher material mixing deep into the fuel that could not be predicted by hydrodynamic mix models [126, 127, 128].

Recently, a fluid electron and kinetic (Vlasov-Fokker-Planck) ion simulation with the electric field approximated using a quasi-neutral model was performed by reference [120] for an Omega ICF capsule. This level of modeling should be able to show the impact of mechanisms 1 and 2 above if they are important. In the study, the simulation observed fuel species separation early on during the hydrodynamic shock convergence phase. However, during the shock rebounce phase, the fuel species homogenized and no decrease in neutron yield was measured. Additionally, the simulation observed an *enhancement* of tail fuel ion population near the fuel-pusher interface due to the long mfp ions from the center of the hot-spot streaming towards the wall. Therefore, for the particular Omega experiment, mechanisms 1 and 2 above could not explain the neutron yield discrepancy between experiments

and simulations. The same suggests a detailed treatment of the earlier time condition near the fuel-pusher interface for non-hydrodynamic mix mechanisms.

In Omega experiments, a strong radial electric field has been measured that could not be explained by quasi-neutral, or ambipolar fluid theory alone [124]. In a theoretical work in reference [15], many sources for this field were discussed. Amongst them, the study offered two credible sources for the field: 1) hydrodynamic shock induced electric field, and 2) a strong charge-separation electric field at the fuel-pusher interface due to the ionization gradient that sets up after an ionization wave passes through the system. Recently, a theoretical study has been conducted by reference [130] to estimate the amount of pusher ion mix into the fuel due to enhanced kinetic effects due to the charge-separation electric field at the ionization gradient. The same study estimated the mix amount of pusher into fuel that could not be predicted by hydrodynamic mix models.

In this chapter, we perform a next level detailed investigation of the fuel-pusher interface mixing spearheaded by reference [130] by conducting a detailed kinetic numerical simulation. The remainder of this study is organized as follows. In section 8.2, we discuss in detail the setup of an ionization gradient at the fuel-pusher interface. In section 8.3, we provide a brief overview of the charge-separation electric field that sets up at the interface, and its characteristics. In section 8.4, we discuss the impact of the charge-separation electric field in pusher ion acceleration and mix into the fuel. In section 8.5, we discuss the numerical setup of the problem including the initial conditions and final simulation time. In section 8.6, we provide details on critical solver settings used to simulate the problem. In section 8.7, we confirm theoretical predictions of field structure and ion acceleration through the numerical simulation at early times. In section 8.8, we discuss the sensitivity of early time field strength as a function of initial conditions. In section 8.9, we discuss the impact of the early time electric field in enhancing and maintaining the kinetic effects of pusher ions for a sustained duration. In section 8.10, we provide numerical results on fractional mix of pusher ions over the fuel at later times. Finally, in section 8.11, we provide conclusions.

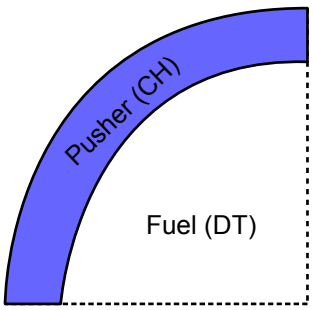


Figure 8.1: Omega plastic ablator capsule filled with equal mixture DT fuel.

8.2 Setup of Ionization Gradient at Fuel-Pusher Interface

We consider an Omega plastic (Hydrocarbon) ablator capsule, filled with an equal mixture of deuterium-tritium (DT) fuel (Figure 8.1). Initially, as the laser impinges on the surface of the capsule, the surface material will be ionized, forming a *coronal plasma*. Subsequently, the hot surface material will blow off of the capsule surface in the *outward direction*. From momentum conservation, this imparts an *inward* rocket-force-like momentum, beginning the implosion phase; refer to Figure 8.2. The laser will continue to impart momentum, and will launch a shockwave to heat and compress the fuel. However, the shockwave is preceded by a faster thermal radiation (or an X-ray) wave and energetic electron heat-flux that will preheat and ionize the capsule and fuel material. Once the fuel-puahser interface is ionized, due to the difference in the charge-state of the pusher and fuel ,($Z_C > Z_{DT} = Z_H$), an *ionization gradient* sets up, as illustrated in Figure 8.3. Since this preheat happens prior to the shock arrival, we can expect a sharp gradient at the fuel-pusher interface on order the ion mean-free-path,λ_{ii}.

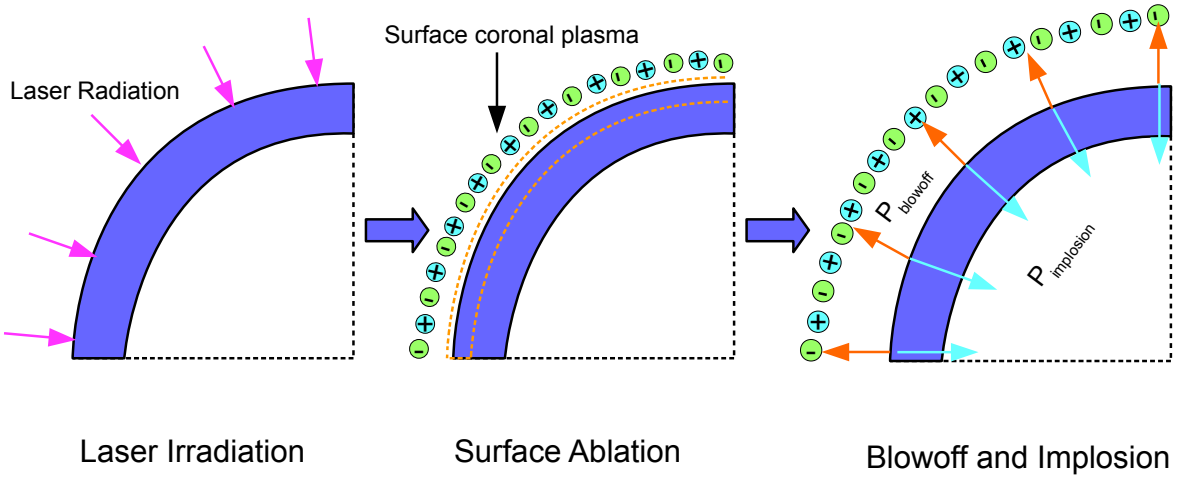


Figure 8.2: Surface blow off and capsule implosion process.

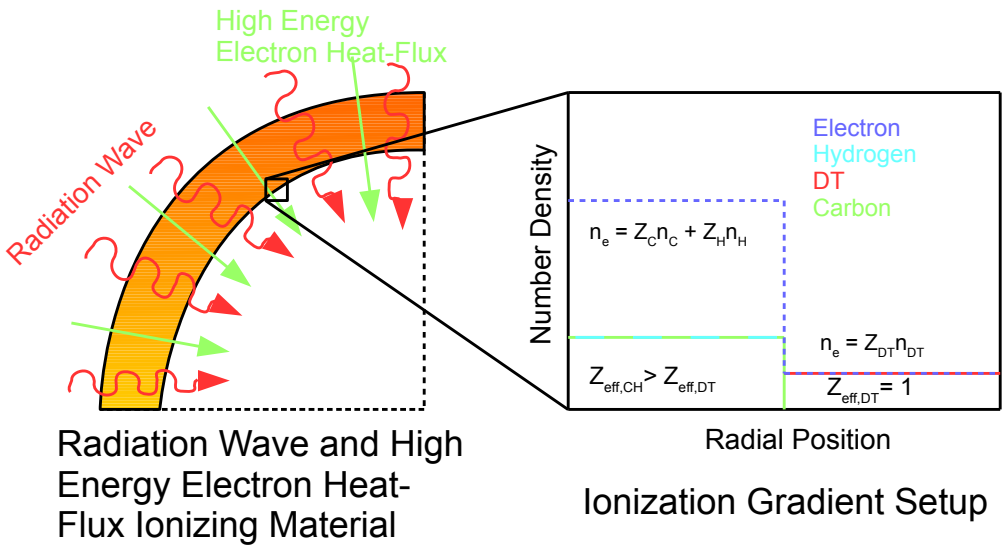


Figure 8.3: Setup of ionization gradient at the fuel-pusher interface.

8.3 Charge Separation and Double Layer Field

Upon the setup of the ionization gradient, due to the sharp gradient-scale length of the interface, electrons on the pusher side will stream into the fuel side as a result of their

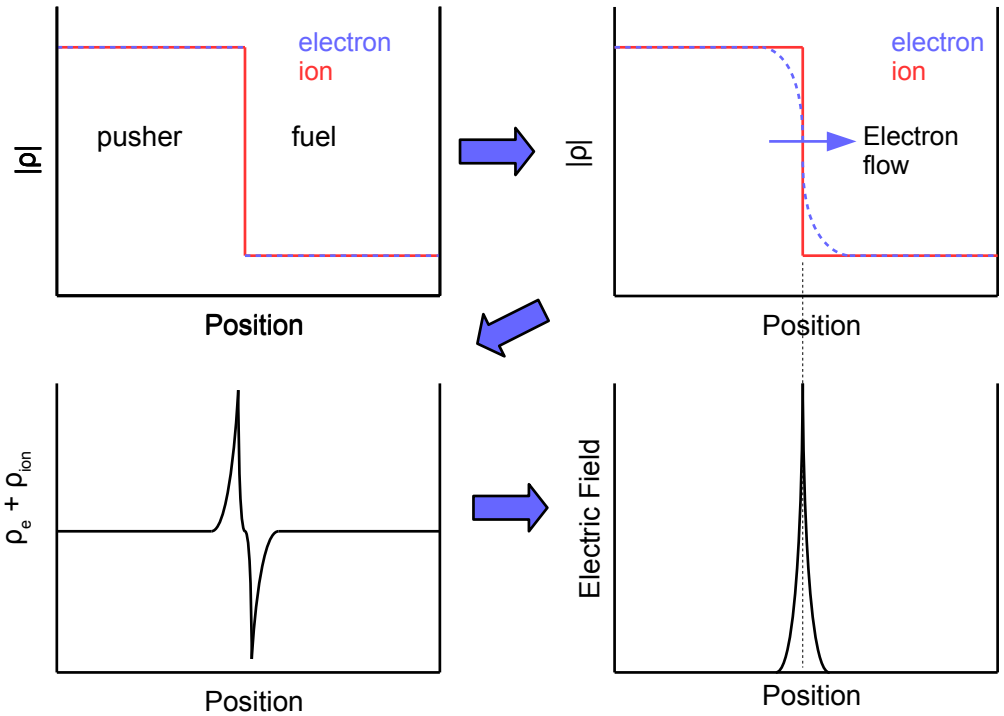


Figure 8.4: Initial charge separation and electric field.

thermal velocity. This will immediately form a charge-separation region, and a subsequent electric field which cannot be captured by an Ambipolar field theory. This field will act to: 1) decelerate the electrons and accelerate the ions coming from the pusher side and 2) accelerate the electrons and decelerate the ions coming from the fuel side, such as to cancel the charge-separation; refer to Figure 8.4. Furthermore, this field is expected to eventually evolve to a structure referred to as a **double-layer** [125]. A double-layer is a region enclosed by two distinct charge-separation zones. The individual charge-separation zones may be on the order of the Debye length, λ_D; however, the double-layer can typically be of the order $\mathcal{O}(10\lambda_D)$, refer to Figure 8.5.

A double-layer electric field is similar in nature to a classic sheath field [61]. A sheath field is an electrostatic potential boundary layer that sets up as a result of charge-separation near a wall which confines the plasma. The purpose of a sheath-field is to repel the light,

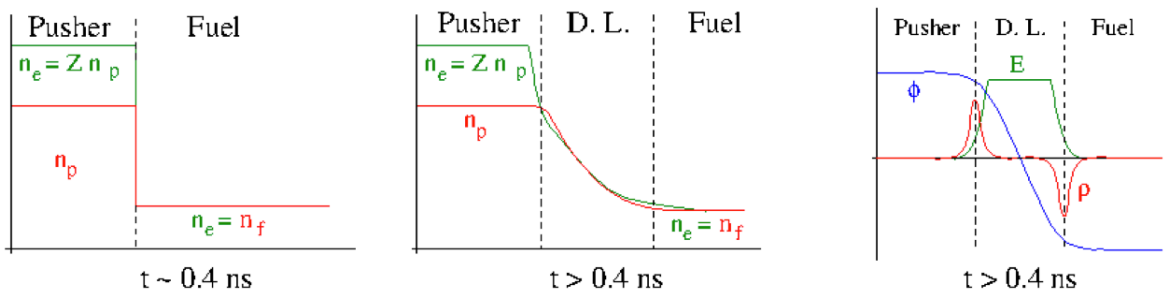


Figure 8.5: Setup of double layer. Initial setup of ionization gradient (left), evolution of density of electron and ion density (middle), and the structure of charge density ρ, electrostatic potential, ϕ, and the electric field, E (right) [130]. The double layer electric field is the region enclosed by the dashed lines.

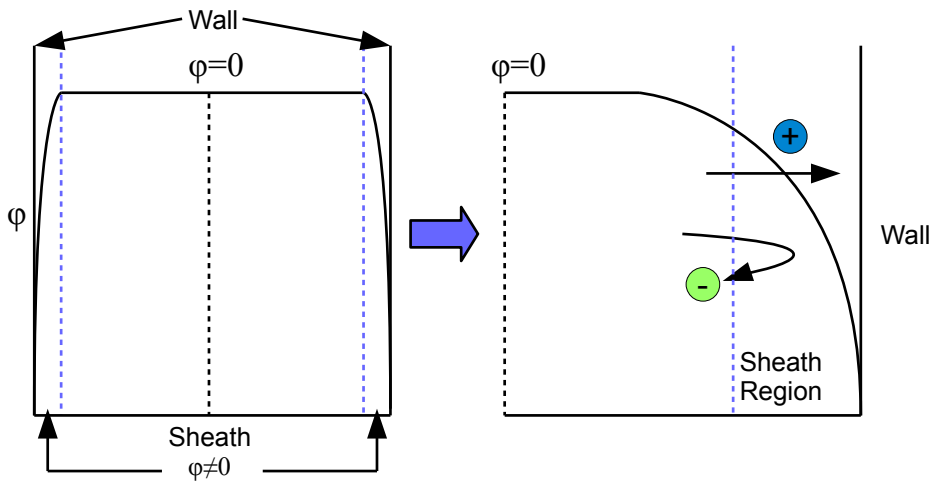


Figure 8.6: Illustration of sheath region.

mobile electrons and confine them electrostatically; refer to Figure 8.6. In a double-layer, instead of a wall, there exists a plasma on both sides of the plasma, and the layer can cause significant acceleration of ions entering from the dense side, into the less dense side.

In a sheath, there exists a **Bohm sheath criteria** in which ions must enter the sheath region at their sound speed **at a minimum** [61]. These ions are accelerated to their sound speed due to a **pre-sheath field** that exists outside of the sheath region and extends to the

interior of the quasi-neutral plasma as illustrated in Figure 8.7. Similarly, the Bohm sheath

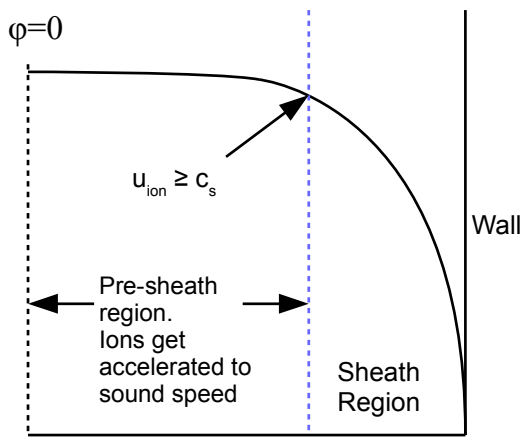


Figure 8.7: Illustration of pre-sheath region.

criterion applies to a double layer in which a pre-sheath like field will exist outside of the double layer region to accelerate the ions to their sound speed prior to entering the layer.

In classic sheath theory, a *"steady-state"* sheath structure can be maintained by a current source coming from an ionization source at the center of the confinement vessel. For a double-layer, the structure is expected to dissipate on ion time-scales. However, the structure may be maintained for a longer duration if a source of electron current can be sustained. In our fuel-pusher interface problem, this source of current will come from the initial implosion velocity of the ionized pusher shell which helps to maintain the sharp electron density gradient.

8.4 Early Time Double-Layer Assisted Kinetic Enhancement of Pusher Mix into Fuel

If the double layer electric field can exist for an appreciable amount of time, a significant number of pusher ions can be accelerated and mixed into the fuel as has been estimated in reference [130]. In an Omega ICF experiment, the laser-pulse is designed to launch a hydrodynamic shock wave in order to achieve high temperature and density of the fuel. When this shock wave catches up to the fuel-pusher interface (shock breakout), pusher ions that mixed prior as a result of the double-lyaer will be dragged deep into the fuel cavity as a result of Coulomb friction. The sequence of process is illustrated in Figure 8.8. From a hydrodynamic simulation conducted on an Omega plastic ablator capsule (Figure 8.9 [129]), the time between the ionization gradient setup and the hydrodynamic shock breakout is estimated to be 0.6[ns]. We will study this first 0.6[ns] duration for the role of the double-layer electric field in enhancing kinetic effects and mix of pusher ions into the fuel.

8.5 Problem Setup

Our initial condition is physically based on a Lagrangian hydrodynamic simulation for an Omega ICF capsule by reference [129]. In Figure 8.9, the left plot represents the position of the fuel Lagrangian cells (red lines) and the ablator/pusher Lagrangian cells (green lines) as a function of time. The right plot represents the effective ionization state of the pusher material (red line) and fuel (blue line) at the (red-green) fuel-pusher interface as a function of time. For the initial condition of our kinetic simulation, we focus at time approximately 0.4 [ns] in Figure 8.9. At this point, a pre-shock radiation wave/electron heat-flux has ionized the pusher to an effective ionization state of $Z_{eff,pusher} \approx 2.5$. The hydrocarbon (CH) plastic shell will have disassociated at this temperature and the resulting charge state of the carbon will be at $Z_C = 4$, and hydrogen will be at $Z_H = 1$.

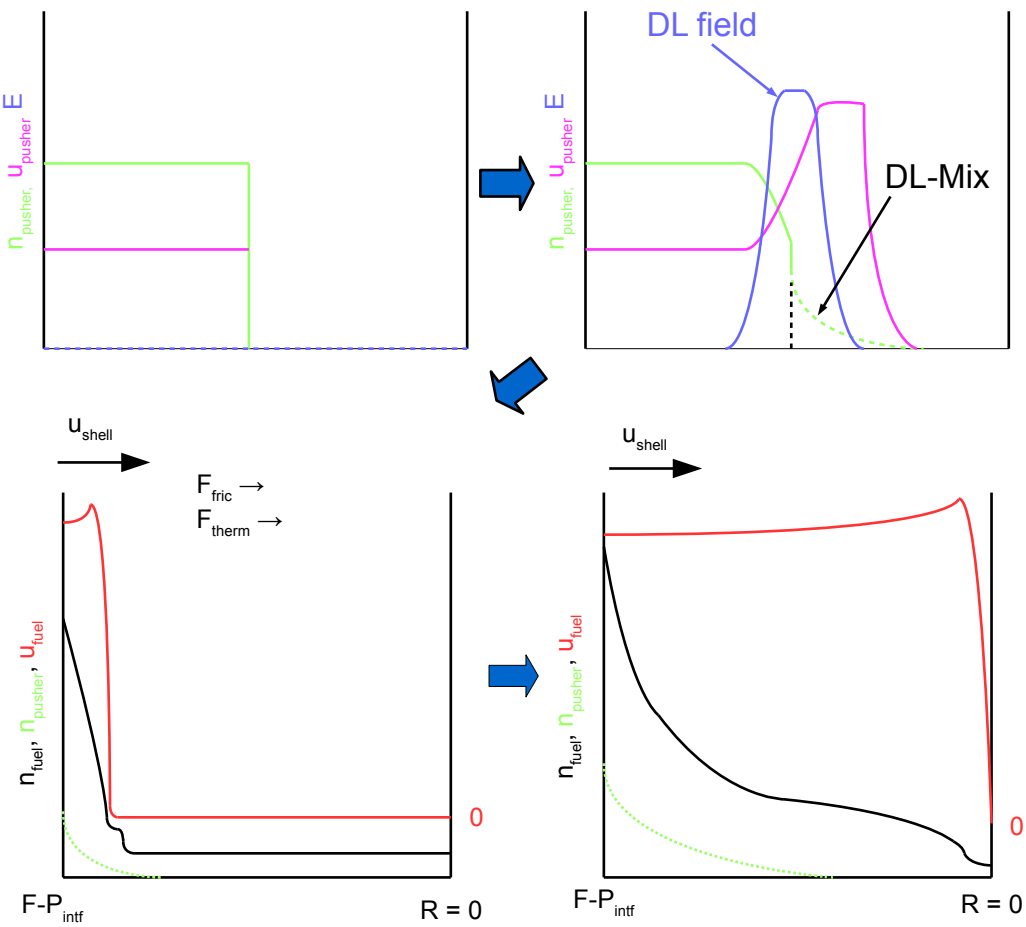


Figure 8.8: Early time double layer mix and later time hydrodynamic shock drag mix.

For this study, we consider four kinetic species: 1) electrons, 2) carbon ions, 3) hydrogen ions, and 4) DT ions. The carbon and hydrogen density on the pusher side is set to $n_C = n_H = 5 \times 10^{21}[\text{cm}^{-3}]$ while the fuel density is set to $n_{DT} = 2.5 \times 10^{21}[\text{cm}^{-3}]$. This yields an electron density on the pusher side of, $n_{e,pusher} = Z_C n_C + Z_H n_H = 25 \times 10^{21}[\text{cm}^{-3}]$ and the fuel side of $n_{e,fuel} = Z_{DT} n_{DT} = 2.5 \times 10^{21}[\text{cm}^{-3}]$. An initial momentum drive of strength $u_{drive,pusher} = 1.5 \times 10^{7}[\text{cm/sec}]$ is given on the pusher side while $u_{drive,fuel} = 0[\text{cm/sec}]$ is given on the fuel side. The values for the driver are obtained by estimating the slope

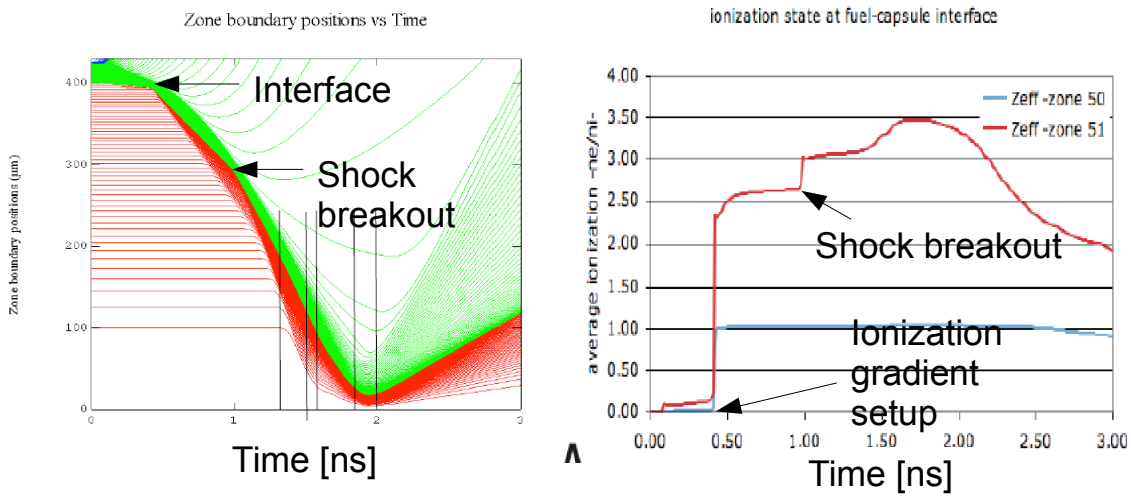


Figure 8.9: Lagrangian time-history (left) and the effective ionization state (right) near the fuel-pusher interface versus time.

on the Lagrangian plot (velocity) for the interface at $t = 0.4$[ns]. The initial temperature is assumed to be isothermal at $T = 50$[eV] for all species. Finally, quasi-neutrality, and hence zero electric field everywhere is initially assumed. The summary of initial condition is illustrated in Figure 8.10.

8.5.1 Models and Approximations

We model the interface physics by a coupled one dimensional configuration space (1D), and one dimensional velocity space (1V), time-dependent Vlasov-Fokker-Planck-Ampère (VFPA) system with no ionization physics. For species α, the Vlasov-Fokker-Planck (VFP) equation reads:

$$\frac{\partial f_\alpha}{\partial t} + v\frac{\partial f_\alpha}{\partial x} + \frac{q_\alpha}{m_\alpha}E\frac{\partial f_\alpha}{\partial v} = \sum_\beta^{N_s} \nu_{\alpha\beta}\left\{D_{\alpha\beta}\frac{\partial^2 f_\alpha}{\partial v^2} + \frac{\partial}{\partial v}\left[(v-u_\beta)\, f_\alpha\right]\right\}, \tag{8.1}$$

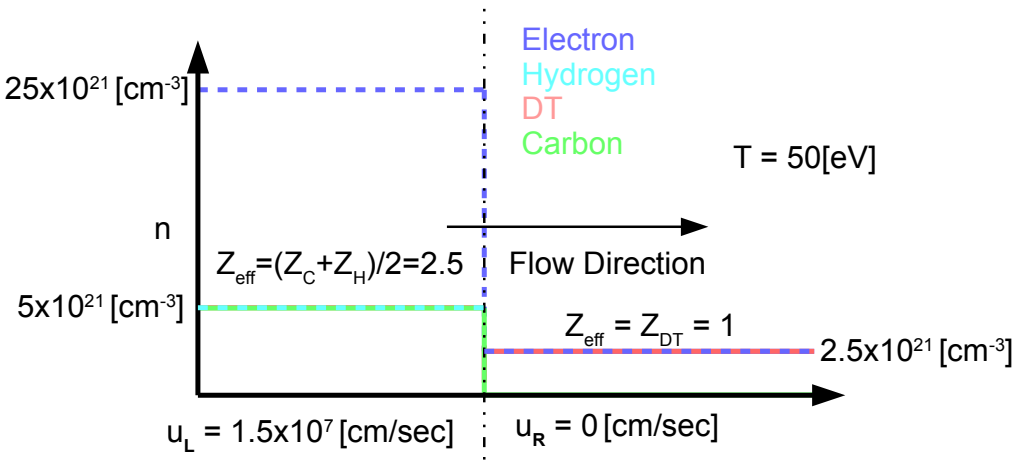


Figure 8.10: Initial condition for the interface problem.

and the electrostatic Ampère's equation as:

$$\epsilon_0 \frac{\partial E}{\partial t} + \sum_{\alpha}^{N_s} q_\alpha n u_\alpha = 0. \tag{8.2}$$

We consider the reduced Fokker-Planck operator [104, 103] which: 1) preserves the equilibrium solution (Maxwellian), 2) has the drag and diffusion physics in the phase-space, and 3) is mass, momentum, and energy conserving in the continuum. However, the collision operator is overly dissipative for fast particles since all particles are forced to relax within a time-scale $\nu_{\alpha\beta}^{-1}$. This limitation will inherently regulate fast particle mix into the fuel.

8.5.2 Numerical Initial Conditions

The problem is normalized by a density, $n^* = 10^{21}[\text{cm}^{-3}]$, mass, $m^* = 1.67 \times 10^{-27}[\text{kg}]$, charge, $q^* = 1.602 \times 10^{-19}[\text{C}]$, temperature, $T^* = 100[\text{eV}]$, and time-scale, $\tau^* = 3.607 \times 10^{-12}[\text{sec}]$. The derived quantities are the velocity, $u^* = \sqrt{T^*/m^*} = 9.79 \times 10^6[\text{cm/sec}]$, length-scale, $L^* = u^*\tau^* = 3.532 \times 10^{-5}[\text{cm}]$, electric field, $E^* = \frac{m^* L^*}{q^*(\tau^*)^2} = 2.83 \times 10^{10}[\text{V/cm}]$, and distribution function, $f^* = n^*/\sqrt{2\pi T^*/m^*} = 4.07 \times 10^{13}[\text{cm}^{-4}\text{sec}]$. Therefore, in this

study, all quantities are non-dimensionalized as:

$$\begin{aligned}
&\widehat{n} = \frac{n}{n^*}, \quad \widehat{m} = \tfrac{m}{m^*}, \quad \widehat{q} = \frac{q}{q^*}, \\
&\widehat{T} = \frac{T}{T^*}, \quad \widehat{t} = \tfrac{t}{\tau^*}, \quad \widehat{u} = \frac{u}{u^*}, \\
&\widehat{x} = \frac{x}{L^*}, \quad \widehat{E} = \tfrac{E}{E^*} \quad \widehat{f} = \frac{f}{f^*}.
\end{aligned}$$

Numerically, the distribution functions are initialized based on a Maxwellian distribution,

$$\widehat{f}_\alpha\left(\widehat{x},\widehat{v},\widehat{t}=0\right) = \frac{\widehat{n}_\alpha\left(\widehat{x},\widehat{t}=0\right)}{\sqrt{2\pi\widehat{T}_\alpha\left(\widehat{x},\widehat{t}=0\right)/\widehat{m}_\alpha}}\exp\left[-\frac{\widehat{m}_\alpha\left(\widehat{v}-\widehat{u}_\alpha\left(\widehat{x},\widehat{t}=0\right)\right)^2}{2\widehat{T}_\alpha\left(\widehat{x},\widehat{t}=0\right)}\right].$$

The initial density, fluid velocity, and temperature are initialized using a hyperbolic tangent function,

$$\widehat{n}_\alpha\left(\widehat{x},\widehat{t}=0\right) = \widehat{a}_{n_\alpha}\tanh\left[\chi\left(\widehat{x}-0.5\widehat{L}_x\right)\right]+\widehat{b}_{n_\alpha},$$

$$\widehat{u}_\alpha\left(\widehat{x},\widehat{t}=0\right) = \widehat{a}_{u_\alpha}\tanh\left[\chi\left(\widehat{x}-0.5\widehat{L}_x\right)\right]+\widehat{b}_{u_\alpha},$$

$$\widehat{T}_\alpha\left(\widehat{x},\widehat{t}=0\right) = \widehat{a}_{T_\alpha}\tanh\left[\chi\left(\widehat{x}-0.5\widehat{L}_x\right)\right]+\widehat{b}_{T_\alpha}.$$

Here, $\widehat{a}_{\mathcal{M}_\alpha}$ and $\widehat{b}_{\mathcal{M}_\alpha}$ are constants defined as,

$$\widehat{a}_{\mathcal{M}} = \frac{\mathcal{M}_R+\mathcal{M}_L}{2}-\mathcal{M}_L,$$

$$\widehat{b}_{\mathcal{M}} = \frac{\mathcal{M}_R+\mathcal{M}_L}{2},$$

where $\mathcal{M}$ is the choice of moment ($\widehat{n}$, $\widehat{u}$, or $\widehat{T}$), the subscripts R and L denote the conditions to the right and left of the interface respectively, $\widehat{L}_x$ is the size of domain in the configuration space, and χ is the smoothing factor which controls the smoothness of the hyperbolic tangent function. Having a finite gradient structure is physically expected since from the time that the thermal ionization wave sets up the ionization gradient to the start of the simulation, some level of dissipation is expected to occur via thermal motion.

For the discussed initial condition, we set $\widehat{n}_{C,L} = \widehat{n}_{H,L} = 5$, $\widehat{n}_{DT,L} = 0.01$, $\widehat{n}_{e,L} = Z_C\widehat{n}_{C,L} + Z_H\widehat{n}_{H,L} + Z_{DT}\widehat{n}_{DT,L} = 25.04$, $\widehat{n}_{C,R} = \widehat{n}_{H,R} = 0.01$, $\widehat{n}_{DT,R} = 2.5$, $\widehat{n}_{e,R} = Z_C\widehat{n}_{C,R} + Z_H\widehat{n}_{H,R} + Z_{DT}\widehat{n}_{DT,R} = 2.55$, $\widehat{u}_{C,L} = \widehat{u}_{H,L} = \widehat{u}_{DT,L} = 1.5$, $\widehat{u}_{C,R} = \widehat{u}_{H,R} = \widehat{u}_{DT,R} = 0$, $\widehat{T}_{C,L} = \widehat{T}_{H,L} = \widehat{T}_{DT,L} = \widehat{T}_{e,L} = 0.5$, $\widehat{T}_{C,R} = \widehat{T}_{H,R} = \widehat{T}_{DT,R} = \widehat{T}_{e,R} = 0.5$, and $\chi = 60$. A $\chi = 60$ equates to a width of the gradient of $\approx 51.1\lambda_{D,avg}$ where $\lambda_{D,avg}$ is the average Debye length based on the pusher and fuel side electron density, n_e at initial condition. Note that a deterministic method is used and for numerical reasons, a value of *zero* cannot be prescribed for the density, $\widehat{n}_\alpha$, or the distribution function, $\widehat{f}_\alpha$. If one does so, the slightest negativity in the solution due to undamped numerical oscillations will begin to introduce *negative* density and temperature. Negative density and temperature is a problem since for the reduced Fokker-Planck operator to remain physical, the collisional diffusion coefficient and collision frequency (which are both a functions of density and temperature) must remain positive. For this reason, the pusher (carbon and hydrogen) density in the fuel side is set to a non-zero, small value relative to the fuel side ($\widehat{n}_{C,R} = \widehat{n}_{H,R} = 0.01$). A similar treatment for the fuel density in the pusher side is also considered ($\widehat{n}_{DT,L} = 0.01$).

For this study, *initially*, we use a configuration space domain size of $\widehat{L}_x = 10$, a configuration space cell count of $N_x = 3000$, a velocity domain size of $[\widehat{v}_{C,min}, \widehat{v}_{C,max}] = [15\widehat{v}_{C,th,L}, 15\widehat{v}_{C,th,L}]$, $[\widehat{v}_{H,min}, \widehat{v}_{H,max}] = [10\widehat{v}_{H,th,L}, 10\widehat{v}_{H,th,L}]$, $[\widehat{v}_{DT,min}, \widehat{v}_{DT,max}] = [10\widehat{v}_{DT,th,L}, 10\widehat{v}_{DT,th,L}]$, $[\widehat{v}_{e,min}, \widehat{v}_{e,max}] = [10\widehat{v}_{e,th,L}, 10\widehat{v}_{e,th,L}]$, $\widehat{v}_{\alpha,th,L} = \sqrt{2\widehat{T}_{\alpha,L}/\widehat{m}_\alpha}$, and a velocity space cell count of $N_{C,v} = 300$, $N_{H,v} = 200$, $N_{DT,v} = 200$, $N_{e,v} = 200$. We will first simulate *fully kinetically* up to about $\widehat{t} = 0.7$ (≈ 2.5[ps]). Afterwards, we will perform a

sequence of *remapping* onto a larger domain size, and switch to a *hybrid* solver (both are discussed shortly) to simulate up to $\widehat{t} \approx 166$ ($\approx 0.6[ns]$).

8.6 Solver

We use the newly developed algorithm discussed in Chapter 7 to solve the coupled VFPA system fully implicitly. The code solves for the multi-species Vlasov-Fokker-Planck-Ampère system deterministically, on a stationary 1D1V Eulerian grid. The code has a variety of initial condition features and solver options. We focus only on key features and options of the code that were critical in simulating the interface physics problem such as: 1) Nonuniform mesh generation, 2) adaptive time-stepping, 3) remapping, 4) hybrid solver option, and 5) open boundary condition. We will also briefly provide the code framework developed for this work.

8.6.1 Nonuniform Mesh Generation

The interface problem is a multi length-scale problem by nature. Early on, the gradient structures are on the order of the very short Debye length, λ_D, and carbon collisional mean-free-path, λ_{CC}. It is therefore critical to resolve these structures for the accuracy of the solution. However, at later times, these short length-scale structures dissipate and begin to approach the longer hydrogen mean-free-path, λ_{HH}, and the hydrogen-electron collisional mean-free-path, λ_{He}. In order to perform the simulation within a reasonable time-frame, it is necessary to focus the mesh resolution in regions where necessary. To achieve this, we use a nonuniform mesh generation scheme. We consider a sine mapping for the cell-face:

$$x_{i+1/2} = L_x \left\{ \xi_{i+1/2} + \frac{\gamma_{\Delta x}}{2\pi} \left[\sin\left(2\pi \xi_{i+1/2}\right) \right] \right\}, \tag{8.3}$$

while the cell-centers are defined as the geometrical center,

$$x_i = \frac{x_{i+1/2} - x_{i-1/2}}{2}. \tag{8.4}$$

Here, $0 \leq \xi < 1$ is the logical coordinate variable and $\gamma_{\Delta x}$ is the mapping factor which controls the non-uniformity of the mesh. For the interface problem, we use $\gamma_{\Delta x} = 0.8$.

8.6.2 Adaptive Time Stepping

Similar to the length-scale, the interface physics is a multi time-scale problem by nature. Due to the early time sharp gradient structure that exists at the interface, a spectrum of electrostatic wave modes can be excited. From an isothermal single fluid assumption, if one performs a dispersion analysis on an electron continuity, momentum equation, and Poisson's equation, one will obtain the following dispersion relationship [61],

$$\omega = \sqrt{\omega_{p,e}^2 + \frac{3}{2}k^2 v_{th}^2}. \tag{8.5}$$

Here, ω is the wave angular frequency for an electrostatic wave as a function of electron plasma frequency $\omega_{p,e}$, wave vector, k, and thermal velocity, v_{th}. The group velocity for a mode with wave vector k is,

$$v_g = \frac{\partial \omega}{\partial k} = \frac{3}{2}\frac{k v_{th}^2}{\sqrt{w_{p,e}^2 + \frac{3}{2}k^2 v_{th}^2}}. \tag{8.6}$$

It is therefore seen that higher frequency modes will travel at a higher group velocity. The dynamical time-scale in which the problem will evolve due to these electrostatic waves can be roughly estimated as,

$$\tau_{p,e} = \frac{\Delta x}{v_g}. \tag{8.7}$$

It can be seen that if there exists a high-frequency mode with an appreciable amplitude traveling through a fine mesh, one must resolve $\tau_{p,e}$ for accuracy reasons. Due to collisions, these wave structures will be damped out eventually. However, when one encounters a strong driver which can maintain a sharp gradient scale-length for an appreciable amount of time, high frequency structures may continue to get excited, or maintained. Eventually, as the structures relax, the high frequency electrostatic modes will damp away, and the dynamical time-scale will approach the thermal relaxation time-scale and other hydrodynamical time-scales. However, an automated detection scheme for transition in these time-scales is difficult to design. For this reason, we use a more intuitive approach to adjust our time-step size.

The adaptive time-step scheme will adjust the time-step size, Δt, from time-step to time-step based on two criterion. For the first criteria, we check if the number of HOLO iteration reaches some maximum allowed value (criterion 1). If it does, we reduce the time-step size accordingly,

$$\Delta t^k = \gamma_{\Delta t} \Delta t^k, \ \gamma_{\Delta t} < 1, \tag{8.8}$$

and redo the time-step. For the second criterion, we check if the nonlinear VFPA system was converged within a certain number of HOLO iterations (criterion 2). If it did, we increase the time-step size for the next time-step accordingly,

$$\Delta t^k = \eta_{\Delta t} \Delta t^{k-1}, \ \eta_{\Delta t} > 1, \tag{8.9}$$

and is checked if it is bounded by the maximum allowed time-step size, $\Delta \widehat{t}_{max}$, set by the user. If the number of HOLO iterations exceeds criterion 2, then we are allowed to move to the next time-step, however, with the time-step size reduced as:

$$\Delta t^k = \gamma_{\Delta t} \Delta t^{k-1}. \tag{8.10}$$

A flow-chart of the adaptive time-stepping scheme used in this study is shown in Figure 8.11. In this study, we used: criterion1 = 20, criterion2 = 10, $\eta_{\Delta t} = 1.05$, $\gamma_{\Delta t} = 0.8$, and

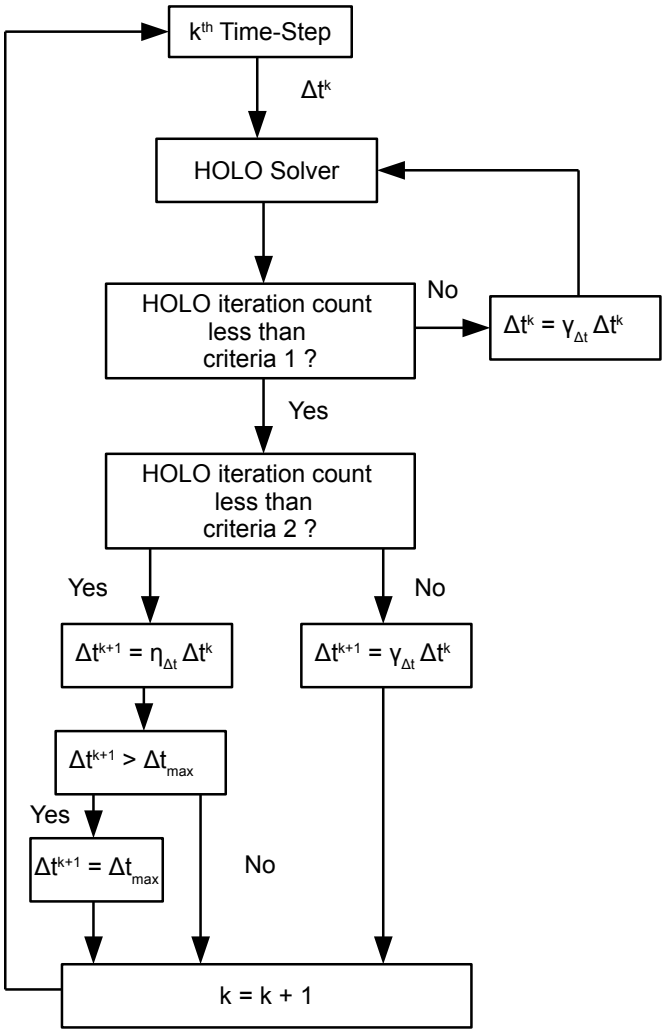


Figure 8.11: Flow diagram of adaptive time-stepping.

$\Delta\widehat{t}_{max} = 0.1$.

8.6.3 Remapping

For a long time integration, the solution structure will eventually propagate out of the boundary. In order to follow the evolution of the structures at longer times, we perform an

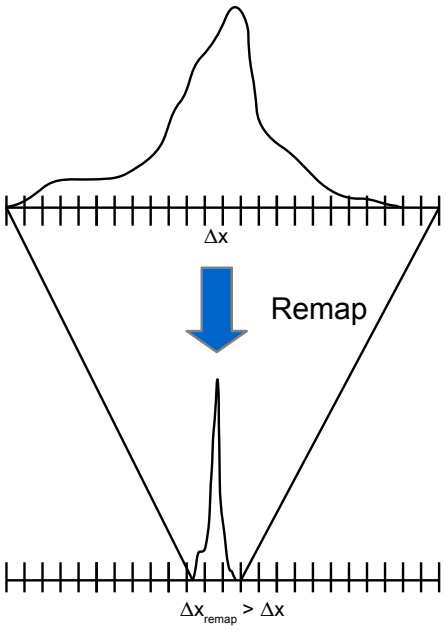


Figure 8.12: Remapping process.

occasional *remapping* of the solution to a larger domain. In Figure 8.12, we illustrate the remapping process. The remapping is achieved by performing a linear interpolation from the fine grid, small domain onto a coarse grid, large domain. The distribution function for different species is remapped while the electric field can either be remapped, or recomputed using a quasi-neutral model,

$$E\left(x, t_{remap}\right) = -\frac{m_e \frac{\partial S_e}{\partial x}}{q_e n_e}.$$

Here, $S_e = \left\langle v^2, f_e \right\rangle_v$ is the electron total stress factor defined as the second velocity moment of the electron distribution function. Depending on the gradient scale-length of the solution and the linear interpolation error associated with the remapping of the field, one will provide

less error for the discrete Gauss-law,

$$GL_{error} = \left| \epsilon_0 \frac{E_{i+1/2} - E_{i-1/2}}{\Delta x_i} - \sum_\alpha q_\alpha n_{\alpha_i} \right|_2 , \tag{8.11}$$

than the other. For the initial field (upon remapping of the distribution function), we choose whichever provides the smaller initial GL_{error}. For this study, we performed four remappings at different points in time. The relationship between the time and domain size is organized below:

- Remap0: $\widehat{t} = 0$, $\widehat{L}_x = 10$.
- Remap1: $\widehat{t} = 0.7$, $\widehat{L}_x = 40$.
- Remap2: $\widehat{t} = 3$, $\widehat{L}_x = 160$.
- Remap3: $\widehat{t} = 20$, $\widehat{L}_x = 600$.
- Remap4: $\widehat{t} = 100$, $\widehat{L}_x = 1000$.

8.6.4 Hybrid Solver

At later times, as the gradient structures dissipate, electrons can be modeled sufficiently as a fluid, using a Braginskii closure [117]. For computational efficiency reasons, at later times, it is therefore advantageous to use a *hybrid* solver in which electrons are modeled as fluid and ions are still modeled fully kinetically. In the hybrid solver, no electron HO equation exists and electron continuity, momentum, and energy equations are solved in the LO system. We remind the reader that because we carry the addition of continuity and momentum equation for the electrons, we still allow for charge-separation (in reference [120], only the energy equation is used and quasi-neutrality is assumed). Unlike the ion LO quantities, the electron quantities are actually evolved from time-step to time-step. The only difference in the actual

implementation between the fully kinetic solver and the hybrid solver is that there is: 1) **no** HO electron solve, 2) **no** reset of the LO electron solution to the HO electron solution upon nonlinear convergence within a time-step, and 3) **no** calculation of *consistency terms* for the electron moment equations.

We briefly discuss the difference in both the *numerical time-scales* and physical time-scales between the fully kinetic solver and the hybrid solver. For the fully kinetic solver, the restrictive numerical time-step size for stability is due to the electron streaming CFL,

$$\Delta t_{CFL,e} = \frac{\min|\Delta x|}{\max|v_e|}. \tag{8.12}$$

However, for the hybrid solver, the limiting time-step size is due to the carbon ion collisional diffusion CFL,

$$\Delta t_{CFL,C_{diff}} = \frac{\min|\Delta v_C^2|}{\max|\nu_{CC} D_{CC}|}. \tag{8.13}$$

For the mesh sizes considered in the study, typically $\Delta t_{CFL,C_{diff}} \approx \Delta t_{CFL,e}$.

For the fully kinetic solver, the restrictive physical time-scale is the inverse electron plasma frequency,

$$\omega_{p,e}^{-1} = \sqrt{\frac{m_e \epsilon_0}{n_e q_e^2}}. \tag{8.14}$$

For the hybrid scheme, the restrictive physical time-scale is the carbon ion self collisional relaxation time-scale,

$$\tau_{CC} = \nu_{CC}^{-1} = \left(1.515 \times 10^{-18} \frac{n_C q_C^4 10}{(m_C/m_p)^{1/2} T_C^{3/2}} \right)^{-1}. \tag{8.15}$$

Therefore for a hybrid solver, a traditional Picard iteration scheme will suffer many iterations when trying to step over τ_{CC} and explicit time integration schemes are required to take time-step sizes that resolve $\Delta t_{CFL,C_{diff}}$. In the hybrid mode, the HOLO algorithm will allow one

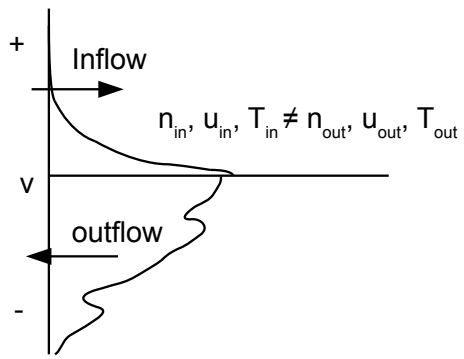


Figure 8.13: Illustration of standard inflow B.C.

to efficiently step over these time-scales and study longer-time integration problems. For the interface problem, we switch to a hybrid solver upon performing the first remapping.

8.6.5 Open Boundary Condition

We discuss the extension of open boundary conditions, which was first developed by reference [131] for the PIC application, to an Eulerian approach. The standard inflow boundary is based on some fixed prescription for a Maxwellian distribution function at the boundary, i.e.

$$f_{B,j} = \frac{n_B}{\sqrt{2\pi T_B/m}} \mathrm{e}^{-\frac{m\left(v_j - u_B\right)^2}{2T_B}}.$$

Here, the subscript B denotes the value at a boundary. This prescription for the boundary condition may become an issue as the bulk structure of the solution approaches the boundary. The distribution function of the incoming Maxwellian may be significantly different from the outgoing distribution function. The condition at later times near the boundary is illustrated in Figure 8.13. As can be seen, at later times, the fluid moment quantities can be significantly different between the solution directly adjacent to the boundary (outflow),

and at the boundary (inflow). This unphysical situation may cause instabilities to arise near the boundary. Therefore, in order to minimize the gradient of moment quantities at the boundary, one redefines the Maxwellian distribution function in which the inflow flux is computed as,

$$f_B^{k+1} = \frac{n_{B+1/2}^{k+1}}{\sqrt{2\pi T_{B+1/2}^{k+1}/m}} \mathrm{e}^{-\frac{m\left(v_j - u_{B+1/2}^{k+1}\right)^2}{2T_{B+1/2}^{k+1}}}, \tag{8.16}$$

$$n_{B+1/2}^{k+1} = \sum_{j=1}^{N_v} \Delta v_j f_{B+1/2,j}^{k+1}, \tag{8.17}$$

$$u_{B+1/2}^{k+1} = \frac{\sum_{j=1}^{N_v} \Delta v_j v_j f_{B+1/2,j}^{k+1}}{\sum_{j=1}^{N_v} \Delta v_j f_{B+1/2,j}^{k+1}}, \tag{8.18}$$

$$T_{B+1/2}^{k+1} = m \frac{\sum_{j=1}^{N_v} \Delta v_j \left(v_j - u_{B+1/2}^{k+1}\right)^2 f_{B+1/2,j}^{k+1}}{\sum_{j=1}^{N_v} \Delta v_j f_{B+1/2,j}^{k+1}}. \tag{8.19}$$

Here, the subscript $B+1/2$ denotes the internal cell index directly adjacent to the boundary. Refer to Figure 8.14. The boundary condition therefore becomes nonlinear. However, we absorb this nonlinearity in the boundary condition through the HOLO iteration. This new definition for the inflow flux will minimize the deviation of the moment quantities between the boundary and the internal cell. This can be illustrated in Figure 8.15.

8.6.6 Code Framework and Architecture

We briefly provide an overview of the structure of the code developed in this study. The high-level framework was completely written in MATLAB for data management. All Krylov

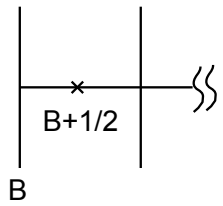


Figure 8.14: Illustration of boundary cell

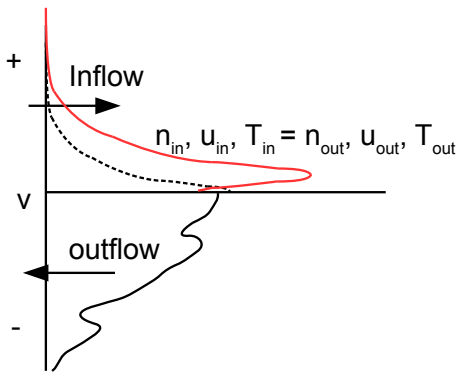


Figure 8.15: Illustration of the open B.C.

routines [59] were executed using MATLAB's built-in routines. MATLAB is also responsible for high-level iteration procedures such as time-stepping and the HOLO iteration. The purpose for making MATLAB manage data structures is to cut down on explicit memory management, which is highly subject to bugs. This allows for rapid code development, which MATLAB is intended for.

The highly work intensive low-level functions such as matrix-vector (matvec) evaluation used in JFNK, and moment calculations used for the HO system is handled by C++ through MATLAB's built in MEX functionality. All C++ routines are parallelized over the grid

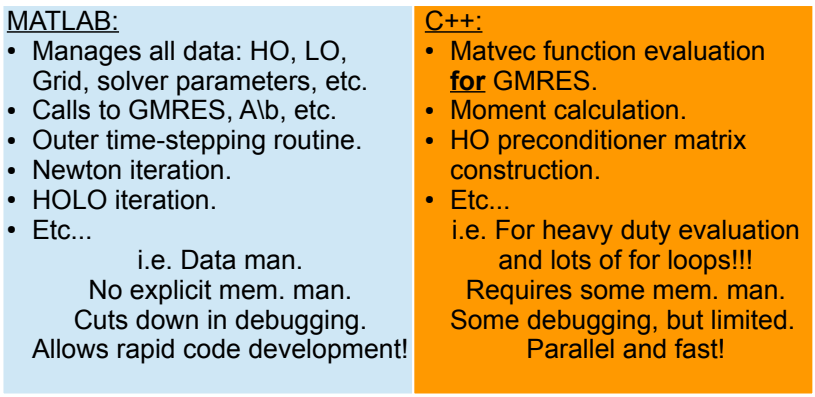


Figure 8.16: Comparison of MATLAB and C++ work distribution.

through an on-node OpenMP [132] implementation. The purpose of making C++ handle the very low-level operations is because of the computational efficiency of a compiled language (C++) over an interpreted language (MATLAB). For functions which require many *for-loops*, interpreted languages such as MATLAB are known for the painfully slow performance. On the other hand, compiled languages such as C++ require explicit memory management and are subject to bugs, however if properly done can obtain orders of magnitude increase in performance over MATLAB. It was therefore critical to split the different tasks between the two programming languages to develop the new code, and to solve the interface problem. A diagram illustrating the responsibilities of MATLAB and C++ is shown in Figure 8.16.

8.7 Initial Field Structure, Pre-Sheath, and Ion-Acceleration

From the double-layer field theory, we should observe the initial gradient structure to generate two stages for the electric field: 1) the classic initial charge-separation electric field at the interface as depicted in Figure 8.4, and 2) evolution into a double-layer electric field. We show

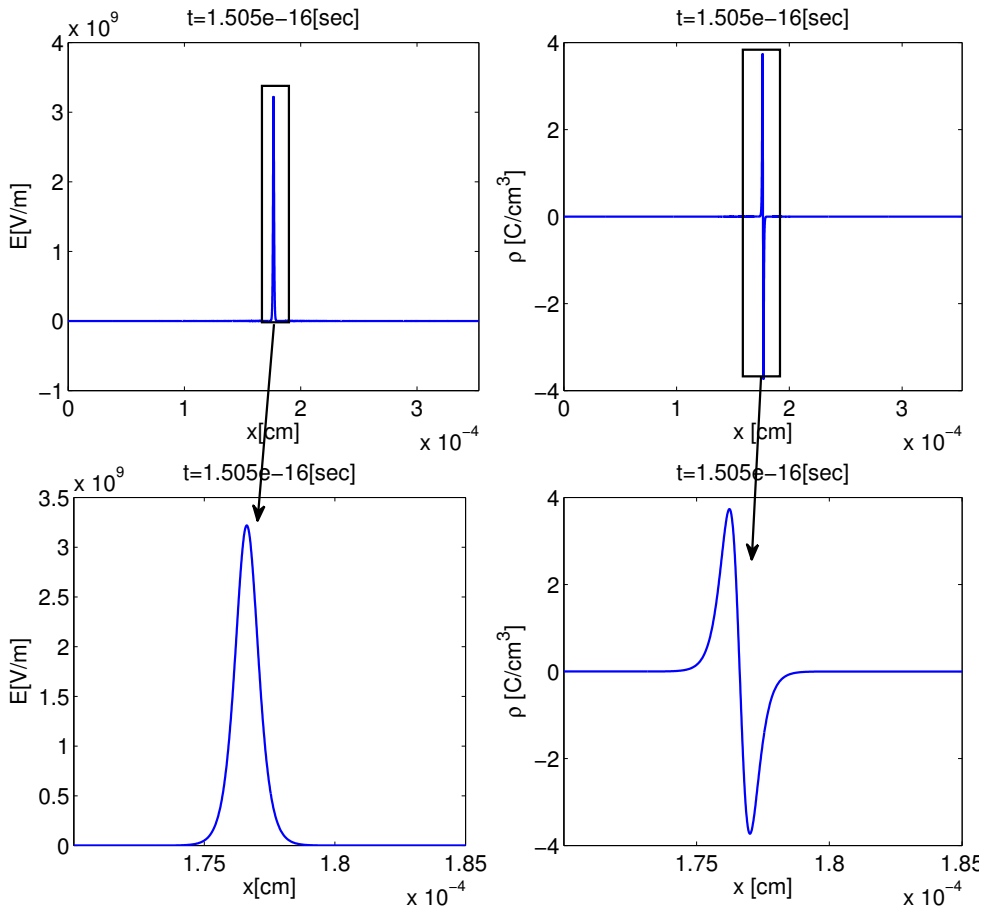


Figure 8.17: Initial charge separation field due to electron streaming.

the initial field structures and their transition at early times. In Figure 8.17, we show the initial field due to electrons streaming across the interface. We see the initial field structure similar to that in Figure 8.4. In Figure 8.18, we show the evolved double-layer electric field that follows the contact surface of the carbon ions. The strength of the field is in good agreement with theory [130], which predicts a field of order $10^9 \leq E \leq 10^{10}$[V/m]. Due to the multi-species consideration, the double layer field structure is more complicated than the simple illustration shown in Figure 8.5. However, general expected trends are observed such as: 1) double layer thickness $\approx 30\lambda_{D,avg}$ (based on $\lambda_{D,avg} \approx 7 \times 10^{-8}$[cm], where the averaging was performed based on initial pusher side and fuel side electron density, n_e), and

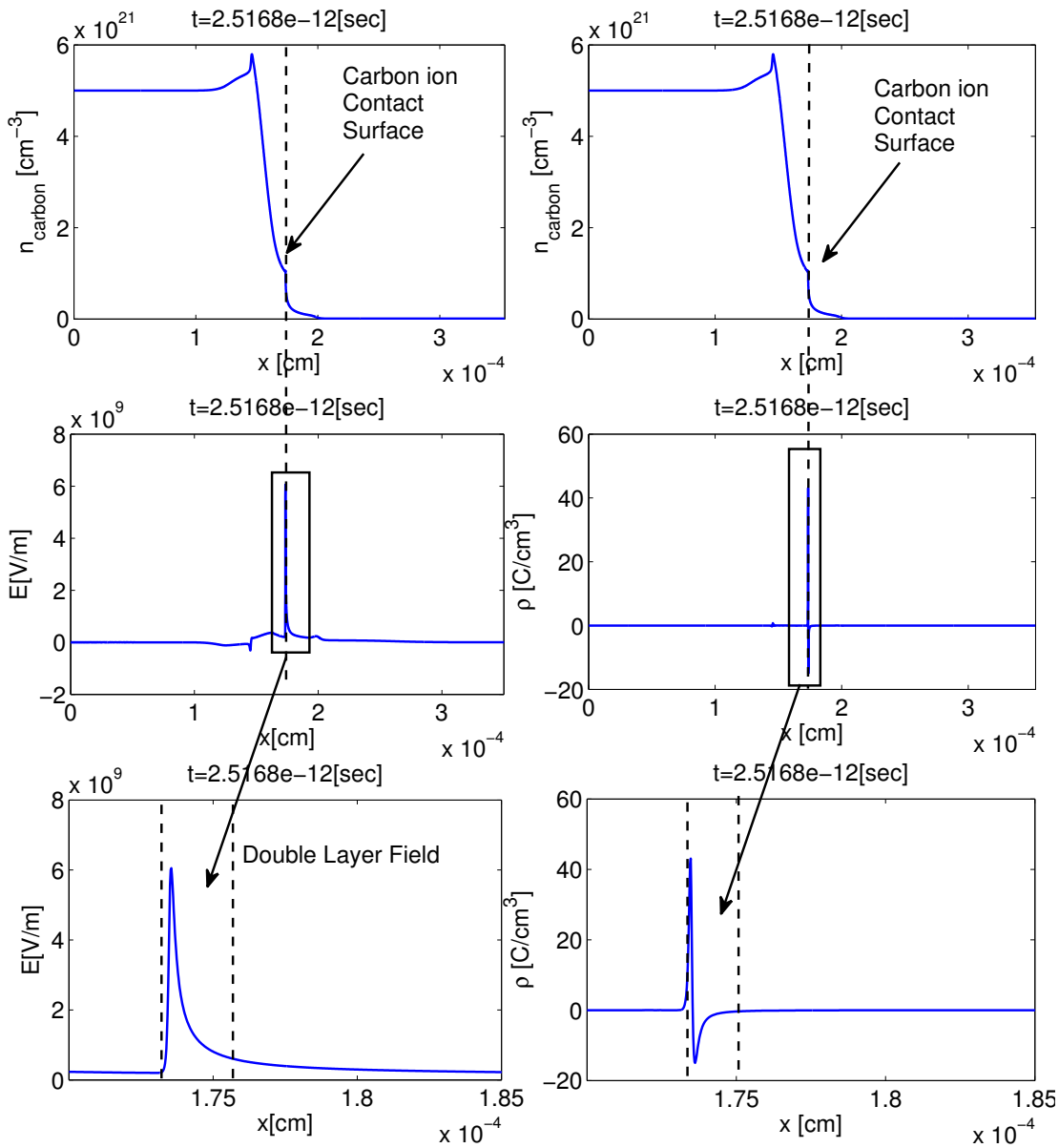


Figure 8.18: Later double layer field at carbon ion contact surface.

2) two distinct charge separation zones.

Similar to a sheath, due to a pre-sheath structure, ions will be accelerated to **at least** sound speed **upon** entering the double-layer. We show the structure of the pre-sheath and

the ion phase-space plot to verify that these structures are indeed observed. In Figure 8.19, we show the double-layer electric field at the carbon ion contact surface, the pre-sheath field that exists behind it, and the carbon ion phase-space plot to illustrate the acceleration of carbon ions to their sound speed, $c^*_{s,carbon}$, prior to entering the double layer. As can be seen from the carbon ion phase-space plot, in the region labeled as the pre-sheath region, carbon ions are accelerated to $\approx 2c^*_{s,carbon}$ prior to entering the region labeled as the double-layer region. Once the carbon enters the double-layer, it is seen to further accelerate to $\approx 4c^*_{s,carbon}$ due to the double-layer field. This is seen to form a beam structure across the carbon ion contact surface. This beam structure is what is responsible for the penetration of carbon ions deep into the fuel and kinetic mixing at early times. We will revisit this shortly.

8.8 Sensitivity Study of Early Time Field

We quantify the sensitivity of the double-layer electric field at early times as a function of varying initial conditions by performing a parametric study. The quantities to vary are the following:

- Density, $\widehat{n}$.
- Driver velocity, $\widehat{u}_L$.
- Temperature of pusher and fuel, $[\widehat{T}_L, \widehat{T}_R]$.
- Configuration space cell resolution, N_x.
- Gradient smoothness factor, χ.

For the parametric study, to speed up the simulation time per case, we use a configuration cell resolution of $N_x = 1000$.

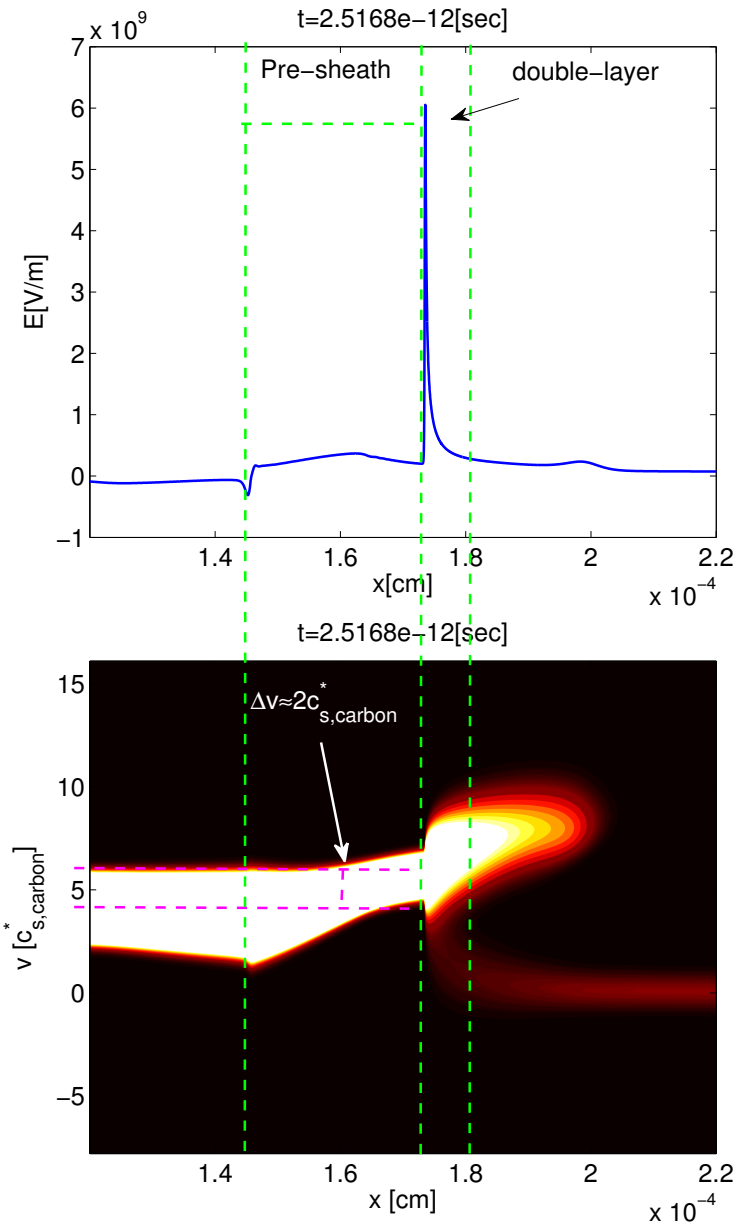


Figure 8.19: Pre-sheath zone and ion acceleration to $\geq c^*_{s,carbon}$ (carbon ion sound speed).

8.8.1 Sensitivity to Density

We discuss the sensitivity due to varying the pusher and fuel density. The density of the pusher side is varied between $\widehat{n}_L = 5$, 2.5, and 1. The initial fuel density is always assumed

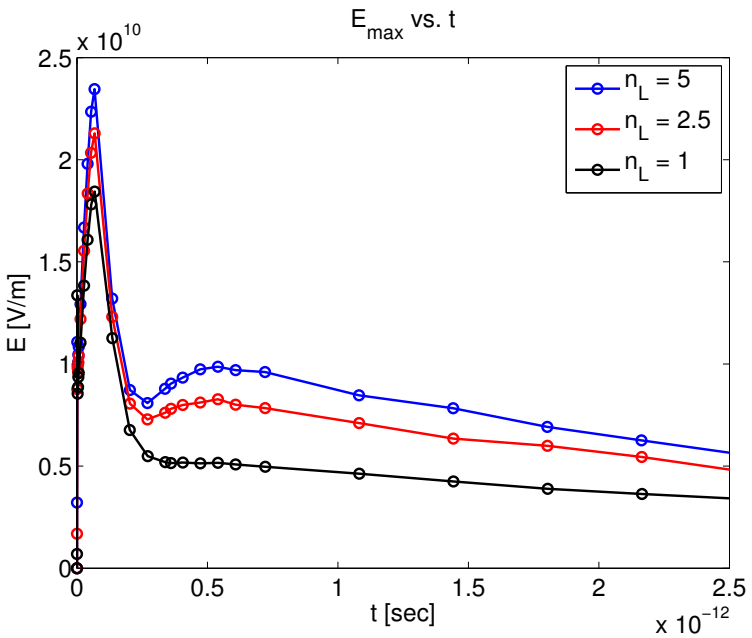


Figure 8.20: Peak field vs. time for various $\widehat{n}$ cases.

to be half of the pusher. The time-history of the peak electric field is shown in Figure 8.20. As can be seen, the strongest electric field is measured for the highest density case. This is expected since for a higher density, there will be more electrons streaming across the interface to cause a larger charge-separation, and a higher flux to sustain a stronger field.

8.8.2 Sensitivity to Driver Strength

We discuss the sensitivity due to varying the driver strength. The driver strength on the pusher side is varied between, $\widehat{u}_L = 0$, 0.75, and 1.5. The time-history of the peak electric field is shown in Figure 8.21. We observe that for a stronger driver, a stronger field is observed both initially and later in time. This observation is consistent with the predictions of stronger sustained field strength due to a strong source of current (driver) via a maintained large electron density gradient.

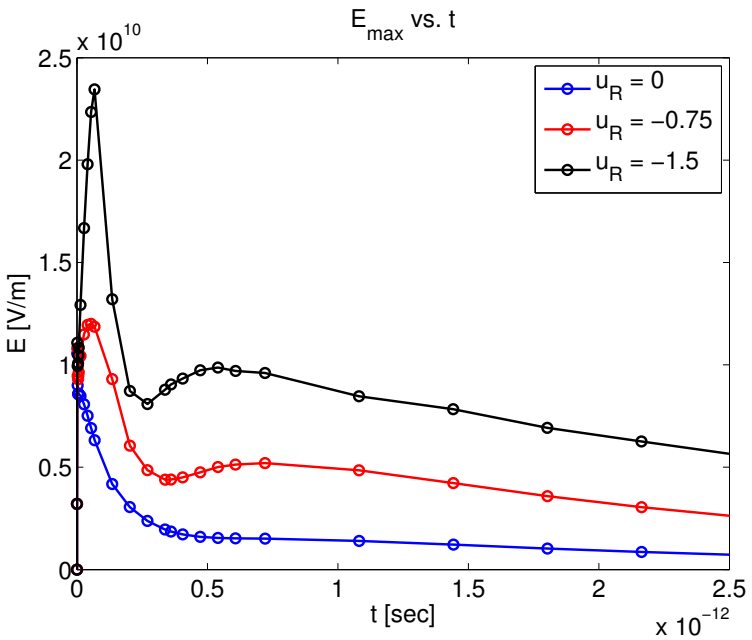


Figure 8.21: Peak field vs. time for various $\widehat{u}_L$ cases.

8.8.3 Sensitivity to Temperature

We discuss the sensitivity due to varying the temperature. The temperature on both sides is varied between $[\widehat{T}_L, \widehat{T}_R] = [1, 1]$, $[1, 0.5]$, $[0.5, 0.5]$, and $[0.5, 0.25]$. The time-history of the peak electric field is shown in Figure 8.22. It can be seen that in general, the higher the temperature, and the gradient in the temperature, the greater the initial field. This can be understood by considering the physical definition of the temperature, which is the second thermal moment of the distribution function. This means that at higher temperature, more electrons will exist at the tail end of the distribution function (higher energy). These high energy electrons can stream across the interface more rapidly than the slower electrons, causing a larger charge-separation. The reason why a gradient in the temperature supports a stronger initial field is because if the distribution is hot on one side and cold on the other, there will be fewer energetic electrons from the cold side to cancel the current supplied from the hot side.

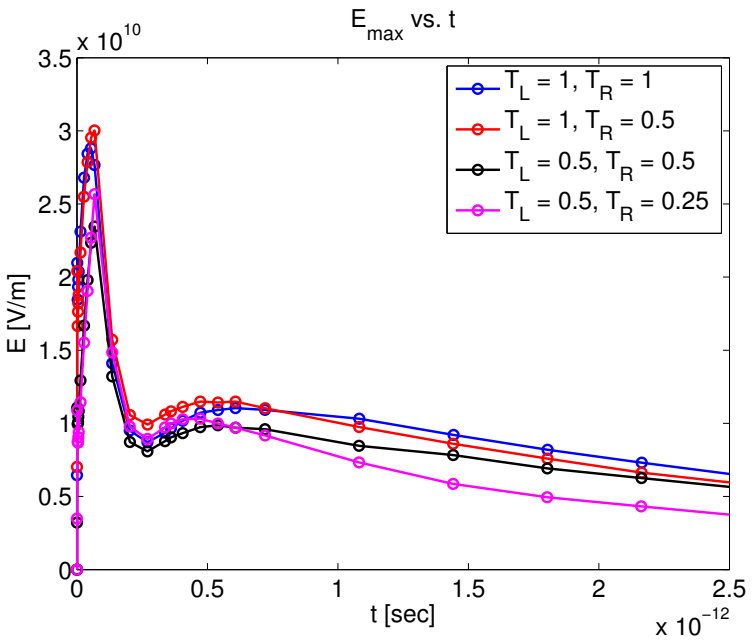


Figure 8.22: Peak field vs. time for various $[\widehat{T}_L, \widehat{T}_R]$ cases.

8.8.4 Sensitivity to Configuration Space Cell Resolution

We discuss the sensitivity due to varying the configuration space cell resolution. The number of configuration space cells is varied by $N_x = 1000$, 2000, and 3000. The time-history of the peak electric field is shown in Figure 8.23. As can be seen, the initial field is not sensitive to the cell resolution. This is because due to the non-uniform mesh, initially, the cell spacing is resolving the fine-scale structures on the order of λ_D and λ_{CC}. However, at later times, we see the lower mesh resolution case having a lower peak field. This is because away from the center, the mesh resolution is decreasing rapidly and the cell spacing is not resolving the fine-scale structures at later times. However, as the fine-scale structures dissipate, the three cases tend to approach the same field strength at even later times.

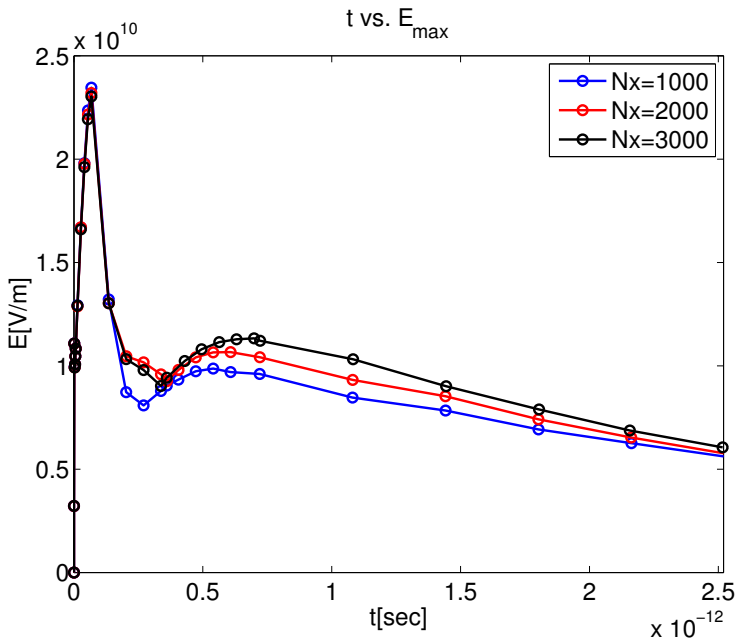


Figure 8.23: Peak field vs. time for N_x cases.

8.8.5 Sensitivity to Initial Gradient Scale-Length

Finally, we discuss the sensitivity due to varying the gradient smoothness factor. The gradient smoothness factor is varied by $\chi = 20$, 60, and 100. The gradient smoothness factor will spread the initial density discontinuity over $20.4\lambda_{D,avg}$, $51.1\lambda_{D,avg}$, and $127.6\lambda_{D,avg}$ for $\chi = 20$, 60, and 100 cases, respectively. $\lambda_{D,avg} \approx 7 \times 10^{-8}$[cm] is the average Debye length of the pusher and fuel side at initial condition. The time-history of the peak electric field is shown in Figure 8.24. As can be seen, the initial field strength is strongly dependent on the initial gradient-scale length of the interface. This is expected as the field strength can be estimated by sheath theory as, $|E| = |-\partial\phi/\partial x| \approx |-\Delta\phi/L| \approx |T/3q_eL|$. Here, L is the characteristic scale length, which for a sheath is $\mathcal{O}(\lambda_D)$ and for a double-layer, is $\mathcal{O}(10\lambda_D)$. By increasing or decreasing the gradient smoothness factor, χ, one is effectively altering L. Therefore, for smaller L (larger χ), the field is expected to be stronger and for larger L (smaller χ), the field is expected to be weaker, as seen in Figure 8.24.

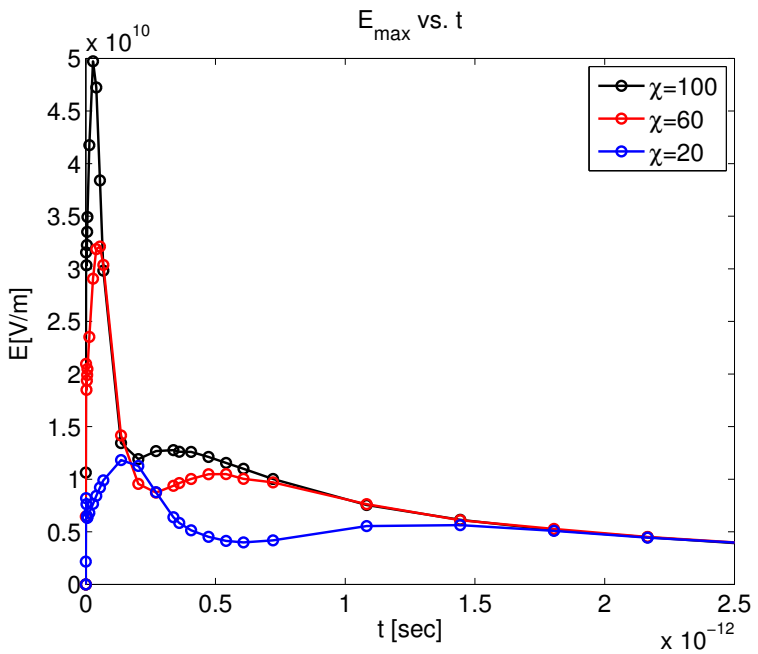


Figure 8.24: Peak field vs. time for χ cases.

8.9 Sustained Kinetic Effects

Due to the sustained strong field at the carbon ion contact surface, the pusher ions can sustain a beam-like structure in the phase-space as can be seen in Figure 8.19. Since the *temperature* is defined as the second thermal moment of the distribution function,

$$T_\alpha = m_\alpha \frac{\left\langle (v-u_\alpha)^2, f_\alpha \right\rangle_v}{n_\alpha}, \tag{8.20}$$

and the beam-structure will effectively increase the width of the distribution function, an increase in temperature is observed. Since the collision frequency is $\nu_{\alpha\alpha} \propto 1/T_\alpha^{3/2}$, this renders the Fokker-Planck collision operator less collisional. We show that due to the strong electric field and the increase in the temperature, the kinetic effects can be sustained for durations much longer than 70[ps] for the carbon ions. To check for the kinetic behavior of the carbon ions, we observe the local Knudsen number, Kn_P, for the carbon ions, which is

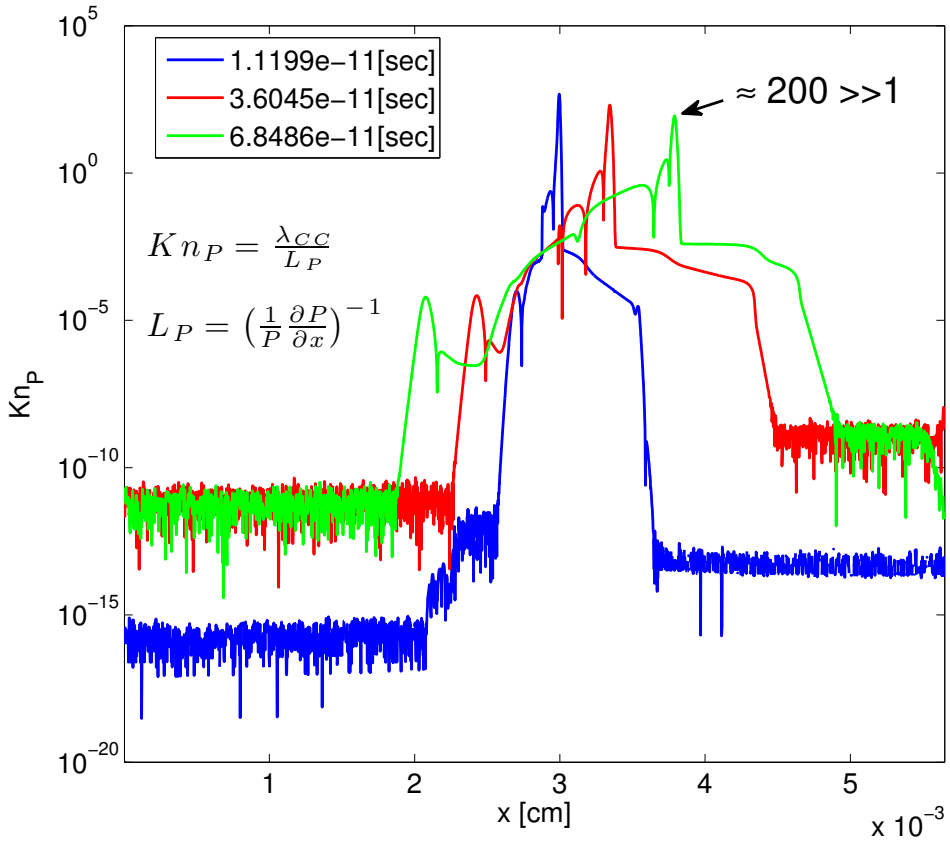


Figure 8.25: Knudsen number of carbon ions at later time.

defined as,

$$Kn_P = \frac{\lambda_{CC}}{L_P}, \tag{8.21}$$

where L_P is the gradient-scale length of pressure,

$$L_P = \left(\frac{1}{P}\frac{\partial P}{\partial x}\right)^{-1}. \tag{8.22}$$

In Figure 8.25, we show the Knudsen number at later times. As can be seen, even at later times at $t \approx 70$[ps], $Kn_P \approx 200$. For hydrodynamic solvers to be accurate $Kn_P \ll 1$ must

hold. This is clearly not the case and the need for a kinetic treatment for the ions are clear.

8.10 Carbon Ion mix into Fuel

In a theoretical study in reference [130], it is predicted that the double-layer electric field can accelerate the carbon ions to $v_{carbon} = 10^7$[cm/sec]. With a carbon ion density at the fuel-pusher interface sustained at $n_{carbon} = 5 \times 10^{21}$[cm^{-3}], approximately 2×10^{16} carbon pusher ions can be mixed into the fuel. As the later time hydrodynamic shock breaks out of the interface and drags the pusher ions and spreads them uniformly in the fuel, they will account for 10% atom fraction of the fuel. This is significantly higher than what hydrodynamic mix predicts [126] at this early time. If this amount of mix can occur, it can account for a factor of three reduction in the final fuel temperature (relative to what hydrodynamic codes predict) due to Bremsstrahlung radiation loss and a heat-capacity effect [130].

We show the time evolution of the amount of carbon ions mixed into the fuel at 0.6[ns] from a more detailed numerical simulation. For our Cartesian 1D, open boundary problem, we define carbon ion *mix* as:

$$N_{C,mix} = A_{surf} \int_{x_{n_{DT}=2.5}}^{x_{tail}} n_C dx. \tag{8.23}$$

Here, $A_{surf} = 0.015$[cm^2] is the prescribed surface area of an Omega capsule from a theoretical study in reference [130] and taken from simulations in [129], x_{tail} is the location of the carbon ion tail in the fuel, $x_{n_{DT}=2.5}$ is the nearest location from the carbon pusher where the fuel density is $n_{DT} = 2.5 \times 10^{21}$[cm^{-3}]. Similarly, the atom fraction of the carbon ions to fuel ions is defined as,

$$f_{mix} = \frac{\int_{x_{n_{DT}=2.5}}^{x_{tail}} n_C dx}{\int_{x_{n_{DT}=2.5}}^{x_{tail}} n_{DT} dx}. \tag{8.24}$$

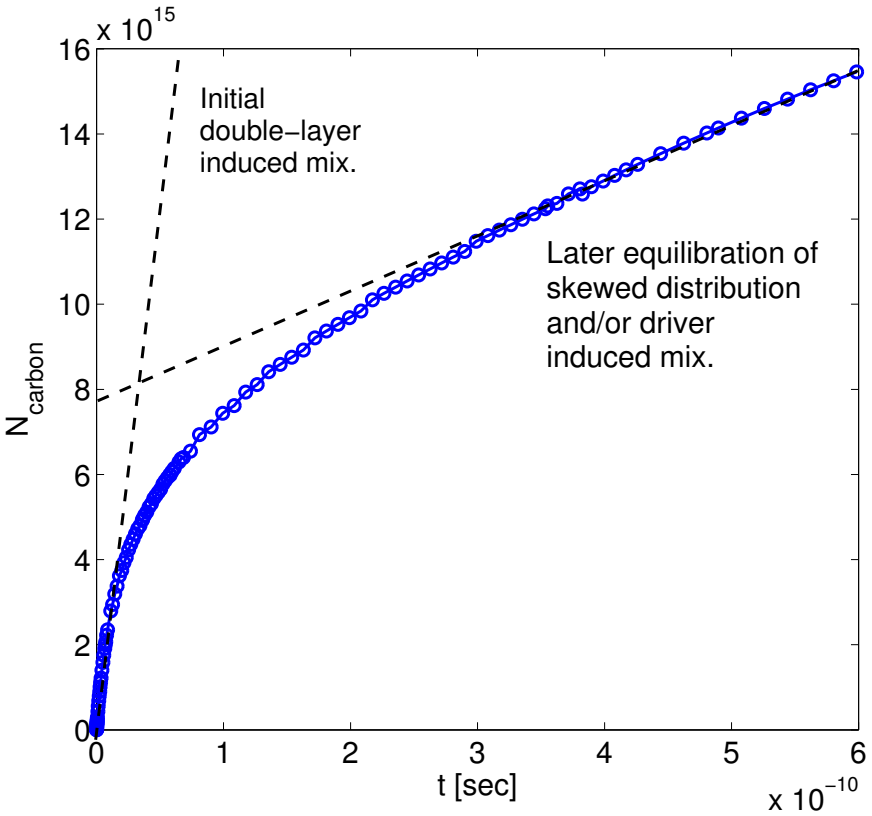


Figure 8.26: Time history of mix.

In Figure 8.26, we show the time-history of $N_{C,mix}$. We briefly comment on the two distinct time-scales of mix shown in Figure 8.26. It is seen that initially, a rapid mix occurs while the it is seen to slow down at later times. The early time rapid rise can be attributed to the strong *acceleration* of the pusher ions from the charge-separation field. Later on, as the field dissipates, the skewed distribution function of the pusher ions is slowly equilibrated from collisions with itself and the fuel, described by the second slope. We see that at 0.6 [ns], approximately 1.55×10^{16} carbon ions have mixed into the fuel. In terms of f_{mix}, this accounts for about 3% of the fuel. However, if we use another measure for the mix, based on the *initial amount* of fuel ions, $N_{DT,init}$, in a similar Omega ICF hydrodynamic simulation [129], $N_{C,mix}/N_{DT,init} \approx 7.8\%$.

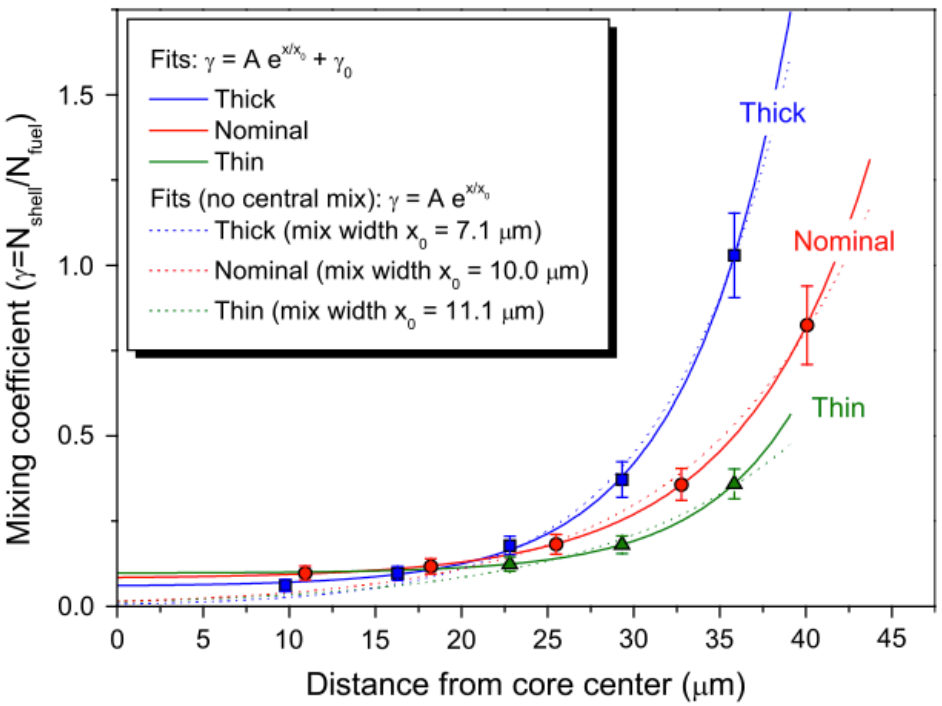


Figure 8.27: Inferred experimental mix from reference [126].

These nonlinear simulation have been able to provide more insight into the time dependent behavior of the double-layer induced mix phenomena. This is expected as the theoretical calculations did not take into account: 1) depletion of carbon material due to mixing (i.e. a constant density, $n_C = 5 \times 10^{21}$ [cm^{-3}], was assumed at the interface at all times), 2) finite *back-scattering* of the pusher material from the fuel region, and 3) dissipation of field strength at longer times. Nonetheless, a similar level of mixing is numerically confirmed at a time *prior* to the hydrodynamic shock breakout (≈ 0.6 [ns]). In an Omega experiment with a similar configuration, an experimental mix amount of about 10% was inferred. Refer to Figure 8.27. In Figure 8.27, the dashed lines show the mix fraction from a hydrodynamic mix model which assumes *zero* mix at the center of the fuel, while the solid lines are fitted without any assumptions in mix at the center. Note that the inferred mix fraction from the experiment is at a later peak compression time (≈ 2[ns]), after the hydrodynamic shock has

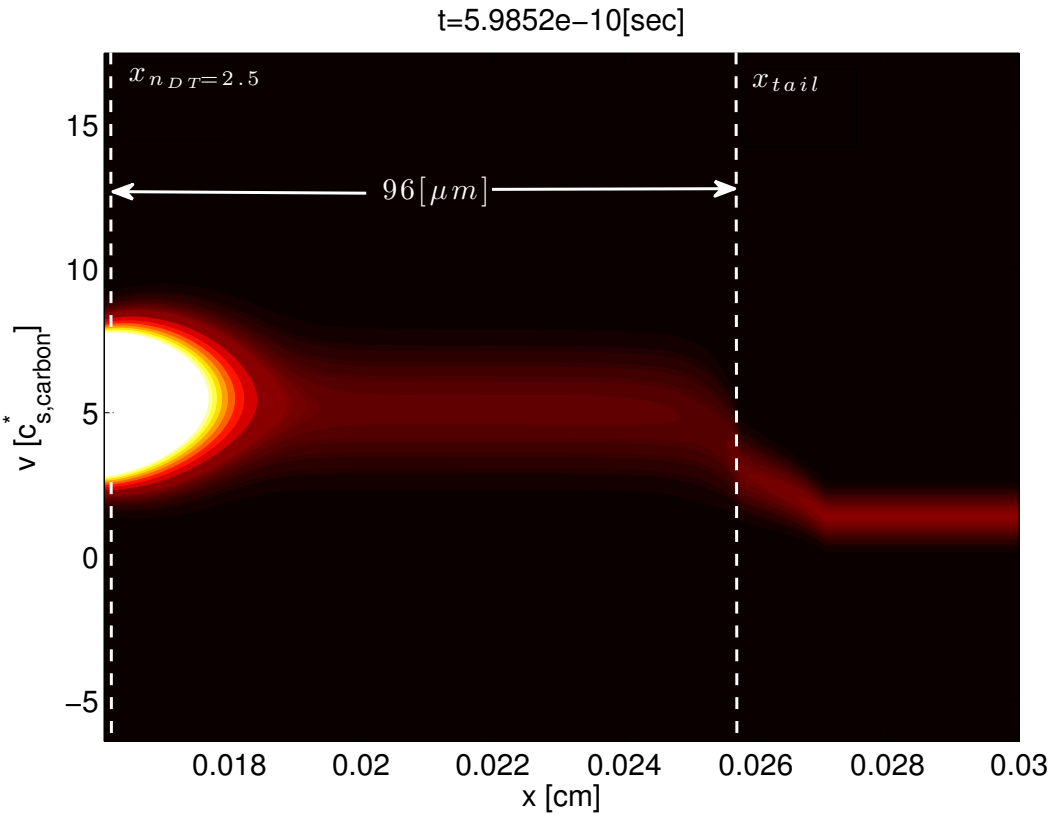


Figure 8.28: Kinetic mix depth of carbon ion into fuel at $t \approx 0.6$[ns].

broken out of the interface. If one considers that the hydrodynamic shock will only cause an increase in mix at later times, the $3 \sim 7.8\%$ value that we measure at the early time can be considered to be the correct order of magnitude.

Finally, we present the *mix depth* of the carbon ions. The depth of carbon ion mix into the fuel is measured based on the definitions for $x_{n_{DT}=2.5}$ and x_{tail} at $t = 0.6$[ns]. In Figure 8.28, the carbon distribution function phase-space plot is shown with the approximate location of $x_{n_{DT}=2.5}$ and x_{tail}. It is seen that approximately $96[\mu m]$ of mix depth is achieved at $t = 0.6$[ns]. This is to be compared to a hydrodynamic model for a similar Omega experiment, which infers approximately 6.8 [μm] mix at peak compression time $t \approx 2$ [ns] [126]. The fully kinetic simulation predicts a much deeper mix compared to what hydrodynamic models

predict.

8.11 Conclusion

In this study, we have applied the newly developed moment-based accelerator algorithm for the Vlasov-Fokker-Planck-Ampère system to simulate an early time charge-separation and kinetically enhanced mixing of pusher ions into the fuel. The approximate CPU time to perform the entire simulation was a week. In contrast, if one was to use a vanilla explicit time-integration algorithm, it would take approximately two years. Therefore, we demonstrated the necessity of the new algorithm.

A range in the electric field strength predicted by theory ($10^9 \leq E \leq 10^{10}$[V/m]) was observed in the simulation and the structure of double-layer and pre-sheath was confirmed. Additionally, carbon ion acceleration to above it's sound speed was achieved in the pre-sheath region, prior to entering the double-layer. This is also consistent with theory. The double-layer field strength at later times was consistent with those measured in experiments [124] and was observed to stay longer with an increase in the driver strength, also as predicted by theory. At later times, we measure a carbon ion mix amount of approximately 1.55×10^{16} into the fuel for the base case, which accounted for approximately 3% based on the f_{mix} measure (equation (8.24)) and approximately 7.8% based on the initial total fuel ion in the capsule, at $t \approx 0.6$[ns]. This value is also consistent with the theoretical predictions made by [130]. When compared to a similar Omega experiment [126], the fractional mix amount is also consistent. Finally, the mix depth that is predicted by the kinetic simulation is shown to be much deeper than what the hydrodynamic mix models can predict, even at earlier times prior to peak-compression. With all the preliminary observations made, and the agreement with theory and experiment, the new mix mechanism may provide further insights into the early time mix of pusher material measured in experiments, but not predicted by hydrodynamic models.

Chapter 9

Conclusions

In this dissertation, we have: 1) developed a moment-based acceleration algorithm to efficiently converge the nonlinearly coupled Vlasov-Fokker-Planck-Ampère system when Δt is chosen to step over the stiff electron time-scales and heavy pusher ion collision time-scales, and 2) applied the new algorithm to solve a kinetic plasma physics problem for an inertial confinement fusion (ICF) application. Specifically, we have investigated the early time charge-separation field, multi-species, and kinetically enhanced mix of pusher material into the fuel. In this final chapter, we 1) review, and highlight the important work that was required to develop the algorithm, and 2) summarize the discovery made on the mix physics of the fuel-pusher interface, due to kinetic ions and a self-consistent charge-separation electric field.

9.1 Review of the Algorithm Development

In this dissertation, we have developed a charge and energy conserving HOLO moment-based accelerator to algorithmically accelerate the convergence of a standard Picard (source) iteration for a Vlasov-Fokker-Planck-Ampère system. In order to develop the algorithm, we

have performed a separate development on:

1. moment acceleration of a collisionless plasma physics problem (chapter 4),
2. charge, momentum, and energy conserving discretization for a collisionless plasma on an Eulerian grid (chapter 5),
3. moment acceleration of a collisional, neutral gas kinetics problem (chapter 6).

Finally, in chapter 7, we have combined the techniques developed and experience gained in chapters 4, 5, and 6 to develop a moment-based accelerator algorithm for the coupled Vlasov-Fokker-Planck-Ampère system. We review some of the key developments required for each aspect of the final algorithm.

Moment Acceleration of a collisionless plasma physics problem

In chapter 4, we developed a moment acceleration algorithm to accelerate the convergence of a standard Picard iteration applied to a collisionless Vlasov-Ampère system. The new algorithm allowed one to efficiently step over the inverse electron plasma frequency, $\omega_{p,e}^{-1}$ when no collisions were considered. The key algorithmic developments were in 1) exposing the stiff hyperbolic waves in the LO system through the use of a density normalized stress-tensor, and 2) the use of the discrete consistency term. Without either, a discretely consistent HO and LO solution, and efficient convergence of the solution could not be obtained.

Charge, momentum, and energy conserving discretization for a collisionless plasma on an Eulerian grid

In chapter 5, we developed a moment acceleration algorithm, together with a charge, momentum, and energy conserving discretization of a Vlasov-Ampère system, applied to an Eulerian grid. Being able to preserve the discrete conservation properties is critical for long

time-integration problems for the credibility of the solution. The key algorithmic development was in introducing two additional discrete nonlinear constraints which enslaved the momentum conserving density to the charge conserving density and charge conserving flux to the energy conserving flux. The additional nonlinear constraints required a nonlinear discretization for the Vlasov equation. We have demonstrated that this nonlinearity in the discretization can be efficiently absorbed in the HOLO iteration, thus not introducing any additional solver cost compared to a non-conservative scheme.

Moment acceleration of a collisional neutral gas kinetics problem

In chapter 6, we developed a moment acceleration algorithm for a collisional neutral gas kinetics problem. The new algorithm allowed one to be able to step over stiff collision time-scales without the complication of fields. The key algorithmic developments were in 1) introducing an energy equation into the LO system, 2) developing a flux interpolation consistency term for a collocated mesh LO system, and 3) developing a collisional moment consistency term which takes into account the *lack* of collisional invariance of the BGK collision operator in the discrete system. We have demonstrated that the combination of the three developments allowed the algorithm to be applied to a strong shock tube problem with a wide variation in the Knudsen number.

Moment acceleration of a Vlasov-Fokker-Planck-Ampère system

In chapter 7, we have combined the charge, momentum, and energy conserving Vlasov-Ampère discretization with an energy conserving discretization of a reduced Fokker-Planck operator to develop a charge and energy conserving Vlasov-Fokker-Planck-Ampère (VFPA) system. We have combined the experience developed in chapters 4, 5, and 6 in order to develop a HOLO moment based acceleration algorithm for the VFPA system. The key additional algorithmic developments were 1) exposing the stiff electron thermal conduction

physics in the LO system, and 2) introducing a consistency term in the HO system in order to take into account the interpolation error associated from interpolating the LO cell-face number density flux to cell-center for the collisional drag operator. In particular, we have demonstrated that without the exposure of the electron thermal conduction physics in the LO system, the iterative scheme can become unstable. Additionally, without the energy equation, the number of HOLO iterations can become large when $\Delta t \gg \tau_{ee}$. Therefore, the new algorithm allows one to investigate long-time integration problems while efficiently stepping over stiff electron time-scales.

9.2 Review of the Interface Physics

When a laser impinges on the ICF fuel capsule, a coronal plasma will form and blow-off of the surface. This will generate a rocket-like momentum source inwards to the fuel. As the laser continues to impinge on the capsule, a thermal radiation wave will propagate inward. The thermal radiation wave will ionize both the capsule and the fuel as it propagates. This sets up an ionization gradient at the fuel-pusher interface, which will act as a source of a strong double-layer electric field. A traditional single fluid neutral radiation hydrodynamic (SFNRH) code cannot capture: 1) this field, 2) multi-species effects, and 3) kinetic effects. Using the newly developed moment-based acceleration algorithm for the Vlasov-Fokker-Planck-Ampère system, we have studied: 1) the early time structure of the charge-separation electric field and its sensitivity, 2) the effect of the electric field in sustaining the kinetic effects for a sustained duration, and 3) the pusher ion mix into the fuel. More importantly, *without* the new algorithm, one cannot investigate this particular problem due to CFL stability constraints of explicit algorithms and inefficiencies of classic implicit algorithms. We summarize the results of the observations made from the simulation of the early time fuel-pusher interface physics.

Charge-Spearation Field, Pre-Sheath and Ion Acceleration

We observe that the electric field transitions through two stages in which the first stage is the classic charge-separation field observed very early on similar to that illustrated in Figure 8.4 and the second stage evolves into a double-layer electric field with similar structure to those illustrated in Figure 8.5. Based on a parametric study of the early time field strength by varying the initial conditions, several expected trends were observed such as a stronger and longer sustained electric field with an increase in the driver strength. Additionally, the strength of the initial field computed from simulation is consistent with what is predicted by the double-layer theory [130] ($10^9 \leq E \leq 10^{10}$[V/m]). Furthermore, the evolved double-layer field is seen to be sustained at a 10^9[V/m] level, similar to what is measured in experiments discussed in reference [124]. It is seen from Figure 8.18 that the double-layer electric field sets up at the carbon ion contact surface. In the region prior to the this double-layer, a pre-sheath structure is predicted to exist from theory. The electric field in the pre-sheath zone will accelerate the carbon ions to above their sound speed such that the carbon ions will *enter* the double-layer zone at a supersonic velocity. In Figure 8.19, we confirm the existence of a pre-sheath field behind the double-layer which indeed does accelerate the carbon ions to above sound speed.

Sustained Kinetic Effects

From the carbon ion phase-space plot shown in Figure 8.19, it can be seen that the pre-sheath field accelerates the carbon ions to above sound speed. It is also seen that these carbon ions are further accelerated once they enter the double-layer to much higher velocities. Once the carbon ions are accelerated in the double-layer, we observe a beam like structure to form for the carbon ions on the fuel side. Recall that the temperature is defined as the second thermal moment of the distribution function and the collision frequency, $\nu_{\alpha\alpha}$, is proportional to $\frac{n_\alpha}{T_\alpha^{3/2}}$. Therefore, due to the electric field, the temperature of the distribution function is enhanced,

making the carbon ions less collisional on the fuel side (or across the contact surface). This means that due to the strong electric field, and the increase in the temperature, the beam structure (kinetic structure) can be maintained for a long time. This can be clearly seen by observing the Knudsen number of the carbon ions at later times as shown in Figure 8.25. It is clearly seen that even at $t \approx 70$[ps], $Kn \gg 1$, which necessitates the importance of kinetic modeling in accurately modeling the pusher mix at early times of capsule implosion.

Mix of Pusher into Fuel

Based on the early time electric field, the pusher ion acceleration to supersonic velocities, and enhancement of kinetic effects, a non-hydrodynamic mixing of carbon ions is predicted. Specifically, the numerical simulation shows that at $t \approx 0.6$[ns], approximately 1.55×10^{16} carbon ions are predicted to mix, prior to the hydrodynamic shock breaking out of the interface. This value agrees well with the theoretical prediction made in reference [130]. Furthermore, this value also agrees well with the experimental measurement from reference [126]. It is also seen that the depth of pusher ion mix into the fuel is predicted to be much deeper than what hydrodynamic mix models can predict.

9.3 Future Work

We have considered the reduced Fokker-Planck operator as the collision operator in this study. We have acknowledged that this collision operator will be overly dissipative for the high speed particles and will hence *limit* the mix amount of pusher ions into the fuel. To obtain a more accurate mix, one must hence consider the full Fokker-Planck operator in terms of the Rosenbluth potential [116]. However, this will require one to depart from the *traditional* approaches of moment-based accelerators. The diffusion and drag coefficients for the full Fokker-Planck operator in terms of the Rosenbluth potential are not completely in

terms of *trivial moments* (i.e. n, nu, U). Therefore, closure of these coefficients from LO quantities becomes a challenge. In order to address this issue, one may need to resort to a partial expansion of the collision operator in terms of some *physics based* basis polynomials. For a strongly collisional system, one may resort to a hermite-sonine polynomial expansion of the collision operator. In the strongly collisional limit, the first few expansions will capture the asymptotic Maxwellian structure. However, this will not be rigorously solving the full collision operator. Therefore, we introduce a consistency term in the HO system in order to retrieve the original equation, similar to what is discussed in Appendix F. For a non-collectively interacting electron transport, one may wish to model the forward peaked Fokker-Planck collision operator using the *forward peaked* moments to expand the collision operator (Appendix H). By doing so and solving the moment equations in the LO system and performing a partial expansion of the collision operator in the HO system in terms of forward peaked moments, one may be able to capture the asymptotic solution structure in the LO system and accelerate the underlying source iteration for the HO system. This will be left for future consideration.

We have also assumed one dimensional in configuration space and one dimensional in velocity space (1D1V) for our Vlasov-Fokker-Planck-Ampère system on a Cartesian geometry with open boundaries. There are two important geometric limitations with the current capability. First, an actual ICF capsule is spherical in nature and hence there exists a finite extent in domain size. Additionally, at later times of $t \approx 0.6$ [ns] where shock breakout is expected to occur, significant compression of the fuel and pusher will take place in an actual spherical geometry as more materials are transported to the smaller, central region. With the current open boundary assumption, this compression cannot be modeled. Furthermore, the 1V assumption inherently causes an over dissipation of particles of all speeds due to the 1V limitation allowing particles to travel either forwards, or backwards. Therefore, for a more realistic modeling of the ICF fuel-pusher mix, we will consider developing the algorithm with 1D2V capability in a spherical geometry.

References

[1] M. Casanova, O. Larroche, "Kinetic Simulation of a Collisional Shock Wave in Plasma", *Phys. Rev. Let.*, **67** (16), (1991) pp. 2143-2146.

[2] F. Vidal, J.P. Matte, M. Casanova, O. Larroche, "Spherical Ion Kinetic Simulations of DT Implosions", *Phys. Rev. Let. E*, **52** (4), (1995), pp. 4568-457.

[3] F. Vidal, J.P. Matte, M. Casanova, O.Larroche, "Ion Kinetic Simulations of the Formation and Propagation of a Planar Collisional Shock Wave in a Plasma", *Phys. Rev. Let. B*, **5**, (1993) pp. 3182-3190.

[4] F. Vidal, J.P. Matte, M. Casanova, and O. Larroche, "Modeling and Effects of Nonlocal Electron Heat Flow in Planar Shock Waves", *Phys. of Plasmas*, **2** (5), (1995) pp. 1412-1420.

[5] O. Larroche, "Ion Fokker-Planck Simulation of D-^{3}He Gas Target Implosions", *Phys. of Plasmas*, **19**, 122706 (2012).

[6] T. Yabe, K.A. Tanaka, "Long Ion Mean-Free Path and Nonequilibrium Radiation Effects on High-Aspect-Ratio Laser-Driven Implosions", *Laser and Particle Beams*, **7** (2) (1989) pp. 259-265.

[7] D.E. Hinkel, et al., "Laser Coupling to Reduced-Scale Hohlraum Targets at the Early Light Program of the National Ignition Facility", *Phys. of Plasmas*, **12**, (2005) 056305.

[8] E.L. Dewald et al., "Radiation-Driven Hydrodynamics of High-Z Hohlraums on the National Ignition Facility", *Phys. Rev. Let.*, **95**, (2005) 215004.

[9] E.L. Dewald et al., "First Hohlraum Drive Studies on the National Ignition Facility", *Phys. of Plasmas*, **13**, (2006) 056315.

[10] M.M. Marinak, et al., "Three-Dimensional HYDRA Simulations of National Ignition Facility Targets", *Phys. of Plasmas*, **8**, (2001) pp. 2275-2280.

[11] N.B. Meezan, et al., "Role of Hydrodynamics Simulations in Laser-Plasma Interaction Predictive capability", *Phys. of Plasmas*, **14**, (2007) 056304.

[12] P.B. Radha, et al., "Multidimensional Analysis of Direct-Drive, Plastic-Shell Implosions on OMEGA", *Phys. of Plasmas*, **12**, (2005) 056307.

[13] P.B. Radha, et al., "Two-Dimensional Simulations of Plastic-Shell, Direct-Drive Implosions on OMEGA", *Phys. of Plasmas*, **12**, 032702, (2005).

[14] C. Bellei, P.A. Amendt, S.C. Wilks, M.G. Haines, D.T. Casey et al., "Species Separation in Inertial Confinement Fusion Fuels", *Phys. of Plasmas*, **20**, (2013) 012701.

[15] P.A. Amendt, J.L. Milovich, S.C. Wilks, C.K. Li, R.D. Petrasso, F.H. Seguin, "Electric Field and Ionization-Gradient Effects on Inertial-Confinement-Fusion Implosions", *Plasma Phys. Control. Fusion*, **51**, (2009) 124048.

[16] P.A. Amendt, S.C. Wilks, C. Bellei, C.K. Li, R.D. Petrasso, "The Potential Role of Electric Fields and Plasma Barodiffusion on the Intertial Confinement Fusion Database", *Phys. of Plasmas*, **18**, (2011) 056308.

[17] M.Y. Jaffrin, R.F. Probstein, "Structure of a Plasma Shock Wave", *Phys. Fluids*, **7**, (1964) pp. 1658-1674.

[18] V.A. Mousseau, "Fully Implicit Kinetic Modelling of Collisioinal Plasmas", *PhD Dissertation*, University of Idaho, (1996).

[19] J.D. Anderson, "Computational Fluid Dynamics The Basic with Applications", *McGraw-Hill Publishing Company*, New York, (1995).

[20] J. Crank, P. Nicolson, "A Practical Method for Numerical Evaluation of Solutions of Partial Differential Equations of the Heat-Conduction Type", *Adv. in Comp. Math.*, **6**, (1996) pp. 207-226.

[21] W.T. Taitano, "Development of a Jacobian-Free-Newton-Krylov Method with Kinetic Enslavement to Implicitly Solve Vlasov-Poisson System in Plasma Physics", Masters Thesis, University of Idaho (2010).

[22] S.Y. Kadioglu, D.A. Knoll, "A Fully Second Order Implicit/Explicit Time Integration Technique for Hydrodynamics Plus Nonlinear Heat Conduction Problems", *J. Comp. Phys.*, **229**, (2010) pp. 3237-3249.

[23] R.J. Mason, "Implicit moment particle simulation of plasmas", *J. Comput. Phys.*, **41**, (2), (1981) pp. 233-244.

[24] A.G. Petschek, D.B. Henderson, "Influence of High-Energy Ion Loss on DT Reaction Rate in Laser Fusion Pellets", *Nucl. Fusion* **19**, (1979), pp. 1678-1680.

[25] K.Molvig, N.M. Hoffman, B.J. Albright, E.M. Nelson, R.B. Webster", "Knudsen Layer Reduction of Fusion Reactivity", *Phys. Rev. Let.* **109** (2012) 095001.

[26] R.P. Drake, "High-Energy-Density Physics', Fundamentals, Inertial Fusion, and Experimental Astrophysics", *Springer*, (2006).

[27] J. Nuckolls, L. Wood, A. Thiessen, G. Zimmerman, "Laser Compression of Matter to Super-High Densities: Thermonuclear (CTR) Applications" *Nature*, **239**, (1972) pp. 139- 142.

[28] J.D. Lindl, "Development of the Indirect-Drive Approach to Inertial Confinement Fusion and the Target Physics Basis for Ignition and Gain", *Phys. of Plasmas*, **2**, (1995) pp. 3933-4024.

[29] J.D. Lindl, et al., "The Physics Basis for Ignition Using Indirect-Drive Targets on the National Ignition Facility", *Phys. of Plasmas*, **11**, (2004) pp. 339-491.

[30] A.H. Stroud, D. Secrest, "Gaussian Quadrature Formulas", Prentice-Hall, (1966).

[31] D.S. Clark, "Detailed Implosion Modeling of DT-Layered Experiments on the National Ignition Facility", 54^{th}, APS-DPP Meeting, Providence, RI, https://scitation.aip.org/journals/doc/PHPAEN-home/DPP/2012/BI3_Clark.pdf, (2012).

[32] C.K. Birdsall, A.B. Langdon, "Plasma Physics via Computer Simulation", McGraw-Hill, New York (2005).

[33] A. Friedman, A.B. Langdon, B.I. Cohen, "A direct method for implicit particle-in-cell simulation", Comm. Plasma Phys. Controlled Fusion 6(6) (1981) pp. 225–236.

[34] B.I. Cohen, A.B. Langdon, A. Friedman, "Implicit time integration for plasma simulation", *J. Comput. Phys.* **46**, (1) (1982) pp. 15–38.

[35] A.B. Langdon, B.I. Cohen, A. Friedman, "Direct implicit large time-step particle simulation of plasmas", *J. Comput. Phys.* **51**, (1) (1983) pp. 107–138.

[36] D.C. Barnes, T. Kamimura, J.N. Leboeuf, T. Tajima, "Implicit particle simulation of magnetized plasmas", *J. Comput. Phys.* **52**, (3) (1983) pp. 480–502.

[37] B.I. Cohen, "Multiple time-scale methods in particle simulations of plasma", *Particle Accelerators* **19**, (1986) pp. 227-236.

[38] A. Friedman, "A second-order implicit particle mover with adjustable damping", *J. Comput. Phys.* **90**, (2) (1990) pp. 292–312.

[39] "Polar Direct Drive – Ignition at 1MJ", *http://www.lle.rochester.edu/media/publications/lle_review/documents/v104/104_03Polar.pdf*

[40] B.I. Cohen, A.B. Langdon, D.W. Hewett, R.J. Procassini, "Performance and optimization of direct implicit particle simulation", *J. Comput. Phys.* **81**, (1) (1989) pp. 151-168.

[41] R.J. Mason, "Implicit moment particle simulation of plasmas", *J. Comput. Phys.*, **41**, (2) (1981) pp. 233–244.

[42] J. Denavit, "Time-filtering particle simulations with $\omega_{pe}\Delta t \gg 1$", *J. Comput. Phys.* **42**, (2) (1981) pp. 337–366.

[43] J.U. Brackbill, D.W. Forslund, "An implicit method for electromagnetic plasma simulation in two dimensions", *J. Comput. Phys.*, **46**, (2) (1982) pp. 271–308.

[44] R.J. Mason, "Hybrid and Collisional Implicit Plasma Simulation Models", in: J.U. Brackbill, B.I. Cohen (Eds.), Multiple Time Scales, Academic Press, (1985).

[45] J.U. Brackbill, D.W. Forslund, "Simulation of low-frequency electromagnetic phenomena in plasmas, in: J.U. Brackbill, B.I. Cohen (Eds.), Multiple Time Scales, Academic Press, (1985).

[46] H.R. Lewis, "Energy-conserving numerical approximations for Vlasov plasmas", *J. Comput. Phys.* **6**, (1970) pp. 136–141.

[47] C.K. Birdsall, N. Maron, "Plasma self-heating and saturation due to numerical instabilities", *J. Comput. Phys.* **36**, (1) (1980) pp. 1–19.

[48] K.J. Bowers, B.J. Albright, L. Yin, B. Bergen, T.J.T. Kwan, "Ultrahigh performance three-dimensional electromagnetic relativistic kinetic plasma simulation", *Phys. Plasmas* **15**, (5) (2008) 055703.

[49] K. Bowers, B. Albright, L. Yin, W. Daughton, V. Roytershteyn, B. Bergen, T. Kwan, "Advances in petascale kinetic plasma simulation with vpic and roadrunner", *J. Physics*: Conference Series **180** (2009) 012055.

[50] K.S. Smith, J.D. Rhodes III, "Full-Core, 2-D LWR Core Calculations with CSMO-4E", Proc. Int. Conf. New Frontiers of Nuclear Technology: Reactor Physics, Safety and High-Performance Computing (PHYSOR 2002), Seaul, Korea, October 7-10, 2002, Am. Nuc. Soc (2002).

[51] D.A. Knoll, H. Park, K.S. Smith, "Application of the Jacobian-Free Newton-Krylov method to nonlinear acceleration of transport source iteration in slab geometry", *Nuc. Sci. and Engn.* **167**, (2) (2011), pg. 122–132.

[52] V.Ya Gol'din, "A quasi-diffusion method for solving the kinetic equation", *USSR Comp. Math. and Math. Phys.*, **4**, (136) (1967).

[53] H. Park, D.A. Knoll, R.M. Rauenzahn, A.B. Wollaber, J.D. Densmore, "A Consistent, Moment-Based, Multiscale Solution Approach for Thermal Radiative Transfer Problems", *Transport Theory and Statistical Physics*, **41** (3-4) (2012), Special Issue: SI, pp. 284–303.

[54] G. Chen, L. Chacón, D.C. Barnes, "An energy- and charge-conserving, implicit, electrostatic particle-in-cell algorithm", *J. Comput. Phys.* **230** (2011) pp. 7018–7036.

[55] S. Markidis, G. Lapenta, "The energy conserving particle-in-cell method", *J. Comput. Phys.*, **230** (2011) pp. 7037-7052.

[56] G. Chen, L. Chacon, D.C. Barnes, "An efficient mixed-precision, hybrid CPU-GPU implementation of a nonlinearly implicit one-dimensional partcicle-in-cell algorithm", *J. Comput. Phys.* **231** (2012) pp. 5374-5388.

[57] L. Chacón, G. Chen, D.C. Barnes, "A charge- and energy-conserving implicit, electrostatic particle-in-cell algorithm on mapped computational meshes", *J. Comput. Phys.* under review.

[58] G. Chen, L. Chacón, "Fluid acceleration of fully implicit particle-in-cell kinetic simulations", in preparation

[59] Y. Saad, "Iterative Methods for Sparse Linear Systems", PWS Publishing Company, Massachusetts (1996).

[60] D.G. Swanson, "Plasma Waves, 2^{nd} edition", Institute of Physics Publishing, Philadelphia, (2003).

[61] F.F. Chen, "Introduction to Plasma Physics and Controlled Fusion", *Volume 1: Plasma Physics*, Springer Publishing, (2006).

[62] D.A. Knoll, D.E. Keyes, "Jacobian-Free Newton-Krylov Method: A survey of approaches and applications", *J. Comput. Phys.*, **193**, (2004) pp. 357-397.

[63] D.A. Knoll, V.A. Mousseau, L. Chaón, J. Reisner, "Jacobian-free newton-krylov methods for the accurate time integration of stiff wave systems", *J. Scientific Comput.*, **25** (112), (2005).

[64] D.G. Anderson, "Iterative procedures for nonlinear integral equations", *J. Assoc. Comput. Machinery*, **12** (1965), pg. 547–560.

[65] T.H. Watanabe, H. Suguma, "Vlasov and drift kinetic simulation methods based on the symplectic integrator", *Trans. Theory and Stat. Phys.*, **34** (2005) pg 287–309.

[66] G. Bird "Molecular Gas Dynamics and the Direct Simulation of Gas Flows", *Oxford Engineering Science Series* Clarendon Press, Oxford, 1995.

[67] J.Y. Yang, J.C. Huang, "Rarefied flow computations using nonlinear model Boltzmann equations", *J. Comput. Phys.* **120**, (1995) pp. 323-339.

[68] Z.H. Li, H.X. Zhang, "Gas-kinetic numerical studies of three-dimensional complex flows on spacecraft re-entry", *J. Comput. Phys.* **228**, (2009) pp. 1116-1138.

[69] L. Mieussens, "Discrete-velocity models and numerical schemes for the Boltzmann-BGK equation in plane and axisymmetric geometries", *J. Comput. Phys.* **162**, (2000), pp. 429-466.

[70] S. Pieraccini, G. Puppo, "Implicit-explicit schemes for BGK kinetic equations", *J. Sci. Comp.* **32**, (2007) pp. 1-28.

[71] F. Filbet, S. Jin, "A class of asymptotic-preserving schemes for kinetic equations and related problems with stiff sources", *J. Comput. Phys.* **229**, (2010), pp. 7625-7648.

[72] P.L. Bhatnagar, E.P. Gross, M. Krook, "A Model for Collision Processes in Gases. I. Small Amplitude Processes in Charged and Neutral One-Component Systems", *Phys. Rev. Let. .* **94**, (3) (1954), pp. 511–525.

[73] C.T. Kelly, "Iterative Methods for Linear and Nonlinear Equations", Society for Industrial and Applied Mathematics (1995).

[74] N.V. Brilliantov and T. Porschel, "Kinetic Theory of Granular Gases", Oxford University Press (2004).

[75] W.T. Taitano, D.A. Knoll, L. Chacón, G. Chen, "Development of a Consistent and Stable Fully Implicit Moment Method for Vlasov-Ampère Particle in Cell (PIC) System", *SIAM J. Sci. Comput.*, **35**, (5) (2013) pp. 126–149.

[76] G.A. Sod, "A Survey of several Finite Difference Methods for Systems of Nonlinear Hyperbolic Conservation Laws", *J. of Comp. Phys.* **27** (1978), pp. 1-31.

[77] S. Bertoluzza, S. Falletta, G. Russo, C.W. Shu, "Numerical Solutions of Partial Differential Equations", Birkhauser Verlag (2009).

[78] J.J. Duderstadt, W.R. Martin, "Transport Theory", Wiley (1979).

[79] C. Hirsch, "Numerical Computation of Internal and External Flows: Volume 2 Computational Methods for Inviscid and Viscous Flows", Wiley (1990).

[80] E.F. Toro, "Riemann Solvers and Numerical Methods for Fluid Dynamics", Springer (2009).

[81] C.W. Shu, "High Order Weighted Essentially Non-Oscillatory Schemes for Convection Dominated Problems", *SIAM Review*, **51**, (2009) pp. 82-126.

[82] B.G. Carlson, K.D. Lathrop, *"Transport Theory-The Method of Discrete Ordinates"*, in *Computing Methods in Reactor Physics*, H. Greenspan, C.N. Kelber, and D. Okrent (eds.), (1968).

[83] J. Reisner, J. Serencsa, S. Shkoller, "A Space-Time Smooth Artificial Viscosity Method for Nonlinear Conservation Laws", *J. Comp. Phys.*, **235**, (2013), pp. 912-933.

[84] J.W. Banks, J.A.F.Hittinger, "A new class of nonlinear finite-volume methods for Vlasov simulation", *IEEE Trans. on Plasma Sci.* **38**, (9), (2010).

[85] T.D. Arber, R.C. Vann, "A critical comparison of Eulerian-grid-baesd Vlasov solvers", *J. Comput. Phys.*, **180**, (2002) pp. 339-357.

[86] C.Z. Cheng, G. Knorr, "The integration of the Vlasov equation in configuration space", *J. Comput. Phys.*, **22**, (1976) pp. 330-351.

[87] F. Filbet, E. Sonnendrücker, P. Bertrand, "Conservative numerical scheme for the Vlasov equation", *J. Comput. Phys.*, **172**, (2001) pp. 176-187.

[88] R.B. Horne, M.P. Freeman, "A new code for electrostatic simulation by numerical integration of the Vlasov and Ampère's equations using MacCormack's method", *J. Comput. Phys.*, **171**, (2001), pp. 182-200.

[89] Y. Cheng, A.J. Chrislieb, X.Zhong, "Energy-conserving discontinuous Galerkin methods for the Vlasov-Ampère system", *J. Comput. Phys.*, **256**, (2014) pp. 630-655.

[90] B.P. Leonard, "A stable and accurate convective modeling procedure based on quadratic upstream interpolation", *Comput. Meth. in Applied. Mech. and Eng.* **19** (1979) pp. 59-98.

[91] B.P. Leonard, S. Mokhtari, *"Beyond First-Order Upwinding: The ULTRA-SHARP Alternative for Non-Oscillatory Steady-State Simulation of Convection"*, *Int J. Num. Meth. Engng.* **30**, (1990) pp. 729-766.

[92] M.A. Shay, J.F. Drake, B. Dorland, "Equation Free Projective Integration: A multiscale method applied to a plasma ion acoustic wave", *J. Comput. Phys.*, **226**, (2007) pp. 571-585.

[93] G. Chen, L. Chacón, C.A. Leibs, D.A. Knoll, W.Taitano, "Fluid preconditioning of Newton-Krylov-based, fully implicit, electrostatic particle-in-cell simulations", *J. Comput. Phys.*, **258**, (2014), pp. 555-567.

[94] W.T. Taitano, L. Chacón, G. Chen, "Charge-and-energy conserving moment-based accelerator for multi-species Vlasov-Fokker-Planck-Ampère system, part I: collisionless aspects", *J. Comput. Phys.*, in preparation, 2013.

[95] R.J. Kingham, A.R. Bell, "Nonlocal magnetic-field generation in plasmas without density gradients", *Phys. Rev. Lett.*, **88**, (2002) 045004.

[96] R.J. Kingham, A.R. Bell, "An implicit Vlasov-Fokker-Planck code to model nonlocal electron transport in 2-D with magnetic fields", *J. Comput. Phys.* **194**, (2004) pp. 1-34.

[97] C.P. Ridgers, R.J. Kingham, A.G.R. Thomas, "Magnetic Cavitation and the Reemergence of Nonlocal Transport in Laser Plasmas", *Phys. Rev. Lett.*, **100**, (2008) 075003.

[98] T.H. Kho, M.G. Haines, "Nonlinear kinetic transport of electrons and magnetic field in laser-produced plasmas", *Phys. Rev. Lett.*, **55**, (1985) pp. 825-828.

[99] J.F. Luciani, P. Mora, A. Bendib, "Magnetic field and nonlocal transport in laser-created plasmas", *Phys. Rev. Lett.*, **55**, (1985) pp. 2421-2424.

[100] E.M. Epperlein, G.J. Rickard, A.R. Bell, "A code for the solution of the Vlasov-Fokker-Planck Equation in 1-D or 2-D", *Comp. Phys. Comm.*, **52**, (1988) pp. 7-13.

[101] R.P.J. Town, A.R. Bell, S.J. Rose, "Fokker-Planck simulations of short-pulse-laser-solid experiments", *Phys. Rev. E*, **50**, (2, Part B) (1994) pp. 1413-1421.

[102] A.G.R. Thomas, M.Tzoufras, A.P.L. Robinson, R.J. Kingham, C.P. Ridgers, "A review of Vlasov-Fokker-Planck numerical modeling of inertial confinement fusion plasma", *J. Comput. Phys.*, **231**, (2012) pp. 1051-1079.

[103] L.R.T. Gardner, G.A. Gardner, S.I. Zaki, "Collisional effects in plasmas modeled by a simplified Fokker-Planck equation", *J. Comput. Phys.*, **107**, (1993).

[104] A. Lenard, I.B. Bernstein, "Plasma oscillations with diffusion in velocity space", *Phys. Rev.*, **112** (1958).

[105] J.S. Chang, G. Cooper, "A practical difference scheme for Fokker-Planck equations", *J. Comput. Phys.*, **6**, (1970) pp. 1-16.

[106] E.M. Epperlein, "Implicit and conservative difference scheme for the Fokker-Planck equation", *J. Comput. Phys.*, **112**, (1994) pp. 291-297.

[107] L. Chacón, D.C. Barnes, D.A. Knoll, G.H. Miley, "An implicit energy conservative 2D Fokker-Planck algorithm I. difference scheme", *J. Comput. Phys.*, **157**, (2000) pp. 618-653.

[108] L. Chacón, D.C. Barnes, D.A. Knoll, G.H. Miley, "An implicit energy conservative 2D Fokker-Planck algorithm II. Jacobian-free Newton-Krylov solver", *J. Comput. Phys.*, **157**, (2000) pp. 654-682.

[109] M. Lemou, L. Mieussens "Fast implicit schemes for the Fokker-Planck-Landau equation", *C.R. Math*, **15**, (2004), pp. 809-814.

[110] V.A. Mousseau, D.A. Knoll, "Fully implicit kinetic solution of collisional plasmas", *J. Comput. Phys.*, **136**, (1997) pp. 308-323.

[111] V.A. Mousseau, "Fully Implicit Kinetic Modeling of Collisional Plasmas", *PhD Dissertation* (1996) University of Idaho.

[112] A.G.R. Thomas, R.J. Kingham, C.P. Ridgers, "Rapid self-magnetization of laser speckles in plasmas by nonlinear anisotropic instability", *New J. Phys.*, **11**, (2009) 033001.

[113] T.W. Johnston, "Cartesian tensor scalar product and spherical harmonic expansions in Boltzmann's equation", *Phys. Rev.*, **120**, (1960) pp. 1103-1111.

[114] J. Wesson, "Tokamaks: second edition', Oxford Science Publications (1997).

[115] P. Wesseling, "An introduction to multigrid methods", Wiley (2006).

[116] M.N. Rosenbluth, W.M. MacDonald, D.L. Judd, "Fokker-Planck Equation for an Inverse-Square Force", *Phys. Rev. Lett.*, **107** (1) (1956) pp. 1-6.

[117] S.I. Braginskii, "Transport Processes in a Plasma", *Reviews of Plasma Physics*, Edited by M.A. Leontovich (Consultants Bureau, New York), pg. 205, vol. 1.

[118] W.T. Taitano, D.A. Knoll, L. Chacón, J. Reisner, A.K. Prinja, "Moment-based acceleration for neutral gas kinetics with BGK collision operator", *TTSP* submitted, 2013.

[119] J.A.Willert, W.T.Taitano, D.A.Knoll, "Leveraging anderson acceleration for improved convergence of iterative solutions to transport systems", *J. Comput. Phys.*, submitted, 2013.

[120] O. Larroche, "Ion Fokker-Planck simulation of D-3He gas target implosions", *Phys. Plasmas* **19** (2012) 122706.

[121] V.N. Goncharov, "Demonstrating ignition hydrodynamic equivalence in cryogenic DT implosions on omega", *APS DPP 2013*, GI3 1, Tuesday.

[122] D.R. Harding, et al., "Cryogenic target-implosion experiments on OMEGA", *J. Phys.*, Conference series **112** (2008) 022001.

[123] H. Rinderknecht, "Quantitative studies of kinetic effects in direct- and indirect-drive inertial confinement fusion implosions", *APS DPP 2013*, GI3 5, Thuesday.

[124] C.K. Li et al., "Monoenergetic-proton-radiography measurements of implosion dynamics in direct-drive inertial-confinement fusion", *Phys. Rev. Lett.* **100** (2008) 225001.

[125] L.P. Block, "A double layer review", *Astophys. and Space Sci.* **55**, (1978) pp. 59-83.

[126] L. Welser-Sherrill, et al., "Inference of ICF implosion core mix using experimental data and theoretical mix modeling", *High Energy Dens. Phys.* **5**, (2009) pp. 249-257.

[127] T. Ma, et al., "Onset of hydrodynamic mix in high-velocity, highly compressed inertial confinement fusion implosions", *Phys. Rev. Lett.* **111**, (2013) 085004.

[128] R.C. Shah, F. Wysocki, Private communication, (2013).

[129] E. Vold, APS DPP 2011, Salk Lake City, UT, LA-UR-11-06397.

[130] D.A. Knoll, L. Chacón, A. Simakov, W. Taitano, APS DPP 2013, Denver, CO, LA-UR-13-28602.

[131] W. Daughton, J. Scudder, H. Karimabadi, "Fully Kinetic Simulations of Undriven Magnetic Reconnection with Open Boundary Conditions", *Phys. of Plasmas*, **13** (7), (2006), pp. 72101-72115.

[132] "The OpenMP® API specification for parallel programming", *http://openmp.org/wp*

[133] E.G. Evstatiev, B.A. Shadwick "Variational formulation of particle algorithms for kinetic plasma simulations", *J. Comput. Physics*, **245** (2013), pp. 376-398.

Appendices

A Exposure of Stiff Hyperbolic Wave in the VA LO System **223**

B JFNK to Solve for VA LO moment system **225**

C Asymptotic Preserving Time Discretization **228**

D VFPA LO System: Continuity, Momentum, and Ampère's Equation **231**

E Block Preconditioning for VFPA LO System **234**

F Discrete Consistency Terms for VFPA **236**

G Picard Iteration for a 0D1V Fokker-Planck Equation **243**

H Moment Acceleration of a Purely Differential HO System **245**

Appendix A

Exposure of Stiff Hyperbolic Wave in the VA LO System

The exposure of stiff electron plasma waves through the use of a density-normalized stress-tensor becomes clear by investigating the linear dispersion relation of a fluid (moment) system:

$$\frac{\partial n}{\partial t} + \frac{\partial}{\partial x} n u_\alpha = 0 \ , \tag{A.1}$$

$$n\left(\frac{\partial u_\alpha}{\partial t} + \frac{1}{2}\frac{\partial u_\alpha^2}{\partial x}\right) = \frac{q_\alpha}{m_\alpha} nE - \frac{\partial}{\partial x}\left(\frac{n_\alpha K_b T_\alpha}{m_\alpha}\right) \ , \tag{A.2}$$

$$\epsilon_0 \frac{\partial E}{\partial t} + \sum_\alpha q_\alpha n u_\alpha = 0 \ . \tag{A.3}$$

Here, $\left[\frac{n_\alpha K_b T_\alpha}{m_\alpha} + \frac{u_\alpha^2}{2}\right]$ represents the definition of our normalized total stress-tensor in 1D. For linearization, we consider $n = n_0 + \tilde{n}$, $u_\alpha = u_{\alpha,0} + \tilde{u}_\alpha$, $E = E_0 + \tilde{E}$ where the subscript 0 indicates some fixed equilibrium term, and the tilde indicates a small perturbation. Assuming

a homogeneous plasma (n_0 = constant, $u_0 = E_0 = 0$, T_0 = constant), dropping high-order terms and expanding, the linearized system reads:

$$\frac{\partial \tilde{n}}{\partial t} + \frac{\partial}{\partial x}\left(\tilde{n} u_{\alpha,0} + n_0 \tilde{u}_\alpha\right) = 0 \,, \tag{A.4}$$

$$m_\alpha n_0 \frac{\partial \tilde{u}_\alpha}{\partial t} = q n_0 \tilde{E} - K_b T_\alpha \frac{\partial \tilde{n}}{\partial x} \,, \tag{A.5}$$

$$\epsilon_0 \frac{\partial \tilde{E}}{\partial t} + \sum_\alpha q_\alpha n_0 \tilde{u}_\alpha = 0 \,. \tag{A.6}$$

Using the ansatz, $\tilde{A} = A_c \mathrm{e}^{i(kx-\omega t)}$, where A_c is the Fourier amplitude, and combining the resulting equations, we obtain the following dispersion relation,

$$-1 + \sum_\alpha \frac{\omega_{p,\alpha}^2}{\omega^2 - k^2 v_{th,\alpha}^2} = 0. \tag{A.7}$$

Here, k is the wave vector, ω is the wave frequency, $\omega_{p,a}^2$ is the plasma wave frequency for the α species, and $v_{th,\alpha}^2$ is the thermal velocity of the α species. Assuming $v_{th,i} \ll \frac{\omega}{k} \ll v_{th,e}$, $\omega_{p,i} \gg \omega$, and $k\lambda_D \ll 1$, we obtain the familiar dispersion relation for an isothermal ion acoustic wave,

$$\frac{\omega^2}{k^2} = \frac{1}{m_i} \frac{K_b T_e}{1 + k^2 \lambda_D^2} + \frac{K_b T_i}{m_i}. \tag{A.8}$$

Without the density normalization, we cannot recover this dispersion relation.

Appendix B

JFNK to Solve for VA LO moment System

The LO system is by itself a nonlinear equation that requires an iterative solution. In this study, a Picard semi-implicit linearization technique was used as a preconditioner for JFNK.

In our semi-implicit scheme, the fastest time-scale physics are solved implicitly while other physics with slower time-scales are lagged from iteration to iteration. Now reconsider our semi-discretized, semi-implicit linearized LO moment system for ion, electron and Ampére equation.

$$\frac{n_e^{LO,k+1,z} - n_e^{LO,k}}{\Delta t} + \frac{\partial}{\partial x}\overline{nu}_e^{LO,k+1,z} = 0 \tag{B.1}$$

$$\frac{\overline{nu}_e^{LO,k+1/2,z} - nu_e^{LO,k}}{\Delta t/2} + \frac{\partial}{\partial x} n_e^{LO,k+1/2,z}\tilde{S}_e^{HO,k+1/2} - \frac{q_e}{m_e} n_e^{LO,k+1/2,z-1} E^{LO,k+1/2,z} - \gamma_{nu_e}^{HO} n_e^{LO,k+1,z} = 0 \tag{B.2}$$

$$\frac{n_i^{LO,k+1,z} - n_i^{LO,k}}{\Delta t} + \frac{\partial}{\partial x}\overline{nu}_i^{LO,k+1,z-1} = 0 \tag{B.3}$$

$$\frac{\overline{nu}_i^{LO,k+1/2,z} - nu_i^{LO,k}}{\Delta t/2} + \frac{\partial}{\partial x} n^{LO,k+1/2,z} \tilde{S}^{HO,k+1/2} - \frac{q_i}{m_i} n_i^{LO,k+1/2,z-1} E^{LO,k+1/2,z} - \gamma_{nu_i}^{HO} n_i^{LO,k+1,z} = 0 \tag{B.4}$$

$$\epsilon_0 \frac{E^{LO,k+1,z} - E^{LO,k}}{\Delta t} + q_e \overline{nu}_e^{LO,k+1/2,z} + q_i \overline{nu}_i^{LO,k+1/2,z} - \overline{\left\langle q_e \overline{nu}_e^{LO,k+1/2,z-1} + q_i \overline{nu}_i^{LO,k+1/2,z-1} \right\rangle} \tag{B.5}$$

Here, the superscript z denotes the LO Picard iteration index and k is the time index. This set of linearized equations allows for a semi-implicit scheme to form a linear system to solve for one variable in terms of others and iterate on slow physics by a Picard iteration. The linearization allows a construction of a single parabolic equation for $\overline{nu}_e^{LO,k+1/2,z}$ from an initially hyperbolic system of equations. The equation is solved for $\overline{nu}_e^{LO,k+1/2,z}$ and from back substitution, the new $n_e^{LO,k+1,z}$, $E^{k+1,z}$, $nu_i^{LO,k+1,z}$ and $n_i^{LO,k+1,z}$ are calculated and the process is repeated until some convergence tolerance is met.

JFNK is a synergistic method between the classic Newton's method and Krylov method. The method works by approximating the Jacobian-vector product (matvec), $\mathbb{J}\mathbf{v}$ from finite differencing,

$$\mathbb{J}\mathbf{v} \approx \frac{\mathbf{G}\left(\mathbf{u} + \epsilon \mathbf{v}\right) - \mathbf{G}\left(\mathbf{u}\right)}{\epsilon} \, . \tag{B.6}$$

Where $\mathbf{G}$, $\mathbf{u}$, $\mathbf{v}$, and ϵ are the nonlinear residual vectors defined in equation (4.44), the solution vector, Krylov vector, and some small perturbation factor respectively. This matvec is evaluated as a function evaluation call in a Krylov solver at each Krylov iteration to effectively solve for the Newton system,

$$\mathbb{J}^z \delta \mathbf{u}^z = -\mathbf{G}^z \, , \tag{B.7}$$

for $\delta\mathbf{u}^z$. Here, the superscript z is the *Newton* iteration index rather than Picard. The Krylov linear iteration is continued until some tolerance is met. With each Krylov solve to invert the Newton system, the solution is updated as,

$$\mathbf{u}^{z+1} = \mathbf{u}^z + \delta\mathbf{u}^z \ , \tag{B.8}$$

until some nonlinear tolerance is achieved. For this study, GMRES was used for the Krylov solver [59]. A left preconditioning technique was employed by using two passes of a semi-implicit Picard method presented above as a physics-based preconditioner (PBP). For a detailed discussion of JFNK and PBP, refer to [62, 63].

Appendix C

Asymptotic Preserving Time Discretization

We discuss the asymptotic preserving time-discretization treatment of the BGK collision operator. Recall that in section 6.4.1 we have treated the streaming operator using Crank-Nicholson while using a different discretization for the collision operator. Consider the semi-discretized BBGK equation with a constant collision time-scale,

$$\frac{f^{n+1}-f^{n}}{\Delta t}+\frac{v}{2}\frac{\partial}{\partial x}\left(f^{n+1}+f^{n}\right)=\frac{f_{M}^{n+1}-f^{n+1}}{\tau}. \tag{C.1}$$

Here, the superscript n is the time-index. We use the Ansatz,

$$f^{n+1}=\widetilde{f}^{n+1}\mathrm{e}^{ikx}, \tag{C.2}$$

and

$$f_{M}^{n+1}=\widetilde{f}_{M}^{n+1}\mathrm{e}^{ikx}, \tag{C.3}$$

in which k is the wave-vector, to obtain,

$$\frac{\widetilde{f}^{n+1}-\widetilde{f}^{n}}{\Delta t}+\frac{ivk}{2}\left(\widetilde{f}^{n+1}+\widetilde{f}^{n}\right)=\frac{\widetilde{f}_{M}^{n+1}-\widetilde{f}^{n+1}}{\tau}. \tag{C.4}$$

Grouping terms and solving for $\widetilde{f}^{n+1}$, we find:

$$\widetilde{f}^{n+1}=\frac{\widetilde{f}_{M}^{n+1}+\widetilde{f}^{n}\tau\left(\frac{1}{\Delta t}-\frac{ivk}{2}\right)}{1+\tau\left(\frac{1}{\Delta t}+\frac{ivk}{2}\right)}. \tag{C.5}$$

Taylor-expanding about $\tau/\Delta t$ and truncating at first order, we find:

$$\widetilde{f}^{n+1}\approx\widetilde{f}_{M}^{n+1}\left(1-\frac{\tau}{\Delta t}-\frac{ivk\tau}{2}\right)+\widetilde{f}^{n}\left(\frac{\tau}{\Delta t}-\frac{ivk\tau}{2}\right). \tag{C.6}$$

To order $\tau/\Delta t$, we obtain the following,

$$\widetilde{f}^{n+1}\approx\widetilde{f}_{M}^{n+1}+\mathcal{O}\left(\tau/\Delta t\right), \tag{C.7}$$

which is the correct asymptotic result for $\Delta t\gg\tau$. If we instead treat the collision operator in a Crank-Nicholson fashion, we obtain,

$$\widetilde{f}^{n+1}\approx\frac{1}{2}\left(\widetilde{f}_{M}^{n+1}+\widetilde{f}_{M}^{n}\right)+\mathcal{O}\left(\tau/\Delta t\right), \tag{C.8}$$

which is not the correct asymptotic solution for $\Delta t\gg\tau$.

We develop a general θ-scheme which adjusts the time-discretization of the collision operator, depending on the local value of τ. The design constraint is to produce a second-order scheme when $\Delta t\ll\tau$, and the correct asymptotic result for $\Delta t\gg\tau$. We propose the following scheme,

$$\frac{f^{k+1}-f^{k}}{\Delta t}+\frac{v}{2}\left(\frac{\partial f}{\partial x}^{k+1}+\frac{\partial f}{\partial x}^{k}\right)=\theta^{k}\frac{f_{M}^{k+1}-f^{k+1}}{\tau^{k+1}}+\left(1-\theta^{k}\right)\frac{f_{M}^{k}-f^{k}}{\tau^{k}}. \tag{C.9}$$

Here, $0.5 < \theta^k < 1.0$ is the time-centering variable, which is defined as:

$$\theta^k = 0.5 + \frac{0.5}{1 + \tau^k/\Delta t}. \tag{C.10}$$

This expression has the correct limits when $\Delta t \ll \tau$, we obtain Crank-Nicholson,

$$\lim_{\tau^k/\Delta t \to \infty} \theta^k = 0.5, \tag{C.11}$$

and when $\Delta t \gg \tau$, we obtain backward Euler,

$$\lim_{\tau^k/\Delta t \to 0} \theta^k = 1, \tag{C.12}$$

which assures an asymptotic preserving time discretization. The parameter is evaluated using the previous time-step value for τ since, for the problems of interest (shocks), we follow the acoustic CFL and the solution is assumed to not vary significantly from time-step to time-step.

Appendix D

VFPA LO System: Continuity, Momentum, and Ampère's Equation

The HOLO algorithm with the LO system comprising of continuity, momentum, and Ampère's equation is discussed. The HO system is:

$$\frac{f^{k+1,z}_{\alpha_{i,j}} - f^{k}_{\alpha_{i,j}}}{\Delta t} + v_{\alpha_j}\frac{\widehat{f}^{k+1/2,z}_{\alpha_{i+1/2,j}} - \widehat{f}^{k+1/2,z}_{\alpha_{i-1/2,j}}}{\Delta x_i} + \left|v_{\alpha_j}\right|\frac{\xi^{k+1,z-1}_{\alpha_{i+1/2,j}}\widehat{f}^{k+1,*,z}_{\alpha_{i+1/2,j}} - \xi^{k+1,z-1}_{\alpha_{i-1/2,j}}\widehat{f}^{k+1,*,z}_{\alpha_{i-1/2,j}}}{\Delta x_i} + \frac{q_\alpha}{m_\alpha}E_i^{k+1/2,z}\left\{\frac{\widetilde{f}^{k+1/2,z}_{\alpha_{i,j+1/2}} - \widetilde{f}^{k+1/2,z}_{\alpha_{i,j-1/2}}}{\Delta v_{\alpha_j}} + \phi^{k+1,z-1}_{\alpha_i}\frac{\widetilde{f}^{k+1,*,z}_{\alpha_{i,j+1/2}} - \widetilde{f}^{k+1,*,z}_{\alpha_{i,j-1/2}}}{\Delta v_{\alpha_j}}\right\} - \sum_{\beta}^{N_s}\left\{\nu^{HO,LO}_{\alpha\beta_i}\left[D^{HO,LO}_{\alpha\beta_i}\frac{\partial_v f_\alpha|_{i,j+1/2} - \partial_v f_\alpha|_{i,j-1/2}}{\Delta v_{\alpha_j}} + \frac{\widetilde{w}^{LO}_{\alpha\beta_{i,j+1/2}}\widetilde{f}_{\alpha_{i,j+1/2}} - \widetilde{w}^{LO}_{\alpha\beta_{i,j-1/2}}\widetilde{f}_{\alpha_{i,j-1/2}}}{\Delta v_{\alpha_j}}\right]\right\}^{k+1/2,z} \quad \text{(D.1)}$$

Here, $\nu^{HO,LO}_{\alpha\beta_i}$ is evaluated using a combination of HO and LO quantities, for example

$$\nu^{HO,LO}_{ee_i} = 9.174 \times 10^{-17} \frac{\left(T^{HO}_{e_i}\right)^{3/2}}{n^{LO}_{e_i}},$$

and similarly, for $D^{HO,LO}_{ei}$,

$$D^{HO,LO}_{ei_i} = \frac{T^{HO}_{e_i}}{m_e} + \frac{T^{HO}_{i_i} - T^{HO}_{e_i}}{m_i} + \left(u^{LO}_{e_i} - u^{LO}_{i_i}\right)^2 + \gamma^{HO}_{\epsilon_{ei_i}}.$$

The LO system is,

$$\frac{n^{LO,k+1}_{\alpha_i} - n^{HO,k}_{\alpha_i}}{\Delta t} + \frac{nu^{LO,k+1/2}_{\alpha_{i+1/2}} - nu^{LO,k+1/2}_{\alpha_{i-1/2}}}{\Delta x_i} = 0. \tag{D.2}$$

$$\frac{nu^{LO,k+1}_{\alpha_{i+1/2}} - nu^{HO,k+1}_{\alpha_{i+1/2}}}{\Delta t} + \frac{\left(n^{LO}_{\alpha_{i+1}} \widetilde{S}^{HO}_{2,\alpha_{i+1}} - n^{LO}_{\alpha_i} \widetilde{S}^{HO}_{2,\alpha_i}\right)^{k+1/2}}{\Delta x_{i+1/2}} - \frac{q_\alpha}{m_\alpha} \left(n^{LO}_\alpha E\right)^{k+1/2}_{i+1/2} + \sum_{\beta \neq \alpha}^{N_s} \left\{ \nu^{HO,LO}_{\alpha\beta} n^{LO}_\alpha \left(u^{LO}_\alpha - u^{LO}_\beta\right) \right\}^{k+1/2}_{\alpha_{i+1/2}} - \gamma^{HO,k+1}_{nu_{\alpha_{i+1/2}}} = 0. \tag{D.3}$$

$$\epsilon_0 \frac{E^{k+1}_{i+1/2} - E^k_{i+1/2}}{\Delta t} + \sum_\alpha^{N_s} q_\alpha n u^{LO,k+1/2}_{\alpha_{i+1/2}} = 0. \tag{D.4}$$

Here, $\widetilde{S}^{HO}_{2,\alpha_i}$ is the density normalized stress tensor which exposes the stiff isothermal wave in the LO system [75] and is defined as the second moment of the distribution function,

$$\widetilde{S}^{HO}_{2,\alpha_i} = \frac{\sum_{j=1}^{N_v} \Delta v_{\alpha_j} v^2_{\alpha_j} f_{\alpha_{i,j}}}{\sum_{j=1}^{N_v} \Delta v_{\alpha_j} f_{\alpha_{i,j}}}. \tag{D.5}$$

The consistency term, $\gamma^{HO,k+1}_{nu_{\alpha_{i+1/2}}}$ is now defined as,

$$\gamma^{HO,k+1}_{nu_{\alpha_{i+1/2}}} = \frac{nu^{HO,k+1}_{\alpha_{i+1/2}} - nu^{HO,k+1}_{\alpha_{i+1/2}}}{\Delta t} + \frac{\left(n^{HO}_{\alpha_{i+1}}\widetilde{S}^{HO}_{2,\alpha_{i+1}} - n^{HO}_{\alpha_i}\widetilde{S}^{HO}_{2,\alpha_i}\right)^{k+1/2}}{\Delta x_{i+1/2}} - \frac{q_\alpha}{m_\alpha}\left(n^{HO}_\alpha E\right)^{k+1/2}_{i+1/2} + \sum_{\beta\neq\alpha}^{N_s}\left\{\nu^{HO}_{\alpha\beta} n^{HO}_\alpha \left(u^{HO}_\alpha - u^{HO}_\beta\right)\right\}^{k+1/2}_{\alpha_{i+1/2}}. \quad \text{(D.6)}$$

Appendix E

Block Preconditioning for VFPA LO System

The LO system is solved with a Jacobian-Free Newton-Krylov (JFNK) solver. For LO JFNK solver, we use a iterated block preconditioning strategy for the separate species. The iterated lower block tridiagonal preconditioning system is shown in equation (E.1). The preconditioning system is only approximately solved by two passes of block Jacobi iteration of equation (E.1). Here, z is the Jacobi iteration index, J is the approximate block Jacobians, and $\delta\mathcal{M}$ is the Newton updates where $\mathcal{M}$ is the solution of choice (δn_e, $\delta n u_e$, δU_e, δE, δn_i, $\delta n u_i$, δU_i). The first block will solve for the coupled electron moment and Ampère system to capture the electron thermal conduction and electron plasma wave. The ion moment equations are solved with the most recent δn_e, $\delta n u_e$, δU_e and δE. The purpose for the ion block solve is to capture the ion plasma wave physics when we step over $\omega_{p,i}^{-1}$.

Appendix E. Block Preconditioning for VFPA LO System

$$
\left[\begin{array}{cccc|ccc}
J_{n_e n_e} & J_{n_e nu_e} & 0 & 0 & 0 & 0 & 0 \\
J_{nu_e n_e} & J_{nu_e nu_e} & J_{nu_e U_e} & J_{nu_e E} & 0 & 0 & 0 \\
J_{U_e n_e} & J_{U_e nu_e} & J_{U_e U_e} & J_{U_e E} & 0 & 0 & 0 \\
0 & J_{E nu_e} & 0 & J_{EE} & 0 & 0 & 0 \\
\hline
0 & 0 & 0 & 0 & J_{n_i n_i} & J_{n_i nu_i} & 0 \\
J_{nu_i n_e} & J_{nu_i nu_e} & 0 & J_{nu_i E} & J_{nu_i n_i} & J_{nu_i nu_i} & J_{nu_i U_i} \\
J_{U_i n_e} & 0 & J_{U_i U_e} & J_{U_i E} & J_{U_i n_i} & J_{U_i nu_i} & J_{U_i U_i}
\end{array}\right]
\left[\begin{array}{c}
\delta n_e^z \\ \delta nu_e^z \\ \delta U_e^z \\ \delta E^z \\ \hline \delta n_i^z \\ \delta nu_i^z \\ \delta U_i^z
\end{array}\right] =
$$

$$
- \left[\begin{array}{c}
F_{n_e} \\
F_{nu_e} + J_{nu_e n_i}\delta n_i^{z-1} + J_{nu_e nu_i}\delta nu_i^{z-1} \\
F_{U_e} + J_{U_e n_i}\delta n_i^{z-1} + J_{U_e nu_i}\delta nu_i^{z-1} + J_{U_e U_i}\delta U_i^{z-1} \\
F_E + J_{E nu_i}\delta nu_i^{z-1} \\ \hline
F_{n_i} \\ F_{nu_i} \\ F_{U_i}
\end{array}\right]. \tag{E.1}
$$

Appendix F

Discrete Consistency Terms for VFPA

The purpose of the discrete consistency terms for the ion energy equation is similar to the collisionless plasma physics application [75], where they only enforce the discrete truncation error between the HO and LO system. However, for the electrons, the discrete consistency terms have the additional role of picking up the *missing physics* in the Braginskii closure (kinetic effects) as proposed in the nonlinear diffusion acceleration (NDA) method for neutron transport application [51]. In NDA, the LO current is approximated through the Fick's law, and the $\widehat{D}$ consistency term picks up both the truncation error and the physics.

In the continuum, both the LO and the HO system solve the same problem. However, after discretization, different truncation errors appear in each system. There is no guarantee that at this point, the two systems solve the same *discrete* problem. The introduction of the discrete consistency term $\gamma_{nu_{\alpha_{i+1/2}}}^{HO,k+1}$ in the momentum equation and $\widehat{\gamma}_{U_{\alpha,i+1/2}}^{HO,k+1/2}$, and $\eta_{\alpha_i}^{HO,k+1/2}$ in the energy equation enslave the discretization error of LO system to the discretization of the HO system. This is similar to the neutron transport [51], photon transport [53], and the collisionless plasma physics application of the HOLO method [75].

We discuss next the different consistency terms associated with the HO and LO systems.

F.0.1 LO Consistency Terms

The discrete consistency terms required by the LO system are similar in motivation to the other applications, but differ in the form. Firstly, the continuity equation *does not* have a discrete consistency term. Due to the staggered mesh in the LO system, as long as discrete consistency is enforced on the **cell face** number density flux, the discrete consistency between the HO and LO continuity equation is ensured. The need for the discrete consistency in the momentum equation, $\gamma^{HO}_{nu_{\alpha_{i+1/2}}}$, is motivated to enforce discrete consistency in the **cell face** number density flux (which automatically satisfies discrete consistency in the continuity equation) and is defined as,

$$\gamma^{HO,k+1}_{nu_{\alpha_{i+1/2}}} = \frac{[nu^2/n+P]^{HO,k+1/2,z}_{\alpha_{i+1}} - [nu^2/n+P]^{HO,k+1/2,z}_{\alpha_i}}{\Delta x_{i+1/2}} - \frac{q_\alpha}{m_\alpha} n^{HO,k+1/2}_\alpha E^{k+1/2} + \sum_{\beta\neq\alpha}^{N_s} \left\{ \nu^{HO}_{\alpha\beta} n^{HO}_\alpha \left(u^{HO}_\alpha - u^{HO}_\beta \right) \right\}^{k+1/2}_{i+1/2} . \tag{F.1}$$

For the energy equation, the formulation of the consistency terms, $\gamma^{HO,k+1}_{U_{\alpha_{i+1/2}}}$ and $\eta^{HO,k+1}_{U_{\alpha_i}}$ closely resembles that from the gas dynamics application of the HOLO algorithm [118]. The consistency terms are not computed by the evaluation of the LO energy equation with HO moment quantities. Instead, we develop the two terms by understanding the physical definition of a local conservation equation and target the purpose of the consistency terms to pickup the discrete truncation error of the separate advection, and source term operator.

The purpose of the $\gamma^{HO,k+1/2}_{U_{\alpha_{i+1/2}}}$ is to pick up the lack of discrete consistency in the LO numerical flux estimation of the advection terms **with** the discrete 2^{nd} moment of the numerical flux of the HO streaming operator (terms ⓐ and ⓑ in equation (7.33)). This is to say, the following relationship is not satisfied, for ions and electron:

Appendix F. Discrete Consistency Terms for VFPA

For ions:

$$\left[\widehat{u}\left(\widehat{U}+\widehat{P}\right)\right]_{\alpha_{i+1/2}}^{HO,k+1/2}+\widehat{Q}_{\alpha_{i+1/2}}^{HO,k+1/2}=\widehat{S}_{3,\alpha_{i+1/2}}^{HO,k+1/2}+\widehat{\Xi}_{3,\alpha_{i+1/2}}^{k+1,*},$$

For electrons:

$$\left[\widehat{u}\left(\widehat{U}+\widehat{P}\right)\right]_{\alpha_{i+1/2}}^{HO,k+1/2}-\frac{\widehat{\kappa}_{\alpha_{i+1/2}}^{HO,k+1/2}}{m_\alpha}\frac{T_{\alpha_{i+1}}^{HO,k+1/2}-T_{\alpha_i}^{HO,k+1/2}}{\Delta x_{i+1/2}}=\widehat{S}_{3,\alpha_{i+1/2}}^{HO,k+1/2}+\widehat{\Xi}_{3,\alpha_{i+1/2}}^{k+1,*}.$$

Here, $\widehat{S}_{3.\alpha_{i+1/2}}^{HO,k+1/2}$ and $\widehat{\Xi}_{3,\alpha_{i+1/2}}^{k+1,*}$ are the discrete 2^{nd} moments of the terms ⓐ and ⓑ in equation (7.33),

$$\widehat{S}_{3,\alpha_{i+1/2}}^{HO,k+1/2}=\frac{1}{2}\sum_{j=1}^{N_v}\Delta v_{\alpha_j}v_{\alpha_j}^2v_{\alpha_j}\widehat{f}_{\alpha_{i+1/2,j}}^{k+1/2}, \tag{F.2}$$

$$\widehat{\Xi}_{3,\alpha_{i+1/2}}^{HO,k+1,*}=\frac{1}{2}\sum_{j=1}^{N_v}\Delta v_{\alpha_j}v_{\alpha_j}^2\left|v_{\alpha_j}\right|\widehat{f}_{\alpha_{i+1/2,j}}^{k+1,*}. \tag{F.3}$$

Therefore, $\gamma_{U_{\alpha_{i+1/2}}}^{HO,k+1}$ for the ion energy equation is given as,

$$\widehat{\gamma}_{U_{\alpha,i+1/2}}^{HO,k+1/2}=\widehat{S}_{3,\alpha_{i+1/2}}^{HO,k+1/2}+\widehat{\Xi}_{3,\alpha_{i+1/2}}^{k+1,*}-\left\{\left[\widehat{u}\left(\widehat{U}+\widehat{P}\right)\right]_{\alpha_{i+1/2}}^{HO,k+1/2}+\widehat{Q}_{\alpha_{i+1/2}}^{HO,k+1/2}\right\}, \tag{F.4}$$

and for electron energy equation as,

$$\widehat{\gamma}_{U_{\alpha,i+1/2}}^{HO,k+1/2}=\widehat{S}_{3,\alpha_{i+1/2}}^{HO,k+1/2}+\widehat{\Xi}_{3,\alpha_{i+1/2}}^{k+1,*}-\left\{\left[\widehat{u}\left(\widehat{U}+\widehat{P}\right)\right]_{\alpha_{i+1/2}}^{HO,k+1/2}-\frac{\widehat{\kappa}_{\alpha_{i+1/2}}^{HO,k+1/2}}{m_\alpha}\frac{T_{\alpha_{i+1}}^{HO,k+1/2}-T_{\alpha_i}^{HO,k+1/2}}{\Delta x_{i+1/2}}\right\}. \tag{F.5}$$

The purpose of the $\eta_{U_{\alpha_i}}^{HO,k+1/2}$ consistency term is to pickup the *lack* of enforcement of the discrete integration by parts property of the discrete velocity space operators in the HO

system. That is to say, the following relationship is not satisfied,

$$\left\{ \frac{q_\alpha}{m_\alpha} n u_{\alpha_i}^{HO,k+1/2} E_i^{k+1/2} + \sum_{\beta \neq \alpha}^{N_s} \left\{ \nu_{\alpha\beta} \left[D_{\alpha\beta} n_\alpha - (S_{2,\alpha} - n u_\alpha u_\beta) \right] \right\}^{HO,k+1/2} \right\} = \mathcal{V}_{\alpha_i}^{HO,k+1/2} \tag{F.6}$$

where, $\mathcal{V}_{\alpha_i}^{HO,k+1/2}$ is the discrete 2^{nd} moment of the discrete velocity space operators (terms ⓒ, ⓓ, ⓔ, and ⓕ),

$$\mathcal{V}_{\alpha_i}^{HO,k+1/2} = \frac{1}{2} \sum_{j=1}^{N_v} \Delta v_{\alpha_j} v_{\alpha_j}^2 \left\{ \frac{q_\alpha}{m_\alpha} E_i^{k+1/2} \left[\frac{\widetilde{f}_{\alpha_{i,j+1/2}}^{k+1/2} - \widetilde{f}_{\alpha_{i,j-1/2}}^{k+1/2}}{\Delta v_{\alpha_j}} + \phi_{\alpha_i}^{k+1} \frac{\widetilde{f}_{\alpha_{i,j+1/2}}^{k+1,*} - \widetilde{f}_{\alpha_{i,j-1/2}}^{k+1,*}}{\Delta v_{\alpha_j}} \right] - \right.$$
$$\left. \sum_{\beta}^{N_s} \left\{ \nu_{\alpha\beta_i}^{HO} \left[D_{\alpha\beta_i}^{HO} \frac{\partial_v \widetilde{f}_{\alpha_{i,j+1/2}} - \partial_v \widetilde{f}_{\alpha_{i,j-1/2}}}{\Delta v_{\alpha_j}} + \frac{\widetilde{w}_{\alpha\beta_{i,j+1/2}}^{HO} \widetilde{f}_{\alpha_{i,j+1/2}} - \widetilde{w}_{\alpha\beta_{i,j-1/2}}^{HO} \widetilde{f}_{\alpha_{i,j-1/2}}}{\Delta v_{\alpha_j}} \right] \right\}^{k+1/2} \right\} \tag{F.7}$$

Therefore, $\eta_{U_{\alpha_i}}^{HO,k+1}$ for both species are computed as,

$$\eta_{\alpha_i}^{HO,k+1/2} = \mathcal{V}_{\alpha_i}^{HO,k+1/2} -$$
$$\left\{ -\frac{q_\alpha}{m_\alpha} n u_{\alpha_{i+1/2}}^{HO,k+1/2} E_{i+1/2}^{k+1/2} - \sum_{\beta \neq \alpha}^{N_s} \left\{ \nu_{\alpha\beta} \left[D_{\alpha\beta} n_\alpha - (S_{2,\alpha} - n u_\alpha u_\beta) \right] \right\}_i^{HO,k+1/2} \right\}. \tag{F.8}$$

We recall an important subtlety in the closure of the electron heat-flux. We have chosen to close the electron heat-flux using a Braginskii approximation. Here, the consistency term, $\gamma_{U_{\alpha_{i+1/2}}}^{HO}$, picks up the discrete truncation error, but also picks up the physics mismatch between the HO and LO system while exposing the majority of the fast, electron thermal conduction physics in the LO system. This is a similar concept as the *drift current* correction in the NDA application of the HOLO method [51]. In the NDA application, one uses a diffusion approximation for the LO current, and the consistency term is used to 1) pick up the discretization mismatch between the HO and LO system, and 2) pickup the physics error in the LO diffusion approximation.

F.0.2 HO Consistency Terms

The discrete consistency terms associated with the HO system are discussed. From equation (7.33), the collision operator requires the diffusion coefficient, $D_{\alpha\beta}$, the collision frequency, $\nu_{\alpha\beta}$, and the thermally fluctuating random velocity, $w_{\alpha\beta}$, evaluated in terms of the LO solution. Recall that $D_{\alpha\beta}$, $\nu_{\alpha\beta}$, and $w_{\alpha\beta}$ are all nonlinear functions of moments. The collisional diffusion coefficient for like-species interaction is defined as,

$$D^{LO}_{\alpha\alpha_i} = \frac{T^{LO}_{\alpha_i}}{m_\alpha} = 2\frac{\left(U^{LO}_{\alpha_i} - 0.5\left(nu^{LO}_{\alpha_i}\right)^2/n^{LO}_{\alpha_i}\right)}{n^{LO}_{\alpha_i}}.$$

The LO system provides, $n^{LO}_{\alpha_i}$, $nu^{LO}_{\alpha_{i+1/2}}$, and $U^{LO}_{\alpha_i}$. Therefore, for the cell centered number density flux, $nu^{LO}_{\alpha_i}$, some interpolation must be performed. One may wish to naively choose a linear interpolation,

$$nu^{LO}_{\alpha_i} = \frac{nu^{LO}_{\alpha_{i+1/2}} + nu^{LO}_{\alpha_{i-1/2}}}{2}.$$

However, this definition is inconsistent with the true cell centered number density flux, defined as,

$$nu^{HO}_{\alpha_i} = \sum_{j=1}^{N_v} \Delta v_{\alpha_j} v_{\alpha_j} f_{\alpha_{i,j}},$$

i.e.,

$$\frac{nu^{HO}_{\alpha_{i+1/2}} + nu^{HO}_{\alpha_{i-1/2}}}{2} \neq nu^{HO}_{\alpha_i}.$$

The interpolation from the cell face flux to the cell center introduces a unique interpolation error. In order to address this interpolation error mismatch, a number density flux interpolation error consistency term is defined as,

$$\gamma^{HO}_{nu,int_{\alpha_i}} = nu^{HO}_{\alpha_i} - \frac{nu^{HO}_{\alpha_{i+1/2}} + nu^{HO}_{\alpha_{i-1/2}}}{2}. \tag{F.9}$$

The purpose of the consistency term is to enslave the interpolated cell center flux to the true HO definition of the cell center flux. This allows the LO interpolated cell center flux to converge to the true HO cell center flux upon nonlinear convergence. The LO cell centered number density flux is computed as,

$$nu^{LO}_{\alpha_i} = \frac{nu^{LO}_{\alpha_{i+1/2}} + nu^{LO}_{\alpha_{i-1/2}}}{2} + \gamma^{HO}_{nu,int_{\alpha_i}}, \tag{F.10}$$

and the LO fluid velocity as,

$$u^{LO}_{\alpha_i} = \frac{nu^{LO}_{\alpha_i}}{n^{LO}_{\alpha_i}} = \frac{\frac{nu^{LO}_{\alpha_{i+1/2}} + nu^{LO}_{\alpha_{i-1/2}}}{2} + \gamma^{HO}_{nu,int_{\alpha_i}}}{n^{LO}_{\alpha_i}}. \tag{F.11}$$

This definition for LO fluid velocity must be used in computing $T^{LO}_{\alpha_i}$, $\nu^{LO}_{\alpha\beta}$, $D^{LO}_{\alpha\beta_i}$, and $w^{LO}_{\alpha\beta_i}$, for the collision operator of the HO system.

We have presented the discrete, energy conserving $\epsilon^*_{\alpha\beta}$ for the light-to-heavy species interaction reduced Fokker-Planck operator in section 7.3.1. Since $\epsilon^*_{\alpha\beta}$ is not in terms of any trivial moments (n, nu, U), it is not immediately clear how to evaluate this term with the LO quantities. We choose to evaluate $\epsilon_{\alpha\beta}$ using the original definition, with a discrete consistency term to make it energy conserving,

$$D^{LO}_{\alpha\beta_i}\big|_{m_\alpha<m_\beta} = \frac{T^{LO}_{\alpha_i}}{m_\alpha} + \epsilon^{LO}_{\alpha\beta_i} + \gamma^{HO}_{\epsilon,\alpha\beta_i}. \tag{F.12}$$

Here, $\gamma^{HO}_{\epsilon,\alpha\beta_i}$ is the discrete consistency term that will enforce energy conservation of the collision operator between species α and β,

$$\gamma^{HO}_{\epsilon,\alpha\beta_i} = \epsilon^*_{\alpha\beta_i} - \epsilon^{HO}_{\alpha\beta_i}. \tag{F.13}$$

We use $\epsilon^{LO}_{\alpha\beta_i}$ to capture the majority of the thermal equilibration effect between the two species, and $\gamma^{HO}_{\epsilon,\alpha\beta_i}$ is simply used to pick-up the small discrete effect that enforces *discrete* energy conservation. Here, one may argue that since $\epsilon_{\alpha\beta}$ scales as the mass ratio and is small,

the term may be closed completely using ϵ^*. $\epsilon_{\alpha\beta}$ is indeed small for *electron-ion* coupling, however, is non-negligible for $ion_\alpha - ion_\beta$ coupling. Therefore, it becomes important to be able to evaluate ϵ in terms of LO quantities if one wishes to step over $\nu^{-1}_{i_\alpha i_\beta}$.

Appendix G

Picard Iteration for a 0D1V Fokker-Planck Equation

Consider the 0D1V Fokker-Planck equation for species α as:

$$\frac{\partial f_\alpha}{\partial t} = \sum_\beta^{N_s} \nu_{\alpha\beta} \left\{ D_{\alpha\beta} \partial_{vv} f_\alpha + \partial_v \left[(v - u_\beta) f_\alpha \right] \right\}. \tag{G.1}$$

To solve equation (G.1) using a Picard iteration, we semi-discretize in time using a backward Euler scheme (for simplicity) at time-step, k, and introduce a Picard iteration index, z, as:

$$\frac{f_\alpha^{k+1,z} - f_\alpha^k}{\Delta t} - \sum_\beta^{N_s} \nu_{\alpha\beta}^{k+1,z-1} \left\{ D_{\alpha\beta}^{k+1,z-1} \partial_{vv} f_\alpha^{k+1,z} + \partial_v \left[\left(v - u_\beta^{k+1,z-1} \right) f_\alpha^{k+1,z} \right] \right\} = 0. \tag{G.2}$$

Here, the implicit collision frequency, $\nu^{k+1,z-1}$, and collisional diffusion coefficient, $D^{k+1,z-1}$, are computed from the number density, $n_\alpha^{k+1,z-1}$, fluid velocity, $u_\alpha^{k+1,z-1}$, and temperature, $T_\alpha^{k+1,z-1}$, at the previous Picard iteration, $z-1$ as:

$$n_\alpha^{k+1,z-1} = \left\langle 1, f_\alpha^{k+1,z-1} \right\rangle_v, \tag{G.3}$$

$$u_\alpha^{k+1,z-1} = \frac{\left\langle v, f_\alpha^{k+1,z-1} \right\rangle_v}{\left\langle 1, f_\alpha^{k+1,z-1} \right\rangle_v}, \tag{G.4}$$

$$T_\alpha^{k+1,z-1} = m_\alpha \frac{\left\langle \left(v - u_\alpha^{k+1,z-1}\right)^2, f_\alpha^{k+1,z-1} \right\rangle_v}{\left\langle 1, f^{k+1,z-1} \right\rangle_v}. \tag{G.5}$$

$$\nu_{\alpha\beta}^{k+1,z-1} = \nu_{\alpha\beta}^{k+1,z-1}\left(n_\alpha^{k+1,z-1}, n_\beta^{k+1,z-1}, T_\alpha^{k+1,z-1}, T_\beta^{k+1,z-1}\right), \tag{G.6}$$

$$D_{\alpha\beta}^{k+1,z-1} = D_{\alpha\beta}^{k+1,z-1}\left(n_\alpha^{k+1,z-1}, n_\beta^{k+1,z-1}, u_\alpha^{k+1,z-1}, u_\beta^{k+1,z-1}, T_\alpha^{k+1,z-1}, T_\beta^{k+1,z-1}\right). \tag{G.7}$$

With the lagged evaluation for ν, u, and D, equation G.2 is linearized and can be solved for $f_\alpha^{k+1,z}$. The Picard iteration algorithm for solving equation (G.2) is summarized in Algorithm 10:

Algorithm 10: Picard iteration algorithm for solving the Fokker-Planck equation.

1 Set $z = 1$;
2 **while** *Fokker-Planck equation not converged* **do**
3 Compute $n_\alpha^{k+1,z-1}$, $u_\alpha^{k+1,z-1}$, and $T_\alpha^{k+1,z-1}$ from equations (G.3), (G.4), and (G.5);
4 Compute $D_{\alpha\beta}^{k+1,z-1}$, and $\nu^{k+1,z-1}$ from equations (G.7) and (G.6);
5 Solve equation (G.2) for $f_\alpha^{k+1,z}$;
6 Increment $z = z + 1$;
7 Check convergence from equation (7.67);
8 **end**

Appendix H

Moment Acceleration of a Purely Differential HO System

We discuss the extension of the moment-based accelerator concept to the angular Fokker-Planck collision operator, which is a purely differential HO system. We first begin by presenting the 1D transport equation with the angular Fokker-Planck operator with absorption and fixed internal source,

$$\mu\frac{\partial\psi}{\partial x}+\Sigma_a\psi=\frac{\Sigma_{tr}}{2}\left[\frac{\partial}{\partial\mu}\left(1-\mu^2\right)\frac{\partial\psi}{\partial\mu}\right]+\frac{Q}{2}\,. \tag{H.1}$$

We now define the *forward peaked* moment of the angular flux as,

$$\mathcal{M}^l=\int_{\mu=-1}^{\mu=+1}\left(1-\mu\right)^l\psi d\mu=\left\langle\left(1-\mu\right)^l,\psi\right\rangle_\mu\,. \tag{H.2}$$

We will now take the l^{th} forward peaked moment of the transport equation,

$$\begin{aligned}\frac{\partial}{\partial x}\left\langle\left(1-\mu\right)^l\mu,\psi\right\rangle_\mu+\Sigma_a\left\langle\left(1-\mu\right)^l,\psi\right\rangle_\mu=\\ \frac{\Sigma_{tr}}{2}\left\langle\left(1-\mu\right)^l,\frac{\partial}{\partial\mu}\left(1-\mu^2\right)\frac{\partial\psi}{\partial\mu}\right\rangle_\mu+\left\langle\left(1-\mu\right)^l,\frac{Q}{2}\right\rangle_\mu\,.\end{aligned} \tag{H.3}$$

Now, defining, $\tilde{\mu} = 1 - \mu$, we will expand and treat each term in the moment of the transport equation in terms of $\tilde{\mu}$. Starting with the streaming operator,

$$(1-\mu)^l \mu = \tilde{\mu}^l \mu = -\tilde{\mu}^l (1 - \mu - 1) = -\tilde{\mu}^l (\tilde{\mu} - 1) = \tilde{\mu}^l - \tilde{\mu}^{l+1}, \tag{H.4}$$

therefore, the streaming moment in terms of $\tilde{\mu}$, with the definition,

$$d\mu = -d\tilde{\mu} \ , \tag{H.5}$$

becomes,

$$\left\langle \left(\tilde{\mu}^l - \tilde{\mu}^{l+1}\right), \psi \right\rangle_{\mu} = -\left\langle \left(\tilde{\mu}^l - \tilde{\mu}^{l+1}\right), \psi \right\rangle_{\tilde{\mu}} = \left(\mathcal{M}^l - \mathcal{M}^{l+1}\right). \tag{H.6}$$

The absorption term,

$$\Sigma_a (1-\mu)^l \psi = \Sigma_a \tilde{\mu}^l \psi \ , \tag{H.7}$$

is simply,

$$-\Sigma_a \left\langle \tilde{\mu}^l, \psi \right\rangle_{\tilde{\mu}} = \Sigma_a \mathcal{M}^l \ . \tag{H.8}$$

The internal fixed source,

$$(1-\mu)^l \frac{Q}{2} = \tilde{\mu}^l \frac{Q}{2} \ , \tag{H.9}$$

defining the l^{th} moment of the internal source as,

$$\mathcal{Q}^l = -\left\langle \tilde{\mu}^l, Q \right\rangle_{\tilde{\mu}} \ , \tag{H.10}$$

becomes,

$$-\frac{1}{2} \left\langle \tilde{\mu}^l, Q \right\rangle_{\tilde{\mu}} = \frac{\mathcal{Q}^l}{2} \ . \tag{H.11}$$

Finally, the Fokker-Planck operator,

$$(1-\mu)^l \frac{\partial}{\partial \mu}\left(1-\mu^2\right)\frac{\partial \psi}{\partial \mu}\ , \tag{H.12}$$

can be rewritten using the identity,

$$\left(1-\mu^2\right) = (1+\mu)(1-\mu) = -(1-\mu-2)\,\tilde{\mu} = -(\tilde{\mu}-2)\,\tilde{\mu} = 2\tilde{\mu}-\tilde{\mu}^2\ , \tag{H.13}$$

and,

$$\frac{\partial}{\partial \mu} = \frac{\partial}{\partial \tilde{\mu}}\frac{\partial \tilde{\mu}}{\partial \mu} = -\frac{\partial}{\partial \tilde{\mu}}\ , \tag{H.14}$$

as:

$$-\frac{\Sigma_{tr}}{2}\left\langle \tilde{\mu}^l, \partial_{\tilde{\mu}}\left(2\tilde{\mu}-\tilde{\mu}^2\right)\partial_{\tilde{\mu}}\psi\right\rangle_{\tilde{\mu}}\ . \tag{H.15}$$

Now performing integration by parts twice, we rewrite the moment of the Fokker-Planck operator as,

$$\frac{\Sigma_{tr}}{2}\left(2l^2\mathcal{M}^{l-1} - l\,(l+1)\,\mathcal{M}^l\right)\ \text{for } l>0\ . \tag{H.16}$$

Therefore, our l^{th} forward peaked moment of the transport equation is written as,

$$\frac{\partial}{\partial x}\left[\mathcal{M}^l - \mathcal{M}^{l+1}\right] + \Sigma_a \mathcal{M}^l = \frac{\Sigma_{tr}}{2}\left[2l^2\mathcal{M}^{l-1} - l\,(l+1)\,\mathcal{M}^l\right] + \frac{\mathcal{Q}^l}{2}. \tag{H.17}$$

Now, we expand the angular flux, ψ, in terms of orthogonal Legendre polynomials,

$$\psi(x,\mu) = \sum_{n=0}^{\infty} P_n(\mu)\,\psi_n(x)\ , \tag{H.18}$$

where $P_n(\mu)$ is the Legendre polynomial of order n and $\psi_n(x)$ is the Legendre moment of the angular flux. We now re-expand the Legendre polynomial in terms of the forward

peaked polynomial, $\tilde{\mu}^l$. Without going into details, we acknowledge that the Legendre basis polynomial can be re-expanded in terms of $\tilde{\mu}$. For illustration purposes of the method, we present the first four terms of the Legendre polynomial in terms of $\tilde{\mu}$ instead of μ,

- $P_0(\mu) = 1 = \tilde{\mu}^0$,
- $P_1(\mu) = \mu^1 = 1 - \tilde{\mu}^1$,
- $P_2(\mu) = \frac{1}{2}(\mu^2 - 1\mu^0) = \frac{3}{2}\tilde{\mu}^2 - 3\tilde{\mu}^1 + 1\tilde{\mu}^0$,
- $P_3(\mu) = \frac{1}{2}(5\mu^3 + 3\mu^1) = \frac{1}{2}(-5\tilde{\mu}^3 + 15\tilde{\mu}^2 - 15\tilde{\mu}^1 + 5\tilde{\mu}^0)$.

From orthogonality, the Legendre moment of the angular flux can be calculated by weighting the expression in equation (H.18) by P_n and taking the inner product over μ,

$$\psi_n = \frac{1}{a_n^2}\langle P_n, \psi\rangle_\mu \ , \tag{H.19}$$

where a_n^2 is some normalization factor for the n^{th} Legendre moment of the angular flux. Therefore, we can re-expand the Legendre moment of the angular flux in terms of the forward peaked moment of the angular flux. From linearity, the first four Legendre moment in terms of the forward peaked moment is,

- $\psi_0 = \frac{1}{a_0^2}\left[\mathcal{M}^0\right]$,
- $\psi_1 = \frac{1}{a_1^2}\left[\mathcal{M}^0 - \mathcal{M}^1\right]$,
- $\psi_2 = \frac{1}{a_2^2}\left[\frac{3}{2}\mathcal{M}^2 - 3\mathcal{M}^1 + \mathcal{M}^0\right]$,
- $\psi_3 = \frac{1}{a_3^2}\left[\frac{1}{2}(-5\mathcal{M}^3 + 15\mathcal{M}^2 - 15\mathcal{M}^1 + 5\mathcal{M}^0)\right]$.

Therefore, the Fokker-Planck collision operator can be expanded as,

$$\frac{\Sigma_{tr}}{2}\frac{\partial}{\partial\mu}\left[\left(1-\mu^2\right)\frac{\partial\psi}{\partial\mu}\right]=\frac{\Sigma_{tr}}{2}\frac{\partial}{\partial\mu}\left[\left(1-\mu^2\right)\frac{\partial}{\partial\mu}\sum_{n=0}^{\infty}\psi_n P_n\right]= \\ \frac{\Sigma_{tr}}{2}\frac{\partial}{\partial\mu}\left[\left(1-\mu^2\right)\frac{\partial}{\partial\mu}\sum_{n=0}^{\infty}P_n\sum_{l=0}^{n}b_{nl}\mathcal{M}^l\right]. \tag{H.20}$$

Here, b_{nl} is the coefficient for the n^{th} Legendre index for the l^{th} forward peaked moment of the angular flux. Now that the Fokker-Planck collision operator is expanded in terms of the forward peaked moments of the angular flux, we wish to explore the structure between the transport equation and the forward peaked moment equations. Recall the forward peaked moment equation in equation (H.17),

$$\frac{\partial}{\partial x}\left[\mathcal{M}^l-\mathcal{M}^{l+1}\right]+\Sigma_a\mathcal{M}^l=\frac{\Sigma_{tr}}{2}\left[2l^2\mathcal{M}^{l-1}-l\left(l+1\right)\mathcal{M}^l\right]+\frac{\mathcal{Q}^l}{2}.$$

As observed, equation for $\mathcal{M}^l$ is coupled with the equation for $\mathcal{M}^{l+1}$ and $\mathcal{M}^{l-1}$ through the streaming and collision moment terms. In solving the moment equation, a truncation must be made such as to close the system of equations. However, suppose if a true $\mathcal{M}^{L+1}$ can be supplied (say from the actual solution of the original transport equation) such that a truncation is not necessary, a closure can be self-consistenty performed such as to not introduce any truncation error and reconstruct the true angular flux, ψ. Similarly, if we have the exact $\mathcal{M}^l$ that satisfied the transport equation, we can satisfy the moment equations exactly such that $\psi=\sum_{n=0}^{L}P_n\sum_{l=0}^{n}b_{nl}\mathcal{M}^l$ is satisfied. This unique structure between the transport equation and the moment equation will be used to construct a moment-based accelerator scheme to accelerate the convergence of the purely differential Fokker-Planck collision operator. We now define a coupled system of higher-dimensional (HO) transport equation and a lower-dimensional (LO) moment equations,

HO equation:

$$\mu\frac{\partial\psi}{\partial x}^{HO}+\Sigma_a\psi^{HO}=\frac{\Sigma_{tr}}{2}\frac{\partial}{\partial\mu}\left[\left(1-\mu^2\right)\frac{\partial}{\partial\mu}\sum_{n=0}^{L}P_n\sum_{l=0}^{n}b_{nl}\mathcal{M}^{LO,l}\right],$$

LO equations:

$$\begin{aligned}
\frac{\partial}{\partial x}\left[\mathcal{M}^{LO,0}-\mathcal{M}^{LO,1}\right]+\Sigma_a\mathcal{M}^{LO,0} &= \frac{\mathcal{Q}^0}{2}\\
\frac{\partial}{\partial x}\left[\mathcal{M}^{LO,1}-\mathcal{M}^{LO,2}\right]+\Sigma_a\mathcal{M}^{LO,1} &= \frac{\Sigma_{tr}}{2}\left[2\mathcal{M}^{LO,0}-2\mathcal{M}^{LO,1}\right]+\frac{\mathcal{Q}^1}{2}\\
\frac{\partial}{\partial x}\left[\mathcal{M}^{LO,2}-\mathcal{M}^{LO,3}\right]+\Sigma_a\mathcal{M}^{LO,2} &= \frac{\Sigma_{tr}}{2}\left[8\mathcal{M}^{LO,1}-6\mathcal{M}^{LO,2}\right]+\frac{\mathcal{Q}^2}{2}\\
&\vdots\\
\frac{\partial}{\partial x}\left[\mathcal{M}^{LO,L}-\mathcal{M}^{HO,L+1}\right]+\Sigma_a\mathcal{M}^{LO,L} &= \frac{\Sigma_{tr}}{2}\left[2L^2\mathcal{M}^{LO,L-1}-L\left(L+1\right)\mathcal{M}^{LO,L}\right]+\frac{\mathcal{Q}^l}{2}.
\end{aligned}$$

There are two significant modification to the original transport equation and moment equations that are important to point out. The first modification is in the finite truncation performed in the *HO* equation for the collision operator. It is observed that the Legendre polynomial expansion of the angular flux expansion in the collision operator is truncated at L^{th} order. The second modification is that for the L^{th} *LO* moment equation, the $\mathcal{M}^{L+1}$ is closed using the *HO* calculation for $\mathcal{M}^{HO,L+1}$. The truncation in the collision operator is performed in order to be implemented on a computer. This is a significant modification as the expansion will only recover the original collision operator in the limit of $n\rightarrow\infty$. Therefore, this truncation introduces a truncation error to the collision operator. We wish to fix this issue by adding an operator consistency term, γ_{FP}, such that we return the original HO equation without any truncation,

$$\mu\frac{\partial\psi}{\partial x}^{HO}+\Sigma_a\psi^{HO}=\frac{\Sigma_{tr}}{2}\frac{\partial}{\partial\mu}\left[\left(1-\mu^2\right)\frac{\partial}{\partial\mu}\sum_{n=0}^{L}P_n\sum_{l=0}^{n}b_{nl}\mathcal{M}^{LO,l}\right]+\gamma_{FP}\ . \tag{H.21}$$

The γ_{FP} acts to pick up the truncation error introduced in the series truncation of the angular flux in the Fokker-Planck operator,

$$\gamma_{FP}=-\frac{\Sigma_{tr}}{2}\frac{\partial}{\partial\mu}\left[\left(1-\mu^2\right)\frac{\partial}{\partial\mu}\sum_{n=0}^{L}P_n\sum_{l=0}^{n}b_{nl}\mathcal{M}^{HO,l}\right]+\frac{\Sigma_{tr}}{2}\frac{\partial}{\partial\mu}\left[\left(1-\mu^2\right)\frac{\partial\psi}{\partial\mu}^{HO}\right] \tag{H.22}$$

Therefore if, $\mathcal{M}^{LO,l} = \mathcal{M}^{HO,l}$, for all l, we recover the original Fokker-Planck collision operator and the HO and LO equations are self-consistently satisfied. Hence, when performing a discretization of ψ on a mesh, we will still require a transport sweep and source iteration. However, the hope of the accelerator is that the moment equation will provide an acceleration to the collision source such that it will reduce the required source iteration. The hope is that the moment solution will effectively provide both, the spatial and angular structure of ψ that results from the collision operator in a much efficient manner compared to a standard source iteration.

Curriculum Vitae



RESEARCH INTERESTS AND BACKGROUND: A broad interest in computational physics algorithm development and implementation, with emphasis on kinetic plasma physics, both collisionless (PIC) and collisional (Vlasov-Fokker-Planck). Strong interest in inertial confinement fusion (ICF) physics and applications.

PERSONAL INTERESTS: Having fun and spending quality time with friends and families. Rock climbing, mountaineering, running, camping, snowboarding, playing the piano, violin, etc.

BEVERAGE OF CHOICE: Scotch

EDUCATION

UNIVERSITY OF NEW MEXICO, Albuquerque, NM
Ph.D. in Nuclear Engineering, May 2014
Dissertation: Moment-Based Accelerators for Kinetic Problems with Application to Inertial Confinement Fusion
Advisors: Dr. Anil K. Prinja, Dr. Dana A. Knoll

UNIVERSITY OF IDAHO, Idaho Falls, ID
M.S. in Nuclear Engineering, Aug. 2010
Thesis: Development of a Jacobian-Free Newton-Krylov Method with Kinetic Enslavement to Implicitly Solve Vlasov-Poisson System in Plasma Physics
Advisors: Dr. Fred Gunnerson, Dr. Dana A. Knoll

EMBRY-RIDDLE AERONAUTICAL UNIVERSITY, Prescott, AZ
B.S. in Space Physics, Dec. 2007
Thesis: Numerical Investigation of Magnetohydrodynamic Flow Control through a Nozzle
Advisors: Dr. Shigeo Hayashibara, Dr. Phillip Anz-Meador

EXPERIENCE

2014-current **XCP-6, Plasma Theory and Applications Group Computational Physics Division, Los Alamos National Lab. (LANL),** Post-Doctoral Research Associate
Mentors: Dr. Andrei Simakov, Dr. Luis Chacòn

2011-2014	**T-3, Solid Mechanics and Fluid Dynamics Group Theoretical Division, Los Alamos National Lab. (LANL),** Graduate Research Assistant Mentor: Dr. Dana A. Knoll
2008-2010	**Center for Space Nuclear Research/Multi-Physics Methods Group, Idaho National Lab. (INL),** Next Degree Student, Research Scientist, CFD Technician Mentors: Dr. Steve Howe, Dr. Dana A. Knoll
2006	**Hbar Technologies, LLC,** Summer Intern, Machine Technician Mentor: Dr. Gerald Jackson
2006	**Embry-Riddle Aeronautical University,** Teacher's Assistant for Fluid Dynamics, Teacher's Assistant for Thermodynamics Professor: Dr. Shigeo Hayashibara

ACTIVITIES Member of the American Physical Society (APS), the Society for Industrial and Applied Mathematics (SIAM), American Institute of Aeronautics and Astronautics (AIAA), and the American Nuclear Society (ANS).

PUBLIC.: PEER REV.

W.T. Taitano, L. Chacón, *"Charge-and-Energy Conserving Moment-Based Accelerator for a Multi-Species Vlasov-Fokker-Planck-Ampère System, Part I: Collisionless Aspects,"*, J. Comp. Phys., in preparation.

W.T. Taitano, D.A. Knoll, L. Chacòn, *"Charge-and-Energy Conserving Moment-Based Accelerator for a Multi-Species Vlasov-Fokker-Planck Ampère System, Part II: Collisional Aspects,"*, J. Comp. Phys., in preparation.

W.T. Taitano, D.A. Knoll, *"Modeling of Kinetic Mix of High-Z Pusher Material into Fuel for ICF Omega Targets,"*, Phys. of Plasmas, in preparation.

W.T. Taitano, D.A. Knoll, L. Chacòn, J. Reisner, A.K. Prinja, *"Moment-Based Acceleration for Neutral Gas Kinetics with BGK Collision Operator,"* Transp. Theory and Stat. Phys., (2014), accepted.

J.A. Willer, **W.T. Taitano**, D.A. Knoll, *"Leveraging Anderson Acceleration for Improved Convergence of Iterative Solutions to Transport Systems,"* J. Comp. Phys., (2014), submitted.

G. Chen, L. Chacòn, C. Leibs, D. Knoll, **W. Taitano**, *" Fluid Preconditioning for Newton-Krylov-Based, Fully Implicit, Electrostatic Particle-in-Cell Simulations,"* J. Comp. Phys., **258** (2013), pp. 555-567.

W.T. Taitano, D.A. Knoll, L. Chacòn, G. Chen, *"Development of a Consistent and Stable Fully Implicit Moment Method for Vlaosv-Ampère Particle-in-Cell (PIC) System,"* SIAM J. Sci. Comp., **35**, 5, (2013), pp. S126-S149.

R.C. Martineau, R.A. Berry, A. Esteve, K.D. Hamman, D.A. Knoll, H. Park, **W. Taitano**, *"Comparison of Natural Convection Flows under VHTR Type Conditions Modeled by both the Conservation and Incompressible Forms of the Navier-Stokes Equations,"* Nuc. Eng. and Design, **240**, 6, (2010), pp. 1371-1385.

D. Gaston, G. Hansen, S. Kadioglu, D.A. Knoll, C. Newman,H. Park, C. Permann, **W.T. Taitano**, *"Parallel Multiphysics Algorithms and Software for Computational Nuclear Engineering,"* J. of Phys.: Conference Series, **180**, (2009), 012012.

PUBLIC.: TALKS

J. Webb, B. Gross, **W. Taitano**, *"Conceptual Design of a CERMET NTR Fission Core using Multiphysics Modeling Techniques,"* 47^{th} AIAA/ASME/SAE/ASEE Joint Propulsion Conference & Exhibit AIAA -2012-5947, (2011).

H. Park, D. Gaston, S. Kadioglu, D. Knoll, R. Martineau, **W. Taitano**, *"Tightly Coupled Multiphysics Simulations for Pebble Bed Reactor,"* Intern. Conf. on Math., Comput. Meth. & Reactor Phys., (2009).

W.T. Taitano, S. Hayashibara, *"Numerical Investigatioin of Magnetohydrodynamics Flow Control through a Nozzle,"* 44^{th} AIAA/ASEM/ SAE/ASEE Joint Propulsion Conference & Exhibit AIAA-2008-4960, (2008).